

National and Kapodistrian University of Athens  
Department of Physics  
Section of Nuclear and Particle Physics



Master's Thesis  
Optimization of  $t\bar{t}+b\bar{b}$  background simulation in the search for  
c-quark Yukawa coupling through the  $t\bar{t}H(b\bar{b}/c\bar{c})$  process in the  
CMS experiment at the LHC

Nikolaos Plastiras  
R.N. 7110112200218

Three Member Examination Committee:  
Vellidis K., A. Prof., Phys. Dept., NKUA (Main Supervisor)  
Sphicas P., Prof., Phys. Dept., NKUA  
Papadimitriou I., A. Prof., Phys. Dept., NKUA

July 17, 2024



# ABSTRACT

The study of the associated production of top and bottom quark-antiquark pairs,  $t\bar{t}+b\bar{b}$ , in proton-proton (pp) collisions at the LHC poses a significant challenge due to the nonnegligible mass of the b quark and the disparate energy scales characterizing interactions involving top and b quarks. Consequently, the determination of appropriate energy scales for the calculation of the  $t\bar{t}+b\bar{b}$  matrix element and the seamless interface of the matrix element with parton distributions and parton showers becomes a non-trivial task. Uncertainties related to the choice of renormalization and factorization scales in matrix element calculations at NLO in QCD, can lead to uncertainties of up to 50% in fiducial and differential cross section predictions of  $t\bar{t}+b\bar{b}$  production. Improved knowledge of this process is therefore of prime interest in order to validate or discard scale choices made for state-of-the-art simulations. The primary objective of this thesis is to optimize the simulation of  $t\bar{t}+b\bar{b}$  production, a pivotal background in numerous searches and measurements. Notably,  $t\bar{t}+b\bar{b}$  is a prominent background in the associated production of a top quark pair with a Higgs boson ( $t\bar{t}H$ ), where the Higgs boson decays to a pair of b or c quarks ( $H \rightarrow b\bar{b}/c\bar{c}$ ). An improved understanding of  $t\bar{t}+b\bar{b}$  production will help reduce the uncertainties in the process  $t\bar{t}H(b\bar{b}/c\bar{c})$ , increasing the sensitivity of the search for c-quark Yukawa coupling, which is an important parameter of the Standard Model, being the Yukawa coupling of a second generation quark.



# ΠΕΡΙΛΗΨΗ

Η μελέτη της συσχετισμένης παραγωγής ζευγών top και bottom κουάρκ-αντικουάρκ ( $t\bar{t}+b\bar{b}$ ), σε συγκρούσεις πρωτονίου-πρωτονίου (p-p) στον LHC αποτελεί σημαντική πρόκληση λόγω της μη αμελητέας μάζας του b κουάρκ και των διαφορετικών ενεργειακών κλιμάκων της ισχυρής αλληλεπίδρασης στις οποίες παράγονται τα top και b κουάρκς. Συνεπώς, η εύρεση κατάλληλων ενεργειακών κλιμάκων για τον υπολογισμό των στοιχείων πίνακα  $t\bar{t}+b\bar{b}$  και η απρόσκοπτη σύνδεσή τους με τους πίδακες παρτονίων (PS) και τις συναρτήσεις κατανομής παρτονίων (PDF) γίνεται δύσκολη υπόθεση. Αβεβαιότητες που σχετίζονται με την επιλογή κλιμάκων επανακανονικοποίησης και παραγοντοποίησης σε υπολογισμούς στοιχείων πινάκων σε NLO τάξη της Κβαντικής Χρωμοδυναμικής (QCD) μπορούν να οδηγήσουν σε αβεβαιότητες έως και 50% στις προβλέψεις των μετρήσεων περιεκτικών και διαφορικών ενεργών διατομών για την παραγωγή  $t\bar{t}+b\bar{b}$ . Η βελτιωμένη γνώση αυτής της διεργασίας είναι, συνεπώς, πολύ σημαντική για τον έλεγχο των επιλογών κλιμάκων που γίνονται για τις πλέον σύγχρονες προσομοιώσεις. Ο κύριος στόχος αυτής της διπλωματικής εργασίας είναι η βελτιστοποίηση της προσομοίωσης της παραγωγής  $t\bar{t}+b\bar{b}$ , ενός καθοριστικού υποβάθρου σε πολλές αναζητήσεις και μετρήσεις. Ειδικότερα, η διεργασία  $t\bar{t}+b\bar{b}$  αποτελεί ένα ισχυρό υπόβαθρο για την συσχετισμένη παραγωγή ενός ζεύγους top κουάρκς και ενός μποζόνιου Higgs ( $t\bar{t}H$ ), όπου το μποζόνιο Higgs διασπάται σε ένα ζεύγος b ή c κουάρκς ( $H \rightarrow b\bar{b}/c\bar{c}$ ). Η καλύτερη κατανόηση της παραγωγής  $t\bar{t}+b\bar{b}$  θα συμβάλλει στην μείωση των αβεβαιοτήτων της διεργασίας  $t\bar{t}H(b\bar{b}/c\bar{c})$ , αυξάνοντας την ευαισθησία αναζήτησης της σύζευξης Yukawa του c κουάρκ, η οποία είναι μία σημαντική παράμετρος του Καθιερωμένου Προτύπου, όντας σύζευξη Yukawa ενός κουάρκ δεύτερης γενιάς.



# Contents

<b>Abstract</b>	<b>iii</b>
<b>Περίληψη</b>	<b>v</b>
<b>List of Tables</b>	<b>xi</b>
<b>List of Figures</b>	<b>xxiii</b>
<b>Introduction</b>	<b>xxv</b>
<b>1 The Standard Model of Particle Physics</b>	<b>1</b>
1.1 Particles of the Standard Model . . . . .	1
1.2 Standard Model as a gauge theory . . . . .	4
1.2.1 Quantum Electrodynamics . . . . .	5
1.2.2 Quantum Chromodynamics . . . . .	8
1.2.3 Electroweak unification . . . . .	10
1.2.4 Spontaneous symmetry breaking . . . . .	13
1.3 The top quark . . . . .	19
1.4 The Higgs boson . . . . .	22
1.5 Associated top-pair and Higgs-boson production . . . . .	26
1.5.1 Associated top-pair and heavy-flavored jets production . . . . .	27
<b>2 Experimental Setup</b>	<b>29</b>
2.1 Large Hadron Collider . . . . .	29
2.1.1 LHC layout and accelerator systems . . . . .	30
2.1.2 Luminosity . . . . .	33
2.2 Compact Muon Solenoid Detector . . . . .	34
2.2.1 Coordinate system and collider quantities . . . . .	35
2.2.2 CMS layout . . . . .	37
2.2.3 Inner tracking system . . . . .	38

2.2.4	Electromagnetic Calorimeter . . . . .	41
2.2.5	Hadronic Calorimeter . . . . .	43
2.2.6	The magnet . . . . .	45
2.2.7	The muon system . . . . .	46
2.2.8	Forward detectors . . . . .	48
2.2.9	Triggering system . . . . .	49
2.3	The L1 muon trigger performance . . . . .	52
<b>3</b>	<b>Event Simulation</b>	<b>57</b>
3.1	Matrix element calculations in perturbative QCD . . . . .	57
3.1.1	Factorization and parton distribution functions . . . . .	58
3.1.2	Higher order QCD calculations . . . . .	61
3.2	The Parton Shower approach . . . . .	63
3.3	Matching NLO calculations with PS . . . . .	65
3.3.1	The POWHEG method . . . . .	65
3.4	The Monte-Carlo method for event generation . . . . .	67
3.5	Structure of a simulated pp collision . . . . .	69
<b>4</b>	<b><math>t\bar{t} + hf</math> jets Analysis</b>	<b>71</b>
4.1	Analysis strategy for $t\bar{t}H$ . . . . .	71
4.1.1	Jet tagging with ParticleNet . . . . .	72
4.1.2	Event classification with Particle Transformer . . . . .	75
4.2	$t\bar{t}+b\bar{b}$ simulation . . . . .	79
4.2.1	Motivation . . . . .	79
4.2.2	Generator configuration . . . . .	81
4.2.3	Observables . . . . .	84
4.2.4	Dileptonic channel . . . . .	84
4.2.5	Semileptonic channel . . . . .	91
4.2.6	Fully hadronic channel . . . . .	95
4.3	Summary . . . . .	99
<b>Bibliography</b>		<b>101</b>
<b>Appendix A - Powheg Box Res <math>t\bar{t}+b\bar{b}</math> Configuration</b>		<b>113</b>
A.1	Collider setup . . . . .	113
A.2	Parameters for the generation of spin correlated $t\bar{t}$ decays . . . . .	113
A.3	Integrator and event generator settings . . . . .	114
A.4	Scale settings . . . . .	114

A.5 Damping . . . . .	115
A.6 Scale and PDF reweighting . . . . .	115
A.7 Parallel runs settings . . . . .	116
A.8 Other settings . . . . .	116
<b>Appendix B - Supplemental Material</b>	<b>117</b>
B.1 DL channel . . . . .	117
B.2 SL channel . . . . .	132
B.3 FH channel . . . . .	145

**x**

# List of Tables

1.1	Bosons and forces of the Standard Model [12] . . . . .	2
1.2	Leptons of the Standard Model [12] . . . . .	3
1.3	Quarks of the Standard Model [12] . . . . .	4
1.4	W-boson-decay branching ratios [12] . . . . .	21
1.5	Higgs-boson-production cross sections assuming $m_H = 125.2$ GeV for a LHC CM energy of $\sqrt{s} = 13$ TeV [72]. . . . .	24
1.6	Higgs-boson-decay branching ratios assuming $m_H = 125.2$ GeV at NLO [72] . .	25
2.1	Overview of the accelerator complex for protons and lead ions. The different accelerators, their design beam energy, and the ionization degree of the lead ions in each phase are summarized in the upper part of the table. The lower part gives some design parameters of the LHC machine. . . . .	32
4.1	Classes definition for jet tagging . . . . .	74
4.2	Number of events generated for each damping parameter across the three channels	84
4.3	Description of all measured observables for each of the three channels . . . . .	85



# List of Figures

1.1	Illustration of the Higgs potential [49] . . . . .	15
1.2	Coupling of fermions and bosons to the Higgs field [52] . . . . .	18
1.3	Feynman diagrams for top quark pair production processes at leading order . . . . .	20
1.4	Cross section of $t\bar{t}$ production as a function of the center-of-mass energy at the CMS experiment [66] . . . . .	20
1.5	Feynman diagrams at leading order for Higgs boson production via (a) gluon-gluon fusion, (b) vector boson fusion (c) Higgsstrahlung and (d) associate production with heavy quarks. . . . .	23
1.6	Higgs-boson (a) production cross sections and (b) branching ratios as a function of $m_H$ at $\sqrt{s} = 13$ TeV [72] . . . . .	25
1.7	Feynman diagrams of the $t\bar{t}H$ process with all possible final states of the $t\bar{t}$ system with the Higgs boson decaying to (a) a pair of b quarks and (b) a pair of c quarks. . . . .	26
1.8	Feynman diagrams of the $t\bar{t} + \text{jets}$ process with all possible final states of the $t\bar{t}$ system with the addition of emission of (a) a pair of b quarks and (b) a pair of c quarks . . . . .	27
2.1	Schematic overview of the LHC. The two beams circulate in opposite directions. Beam 1 (blue) is moving clockwise around the ring and beam 2 (red) moves counter-clockwise. The two beams can collide only in the regions containing the four experiments [82]. . . . .	30
2.2	The CERN accelerator complex [88] . . . . .	31
2.3	Cumulative delivered and recorded luminosity versus time for 2010-2012, 2015-2018, and 2022-2023 (pp data only) [95] . . . . .	34
2.4	(a) Schematic overview of the CMS detector [96] and (b) the right-handed coordinate system [97] . . . . .	35
2.5	Pseudorapidity as a function of the polar angle $\theta$ [98] . . . . .	36
2.6	Slice showing CMS sub-detectors and how particles interact with them [99] . . . . .	37

2.7	Schematic overview of the CMS tracking system [85]. The silicon pixel detector in the center is surrounded by the silicon strip detector which consists of endcaps and different barrel components. . . . .	38
2.8	Sketch of a typical pixel sensor used in the pixel detector [100] . . . . .	39
2.9	Schematic structure of a CMS silicon microstrip sensor [103] . . . . .	40
2.10	Simulated cascades inside electromagnetic crystals [109]. . . . .	41
2.11	A schematic view of the CMS Electromagnetic calorimeters [107]. . . . .	42
2.12	A quadrant of the CMS hadronic calorimeter [114]. . . . .	44
2.13	Value of $ B $ (left) and field lines (right) predicted on a longitudinal section of the CMS detector, for the underground model at a central magnetic flux density of 3.8T. Each fieldline represents a magnetic flux increment of 6 Wb [105]. . . . .	45
2.14	Schematic view in the $r - z$ plane of a CMS detector quadrant [123]. . . . .	47
2.15	The CASTOR calorimeter [127]. . . . .	49
2.16	Diagram of the CMS L1 Trigger system [129] . . . . .	50
2.17	The single-muon L1 Trigger efficiency for 2024 data as a function of probe muon $p_T$ . . . . .	53
2.18	The single-muon L1 Trigger efficiency for 2024 data as a function of probe muon (a) $\eta$ and (b) $\phi$ . . . . .	53
2.19	Heatmap of the single-muon L1 Trigger efficiency for 2024 data . . . . .	54
2.20	The charge misidentification for 2024 data as a function of the reconstructed muon $p_T$ . . . . .	55
2.21	Heatmap of the charge misidentification for 2024 data . . . . .	55
3.1	LO contributions to the DGLAP splitting kernels . . . . .	60
3.2	NNPDF3.1 NNLO pdf as a function of the momentum fraction $x$ of partons in a proton. The NNPDF3.1 NNLO pdf set is evaluated at two different scales $\mu_F^2$ . On the left at lower energy scale $\mu_F^2 = 10\text{GeV}^2$ and on the right at higher energy scale $\mu_F^2 = 10^4\text{GeV}^2$ . The gluon pdfs (red) are scaled by a factor of 1/10 as their contribution is by far dominant at low momentum fraction $x$ [145]. . . . .	61
3.3	Example of (a) Born, (b) Real and (c) Virtual Feynman diagrams . . . . .	61
3.4	The simulation chain for a typical process at hadron colliders. The red blob in the center represents the hard collision, surrounded by a tree-like structure representing Bremsstrahlung as simulated by parton showers. The purple blob indicates a secondary hard scattering event. Parton-to-hadron transitions are represented by light green blobs, dark green blobs indicate hadron decays, while yellow lines signal soft photon radiation [162]. . . . .	70

4.1 (a) The architecture of the ParticleNet. (b) The structure of the EdgeConv block [163] . . . . .	73
4.2 Jet tagging categories used in the analysis. The C and B categories with indices 2 or higher are considered tightly tagged (red), one or higher medium (magenta + red), zero and higher loose (purple + magenta + red). . . . .	75
4.3 The architecture of (a) Particle Transformer (b) Particle Attention Block (c) Class Attention Block [164] . . . . .	76
4.4 Renormalized scores in the search region with all years combined for the $t\bar{t}H$ categories (top) and the $t\bar{t}Z$ categories (bottom) in the FH channel. Data points are not included because the analysis is blinded. . . . .	77
4.5 Renormalized scores in the search region with all years combined for $t\bar{t}+jets$ categories in the FH channel. Data points are not included because the analysis is blinded. . . . .	78
4.6 Ratio of normalized differential cross section predictions of the Powheg+OL+P8 $t\bar{t}+bb$ 4fs modeling approach with different $\mu_R$ and $\mu_F$ scale settings relative to the measured normalized differential cross sections for (a) the number of jets and (b) $H_T$ of jets in the $\geq 5$ jets: $\geq 3b$ phase space [168] . . . . .	79
4.7 Ratio of normalized differential cross section predictions of the Powheg+OL+P8 $t\bar{t}+bb$ 4fs modeling approach with different $\mu_R$ and $\mu_F$ scale settings relative to the measured normalized differential cross sections for (a) the extra light jet and (b) $H_T$ of light jets in the $\geq 6$ jets: $\geq 3b, \geq 3$ light phase space [168] . . . . .	80
4.8 Fiducial cross sections measurement compared to the Powheg+OL+P8 4fs signal model and alternative $\mu_R$ and $\mu_F$ scale choices. Variations of the $\mu_R$ and $\mu_F$ scales by factors of two up and down are indicated via triangles. The nominal values for $\mu_F$ and $\mu_R$ correspond to $\xi_F = 0.5, \xi_R = 0.5$ respectively [169]. . . . .	80
4.9 Distribution of the transverse momentum of (a) the $t/\bar{t}$ and (b) the $b/\bar{b}$ quarks for the six different settings used in the simulation. The lower panel shows the ratio of the nominal setting to the variations. The shaded bands represent statistical uncertainties. The last bins contain the overflow events. . . . .	86
4.10 Distribution of $H_T$ for (a) $t\bar{t}$ , (b) prompt $bb$ and (c) $bb$ , originating from top quarks, systems for the six different settings used in the simulation. The lower panel shows the ratio of the nominal setting to the variations. The shaded bands represent statistical uncertainties. The last bins contain the overflow events. . . . .	87
4.11 Distribution of the angular separation of (a) $t\bar{t}$ and (b) prompt $bb$ systems for the six different settings used in the simulation. The lower panel shows the ratio of the nominal setting to the variations. The shaded bands represent statistical uncertainties. The last bins contain the overflow events. . . . .	88

4.12 Distributions of (a) invariant mass and (b) $H_T$ of the $t\bar{t}+b\bar{b}$ system for the six different settings used in the simulation. The lower panel shows the ratio of the nominal setting to the variations. The shaded bands represent statistical uncertainties. The last bins contain the overflow events. . . . .	88
4.13 Distribution of (a) the transverse momentum of all the leptons (charged and neutral) and (b) the $H_T$ of $\ell^-\ell^+$ system for the six different settings used in the simulation. The lower panel shows the ratio of the nominal setting to the variations. The shaded bands represent statistical uncertainties. The last bins contain the overflow events. . . . .	89
4.14 Distribution of $H_T$ for (a) $e^-e^+$ , (b) $\mu^-\mu^+$ , (c) $\tau^-\tau^+$ , (d) $e\mu$ (e) $e\tau$ and (f) $\mu\tau$ systems for the six different settings used in the simulation. The lower panel shows the ratio of the nominal setting to the variations. The shaded bands represent statistical uncertainties. . . . .	89
4.15 Distribution of the transverse momentum of the extra light jet for the six different settings used in the simulation. The lower panel shows the ratio of the nominal setting to the variations. The shaded bands represent statistical uncertainties. The last bins contain the overflow events. . . . .	90
4.16 Distribution of $H_T$ for (a) $t\bar{t}$ , (b) prompt $b\bar{b}$ and (c) $b\bar{b}$ , originating from top quarks, systems for the six different settings used in the simulation. The lower panel shows the ratio of the nominal setting to the variations. The shaded bands represent statistical uncertainties. The last bins contain the overflow events. . . .	91
4.17 Distribution of the transverse momentum of (a) the $t/\bar{t}$ and (b) the $b/\bar{b}$ quarks for the six different settings used in the simulation. The lower panel shows the ratio of the nominal setting to the variations. The shaded bands represent statistical uncertainties. The last bins contain the overflow events. . . . .	92
4.18 Distribution of (a) invariant mass and (b) $H_T$ for the $t\bar{t}+b\bar{b}$ system for the six different settings used in the simulation. The lower panel shows the ratio of the nominal setting to the variations. The shaded bands represent statistical uncertainties. The last bins contain the overflow events. . . . .	92
4.19 Distribution of the transverse momentum of (a) light flavor quarks and (b) leptons, and (c) the $H_T$ of $\bar{q}q'$ system for the six different settings used in the simulation. The lower panel shows the ratio of the nominal setting to the variations. The shaded bands represent statistical uncertainties. The last bins contain the overflow events. . . . .	93

4.20 Distribution of $H_T$ for (a) ud (b) cs (c) us and (d) cd systems for the six different settings used in the simulation. The lower panel shows the ratio of the nominal setting to the variations. The shaded bands represent statistical uncertainties. The last bins contain the overflow events. . . . .	94
4.21 Distribution of the transverse momentum of the extra light jet for the six different settings used in the simulation. The lower panel shows the ratio of the nominal setting to the variations. The shaded bands represent statistical uncertainties. The last bin contains the overflow events. . . . .	95
4.22 Distribution of the transverse momentum of (a) the $t/\bar{t}$ and (b) the $b/\bar{b}$ quarks for the six different settings used in the simulation. The lower panel shows the ratio of the nominal setting to the variations. The shaded bands represent statistical uncertainties. The last bins contain the overflow events. . . . .	95
4.23 Distribution of $H_T$ for (a) $t\bar{t}$ , (b) prompt $b\bar{b}$ and (c) $b\bar{b}$ , originating from top quarks, systems for the six different settings used in the simulation. The lower panel shows the ratio of the nominal setting to the variations. The shaded bands represent statistical uncertainties. The last bins contain the overflow events. . . . .	96
4.24 Distribution of (a) invariant mass and (b) $H_T$ for the $t\bar{t}+b\bar{b}$ system for the six different settings used in the simulation. The lower panel shows the ratio of the nominal setting to the variations. The shaded bands represent statistical uncertainties. The last bins contain the overflow events. . . . .	97
4.25 Distribution of (a) the transverse momentum of all the quarks and (b) the $H_T$ of $\bar{q}q'$ system for the six different settings used in the simulation. The lower panel shows the ratio of the nominal setting to the variations. The shaded bands represent statistical uncertainties. The last bins contain the overflow events. . . . .	97
4.26 Distribution of $H_T$ for (a) ud (b) cs (c) us and (d) cd systems for the six different settings used in the simulation. The lower panel shows the ratio of the nominal setting to the variations. The shaded bands represent statistical uncertainties. The last bins contain the overflow events. . . . .	98
4.27 Distribution of the transverse momentum of the extra light jet for the six different settings used in the simulation. The lower panel shows the ratio of the nominal setting to the variations. The shaded bands represent statistical uncertainties. The last bins contain the overflow events. . . . .	99
B.1 Distributions of (a) energy, (b) reconstructed mass, (c) azimuthal angle and (d) rapidity of the $t/\bar{t}$ quarks for the six different settings used in the simulation. The lower panel shows the ratio of the nominal setting to the variations. The shaded bands represent statistical uncertainties. The last bins contain the overflow events.	118

B.2 Distributions of (a) transverse momentum, (b) invariant mass, (c) angular separation and (d) rapidity of the $t\bar{t}$ system for the six different settings used in the simulation. The lower panel shows the ratio of the nominal setting to the variations. The shaded bands represent statistical uncertainties. The last bins contain the overflow events. . . . .	119
B.3 Distributions of (a) energy, (b) transverse momentum, (c) azimuthal angle and (d) pseudorapidity of all the $b/\bar{b}$ quarks for the six different settings used in the simulation. The lower panel shows the ratio of the nominal setting to the variations. The shaded bands represent statistical uncertainties. The last bins contain the overflow events. . . . .	120
B.4 Distributions of (a) transverse momentum, (b) invariant mass, (c) angular separation and (d) rapidity of the $b\bar{b}$ system, related to top quarks, for the six different settings used in the simulation. The lower panel shows the ratio of the nominal setting to the variations. The shaded bands represent statistical uncertainties. The last bins contain the overflow events. . . . .	121
B.5 Distributions of (a) transverse momentum, (b) invariant mass, (c) angular separation and (d) rapidity of the prompt $b\bar{b}$ system for the six different settings used in the simulation. The lower panel shows the ratio of the nominal setting to the variations. The shaded bands represent statistical uncertainties. The last bins contain the overflow events. . . . .	122
B.6 Distributions of (a) energy, (b) transverse momentum, (c) azimuthal angle and (d) pseudorapidity of all the leptons (charged and neutral) for the six different settings used in the simulation. The lower panel shows the ratio of the nominal setting to the variations. The shaded bands represent statistical uncertainties. The last bins contain the overflow events. . . . .	123
B.7 Distributions of (a) transverse momentum, (b) invariant mass, (c) angular separation and (d) rapidity of the $\ell^-\ell^+$ system for the six different settings used in the simulation. The lower panel shows the ratio of the nominal setting to the variations. The shaded bands represent statistical uncertainties. The last bins contain the overflow events. . . . .	124
B.8 Distributions of (a) transverse momentum, (b) invariant mass, (c) angular separation and (d) rapidity of the $e^-e^+$ system for the six different settings used in the simulation. The lower panel shows the ratio of the nominal setting to the variations. The shaded bands represent statistical uncertainties. The last bins contain the overflow events. . . . .	125

B.9 Distributions of (a) transverse momentum, (b) invariant mass, (c) angular separation and (d) rapidity of the $\mu^-\mu^+$ system for the six different settings used in the simulation. The lower panel shows the ratio of the nominal setting to the variations. The shaded bands represent statistical uncertainties. The last bins contain the overflow events. . . . .	126
B.10 Distributions of (a) transverse momentum, (b) invariant mass, (c) angular separation and (d) rapidity of the $\tau^-\tau^+$ system for the six different settings used in the simulation. The lower panel shows the ratio of the nominal setting to the variations. The shaded bands represent statistical uncertainties. The last bins contain the overflow events. . . . .	127
B.11 Distributions of (a) transverse momentum, (b) invariant mass, (c) angular separation and (d) rapidity of the $e\mu$ system for the six different settings used in the simulation. The lower panel shows the ratio of the nominal setting to the variations. The shaded bands represent statistical uncertainties. The last bins contain the overflow events. . . . .	128
B.12 Distributions of (a) transverse momentum, (b) invariant mass, (c) angular separation and (d) rapidity of the $e\tau$ system for the six different settings used in the simulation. The lower panel shows the ratio of the nominal setting to the variations. The shaded bands represent statistical uncertainties. The last bins contain the overflow events. . . . .	129
B.13 Distributions of (a) transverse momentum, (b) invariant mass, (c) angular separation and (d) rapidity of the $\mu\tau$ system for the six different settings used in the simulation. The lower panel shows the ratio of the nominal setting to the variations. The shaded bands represent statistical uncertainties. The last bins contain the overflow events. . . . .	130
B.14 Distributions of (a) energy, (b) transverse momentum, (c) azimuthal angle and (d) pseudorapidity of the extra light jet for the six different settings used in the simulation. The lower panel shows the ratio of the nominal setting to the variations. The shaded bands represent statistical uncertainties. The last bins contain the overflow events. . . . .	131
B.15 Distributions of (a) energy, (b) reconstructed mass, (c) azimuthal angle and (d) rapidity of the $t/\bar{t}$ quarks for the six different settings used in the simulation. The lower panel shows the ratio of the nominal setting to the variations. The shaded bands represent statistical uncertainties. The last bins contain the overflow events.	132

B.16 Distributions of (a) transverse momentum, (b) invariant mass, (c) angular separation and (d) rapidity of the $t\bar{t}$ system for the six different settings used in the simulation. The lower panel shows the ratio of the nominal setting to the variations. The shaded bands represent statistical uncertainties. The last bins contain the overflow events. . . . .	133
B.17 Distributions of (a) energy, (b) transverse momentum, (c) azimuthal angle and (d) pseudorapidity of all the $b/\bar{b}$ quarks for the six different settings used in the simulation. The lower panel shows the ratio of the nominal setting to the variations. The shaded bands represent statistical uncertainties. The last bins contain the overflow events. . . . .	134
B.18 Distributions of (a) transverse momentum, (b) invariant mass, (c) angular separation and (d) rapidity of the $b\bar{b}$ system, related to top quarks, for the six different settings used in the simulation. The lower panel shows the ratio of the nominal setting to the variations. The shaded bands represent statistical uncertainties. The last bins contain the overflow events. . . . .	135
B.19 Distributions of (a) transverse momentum, (b) invariant mass, (c) angular separation and (d) rapidity of the prompt $b\bar{b}$ system for the six different settings used in the simulation. The lower panel shows the ratio of the nominal setting to the variations. The shaded bands represent statistical uncertainties. The last bins contain the overflow events. . . . .	136
B.20 Distributions of (a) energy, (b) transverse momentum, (c) azimuthal angle and (d) pseudorapidity of all the leptons (charged and neutral) for the six different settings used in the simulation. The lower panel shows the ratio of the nominal setting to the variations. The shaded bands represent statistical uncertainties. The last bins contain the overflow events. . . . .	137
B.21 Distributions of (a) energy, (b) transverse momentum, (c) azimuthal angle and (d) pseudorapidity of the light flavor quarks, related to W bosons, for the six different settings used in the simulation. The lower panel shows the ratio of the nominal setting to the variations. The shaded bands represent statistical uncertainties. The last bins contain the overflow events. . . . .	138
B.22 Distributions of (a) transverse momentum, (b) invariant mass, (c) angular separation and (d) rapidity of the $\bar{q}q'$ system for the six different settings used in the simulation. The lower panel shows the ratio of the nominal setting to the variations. The shaded bands represent statistical uncertainties. The last bins contain the overflow events. . . . .	139

B.23 Distributions of (a) transverse momentum, (b) invariant mass, (c) angular separation and (d) rapidity of the ud system for the six different settings used in the simulation. The lower panel shows the ratio of the nominal setting to the variations. The shaded bands represent statistical uncertainties. The last bins contain the overflow events. . . . .	140
B.24 Distributions of (a) transverse momentum, (b) invariant mass, (c) angular separation and (d) rapidity of the cs system for the six different settings used in the simulation. The lower panel shows the ratio of the nominal setting to the variations. The shaded bands represent statistical uncertainties. The last bins contain the overflow events. . . . .	141
B.25 Distributions of (a) transverse momentum, (b) invariant mass, (c) angular separation and (d) rapidity of the us system for the six different settings used in the simulation. The lower panel shows the ratio of the nominal setting to the variations. The shaded bands represent statistical uncertainties. The last bins contain the overflow events. . . . .	142
B.26 Distributions of (a) transverse momentum, (b) invariant mass, (c) angular separation and (d) rapidity of the cd system for the six different settings used in the simulation. The lower panel shows the ratio of the nominal setting to the variations. The shaded bands represent statistical uncertainties. The last bins contain the overflow events. . . . .	143
B.27 Distributions of (a) energy, (b) transverse momentum, (c) azimuthal angle and (d) pseudorapidity of the extra light jet for the six different settings used in the simulation. The lower panel shows the ratio of the nominal setting to the variations. The shaded bands represent statistical uncertainties. The last bins contain the overflow events. . . . .	144
B.28 Distributions of (a) energy, (b) reconstructed mass, (c) azimuthal angle and (d) rapidity of the $t/\bar{t}$ quarks for the six different settings used in the simulation. The lower panel shows the ratio of the nominal setting to the variations. The shaded bands represent statistical uncertainties. The last bins contain the overflow events.	145
B.29 Distributions of (a) transverse momentum, (b) invariant mass, (c) angular separation and (d) rapidity of the $t\bar{t}$ system for the six different settings used in the simulation. The lower panel shows the ratio of the nominal setting to the variations. The shaded bands represent statistical uncertainties. The last bins contain the overflow events. . . . .	146

B.30 Distributions of (a) energy, (b) transverse momentum, (c) azimuthal angle and (d) pseudorapidity of all the $b/\bar{b}$ quarks for the six different settings used in the simulation. The lower panel shows the ratio of the nominal setting to the variations. The shaded bands represent statistical uncertainties. The last bins contain the overflow events. . . . .	147
B.31 Distributions of (a) transverse momentum, (b) invariant mass, (c) angular separation and (d) rapidity of the $b\bar{b}$ system, related to top quarks, for the six different settings used in the simulation. The lower panel shows the ratio of the nominal setting to the variations. The shaded bands represent statistical uncertainties. The last bins contain the overflow events. . . . .	148
B.32 Distributions of (a) transverse momentum, (b) invariant mass, (c) angular separation and (d) rapidity of the prompt $b\bar{b}$ system for the six different settings used in the simulation. The lower panel shows the ratio of the nominal setting to the variations. The shaded bands represent statistical uncertainties. The last bins contain the overflow events. . . . .	149
B.33 Distributions of (a) energy, (b) transverse momentum, (c) azimuthal angle and (d) pseudorapidity of the light flavor quarks, related to W bosons, for the six different settings used in the simulation. The lower panel shows the ratio of the nominal setting to the variations. The shaded bands represent statistical uncertainties. The last bins contain the overflow events. . . . .	150
B.34 Distributions of (a) transverse momentum, (b) invariant mass, (c) angular separation and (d) rapidity of the $\bar{q}q'$ system for the six different settings used in the simulation. The lower panel shows the ratio of the nominal setting to the variations. The shaded bands represent statistical uncertainties. The last bins contain the overflow events. . . . .	151
B.35 Distributions of (a) transverse momentum, (b) invariant mass, (c) angular separation and (d) rapidity of the ud system for the six different settings used in the simulation. The lower panel shows the ratio of the nominal setting to the variations. The shaded bands represent statistical uncertainties. The last bins contain the overflow events. . . . .	152
B.36 Distributions of (a) transverse momentum, (b) invariant mass, (c) angular separation and (d) rapidity of the cs system for the six different settings used in the simulation. The lower panel shows the ratio of the nominal setting to the variations. The shaded bands represent statistical uncertainties. The last bins contain the overflow events. . . . .	153

B.37 Distributions of (a) transverse momentum, (b) invariant mass, (c) angular separation and (d) rapidity of the us system for the six different settings used in the simulation. The lower panel shows the ratio of the nominal setting to the variations. The shaded bands represent statistical uncertainties. The last bins contain the overflow events. . . . .	154
B.38 Distributions of (a) transverse momentum, (b) invariant mass, (c) angular separation and (d) rapidity of the cd system for the six different settings used in the simulation. The lower panel shows the ratio of the nominal setting to the variations. The shaded bands represent statistical uncertainties. The last bins contain the overflow events. . . . .	155
B.39 Distributions of (a) energy, (b) transverse momentum, (c) azimuthal angle and (d) pseudorapidity of the extra light jet for the six different settings used in the simulation. The lower panel shows the ratio of the nominal setting to the variations. The shaded bands represent statistical uncertainties. The last bins contain the overflow events. . . . .	156



# Introduction

The Standard Model of elementary particles (SM) is a quantum field theory, developed in the 1970s, describing the elementary particles and their interactions. Despite its successes in explaining various phenomena, the SM leaves several key questions unanswered, including the nature of dark matter, neutrino oscillations [1–3], the hierarchy problem, and the strong CP problem. These limitations underscore the need for models beyond the Standard Model (BSM) to comprehensively account for observed phenomena in particle physics.

Experimental validation of BSM theories often relies on probing the properties of SM particles for deviations or anomalies. Such investigations are conducted at high-energy colliders like the Large Hadron Collider (LHC) at CERN, which provides a fertile ground for exploring new physics. With the discovery of the Higgs boson in 2012 by the ATLAS and the CMS collaborations with a mass of approximately 125 GeV [4–6], the last component of the SM was found. A chain of experiments have been undertaken to study its properties at the LHC.

This project takes part in the CMS collaboration, aiming to probe the production of the Standard Model Higgs boson associated with a top quark pair ( $t\bar{t}H$ ). Specifically,  $t\bar{t}H$  has been established as a powerful channel in the search of  $H \rightarrow b\bar{b}$ . As technology advances, our attention turns to even more challenging searches, such as the  $H \rightarrow c\bar{c}$  decay, which represents a crucial test of the fermion mass generation mechanism in the Standard Model.

In this context, the associated production of top and bottom quark-antiquark pairs,  $t\bar{t}+b\bar{b}/c\bar{c}$ , emerges as a leading background. The understanding of the  $t\bar{t}+b\bar{b}/c\bar{c}$  process is important in this measurement, as an accurate and reliable description of the  $t\bar{t}+b\bar{b}/c\bar{c}$  process will allow for a measurement of the signal process under scrutiny with high accuracy.

This thesis is structured as follows: Chapter 1 presents an introduction of the theoretical background. In chapter 2, the LHC and CMS experiment are introduced. Chapter 3 gives a short overview of the event simulation procedure.

In chapter 4, a MC generator study for  $t\bar{t}+b\bar{b}$  background process modelling is presented. Some MC generator free parameters are varied and the sensitivity of the events on these free parameters are analysed. The aim of this study is to obtain a better understanding of this important and irreducible background process for the  $t\bar{t}H(b\bar{b}/c\bar{c})$  search and thereby improve the sensitivity of measuring this process.



# 1 The Standard Model of Particle Physics

The Standard Model (SM) of particle physics describes the theoretical framework in which the work of this thesis is interpreted. In Section 1.1 a brief overview of the particles of the SM is given. The interactions and properties of these particles are described by gauge theories which are discussed in Section 1.2. In particular, in Section 1.2.1, a brief overview of Quantum Electrodynamics is presented followed by the description of Quantum Chromodynamics in Section 1.2.2. The discussion continues with the electroweak unification, an important aspect of the SM, in Section 1.2.3. Based on these discussions, an open question of the SM is the origin of particle masses, which will be discussed in Section 1.2.4. In Sections 1.3 and 1.4 a quick overview of the top quark and the Higgs boson is presented respectively followed by the associated production of these two particles in Section 1.5. Finally, in Section 1.5.1 the production of top quark-antiquark pairs with the addition of emitted jets is emphasized, the main subject of this thesis.

All discussions and results in this thesis are presented using natural units, following the convention  $c = \hbar = 1$ . To this effect, energies, momenta and masses all have units of energy, commonly expressed in electronvolt,  $1\text{eV} = 1.6 \cdot 10^{-19}\text{J}$ . Similarly, electric charge is given in elementary units,  $1e = 1.6 \cdot 10^{-19}\text{C}$ . Additionally, throughout this thesis, Einstein's convention of summation over repeated indices is employed.

## 1.1 Particles of the Standard Model

In the SM, the elementary particles are divided into two categories according to their spin: fermions and bosons. Fermions are particles with half-integer spin that adhere to Fermi-Dirac statistics [7, 8], which does not allow two identical particles to occupy the same quantum state (Pauli exclusion principle) [9]. The Pauli principle allows fermions to build complex structures such as atoms or nuclei, which are organised at varying energy levels governed by the quantum state of the particles. These complex structures constitute all visible matter of the universe which makes fermions the building blocks of our world. Bosons are particles with integer spin and adhere to Bose-Einstein statistics [10, 11], which allows multiple bosons to occupy the

same quantum state. Bosons are the force carriers of the SM and as such are responsible for the interactions of fundamental particles.

## Bosons and Interactions

In the SM, three of the four fundamental forces are described, the electromagnetic force, the weak force, and the strong force. The gravitational force cannot be described by the SM<sup>1</sup>. In Table 1.1 the bosons of the SM and some of their properties are summarized.

Table 1.1. Bosons and forces of the Standard Model [12]

Force	Gauge boson	Multiplicity	Charge	Spin	Mass [GeV]
Electromagnetic	Photon ( $\gamma$ )	1	0	1	0
Weak(charged)	W bosons ( $W^\pm$ )	2	$\pm 1$	1	$80.377 \pm 0.012$
Weak (neutral)	Z boson(Z)	1	0	1	$91.188 \pm 0.002$
Strong	Gluons (g)	8	0	1	0
Higgs boson		1	0	0	$125.25 \pm 0.17$

The electromagnetic interaction is mediated by photons,  $\gamma$ . Photons are massless spin-1 particles without any charge. Their interactions are described in quantum electrodynamics (QED) as will be introduced in Section 1.2.1. Since the force carrier is massless, the electromagnetic force has an infinite interaction range.

The force carriers for the weak interaction are the charged  $W^+$ ,  $W^-$  bosons and the neutral Z boson, discovered at CERN in 1983 [13, 14]. The  $W^\pm$  bosons are the only known particles to change the flavor of fermions. Both, the  $W^\pm$  and Z bosons are massive, i.e. they have a mass of the order of 100 GeV. As a result, the weak force acts on short range, in the order of approximately  $10^{-3}$  fm.

The EM and weak forces can be unified to the electroweak force via the Glashow-Salam-Weinberg model [15–17]. This unification describes all three bosons (W boson, Z boson, photon) and both forces, as will be explained in Section 1.2.3. The unified theory, though, could not explain the origin of the mass of W and Z bosons. This intricate fact implies that there is something fundamental hidden in the SM. Specifically, it means that the gauge symmetry for the electroweak interaction  $SU(2)_L \otimes U(1)_Y$  is broken. This symmetry breaking is explained via the Higgs mechanism<sup>2</sup>, as detailed in Section 1.2.4. With the Higgs mechanism, the Higgs boson is introduced to the SM, which is a neutral scalar (spin-0) boson. By construction, the

<sup>1</sup>Quantum gravity effects are not sensitive to the current accessible energy scale.

<sup>2</sup>This mechanism is also called NGAEBHGHKMP mechanism (Nambu-Goldstone-Anderson-Englert-Brout-Higgs-Gilbert-Hagen-Kibble-Migdal-Polyakov) [18–30]. For readability purposes, the name Higgs mechanism will be used.

$W^\pm$  and  $Z$  bosons obtained their masses through interactions with the Higgs field. From the same mechanism, the Higgs boson itself also, obtained its mass, which was first successfully measured at the LHC experiments ATLAS and CMS in 2012 [4–6].

Finally, the SM also describes the strong interaction, which is responsible for the hadronization of particles and the formation of atomic nuclei. The force carriers of the strong force are gluons. The gluons are massless and electrically neutral like the photons, but they have nine different color charge combinations, grouped into a color octet and a singlet with three different color charges. Unlike photons, gluons do carry color charge by themselves, and thus they can directly interact with one another. The strong force strength has a dynamic behaviour, resulting in the fact that its strength becomes larger if the colored charge particles are further apart.

## Fermions

The fermions of the SM can be classified into two subgroups: quarks and leptons. The difference between these two groups lies in their interactions. There are 3 generations of fermions, each of which includes two leptons and two quarks, for a total of 12 fermions. In addition to these, each particle in the SM has a corresponding antiparticle with opposite charge but otherwise identical properties. Table 1.2 provides an overview of leptons, whereas Table 1.3 presents the quarks.

Table 1.2. Leptons of the Standard Model [12]

Gen.	Particle	Charge	Mass [MeV]
1	Electron ( $e$ )	-1	0.511
	Electron neutrino ( $\nu_e$ )	0	$< 1.1 \cdot 10^{-6}$
2	Muon ( $\mu$ )	-1	105.7
	Muon neutrino ( $\nu_\mu$ )	0	$< 0.19$
3	Tau ( $\tau$ )	-1	$1776.86 \pm 0.12$
	Tau neutrino ( $\nu_\tau$ )	0	$< 18.2$

Leptons are fermions that interact via the electroweak force, but not the strong force as they do not carry color charge. Each generation of leptons consists of a charged lepton and a neutral lepton. The charged leptons are electron, muon and tau ( $e, \mu, \tau$ ) and carry a charge of  $-1$  while the neutral leptons are the electron neutrino, muon neutrino and tau neutrino ( $\nu_e, \nu_\mu, \nu_\tau$ ). Obviously, due to the zero electric charge, the neutrinos interact exclusively via the weak interaction. Furthermore, all charged leptons have non-zero mass, while in the SM, the neutrinos are considered to be massless. The charged lepton of the first generation, the electron, which is the lightest of the three, is the only stable particle while the other, heavier ones, muon

and tau, decay into electrons via the charged current of the electroweak interaction. Hence, electrons are one of the fundamental particles in atomic physics, responsible for the formation of atoms.

Table 1.3. Quarks of the Standard Model [12]

Gen.	Particle	Charge	Mass [GeV]
1	Up quark (u)	2/3	$(2.16_{-0.26}^{+0.49}) \cdot 10^{-3}$
	Down quark (d)	-1/3	$(4.67_{-0.17}^{+0.48}) \cdot 10^{-3}$
2	Charm quark (c)	2/3	$1.27 \pm 0.02$
	Strange quark (s)	-1/3	$(93.4_{-3.4}^{+8.6}) \cdot 10^{-3}$
3	Top quark (t)	2/3	$172.69 \pm 0.30$
	Bottom quark (b)	-1/3	$4.18_{-0.02}^{+0.03}$

Quarks are fermions that interact both with the electroweak and the strong force and together with the gluons are the only known fundamental particles that carry color charge. Each generation consists of a pair of an up-type quark that has electric charge  $+2/3$  and a down-type quark that carries electric charge equal to  $-1/3$ . The first generation of quarks consists of the up quark and the down quark, which can be considered as ground states of the quark sector and primarily make up the nucleons (protons and neutrons), the building blocks of atomic nuclei. The second generation of quarks consists of charm and strange quarks and the third generation consists of top and bottom quarks. The quarks within each generation become progressively heavier, with the top quark standing out as the heaviest fundamental particle in the SM, with mass equal to  $172.69 \pm 0.3$  GeV.

Quarks undergo a process called hadronization, forming color-neutral bound states with integer electromagnetic charge, known as hadrons. The hadrons can be further categorized into mesons, which are a combination of a quark and an antiquark, and (anti)baryons which are combinations of three quarks or antiquarks. This hadronization is explained through the color confinement property of QCD, discussed in Section 1.2.2. Notably, the top quark's substantial width of  $\sim 1.5$  GeV leads to a brief lifespan shorter than the timescale of hadronization ( $\sim 10^{-24}$  s), preventing it from experiencing hadronization and causing it to decay as a free particle.

## 1.2 Standard Model as a gauge theory

The SM is a well-established theoretical model formulated in quantum field theory describing all the elementary particles and fundamental interactions in our Universe with the exception

of the gravitational interaction. The SM is based on the principle of symmetry, where different particles or fields of specific properties are described by different irreducible representations of a symmetry group. The fundamental interactions between these particles are precisely delineated by defining their gauge symmetry group according to a set of transformation laws. The local gauge symmetry group related to the strong, weak and the electromagnetic interactions in the SM is:

$$SU(3)_C \otimes SU(2)_L \otimes U(1)_Y \quad (1.1)$$

where the subscript  $C$  is the color charge,  $L$  indicates that the  $SU(2)$  symmetry group is exclusive to left-handed fields and  $Y$  is the hypercharge relating the electric charge and the weak isospin. The symmetry group  $SU(3)_C$  represents the strong interaction described by Quantum Chromodynamics (QCD), where 3 (the dimension of the group) indicates the number of color charges (red, green, blue), while the electromagnetic and the weak interactions are unified as electroweak interaction under  $SU(2)_L \otimes U(1)_Y$  symmetry group [17].

Mathematically, the SM of particle physics is formulated as a relativistic quantum theory in which the elementary particles are described as quantum fields. The quantum fields are described by Lagrangian densities:

$$\mathcal{L} = \mathcal{L}[\psi, \partial_\mu \psi] \quad (1.2)$$

These Lagrangian densities include the dynamics of the quantum fields and their interactions. Particles in the SM are described as excitations of the quantum fields, represented by quantum field operators  $\psi(x)$ , where  $x$  are four-dimensional space-time coordinates. The Lagrangian density is also a function of the gradient of the field  $\partial_\mu \psi(x)$ , where  $\partial_\mu = \partial/\partial x_\mu$  is the four-dimensional partial derivative w.r.t.  $x$  with  $\mu = 0, 1, 2, 3$ .

### 1.2.1 Quantum Electrodynamics

QED describes the dynamics of electrically charged particles and the photon. The description of QED was first formulated in works of S. Tomonaga [31], J. Schwinger [32, 33], R. Feynman [34–36], and F. Dyson [37, 38]. The Lagrangian density of a free fermion field (which can for example be an electron or a quark) with particle mass  $m$  can be postulated as [39]

$$\mathcal{L}_{Dirac} = \bar{\psi}(i\gamma^\mu \partial_\mu)\psi - m\bar{\psi}\psi \quad (1.3)$$

where  $\gamma^\mu$  are the four-dimensional Dirac matrices and  $\bar{\psi} = \psi^\dagger \gamma^0$  is the adjoint field. Essentially, the first term of the Lagrangian density describes the kinematic behavior of the field  $\psi$ , while the second term describes the particle at rest, quantified via its mass  $m$ . Using the Euler-Lagrange

equation this yields the Dirac equation for a free fermion with mass  $m$ ,

$$(i\gamma^\mu \partial_\mu - m)\psi(x) = 0 \quad (1.4)$$

The Lagrangian is invariant under the  $U(1)$  global transformation. However, such transformation on the field at one point in space-time should not be correlated to any point in the whole Universe, otherwise this would violate special relativity, as no information can spread faster than light. Therefore a field should be transformed locally by taking into account of its continuous space and time coordinates  $x_\mu$ :

$$\psi(x) \rightarrow \psi'(x) = e^{i\alpha(x)Q} \psi(x) \quad (1.5)$$

where  $\alpha(x)$  is the arbitrary function dependent on space-time and  $Q$  is the electromagnetic charge operator. Nonetheless, the transformed Lagrangian that followed is not locally  $U(1)_{EM}$  invariant. In order to make a Lagrangian invariant under a local transformation, one needs to "gauge" the invariance by adding an extra term to the Lagrangian. The Lagrangian in Eq. 1.3 is made invariant by considering an interaction term between a spin  $\frac{1}{2}$  field and a spin 1 field in the form of:

$$\mathcal{L}_{int} = -gA_\mu \bar{\psi} \gamma^\mu \psi \quad (1.6)$$

so that the Lagrangian density can be written as:

$$\mathcal{L}_{QED} = \mathcal{L}_{Dirac} + \mathcal{L}_{int} = \bar{\psi}(i\gamma^\mu \partial_\mu)\psi - m\bar{\psi}\psi - gA_\mu \bar{\psi} \gamma^\mu \psi \quad (1.7)$$

where  $g$  is an arbitrary coupling constant that determines the interaction strength of the two fields. The gauge transformation dictates that the spin 1 gauge field  $A_\mu = (\Phi(x), \vec{A}(x))$  (the physical photon field) transforms as:

$$A_\mu(x) \rightarrow A'_\mu(x) = A_\mu(x) + \partial_\mu \alpha(x) \quad (1.8)$$

Alternatively, the partial derivative  $\partial_\mu$  can also be replaced with the gauge covariant derivative

$$\mathcal{D}_\mu = \partial_\mu + igA_\mu(x) \quad (1.9)$$

yielding the same invariance behavior. The additional term in Eq. 1.7 describes the interaction of photons and fermions. What is not yet included in this equation is the description of the propagation (i.e. kinematics) of the photon field. By construction, the field  $A_\mu(x)$  is a boson

field, whose equation of motion is described by the Proca equation,

$$(\partial_\mu \partial^\mu - m_A^2) A^\nu = 0 \quad (1.10)$$

corresponding to the Lagrangian density

$$\mathcal{L}_{Proca} = -\frac{1}{4} F^{\mu\nu} F_{\mu\nu} + \frac{1}{2} m_A^2 A^\nu A_\nu \quad (1.11)$$

Here,  $F^{\mu\nu} = (\partial^\mu A^\nu - \partial^\nu A^\mu)$  is the field strength tensor, which describes the EM field components at space-time point  $x$  and their derivatives w.r.t. space and time. In Eq. (1.11), the first term can be associated with the kinetic energy of the vector field and the second term with the particle of the field at rest, quantified by its mass  $m_A$ . This is a generalized description of a vector field. Adding Eq. (1.11) to the QED Langrangian in Eq. (1.7) shows that the first term which is the kinetic term is indeed invariant under the  $U(1)$  transformation while the second one which is the mass term, is not. This implies for QED that the particle associated with the photon field (i.e. the photon) has to be massless such that the second term vanishes and the gauge invariance is retained. In summary, this yields the full QED Lagrangian density

$$\mathcal{L}_{QED} = \bar{\psi}(i\gamma_\mu \partial^\mu)\psi - m\bar{\psi}\psi - gA_\mu\bar{\psi}\gamma^\mu\psi - \frac{1}{4}F^{\mu\nu}F_{\mu\nu} \quad (1.12)$$

or using the covariant derivative defined in Eq. (1.9), Eq. (1.12) can be written as:

$$\mathcal{L}_{QED} = \bar{\psi}(i\gamma_\mu D^\mu - m)\psi - \frac{1}{4}F^{\mu\nu}F_{\mu\nu} \quad (1.13)$$

Noether's theorem [40] states that the transformation in Eq. (1.5) under the internal symmetry  $U(1)_{EM}$  is connected to a conserved quantity. The Noether's current corresponds to an electric four-current:

$$j_{EM}^\mu = -g\bar{\psi}\gamma^\mu\psi \quad (1.14)$$

and the conserved quantity, the electric charge,  $Q$ , is determined by integrating  $j_{EM}^0$ :

$$Q = -g \int d^3x \bar{\psi}\gamma^0\psi \quad (1.15)$$

In the quantum framework, the quantum field  $\Psi$  is related to the probability amplitude, and the total probability over all space must be 1. Therefore, the integral of the probability density  $\bar{\psi}\gamma^0\psi$  over space must equal 1:

$$\int d^3x \bar{\psi}\gamma^0\psi = 1 \quad (1.16)$$

By this assertion, Eq. (1.15) implies the coupling strength  $-g$  is in fact the conserved quantity, which for electromagnetism is the electric charge.

### 1.2.2 Quantum Chromodynamics

QCD is the theory describing the strong interaction between quarks and gluons, which are the fundamental constituents of hadrons such as protons and neutrons. The formulation of QCD originated from the works of H. Fritzsch [41], M. Gell-Mann [42, 43] and G. Zweig [44]. The basic building blocks of QCD are quarks, which carry color charge, and gluons, the mediators of the strong force, which also carry color charge. For free quarks, the Lagrangian is expressed as:

$$\mathcal{L}_{quarks} = \sum_j \bar{q}_j(x)(i\gamma_\mu \partial^\mu - m_{q_j})q_j(x) \quad (1.17)$$

where  $q_j$  signifies the quark fields, and  $m_{q_j}$  denotes their respective masses. Under the gauge transformations, the quark fields transform in the fundamental representation of the  $SU(3)_C$  color group. This transformation is mathematically expressed as:

$$q_j \rightarrow q'_j = U_{jk}q_k \quad (1.18)$$

where the unitary transformation matrix  $U$  is defined as:

$$U(\theta) = e^{i\theta_\alpha(x)T_\alpha}, \quad \alpha = 1, \dots, 8 \quad (1.19)$$

Here,  $T_\alpha$  represents the generators of the  $SU(3)_C$  group, corresponding to the eight gluon color charges, and are given by:

$$T^\alpha = \frac{1}{2}\lambda^\alpha \quad (1.20)$$

where  $\lambda^\alpha$  are the Gell-Mann matrices.

To ensure that the QCD Lagrangian remains invariant under local  $SU(3)_C$  gauge transformations, a covariant derivative must be introduced. The covariant derivative  $\mathcal{D}_\mu$  acts on the quark fields and includes the coupling to the gluon field  $A_\mu^a$ , expressed as:

$$\mathcal{D}_\mu = \partial_\mu + ig_s A_\mu^a T^a \quad (1.21)$$

where  $g_s$  is the strong coupling constant,  $A_\mu^a$  are the gluon fields. With the covariant derivative, the Lagrangian density for the quarks, becomes:

$$\mathcal{L}_{quarks} = \sum_j \bar{q}_j(i\gamma_\mu \mathcal{D}^\mu - m_q)q_j \stackrel{(1.21)}{=} \sum_j \bar{q}_j \left[ \delta_{jk}(i\gamma_\mu \partial^\mu - m_q) - g_s \gamma_\nu A_\nu^a T_{jk}^a \right] q_k \quad (1.22)$$

The term involving the gluon fields ensures that the Lagrangian remains gauge invariant. Incorporating the kinematic terms of the fields, we can define the Lagrangian for the gauge fields, mirroring the approach in QED:

$$\mathcal{L}_{gauge} = -\frac{T_F}{2} F_{\mu\nu}^a F^{a\mu\nu} \quad (1.23)$$

where the Dynkin index  $T_F$  for 3 colors equals  $1/2$  and  $F_{\mu\nu}^a$  is the gluon field strength tensor which is defined as:

$$F_{\mu\nu}^a = \partial_\mu A_\nu^a - \partial_\nu A_\mu^a - g_s f^{abc} A_\mu^b A_\nu^c \quad (1.24)$$

with  $f^{abc}$  being the structure constants of the  $SU(3)_C$  group. Thus, the full Lagrangian density for QCD,  $\mathcal{L}_{QCD} = \mathcal{L}_{quarks} + \mathcal{L}_{gauge}$  can be expressed, similar to that of QED, as:

$$\mathcal{L}_{QCD} = \sum_j \bar{q}_j (i\gamma^\mu \mathcal{D}_\mu - m_i) q_j - \frac{1}{4} F_{\mu\nu}^a F^{a\mu\nu} \quad (1.25)$$

While both QED and QCD describe interactions mediated by gauge fields, a fundamental distinction arises from the non-Abelian nature of the  $SU(3)_C$  gauge group in QCD. In QED, the field tensor for the electromagnetic field is straightforward, with no self-interaction terms. However, in QCD, as we can see from the gluon field tensor (1.24), there is an additional term proportional to the gluon fields themselves, reflecting the self-interaction of the gluons. This self-interaction leads to the confinement property of QCD [45–47]. Due to the gluon self-interactions, strings of gluons are formed between quarks. As two quarks are pulled apart, a flux tube of gluons is formed between the quarks. With increasing distance between the quarks the energy stored in these flux tubes increases until the energy becomes large enough to create a new pair of quarks which form bound states with the already existing quarks. This essentially prevents single quarks from existing as they rather form color-neutral hadrons.

## Running coupling

The previously mentioned coupling constants are inaccurately termed as such since their coupling strengths are not constant. These strengths are depended by the energy scale  $Q^2$  where the interactions occur. This effect is especially significant in strong couplings, which are controlled by the strength parameter,  $\alpha_s$ , due to the gluon self-interactions. These interactions, along with the vacuum fluctuations, create a screening effect for color-charged particles which effectively varies the color charge of the particle. To accommodate these effects, couplings depending on  $\alpha_s$  can be expanded perturbatively when  $\alpha_s \ll 1$ . However, expansions may encounter divergences at high momenta  $Q$  when higher orders of  $\alpha_s$  are neglected. Renormalization scales  $\mu$  are then introduced to counteract these issues, preventing theories from

becoming nonsensical in divergent limits. By introducing a renormalization scale, calculated observables (e.g., cross sections) become scale-dependent at finite perturbation theory orders. Of course, a calculation of the observables to all perturbation theory orders, eliminates this, non-physical, scale dependency. The evolution of the coupling is described by renormalization group equations, connecting observables at different energy scales  $Q$  to a reference scale  $\mu^2$ . Consequently, knowing an observable at scale  $\mu^2$  allows its determination at any arbitrary scale  $Q$ . For the strong coupling constant, this approach provides precision up to subleading orders in  $\alpha_s$ :

$$a_s(Q^2) = \frac{a_s(\mu^2)}{1 + \mathcal{B}a_s(\mu^2)\ln(Q^2/\mu^2)} \quad (1.26)$$

where the  $\mathcal{B}$  depends on the numbers of fermionic and bosonic loops:

$$\mathcal{B} = \frac{11N_c - 2N_f}{12\pi} \quad (1.27)$$

with  $N_C$  being the number of colors and  $N_f$  the number of quark flavors. For the SM, where  $N_C = 3$  and  $N_f \leq 6$ ,  $\mathcal{B}$  is greater than zero and hence  $\alpha_s$  decreases with increasing  $Q^2$ . In the limit of high energy, the coupling strength  $\alpha_s$  is very small and thus color charged particles behave as if they were free particles. This property of QCD is known as asymptotic freedom. On the other side of the spectrum, at lower energy scales, this leads to the confinement property of QCD as discussed before. In cases where the coupling strength  $\alpha_s$  becomes too large, a perturbative expansion in  $\alpha_s$  is no longer possible. This regime is referred to as the non-perturbative regime of QCD where for example the hadronization of color-charged particles is calculated.

### 1.2.3 Electroweak unification

The weak interaction can theoretically be incorporated into the Standard Model similar to the Electromagnetic interaction. However, measurements like the Wu experiment [48], demonstrated that the weak force, mediated by W and Z bosons, behaves differently compared to the EM force. It was observed that the charged current of the weak interaction, involving W bosons, interacts exclusively with left-handed fermions and right-handed antifermions, indicating that the weak interaction does not maintain parity symmetry. The chiral symmetry is described via the  $\gamma^5 = i\gamma^0\gamma^1\gamma^2\gamma^3$  operator. It can be used to project the left- and right-handed parts of the fermionic field  $\psi$ , as

$$\begin{aligned} \psi_L &= \frac{1}{2}(1 - \gamma^5)\psi \\ \psi_R &= \frac{1}{2}(1 + \gamma^5)\psi \end{aligned} \quad (1.28)$$

The charged current of the weak interaction is shown to only act on the left-handed parts of  $\psi$ , i.e. only on  $\psi_L$ . At the same time, the EM interaction still acts indistinguishably on left- and right-handed fermion fields. Therefore, this requires a modification of the previously introduced QED Lagrangian density and transformation behavior in order to encompass both features. This is referred to as the electroweak unification and was first described via the Glashow-Salam-Weinberg theory [15–17].

The gauge transformation that can describe the required behavior is the  $SU(2)_L \otimes U(1)_Y$  group. To accommodate the idea of parity violation in SM, only the left-chiral fields are written as  $SU(2)_L$  doublets as the fields are mixed and transformed into each other. Following the same line of thought, the right-chiral fields are described by  $SU(2)$  singlets as they do not transform into each other. Therefore under the electroweak gauge symmetry  $SU(2)_L \otimes U(1)_Y$ , the right-chiral fields transform as a singlet, as we saw in the previous section, but with a different charge operator:

$$\psi_R \rightarrow \psi'_R = e^{i\beta(x)Y}\psi_R \quad (1.29)$$

while the left-handed fermion fields transform as a doublet:

$$\psi_L \rightarrow \psi'_L = e^{i\vec{\alpha}(x)\vec{I}+i\beta(x)Y}\psi_L \quad (1.30)$$

As before,  $\vec{\alpha}(x) = (\alpha_1(x), \alpha_2(x), \alpha_3(x))$  and  $\beta(x)$  are arbitrary real functions of the space-time coordinates. There are three generators of the  $SU(2)_L$  group<sup>3</sup>, called isospin vector operators, given as

$$I_i = \frac{\sigma_i}{2} \quad i = 1, 2, 3 \quad (1.31)$$

where  $\sigma_i$  are the familiar Pauli spin matrices:

$$\sigma_1 = \begin{pmatrix} 0 & 1 \\ 1 & 0 \end{pmatrix} \quad \sigma_2 = \begin{pmatrix} 0 & -i \\ i & 0 \end{pmatrix} \quad \sigma_3 = \begin{pmatrix} 1 & 0 \\ 0 & -1 \end{pmatrix} \quad (1.32)$$

The parameter  $Y$  in Eq. (1.29), is the corresponding charge operator for the  $U(1)_Y$  group and it is called the weak hypercharge operator. This parameter relates the two conserved quantities  $Q$  and  $I_3$  according to the Gell-Mann-Nishijima relation [11]:

$$Y = 2(Q - I_3) \quad (1.33)$$

The weak isospin doublet is defined by the eigenstate of  $\frac{1}{2}\sigma_3$  generator and the corresponding eigenvalues are the isospin charge  $+\frac{1}{2}$  and  $-\frac{1}{2}$ . Hence, the following notation is adopted to

<sup>3</sup>The generators of  $SU(2)$  are a  $2 \times 2$  Hermitian traceless matrices corresponding to 3 degrees of freedom.

distinguish between the handedness:

$$\begin{aligned}\psi_L^{lepton} &= \begin{pmatrix} v_l \\ l^- \end{pmatrix}_L & \psi_R^{lepton} &= l_R^- \\ \psi_L^{quark} &= \begin{pmatrix} u^f \\ d'^f \end{pmatrix}_L & \psi_R^{quark} &= u_R^f, d_R^f\end{aligned}\tag{1.34}$$

In order for the electroweak Lagrangian density to be gauge invariant under the above transformations (Eq. (1.29, 1.30), we introduce the gauge covariant derivative

$$\mathcal{D}_\mu = \partial_\mu - ig' B_\mu \frac{Y}{2} - ig \frac{\sigma_i}{2} W_\mu^i\tag{1.35}$$

for which:

$$\mathcal{D}_\mu \psi_L = \partial_\mu \psi_L - \frac{i}{2} (g' Y B_\mu + g \sigma_i W_\mu^i) \psi_L\tag{1.36}$$

$$\mathcal{D}_\mu \psi_R = \partial_\mu \psi_R - \frac{i}{2} g' Y B_\mu \psi_R\tag{1.37}$$

where,  $W_\mu^i$ ,  $i = 1, 2, 3$  are the gauge fields that are associated with  $SU(2)_L$  group with  $g'$  being the coupling strength of the group, while  $B_\mu$  is the gauge field associated with the  $U(1)_Y$  group and  $g$  its coupling strength. This construction results in three vector fields  $W_\mu^i$ , only acting on the left-handed spinor, and another vector field  $B_\mu$  acting homogeneously on both spinor projections. The above transformations result into a local invariant Lagrangian for each gauge field:

$$\mathcal{L}_{gauge} = -\frac{1}{4} B_{\mu\nu} B^{\mu\nu} - \frac{1}{4} W_{\mu\nu}^i W^{i,\mu\nu}\tag{1.38}$$

where  $W_{\mu\nu}^i$  are the field strength tensors of the weak isospin following

$$W_{\mu\nu}^i = \partial_\mu W_\nu^i - \partial_\nu W_\mu^i + g \epsilon_{ijk} W_\mu^j W_\nu^k\tag{1.39}$$

and  $B_{\mu\nu}$  the field strength tensor of the hypercharge defined analog to  $F_{\mu\nu}$  in Section 1.2.1

$$B_{\mu\nu} = \partial_\mu B_\nu - \partial_\nu B_\mu\tag{1.40}$$

The last term in Eq. (1.39) arises from the non-Abelian nature of the group  $SU(2)$ , since the generators  $\sigma_i$  ( $i = 1, 2, 3$ ) do not commute with each other.

By summing the Lagrangian density in Eq. (1.38) with the corresponding Lagrangian for the

interaction terms between gauge bosons and fermions we get the full electroweak Lagrangian:

$$\mathcal{L}_{EW} = \bar{\psi}_L (i\gamma^\mu \mathcal{D}_\mu) \psi_L + \bar{\psi}_R (i\gamma^\mu \mathcal{D}_\mu) \psi_R - \frac{1}{4} W_{\mu\nu}^i W^{i,\mu\nu} - \frac{1}{4} B_{\mu\nu} B^{\mu\nu} \quad (1.41)$$

Altogether, this transformation behavior fulfills the requirements set towards the theory, i.e. is maximally parity violating. In other words, the interaction of a particle changes depending on the parity of the coordinate system. Performing a parity operation, changing the space coordinates  $\vec{x}$  to  $-\vec{x}$ , alters how particles interact, as this operation equates to changing particle chirality. The theory yields four gauge fields, from which the physical gauge bosons of the electroweak interaction can be obtained from linear combinations,

$$W_\mu^\pm = \frac{1}{\sqrt{2}} (W_\mu^1 \mp iW_\mu^2) \quad (1.42)$$

and

$$Z_\mu = \cos \theta_W W_\mu^3 - \sin \theta_W B_\mu \quad (1.43)$$

$$A_\mu = \sin \theta_W W_\mu^3 + \cos \theta_W B_\mu \quad (1.44)$$

The first equation (1.42) describes the W boson fields responsible for charged current interactions. From the other equations, two neutral current mediators are obtained, one being the photon field  $A_\mu$  and the other the Z boson field  $Z_\mu$ . These neutral fields are mixed states of the  $W_\mu^3$  and  $B_\mu$  fields rotated via the Weinberg angle  $\theta_W$ , related to the coupling strengths  $g$  and  $g'$  via

$$\cos \theta_W = \frac{g}{\sqrt{g^2 + g'^2}}, \quad \text{and} \quad \sin \theta_W = \frac{g'}{\sqrt{g^2 + g'^2}} \quad (1.45)$$

Experimentally, the force carriers of the weak interaction, the W and Z bosons, are proven to be massive, but the construction in Eq. (1.41) does not allow for mass terms of the gauge fields  $W_\mu^i$  and  $B_\mu$ . This problem will be addressed in the following section.

## 1.2.4 Spontaneous symmetry breaking

For the QED Lagrangian,  $\mathcal{L}_{QED}$  (Eq 1.7), it is evident that the mass of the photon must be zero in order to satisfy the  $U(1)$  local gauge symmetry. Similarly, the Lagrangian for QCD, as shown in Equation (1.25) demonstrates the same restriction. The mass term for the gluon fields is forbidden by the  $SU(3)_C$  gauge symmetry. Therefore, the mediating bosons for the strong interactions are also massless.

While the prohibition of mass terms for the bosons of QED and QCD is not a problem, this

requirement also applies to the  $SU(2)_L$ , posing an issue for the W and Z bosons, for which we know that are massive. This contradiction is solved by introducing a spontaneous symmetry breaking mechanism in which the electroweak gauge symmetries are retained but are not present in the energetic ground state of the system, allowing for the introduction of non-zero boson masses. This spontaneous symmetry breaking is described via the Higgs mechanism [18–30].

## The Higgs mechanism

The Higgs mechanism predicts the existence of a scalar boson, the Higgs boson, which gives mass to the weak bosons, thus providing a way to generate mass terms while preserving gauge invariance in the Lagrangian.

We consider a locally  $SU(2)$  and  $U(1)$  invariant Lagrangian for spin-0 fields:

$$\mathcal{L}_{Higgs} = (\mathcal{D}_\mu \Phi)^\dagger (\mathcal{D}^\mu \Phi) - V(\Phi) \quad (1.46)$$

where  $\Phi$  is a  $SU(2)$  isospin doublet of complex scalar field with hypercharge  $Y = 1$  in order to retain the invariance of the group:

$$\Phi = \begin{pmatrix} \phi_+ \\ \phi_0 \end{pmatrix} = \frac{1}{\sqrt{2}} \begin{pmatrix} \phi_1 + i\phi_2 \\ \phi_3 + i\phi_4 \end{pmatrix} \quad (1.47)$$

with  $\phi_+$  being positively charged and  $\phi^0$  neutral. The Higgs potential,  $V(\Phi)$  is an interaction energy characterized by two independent parameters,  $\mu, \lambda$

$$V(\Phi) = \mu^2 \Phi^\dagger \Phi + \lambda (\Phi^\dagger \Phi)^2 \quad (1.48)$$

with  $\lambda > 0$  required for vacuum stability. When  $\mu^2 > 0$ , the minimum of the potential occurs when both fields ( $\phi_+$  and  $\phi_0$ ) are at zero. In this case, the electroweak symmetry is unbroken in the vacuum because a gauge transformation acting on the ground state does not change it. On the other hand, if  $\mu^2 < 0$ , the minimum of the potential has an infinite number of degenerate states that satisfy  $\Phi^\dagger \Phi = \mu^2/2\lambda$  and the physical vacuum state will correspond to any particular point on the circle of Figure 1.1. Having to choose a particular point breaks the global  $U(1)$  symmetry of the Lagrangian. Without loss of generality, in this scenario, the ground state  $\Phi_0$  can be chosen to be:

$$\Phi_0 = \frac{1}{\sqrt{2}} \begin{pmatrix} 0 \\ v \end{pmatrix} \quad (1.49)$$

where  $v = \sqrt{-\mu^2/\lambda}$  is the vacuum expectation value (VEV).

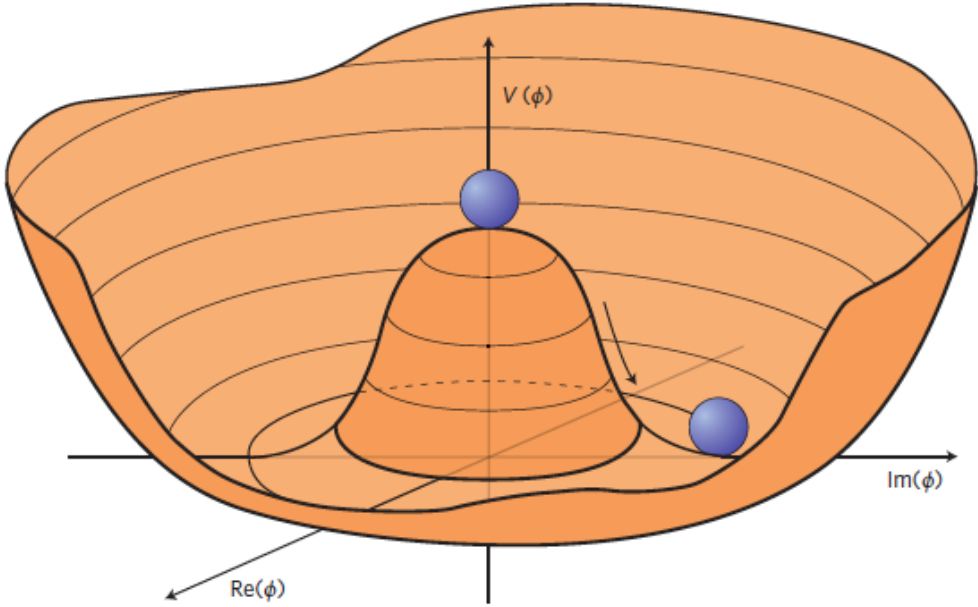


Figure 1.1. Illustration of the Higgs potential [49]

The expansion of the ground state of the field  $\Phi$  around the minimum can be parameterized with the real scalar field  $h$  as:

$$\Phi(x) = \frac{1}{\sqrt{2}} \begin{pmatrix} 0 \\ v + h(x) \end{pmatrix} \quad (1.50)$$

and finally, the potential  $V(\Phi)$  can be rewritten as:

$$V(\Phi) = -\lambda v^2 h^2(x) - \lambda v h^3(x) - \frac{\lambda}{4} h^4(x) \quad (1.51)$$

The second and third terms represent the cubic and quartic self-coupling of the Higgs boson. Instead, from the first term, the value of the Higgs mass is obtained as:

$$m_h^2 = \lambda v^2 = -2\mu^2 \quad (1.52)$$

In contrast to the weak boson self-interactions, which have a gauge nature, the Higgs boson self-interactions are purely related to the parameters of the scalar sector of the theory and entirely determined from the Higgs boson mass and the VEV. Consequently, their experimental measurement represents a crucial test of the validity and coherence of the SM.

The massive gauge vector bosons can be obtained by replacing the vacuum expectation value of the  $\Phi$  field in the EW Lagrangian with the additional invariant term due to the scalar field part. The H scalar field naturally acquires mass through self-interaction. When they interact with the vacuum, the gauge fields  $W_\mu^1, W_\mu^2, W_\mu^3$  gain a mass term in the form of  $\frac{1}{2}M^2 W_\mu^\mu$ , whereas the boson field associated with the photon remains massless. This means that despite

breaking all the  $SU(2) \otimes U(1)$  symmetries, the Higgs field maintains the  $U(1)$  symmetry, leaving the vacuum electrically neutral. Remembering the relations in Equations (1.42), (1.43) and (1.44), the masses of the  $W^\pm$  and Z bosons can be expressed with the weak coupling constants and the vacuum expectation value as:

$$m_W = \frac{1}{2} v g \quad m_Z = \frac{1}{2} v \sqrt{g^2 + g'^2} = \frac{g v}{2 \cos \theta_W} \quad m_\gamma = 0 \quad (1.53)$$

The theory does not predict all the free parameters, nevertheless, the input is given from experimental values. For example, it is possible to determine the value of  $v$ , the scale of the electroweak theory, by measuring the Fermi constant  $G_F$  from the muon lifetime [50].  $G_F$  is related to the W boson mass by  $\frac{G_F}{\sqrt{2}} = \frac{g^2}{8m_W^2}$ . The resulting value of  $v$  is:

$$v^2 = \frac{1}{\sqrt{2} G_F} \approx (246 \text{ GeV})^2 \quad (1.54)$$

## Fermion masses

For weak interactions, the problem of massless particles does not only affect the bosons. Since under the  $SU(2)_L$  left-handed particles transform as weak isospin doublets and right-handed particles as isospin singlets, the mass term of a spinor field written as chiral states also breaks the required gauge invariance. Even with the introduction of the spontaneous symmetry breaking mechanism and the Higgs field, fermion masses would still break gauge invariance under  $SU(2)$ . Hence an additional mechanism has to be introduced in order to explain the massive fermions. As the Higgs field is responsible for the generation of boson masses, a mechanism is introduced that explains the origin of the fermion masses also via the interaction with the Higgs field. This interaction is called the Yukawa interaction [51], constituting a linear coupling of the Higgs field  $\Phi$  with the fermion fields  $\psi$ ,

$$\mathcal{L}_{Yukawa,f} = -y_f (\bar{\psi}_L^f \Phi \psi_R^f + \bar{\psi}_R^f \Phi^\dagger \psi_L^f) \quad (1.55)$$

where the superscript runs over all quarks and charged leptons. The different  $y_f$  constants are known as Yukawa couplings of the particle  $f$  to the Higgs field. For the electron  $SU(2)$  doublet, the element with this coupling can be written as

$$\mathcal{L}_e = -y_e \left[ (\bar{\nu}_e \bar{e})_L \begin{pmatrix} \phi_+ \\ \phi_0 \end{pmatrix} e_R + \bar{e}_R (\phi_+^* \phi_0^*) \begin{pmatrix} \nu_e \\ e \end{pmatrix}_L \right] \quad (1.56)$$

Here, obviously,  $y_e$  denotes the Yukawa coupling of the electron to the Higgs boson. After spontaneously breaking the symmetry and thus using the expression of the Higgs field from Eq.

(1.50), the Lagrangian becomes:

$$\mathcal{L}_e = -\frac{\nu y_e}{\sqrt{2}} \bar{e}_L e_R - \frac{y_e}{\sqrt{2}} \bar{e}_L h e_R - \frac{\nu y_e}{\sqrt{2}} \bar{e}_R e_L - \frac{y_e}{\sqrt{2}} \bar{e}_R h e_L \quad (1.57)$$

The first term of the Lagrangian in Eq. (1.57) gives mass to the electron, which mass can be inferred as  $m_e = y_e \nu / \sqrt{2}$ . The second term represents the coupling of the electron and the Higgs boson itself. No other interactions of fermions and the Higgs bosons or Higgs field are predicted by this formalism unlike for the bosons where also cubic and quartic interactions are predicted.

The non-zero vacuum expectation value occurs only in the neutral part of the Higgs doublet due to the form in the ground state in Equation (1.50). This implies that the combination  $\bar{\psi}_L^f \Phi \psi_R^f + \bar{\psi}_R^f \Phi^\dagger \psi_L^f$  can only generate masses for the leptons in the lower component of an  $SU(2)$  doublet. This explains why the neutrinos do not get mass through the Higgs mechanism.

The process is analogous for quarks with the difference that, unlike the neutrinos, the up-type quarks do have right-chiral part. Thus, the Yukawa coupling of the fermions to the Higgs field is universally expressed as:

$$y_f = \sqrt{2} \frac{m_f}{\nu} \quad (1.58)$$

with  $f$  being every fermion except the neutrinos, i.e.,  $f = e, \mu, \tau, d, u, s, c, b, t$ . It is obvious, that, from this mechanism, the mass of the fermions is determined by the Yukawa coupling constant  $y_f$  and the VEV  $\nu$ . Therefore, in order to define the masses, which are not determined by the theory, the Yukawa couplings have to be measured experimentally.

The measurement of the coupling of the fermions (and bosons) to the Higgs boson is an active field of study. While the coupling of the heaviest fermions to the Higgs boson has been established already, the couplings to lighter fermions still have to be measured. Due to the linear dependence of the Yukawa coupling strength to the mass of the fermion, the coupling measurements of lighter fermions are more difficult, as the small coupling strength is translated to lower rates of the process of interest. In Figure 1.2, the current state of coupling measurements of fermions and bosons to the Higgs boson is shown.

Finally, theoretical indications and experimental proofs have led to the conclusion that quarks as free particles are mass eigenstates but appear as  $SU(2)$  eigenstates in the electroweak interaction: the latter is a combination of the former, and vice versa [53]. In particular, the introduction of quark mixing between EW  $q'$  and mass eigenstates  $q$  is needed to explain the experimental observation of the transitions between the upper and lower components of a quark flavor doublet across different families, e.g. from a  $u$  to a  $s$  quark, as well as the violation of charge and parity (CP) conservation in the SM [54, 55]. This implies that the quark flavor eigenstates do not coincide with the weak isospin eigenstates, but the lower components

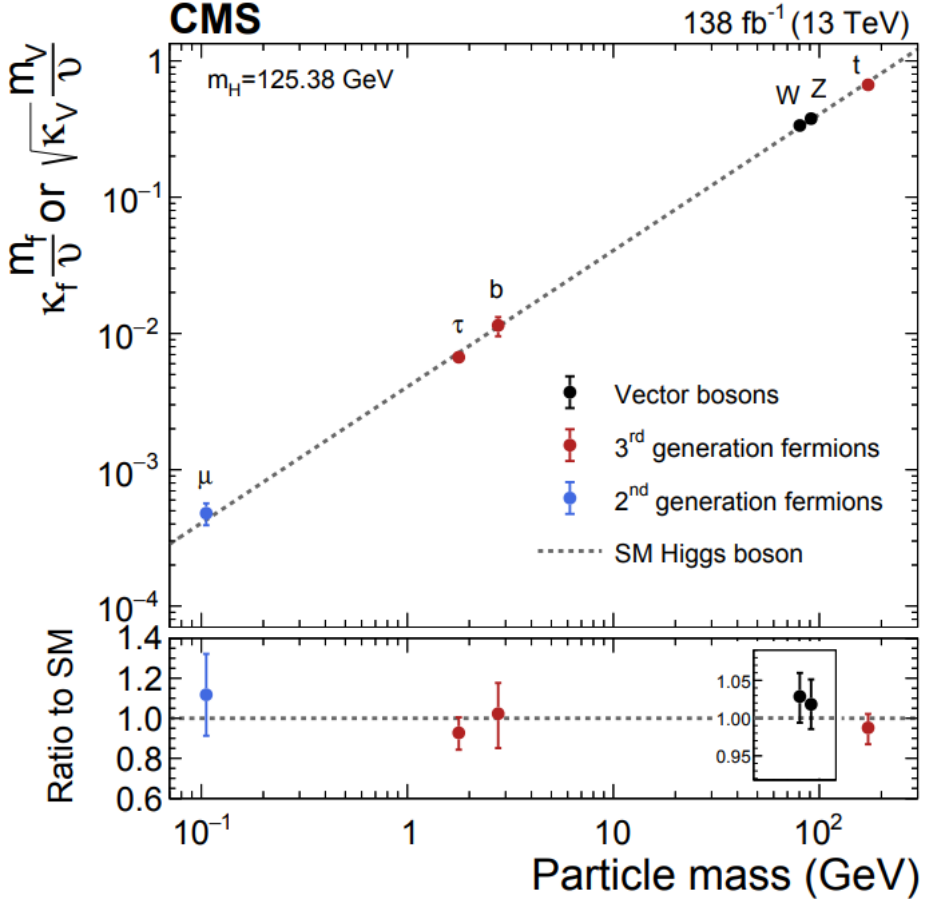


Figure 1.2. Coupling of fermions and bosons to the Higgs field [52]

of the doublets are rotated relative to one another. More explicitly, the corresponding mixing between the lower components of the weak isospin eigenstates  $d'$ ,  $s'$  and  $b'$  are related to the lower components of the flavor eigenstates  $d$ ,  $s$  and  $b$  as:

$$\begin{pmatrix} d' \\ s' \\ b' \end{pmatrix} = \begin{pmatrix} V_{ud} & V_{us} & V_{ub} \\ V_{cd} & V_{cs} & V_{cb} \\ V_{td} & V_{ts} & V_{tb} \end{pmatrix} \begin{pmatrix} d \\ s \\ b \end{pmatrix} \quad (1.59)$$

The rotation matrix  $V_{CKM}$  is the Cabibbo-Kobayashi-Maskawa (CKM) matrix describing the transition probabilities between flavors. In the SM, it is assumed to be unitary: the single matrix elements are free parameters of the theory, and all the values have been determined experimentally with very high precision [56]. Large diagonal terms and small off-diagonal values characterize the CKM matrix. As a result, transitions between generations are significantly suppressed, and bottom quarks, for example, acquire a long lifetime. Additionally, as a consequence of quark mixing, flavor-changing neutral currents are not allowed at tree level [57], which explains why they are difficult to observe.

The existence of the mixing is related to many physical examples, e.g. charge-parity (CP) vi-

olation, Glashow-Iliopoulos-Maiani (GIM) mechanism, flavor changing neutral currents (FCNC). However, an analogue of this matrix for the leptons is not present in the SM, since no right-handed neutrinos are included in the theory. Only because neutrino oscillations have been detected experimentally [1–3], a similar mixing in the leptonic sector could be introduced to describe neutrinos as both flavor and mass eigenstates. This could be handled by the addition of a lepton mixing matrix, the Pontecorvo-Maki-Nakagawa-Sakata (PMNS) matrix [58, 59], which emerges naturally as a consequence of the seesaw mechanism [60] and has distinct phases depending on whether neutrinos are Dirac or Majorana particles [61]. The values of the masses of neutrinos are still unknown; however upper limits have been determined in experiments down to 0.8 eV [62].

## 1.3 The top quark

The existence of the third-generation quarks was suggested to explain observations of CP violation. The observation of the b quark at Fermilab in 1977, confirmed the hypothesis and opened the quest for the top quark. The first experimental observation was reported independently by the CDF [63] and  $D\emptyset$  [64] Collaborations in 1995 at the Fermilab Tevatron using proton-antiproton collisions at a center of mass energy of  $s = 1.8$  TeV.

The top quark ( $t$ ) is the up-type quark of the third generation of fermions. Its most distinctive feature is its mass, which is the largest among all fundamental particles. The left-handed top quark is the  $Q = 2/3$  and  $I_3 = +1/2$  member of the weak isospin doublet that also contains the bottom quark. The right-handed top quark is the  $SU(2)_L$  weak isospin singlet ( $Q = 2/3$  and  $I_3 = 0$ ). The top quark is often regarded as a window for new physics since it provides the highest natural energy scale to test the SM.

### Production mechanism

The production of  $t\bar{t}$  events via the strong interaction is the largest source of production of top quarks in hadron collisions as opposed to the single top production via the weak interaction. The  $t\bar{t}$  process is one of the most important at LHC because it allows us to precisely study the properties of the top quark. Additionally, due to the dominance of this production mode, the  $t\bar{t}$  production is also a major background in many measurements and searches for rare processes.

At LHC, gluon fusion dominates with 90% of the  $t\bar{t}$  production. It is followed by the quark-antiquark annihilation, which accounts for 10% of the total  $t\bar{t}$  production. The leading-order Feynman diagrams are illustrated in Figure 1.3. When considering higher orders, the  $t\bar{t}$  system is often accompanied by emissions of additional jets.

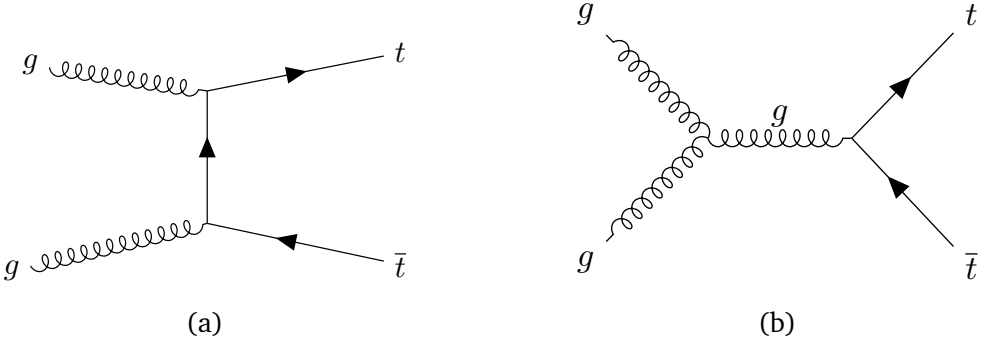


Figure 1.3. Feynman diagrams for top quark pair production processes at leading order

The  $t\bar{t}$  production cross section has been studied at various center-of-mass energies for  $p\bar{p}$  collisions. The measurements are compared to the theoretical prediction, showing good agreement as in Figure 1.4. For  $\sqrt{s}=13$  TeV, the predicted  $t\bar{t}$  cross section for  $m_t = 172.5$  GeV is [65]:

$$\sigma_{t\bar{t}} = 833.9^{+20.5}_{-30.0}(\text{scale}) \pm 21.0(\text{PDF} + \alpha_s)^{+23.18}_{-22.45}(\text{mass}) \text{ pb} \quad (1.60)$$

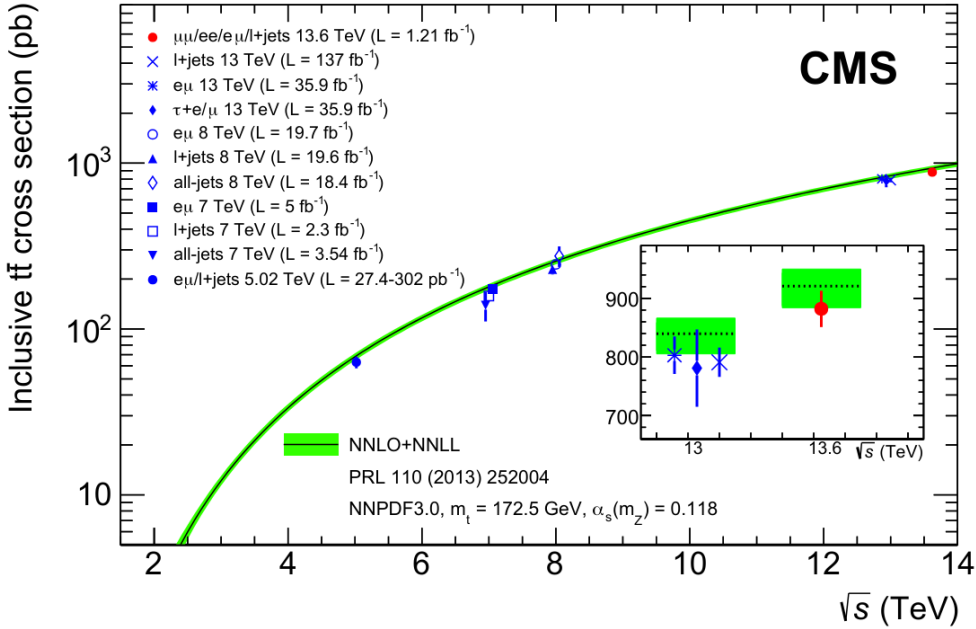


Figure 1.4. Cross section of  $t\bar{t}$  production as a function of the center-of-mass energy at the CMS experiment [66]

## Decay mechanism

Due to its large mass, the top quark decays with a lifetime of  $\tau_t = 5 \times 10^{-25}$  s [12]. Actually, it is shorter than its hadronization timescale ( $1/\Lambda_{QCD} \sim 10^{-24}$  s). This represents an opportunity to study quarks in a free state, something that is quite exceptional due to color confinement,

as explained in Section 1.2.2. In fact, the top quark is the only quark that can be investigated unboundedly. Its lifetime is also smaller than the spin decorrelation timescale ( $m_t/\Lambda_{QCD}^2 \sim 10^{-21}$  s [67],  $m_t$  being the mass of the top quark), implying that the top-quark states conserve their spin state from its production to its decay. Therefore, the top-quark properties, such as the spin information and the top-quark polarization, can also be accessed through its decay products and, consequently, be measured.

Due to the large value of the  $V_{tb}$  element of the CKM matrix, the top quark is expected to decay almost entirely ( $\sim 99.8\%$ ) to a b quark and a W boson ( $t \rightarrow W b$ ). The final-state decay is classified according to the subsequent decay of the W boson. Since the W bosons are massive vector bosons, their lifetime is very short ( $\tau_W \approx 3 \times 10^{-25}$  s) and hence they will rapidly decay to leptons or quarks that will form hadrons. Due to its large mass, the W boson can decay to any quark except the top quark. For the  $W^+$ , the branching ratios<sup>4</sup> (BRs) for the different decay modes are presented in Table 1.4

Table 1.4. W-boson-decay branching ratios [12]

Decay mode	Branching ratio [%]
$W^+ \rightarrow e^+ \nu_e$	$10.71 \pm 0.16$
$W^+ \rightarrow \mu^+ \nu_\mu$	$10.63 \pm 0.15$
$W^+ \rightarrow \tau^+ \nu_\tau$	$11.38 \pm 0.21$
$W^+ \rightarrow q\bar{q}$ (hadrons)	$67.41 \pm 0.27$
$W^+ \rightarrow$ invisible	$1.4 \pm 2.9$

For the conjugate process involving the  $W^-$ , the BRs are the same. Therefore, the W boson decay and consequently the top-quark decay can be classified either as leptonic or hadronic.

## Decay channels

There are three different decay channels of the  $t\bar{t}$ , depending on the decay of the W-bosons:

- **Fully-Hadronic (FH):** Both W bosons decay into quarks, mostly as  $W^+/W^- \rightarrow u\bar{d}/\bar{u}d$  and  $W^+/W^- \rightarrow c\bar{s}/\bar{c}s$ , they hadronize and lead to the experimental signature of six jets in the final state. Although this decay mode has a relatively high branching ratio of approximately 46% at parton level and  $\approx 55\%$  at hadron level, its analysis is challenging due to significant background contributions from multijet processes and the combinatorial ambiguities in the reconstruction of the events.

---

<sup>4</sup>For each decay mode, the branching ratio (BR) is defined as the fraction times that the particle decays in that particular mode with respect to total possible decays.

- **Semi-Leptonic (SL):** Only one W decays into hadrons and the other decays into leptons: the final state comprises four jets, one charged lepton and one neutrino in the final state. The branching ratio is approximately 45% at parton level and  $\approx 38\%$  at hadron level, but the multijet background is significantly suppressed by the isolation requirements on the charged lepton. Furthermore, to reconstruct the complete event kinematics, the momentum vector of a single neutrino can be retrieved with good efficiency from a missing transverse momentum measurement in combination with a constraint on the W boson mass.
- **Di-Leptonic (DL):** Both W bosons decay into leptons: the final state features two jets, two oppositely-charged leptons and two neutrinos. The combined branching ratio  $\approx 9\%$  at parton level and  $\approx 7\%$  at hadron level, is the smallest, but the signature is distinct. The full event reconstruction is challenging because the neutrinos are neither detectable nor unambiguously retrievable utilizing the missing transverse momentum balance.

## 1.4 The Higgs boson

The Higgs boson represents the quantum of the scalar field introduced in Section 1.2.4, in the discussion of the electroweak symmetry breaking. In the SM, the Higgs boson is expected to be electrically neutral, free of spin, and CP-even ( $\Theta\Pi = 0^+$ ) with a decay width of approximately 4 MeV.

The signatures for SM Higgs boson detection at collider experiments depend on the production process and the decay pattern. Both the production and the decay contribute to the specific kinematic features which can be used to distinguish signal from the background events.

A multitude of experimental searches on Higgs boson were performed during the first run period of LHC with proton-proton collisions at  $\sqrt{s} = 7, 8$  TeV. On 4 July 2012, the observation of a new particle at a mass of approximately 125 GeV with Higgs boson-like properties was finally reported by the CMS [4] and ATLAS [5] Collaborations with integrated luminosity of 5.1 (5.3)  $\text{fb}^{-1}$  at 7 (8) TeV. Subsequent measurements of the new particle properties such as spin, parity, and coupling strength to SM particles are found to be consistent, within the experimental uncertainties, with the expectation for the SM Higgs boson [68–71]. The full Run-II dataset collected during the LHC proton-proton collisions at a higher energy  $\sqrt{s} = 13$  TeV provides more statistical power to further constrain the Higgs boson mass measurement and elucidate other production and decay modes.

## Production mechanisms

One of the reasons the Higgs boson was the last of the SM's fundamental particles to be discovered is its relatively high mass, which required significant energy for its production. Even in high-energy collisions, the production of a Higgs boson is a rare event. Only a tiny fraction of collisions at the LHC produce a Higgs boson, so vast numbers of collisions had to be analysed to find the Higgs boson.

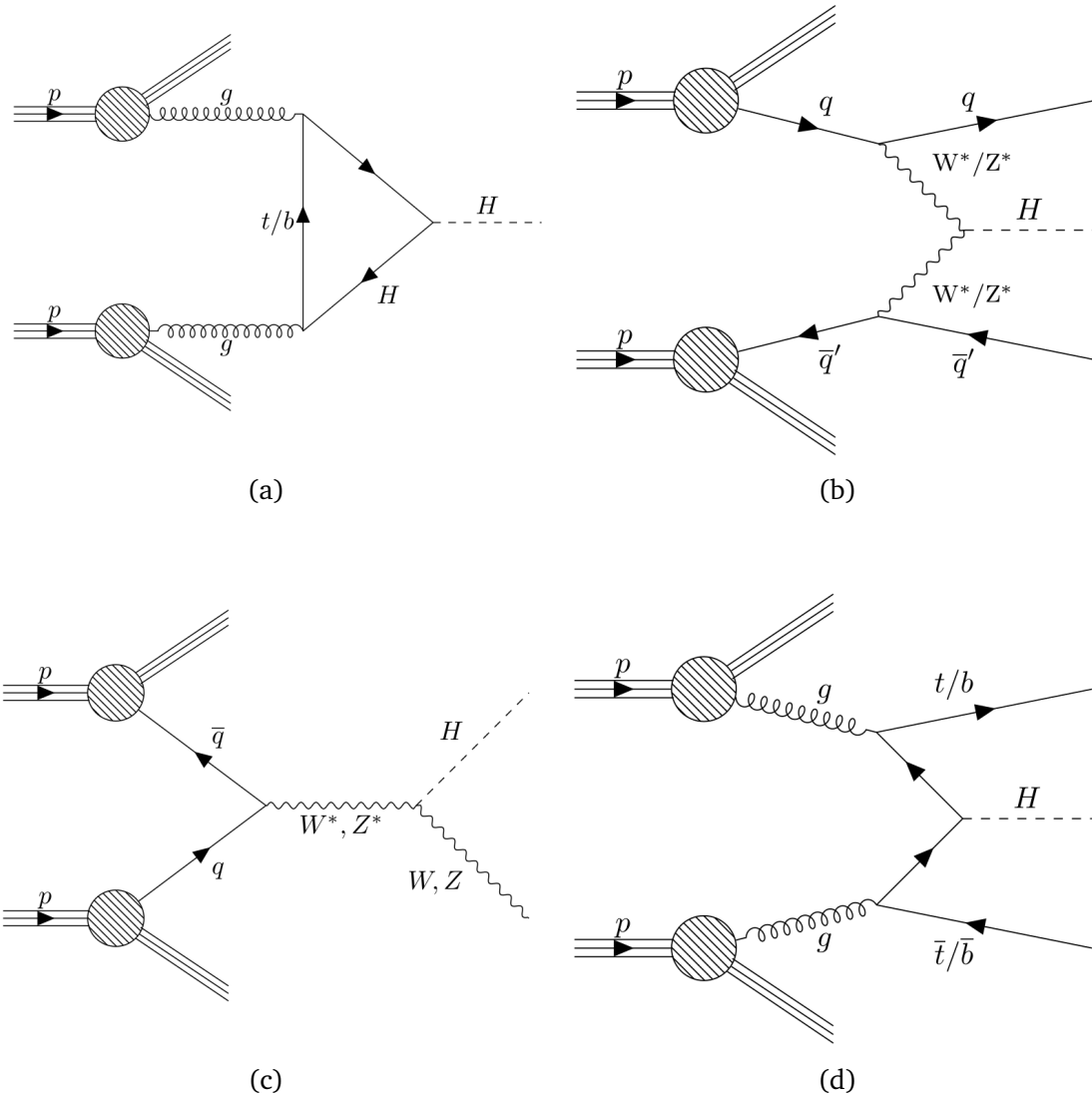


Figure 1.5. Feynman diagrams at leading order for Higgs boson production via (a) gluon-gluon fusion, (b) vector boson fusion (c) Higgsstrahlung and (d) associate production with heavy quarks.

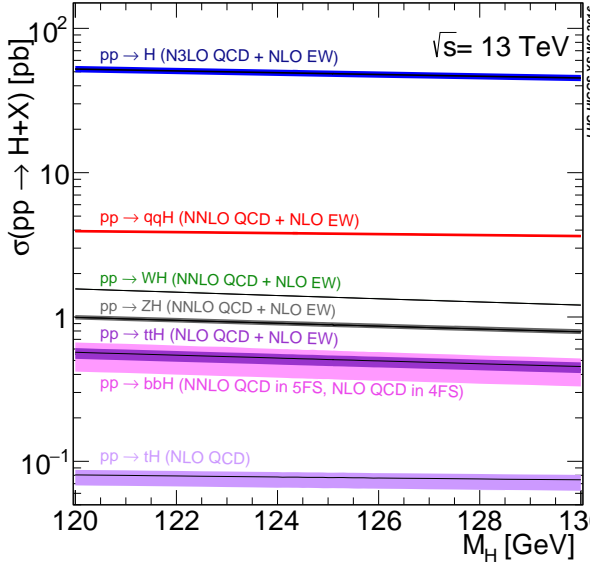
The four dominant processes for Higgs-boson production at LHC are summarised in Figure 1.5. These processes are:

- **Gluon-gluon fusion** (ggF): The process  $g g \rightarrow H$  has to be mediated by a massive fermion loop. This is due to the fact that there is no direct gluon-Higgs-boson coupling within the SM. Although in principle all quarks should be included in the loop, in practice it is the top quark the one doing so because its coupling to the Higgs boson is 40 times stronger than the next-heaviest fermion, the bottom quark. Due to the abundance of gluons in pp collisions, the ggF is very favoured at the LHC.
- **Vector boson fusion** (VBF): The second most important mode is the radiation by the incoming quarks of a pair of W or Z bosons that fuse to form a Higgs boson. The vector bosons ( $V = W$  or  $Z$ ) of the process  $V\bar{V} \rightarrow H$  are originated from initial state quarks which scatter through the final state (changing their flavors in the case of W fusion) producing two forward jets.
- **Higgsstrahlung** (VH): There is another significant contribution involving the W or Z bosons, the Higgsstrahlung or associated  $WH$  or  $ZH$  production. Here, an off-shell W or Z boson (formed from the annihilation of two quarks) radiates a Higgs boson via  $V^* \rightarrow VH$ .
- **Quark-pair associated production** ( $q\bar{q}H$ ): In this mode, the Higgs is produced from a  $q\bar{q}$  pair via  $q\bar{q} \rightarrow H$  with a  $q\bar{q}$  final state. Typically, the involved quark pair is either a  $b\bar{b}$  or  $t\bar{t}$ . In the case of  $t\bar{t}$ , the top quarks decay before hadronizing, leading to final states with a high number of physics objects.

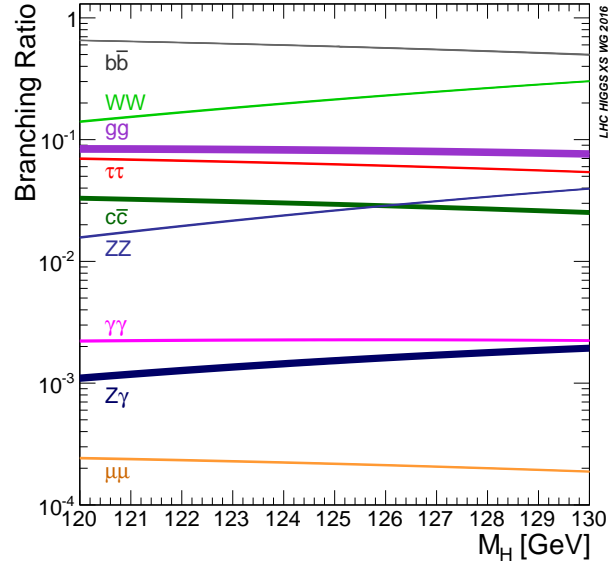
The cross-section of the different mechanisms for single-Higgs-boson production at  $\sqrt{s} = 13$  TeV as a function of  $m_H$  are shown in Figure 1.6a, while assuming a  $m_H = 125.2$  GeV, the Higgs-boson production cross-sections for the different modes are presented in Table 1.5.

Table 1.5. Higgs-boson-production cross sections assuming  $m_H = 125.2$  GeV for a LHC CM energy of  $\sqrt{s} = 13$  TeV [72].

Production mode	Cross section [pb]
ggF	$48.44^{+2.72}_{-3.60}$
VBF	$3.78 \pm 0.08$
WH	$1.37 \pm 0.03$
ZH	$0.89 \pm 0.04$
$t\bar{t}H$	$0.51 \pm 0.04$
$b\bar{b}H$	$0.49 \pm 0.1$



(a)



(b)

Figure 1.6. Higgs-boson (a) production cross sections and (b) branching ratios as a function of  $m_H$  at  $\sqrt{s} = 13$  TeV [72]

## Decay channels

The Higgs boson has a very short lifetime ( $\tau_H = 1.6 \times 10^{-22}$  [72]) and hence, is always detected through its decay products. Figure 1.6b shows the branching ratio as a function of  $m_H$  for the different Higgs-boson decay modes.

Table 1.6. Higgs-boson-decay branching ratios assuming  $m_H = 125.2$  GeV at NLO [72]

Decay mode	Branching ratio [%]
$H \rightarrow b\bar{b}$	$57.92 \pm 0.007$
$H \rightarrow W^+W^-$	$21.70 \pm 0.003$
$H \rightarrow gg$	$8.172 \pm 0.004$
$H \rightarrow \tau^-\tau^+$	$6.240 \pm 0.001$
$H \rightarrow c\bar{c}$	$2.876 \pm 0.002$
$H \rightarrow ZZ$	$2.667 \pm 0.001$
$H \rightarrow \gamma\gamma$	$0.227 \pm 0.001$
$H \rightarrow Z\gamma$	$0.155 \pm 0.003$
$H \rightarrow \mu^-\mu^+$	$0.02165 \pm 0.00004$

Despite the expected large Yukawa coupling between the Higgs boson and the top quark, the  $H \rightarrow t\bar{t}$  is forbidden since  $m_H < 2m_t$ . Consequently, the most prominent decay mode is  $H \rightarrow b\bar{b}$  followed by  $H \rightarrow W^+W^-$ . This is why for the  $tHq$  searches, the channel in which the

Higgs decay to  $b\bar{b}$  is the one with higher statistics. For the other fermionic decays, the decay rates are ordered by the fermion masses, with  $\tau^+\tau^-$  decay mode being the biggest among the leptonic ones. Regardless of the expected large coupling between the weak-force bosons and the Higgs boson, the  $H \rightarrow VV^*$  is suppressed due to the requirement that one vector boson has to be produced off-shell<sup>5</sup>.

Sorted by importance and assuming a Higgs-boson mass equal to 125.2 GeV, the BRs for the Higgs boson are listed in Table 1.6.

## 1.5 Associated top-pair and Higgs-boson production

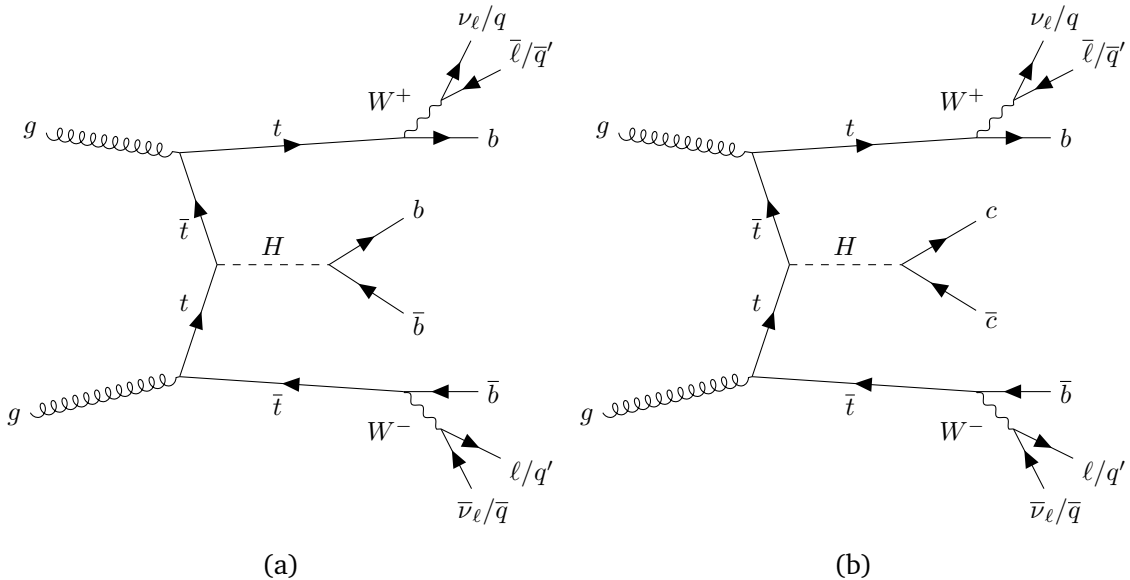


Figure 1.7. Feynman diagrams of the  $t\bar{t}H$  process with all possible final states of the  $t\bar{t}$  system with the Higgs boson decaying to (a) a pair of  $b$  quarks and (b) a pair of  $c$  quarks.

The associated production of a Higgs boson and a top quark-antiquark pair ( $t\bar{t}H$ ) provides a direct probe of the top-Higgs coupling as illustrated by the Feynman diagram in Fig. 1.7, and has recently been observed by the ATLAS and CMS Collaborations [73, 74]. Moreover, Higgs boson decays to pairs of bottom quarks have also been observed [75, 76], thereby directly probing the Yukawa interactions between the Higgs boson and top as well as bottom quarks for the first time. Overall, the observed interactions with gauge bosons and third-generation fermions, alongside all measured properties, are consistent with the predictions of the Standard Model. One of the upcoming key objectives of the LHC physics program is to investigate interactions involving second generation fermions. The CMS Collaboration recently announced

<sup>5</sup>Off-shell means that the particle is produced virtually and it does not satisfy the energy-momentum relation:  $E^2 = p^2 + m^2$ .

initial findings of Higgs boson decays into muons [77]. A critical upcoming milestone is observing its coupling to second-generation quarks and more specifically the coupling to the charm quark. In order to achieve this, ATLAS and CMS Collaborations target the associated production of a Higgs boson with a top quark-antiquark pair, where the Higgs boson decay to a charm quark-antiquark pair. However, the small branching fraction predicted by the SM, ubiquitous production of quark and gluon jets at the LHC, and the difficulty of identifying charm quark jets in a hadronic environment, including distinguishing them from bottom quark jets, make this a challenging measurement.

### 1.5.1 Associated top-pair and heavy-flavored jets production

The dominant background for  $t\bar{t}H$  process arises from pure top quark production. In the case of additionally emitted jets ( $t\bar{t} + \text{jets}$ ), mostly heavy-flavor jets ( $t\bar{t} + b\bar{b}/c\bar{c}$ ), the process has very similar final-state content and kinematic topology as the  $t\bar{t}H$ ,  $H \rightarrow b\bar{b}/c\bar{c}$  one.

In fact, analogously to the  $t\bar{t}H$ , we can define the same three decay channels since we have again  $t\bar{t}$  as an intermediate state, while the additionally emitted jets correspond to the jets produced from the Higgs decay, resulting in the exact same (but non-resonant) final states, as shown in Fig. 1.8.

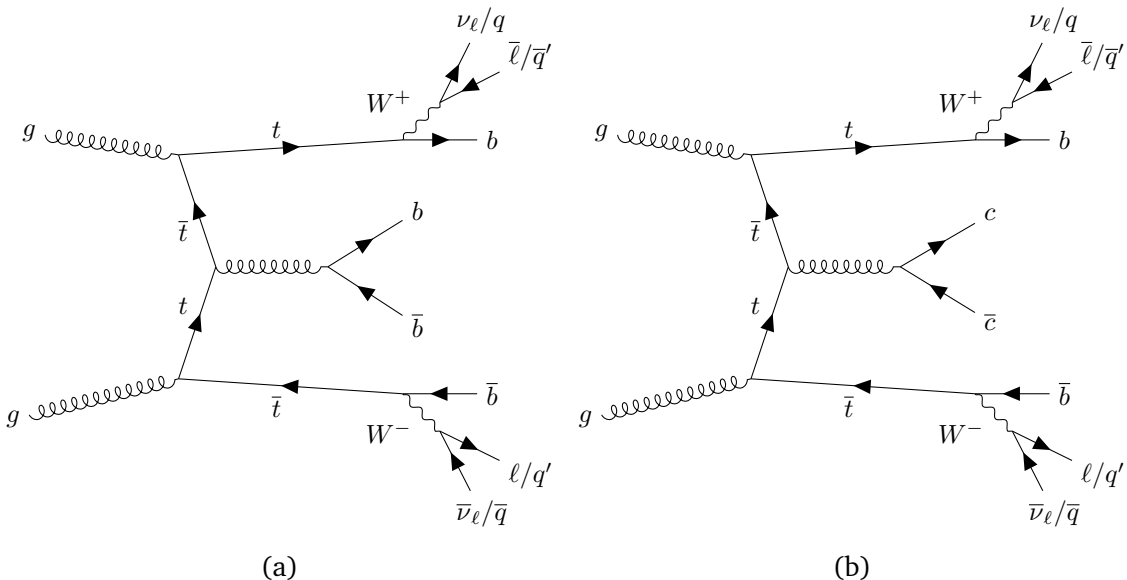


Figure 1.8. Feynman diagrams of the  $t\bar{t} + \text{jets}$  process with all possible final states of the  $t\bar{t}$  system with the addition of (a) a pair of  $b$  quarks and (b) a pair of  $c$  quarks

The main analysis of this thesis, presented in Chapter 4, studies this irreducible background at a parton level, using simulated events, in order to better understand this process and thereby improve the sensitivity of the  $t\bar{t}H(b\bar{b}/c\bar{c})$  measurement.



## 2 Experimental Setup

The theories within the Standard Model, along with any other theories aimed at explaining unresolved phenomena, must undergo experimental testing. The close cooperation between comprehending the processes in particle physics and conducting experimental tests is an important aspect of this field of science. This chapter provides a brief introduction to the experimental setup utilized for the results presented in this thesis.

In Section 2.1 the LHC layout and its performance during the data taking periods are presented. The CMS detector layout and its subsystem technologies are highlighted in Section 2.2. Finally, in Section 2.3 a brief overview of the muon trigger performance for the start of 2024 data-taking period is presented as part of the work done for this thesis.

### 2.1 Large Hadron Collider

The LHC is the largest and most powerful particle accelerator ever built, operating at the European Organization for Nuclear Research (CERN<sup>1</sup>) laboratory, near Geneva, Switzerland [78, 79]. It has a circumference of 26.7 km and is built in the same tunnel that previously housed the Large Electron Positron (LEP) Collider. It is located between 45 and 170 metres below ground level and has a slight slope of 1.23% towards Lake Geneva. The LHC was designed to collide two high energy proton beams with a maximum center of mass energy of 14 TeV<sup>2</sup>. Additionally, it facilitates collisions of heavy ion beams across a spectrum of atomic numbers, reaching energies up to 5 TeV per nucleon.

The machine consists of two parallel rings hosting counter-rotating proton beams that are accelerated to nearly the speed of light and collide at the 4 interaction points. There are multiple magnets in different sizes and varieties, aiming at keeping the beams in circular orbit, focusing and squeezing them before collision. More specifically there are 1232 dipole magnets 15 m in length which bend the beams and 392 quadrupole magnets, each 5–7 m long, which focus the beams. There are also higher order magnets (hexapoles, octapoles) which correct and

---

<sup>1</sup>Conseil Européen pour la Recherche Nucléaire

<sup>2</sup>The maximum operating energy of the LHC so far is  $\sqrt{s} = 13.6$  TeV [80]

compress the beam just before the interaction in order to increase the collision probability. All magnets are superconducting, i.e. they have almost zero electrical resistance so that they can accept high current intensities and thus generate a magnetic field of more than 8 T. However, in order to achieve the superconductivity of the magnets, it is required to be cooled to very low temperatures,  $-271.3^{\circ}\text{C}$ , which is only possible using superfluid helium [81].

### 2.1.1 LHC layout and accelerator systems

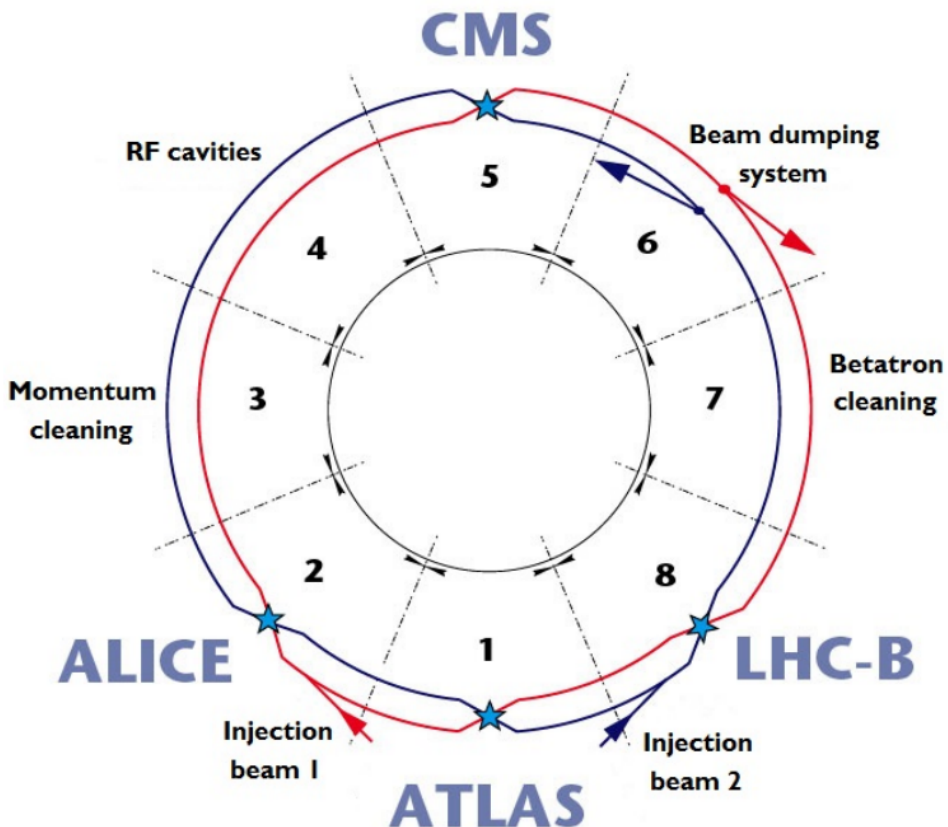


Figure 2.1. Schematic overview of the LHC. The two beams circulate in opposite directions. Beam 1 (blue) is moving clockwise around the ring and beam 2 (red) moves counter-clockwise. The two beams can collide only in the regions containing the four experiments [82].

The LHC layout follows the LEP tunnel geometry. The accelerator is divided into 8 sectors as shown in Figure 2.1. One sector extends from one straight section to the next containing one arc in between. The straight sections are named point 1 to point 8. The arcs are filled with the dipole bending magnets in a regular FODO<sup>3</sup> structure [82]. The experimental regions with the

<sup>3</sup>A FODO cell consists of a focusing quadrupole (FQ), a drift octapole (O), a defocusing quadrupole (DQ) and a second drift [83].

detectors and other key equipment are placed in the straight sections. Currently, only 4 of these sections are occupied by detectors, where the beams intersect and share a common beam pipe for a short distance, forming the experimental insertions. The two general purpose detectors, ATLAS [84] and CMS [85], are located at diametrically opposed straight sections at interaction points 1 and 5 respectively. The two smaller experiments, ALICE [86] and LHCb [87] are located at point 2 and point 8, together with LHC's beam injection points. The injection kick occurs in the vertical plane to the beams and the injection beams arrive at the LHC from below the reference plane. Points 3 and 7 contain two collimation systems each and point 4 contains RF systems that accelerate the beam particles. The beams are extracted from the machine at point 6 which contains the beam dump insertion.

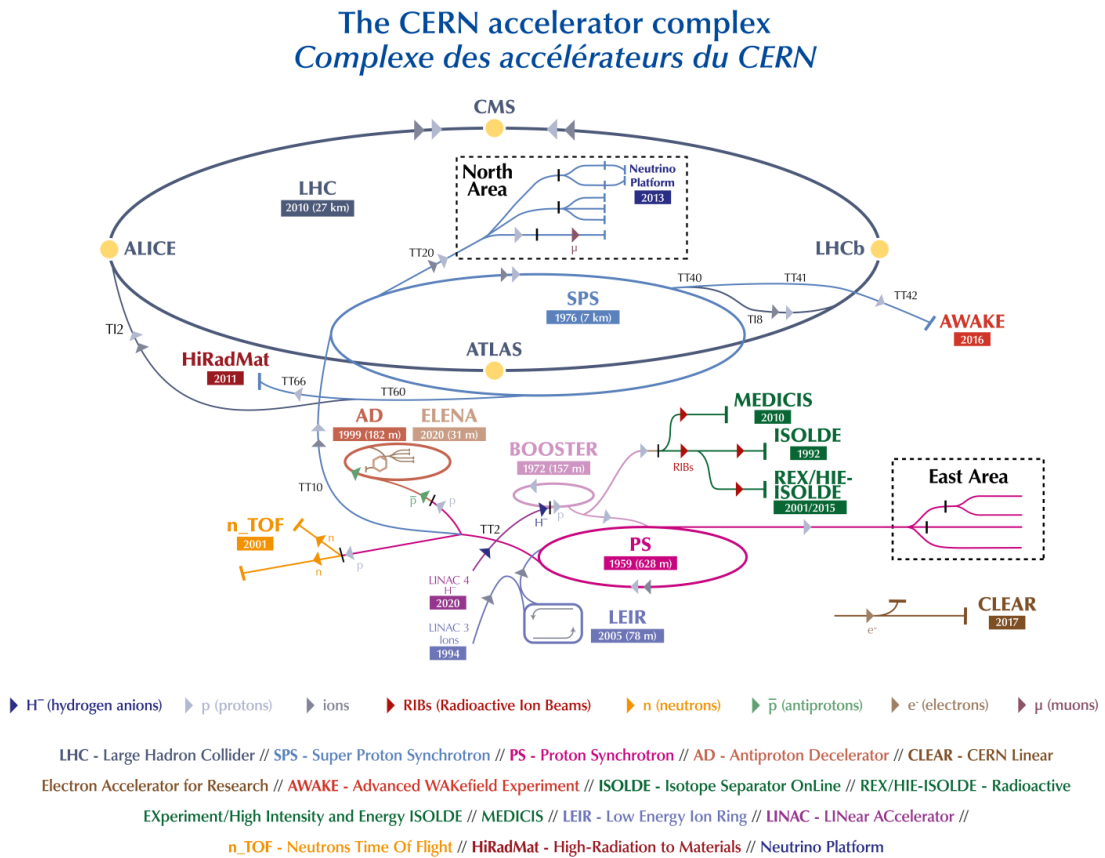


Figure 2.2. The CERN accelerator complex [88]

As far as the acceleration of the beams, an accelerator complex consisting of multiple pre-acceleration steps is used, the last one being the LHC. The full accelerator complex at CERN is shown in Figure 2.2. The source of the proton beam is a bottle of hydrogen gas. An electric field is used to strip hydrogen atoms of their electrons and yield protons. The first accelerator in the

chain is LINAC 4<sup>4</sup> and accelerates the protons to energy of 160 MeV. Then the proton beam is injected into the Proton Synchrotron Booster (PSB) [90] which accelerates protons to 1.4 GeV. The next in the accelerator chain is the Proton Synchrotron (PS) [91] which pushes the proton beam up to 25 GeV and the Super Proton Synchrotron (SPS) [92] where the beam is further accelerated up to 450 GeV. Then the protons are split and injected in the LHC beam pipes where they circulate for about 20 minutes before they reach their final energy. Protons are aggregated in bunches containing  $1.15 \cdot 10^{11}$  protons each. The bunches are separated in intervals of 25 ns.

In the case of heavy ion operations, the LHC is filled with two beams of lead ions which pass through a similar acceleration chain as the protons. The lead ions are produced with an electron cyclotron resonance [93]. A very high plasma density can be attained by the use of microwave frequencies, thus adequate for the production of multi-charged ions. Many different charge states are obtained with a maximum around the charge state  $\text{Pb}^{29+}$ . These are selected and accelerated to 4.2 MeV/u before passing through a carbon foil which strips further electrons off the lead ions yielding mainly  $\text{Pb}^{54+}$ . The beam is then accumulated and accelerated to 72 MeV/u in the Low Energy Ion Ring (LEIR) [94] and transferred to the PS, where it is further accelerated to 5.9 GeV/u. After passing the beam through a second foil where it is fully stripped to  $\text{Pb}^{84+}$ , it is sent to the SPS for a last pre-acceleration to 177 GeV/u. This beam is then transferred to the LHC that accomplishes the final acceleration step before the beams are brought to collision. Table 2.1 summarizes the pre-acceleration steps for both protons and lead ions and gives some of the design parameters of the LHC.

Table 2.1. Overview of the accelerator complex for protons and lead ions. The different accelerators, their design beam energy, and the ionization degree of the lead ions in each phase are summarized in the upper part of the table. The lower part gives some design parameters of the LHC machine.

Protons		Lead Ions		
Accelerator	Energy	Accelerator	Energy	$^{208}\text{Pb}$ charge state
LINAC 4	160 MeV	LINAC 3	4.2 MeV/u	$\text{Pb}^{29+}$
PSB	1.4 GeV	LEIR	72 MeV/u	$\text{Pb}^{54+}$
PS	25 GeV	PS	5.9 GeV/u	$\text{Pb}^{54+}$
SPS	450 GeV	SPS	177 GeV/u	$\text{Pb}^{84+}$
LHC	7 TeV	LHC	2.76 TeV/u	$\text{Pb}^{84+}$
2808 bunches		592 bunches		
$1.15 \cdot 10^{11}$ protons/bunch		$7 \cdot 10^7$ lead ions/bunch		
$\mathcal{L} = 10^{34} \text{cm}^{-2}\text{s}^{-1}$		$\mathcal{L} = 10^{27} \text{cm}^{-2}\text{s}^{-1}$		

<sup>4</sup>Before being replaced by LINAC 4 in 2020, the first accelerator was LINAC 2, which accelerated protons up to 50 MeV [89]

## 2.1.2 Luminosity

The luminosity  $\mathcal{L}$  is one of the most important parameters of an accelerator. It is a measure of the flux density of beam particles created by the accelerator at the collision point. The number of collisions in a given time interval is given by

$$\frac{dN}{dt} = \mathcal{L}\sigma \implies N = \sigma \int dt \cdot \mathcal{L} \quad (2.1)$$

where  $\sigma$  is the cross-section of the considered process. The machine's instantaneous luminosity depends only on the beam parameters and can be written as:

$$\mathcal{L} = \frac{N_b^2 n_b f_{rev} \gamma_r}{4\pi \epsilon_n \beta^*} F \quad (2.2)$$

where  $N_b$  is the number of particles per bunch,  $n_b$  the number of bunches per beam,  $f_{rev}$  the revolution frequency,  $\gamma_r$  the relativistic gamma factor,  $\epsilon_n$  the normalized transverse beam emittance,  $\beta^*$  the beta function at the collision point and  $F$  the geometric luminosity reduction factor due to the crossing angle at the interaction point:

$$F = 1/\sqrt{1 + \left(\frac{\theta_c \sigma_z}{2\sigma^*}\right)^2} \quad (2.3)$$

where  $\theta_c$  is the full crossing angle at the interaction point,  $\sigma_z$  the RMS bunch length and  $\sigma^*$  the transverse RMS beam size at the interaction point. The design luminosity of the LHC is  $\mathcal{L} = 10^{34} cm^{-2}s^{-1}$  for pp-collisions and  $\mathcal{L} = 10^{27} cm^{-2}s^{-1}$  for the lead ion beams [78].

The integral of instantaneous luminosity over time is called integrated luminosity and it is a measure of the collected data size.

$$L_{int} = \int dt \cdot \mathcal{L} \quad (2.4)$$

Integrated luminosity is an important parameter that directly relates to the number of observed events. It is usually expressed in units of inverse femtobarn  $1 fb^{-1} = 10^{39} cm^{-2}$ . Figure 2.3 shows the integrated luminosity delivered by the LHC and collected by the CMS experiment, during the Run 1 (2010-2012), the Run 2 (2015-2018) and Run 3 (2022-2023) data-taking for pp collisions. The Run 1 of data taking lasted from 2010 to 2012. In its initial year, the LHC operated at a center-of-mass energy of  $\sqrt{s} = 7$  TeV, yielding an integrated luminosity of approximately  $5.59 fb^{-1}$  collected by the CMS experiment. Subsequently, during the latter portion of Run 1, the center-of-mass energy was elevated by 1 TeV, resulting in an integrated

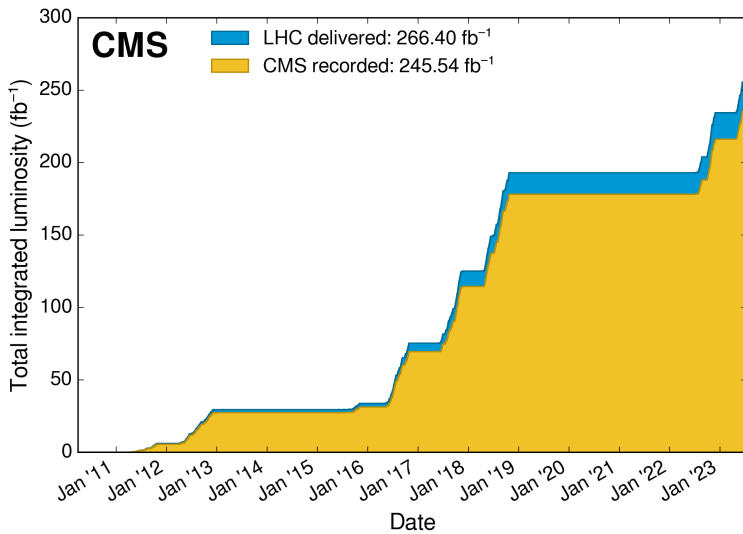


Figure 2.3. Cumulative delivered and recorded luminosity versus time for 2010-2012, 2015-2018, and 2022-2023 (pp data only) [95]

luminosity of around  $21.79\text{fb}^{-1}$ . Following this phase, both the LHC apparatus and the detectors underwent maintenance and enhancements during a period known as Long Shutdown (LS) 1, spanning from 2013 to 2015. The subsequent data collection phase, termed Run 2, transpired from 2015 to 2018. Throughout this interval, the LHC operated at a center-of-mass energy of  $\sqrt{s} = 13\text{ TeV}$ , facilitating the accumulation of an integrated luminosity of approximately  $150\text{fb}^{-1}$  by the CMS experiment, of which approximately  $140\text{fb}^{-1}$  was certified as good for physics analysis. Presently and after another LS, the LHC is undergoing Run 3, slated to continue until 2025. For Run 3, the center-of-mass energy has once again increased to  $\sqrt{s} = 13.6\text{ TeV}$ . Following the conclusion of Run 3, an LS3 is scheduled, during which the LHC will undergo significant upgrades in preparation for the High Luminosity LHC (HL-LHC).

## 2.2 Compact Muon Solenoid Detector

The Compact Muon Solenoid (CMS) detector is one of two largest general-purpose devices at the LHC and operates at interaction point 5. It has a length of 28.7 m, diameter of 15 m and it weights 14 ktonnes. It is designed to record all (stable) particles produced in the pp collisions, except of neutrinos (see Fig. 2.4a). As most particles produced in the pp collisions have lifetimes that are too short to be directly recorded in such a detector, mostly only the particles from the decay of primary particles are recorded in the detector itself. The origin of these particles, i.e. the process in the pp collision, has to be inferred via reconstruction algorithms and data analysis.

CMS was initially conceived to unravel the mysteries surrounding electroweak symmetry breaking, particularly through the pursuit of the Higgs boson and searches for Beyond the Standard Model (BSM) phenomena at TeV energy scales such as natural supersymmetry. Now CMS has extended its physics program beyond these realms. A plethora of analyses are performed, exploiting the full range of pp and heavy-ion collision data.

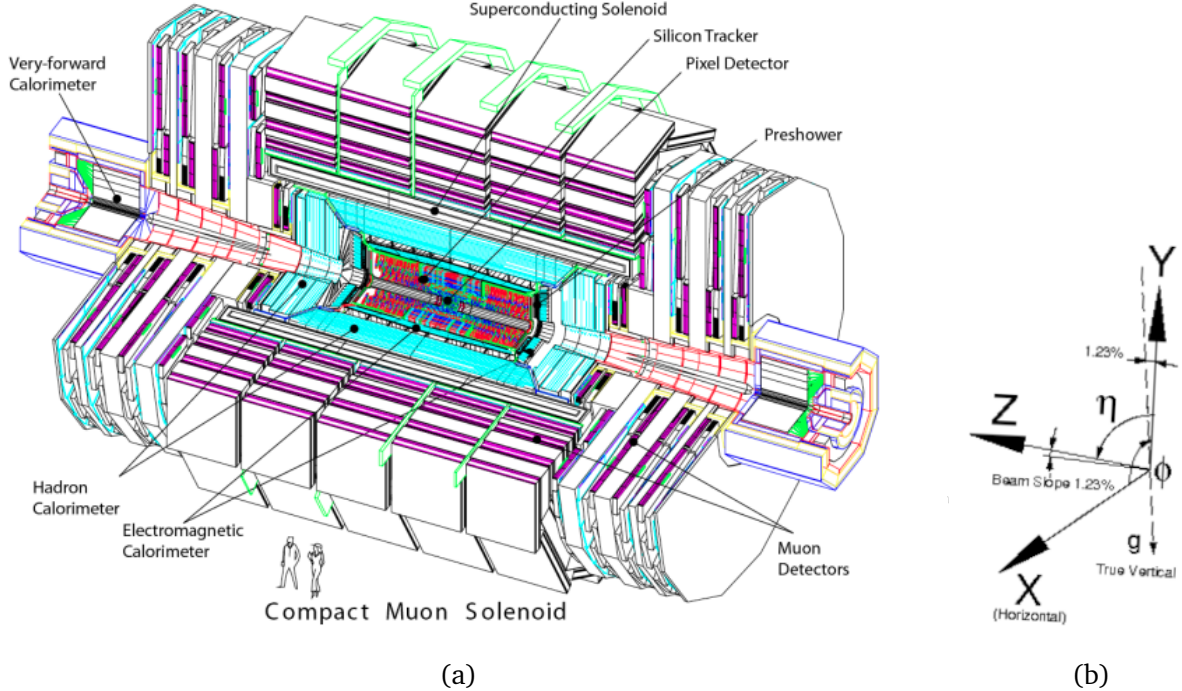


Figure 2.4. (a) Schematic overview of the CMS detector [96] and (b) the right-handed coordinate system [97]

## 2.2.1 Coordinate system and collider quantities

At the CMS experiment, a right-handed coordinate system is used (Figure 2.4b), where the  $x$  axis is defined towards the center of the LHC and the  $y$  axis points upwards. The  $z$  axis is defined in the direction of the beam. Since the plane of the LHC ring has a slight slope of 1.23% with respect to the horizontal by construction, the coordinate system of CMS is tilted accordingly. The CMS detector is cylindrical with the center being the pp interaction point. Correspondingly, an azimuthal angle  $\phi$  is defined in the  $(x, y)$ -plane, and a polar angle  $\theta$  relative to the beam direction. The collisions and resulting processes are symmetrical in  $\phi$ .

Both colliding beams feature protons with identical energies, resulting in equal but opposite momenta along the  $z$  direction, while exhibiting negligible momentum in the  $(x, y)$ -plane. Since protons are composite particles, their constituent partons are the entities that undergo collisions, behaving as quasi-free particles due to the asymptotic freedom of QCD. The mo-

momentum fraction carried by the partons in a single proton-proton collision remains uncertain, rendering the total momentum along the  $z$  direction indeterminate. Consequently, it is convenient to define a quantity that is invariant against (unknown) boosts in the  $z$  direction, such as the transverse momentum.

$$p_T = \sqrt{p_x^2 + p_y^2} \quad (2.5)$$

The transverse momentum quantifies the momentum in the  $(x,y)$ -plane.

Another common quantity is the rapidity,  $y$ , which is defined as

$$y = \frac{1}{2} \left( \frac{E + p_z}{E - p_z} \right) \quad (2.6)$$

Differences in the rapidity are invariant against Lorentz boosts along the  $z$  direction, resulting in a suitable quantity to measure the angular separation of two particles.

However, because of the high energies that we encounter in particle physics, we are interested in the limit where  $|\vec{p}| \gg m$ , i.e. the limit where  $m \rightarrow 0$ . In this limit the rapidity takes another form, which we call pseudorapidity,  $\eta$ :

$$\eta \equiv \lim_{m \rightarrow 0} \frac{1}{2} \ln \left( \frac{E + p_z}{E - p_z} \right) \quad (2.7)$$

which, because  $E \approx |\vec{p}|$  and  $p_z = |\vec{p}| \cos \theta$ , can be written as:

$$\eta = \frac{1}{2} \ln \left( \frac{|\vec{p}| + |\vec{p}| \cos \theta}{|\vec{p}| - |\vec{p}| \cos \theta} \right) = \frac{1}{2} \ln \left( \frac{1 + \cos \theta}{1 - \cos \theta} \right) = -\ln \left[ \tan \left( \frac{\theta}{2} \right) \right] \quad (2.8)$$

The pseudorapidity is defined such that  $\eta = 0$  is perpendicular to the beam axis and  $\eta \rightarrow \pm\infty$  is parallel to the beam axis (Figure 2.5). Angular distances in the  $(\theta, \phi)$ -plane are usually quantified with  $\Delta R$ ,

$$\Delta R = \sqrt{(\Delta \phi)^2 + (\Delta \eta)^2} \quad (2.9)$$

using the pseudorapidity  $\eta$  instead of the polar angle  $\theta$

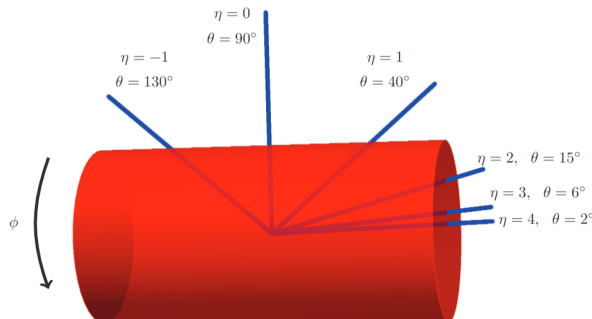


Figure 2.5. Pseudorapidity as a function of the polar angle  $\theta$  [98]

## 2.2.2 CMS layout

The detector's geometry is specifically designed for optimal particle detection and maximum reconstruction performance. It is cylindrical, with its axis along the beam line and the collision region centered at its geometrical center. Comprising the central region are the barrel sections, constructed from 5 distinct wheels, while the forward regions are covered by disks known as endcaps. The structure of the detector resembles that of a cylindrical onion, i.e. it consists of several concentric layers, each of which is designed for a different purpose. The interaction of the colliding particles with the detector materials result in electric signal. This signal is measured, digitised and finally analysed by computers.

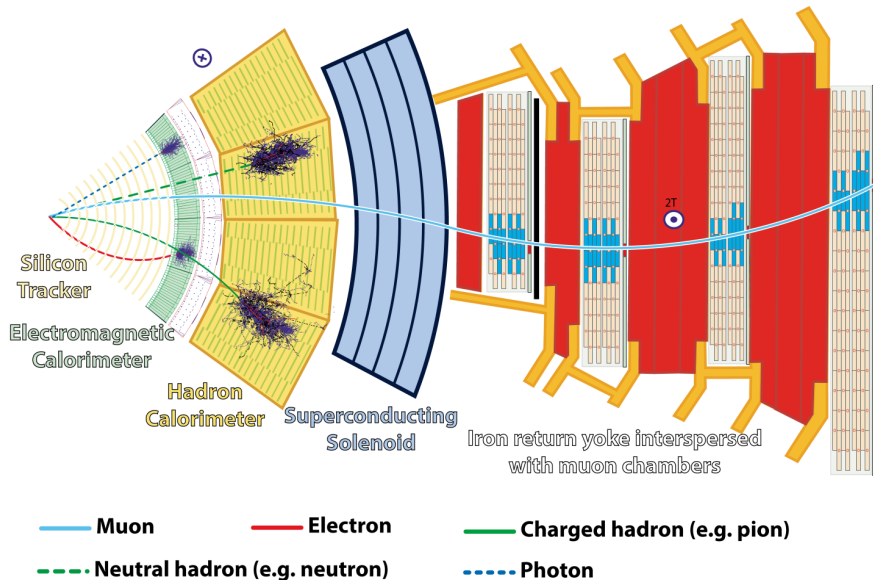


Figure 2.6. Slice showing CMS sub-detectors and how particles interact with them [99]

As shown in Figure 2.6, the barrel is comprised of five main parts. The tracker is a cylinder of 5.8 m long and diameter of 2.6 m. Its purpose is the identification of charged particles and the measurement of their trajectories, momenta and charges. Outside the tracker, the electromagnetic and hadronic calorimeters are located sequentially. The electromagnetic calorimeter (ECAL) is designed to detect electrons and photons and surrounds the tracker with an outer radius of 1.75 m. The hadronic calorimeter (HCAL) is designed to detect jets of hadrons and has an outer radius of 3 m.

The precise momentum measurement of high-energy charged particles requires large bending power by a strong magnetic field. This is achieved by the main feature of the CMS detector, the superconducting solenoid magnet. It generates a 3.8 T, nearly homogeneous magnetic field, parallel to the beam line. The large magnetic field provides strong bending on the muon tracks, before they enter the muon chambers. The solenoid accommodates the tracker and the calorimeters within its volume.

Outside the solenoid, the muon system is integrated in the iron return yoke frame which confines the magnetic field outside the solenoid to allow for momentum measurement with the muon detectors, as well as to protect the detector electronics. The muon detection utilizes gas ionization technology and its purpose is to identify and measure the momentum and charge of the muons.

The detector has almost full solid angle coverage. The central barrel region covers up to  $|\eta| < 1.48$  and the two endcaps cover up to  $|\eta| < 3$ . In the very forward regions of HCAL the coverage of pseudorapidity is extended to  $\eta = 5$ .

The following subsections describe the different detector components, starting at the nominal interaction point in the center of the detector and following the geometric order radially outwards. A detailed review of the CMS detector can be found in [85, 96]

### 2.2.3 Inner tracking system

The innermost part of the CMS detector is the tracking system. Its purpose is to provide precise and efficient measurement of charged particle trajectories through the ionization they produce along their path. Charged particles traversing the tracker induce electron-hole pairs, which create measurable currents that are digitized. The resulted “hits” are grouped into tracks using advanced pattern recognition algorithms and reconstruct a trajectory per particle. The origin or “vertex” and the direction of flight of the particle are also indicated by the reconstructed trajectory.

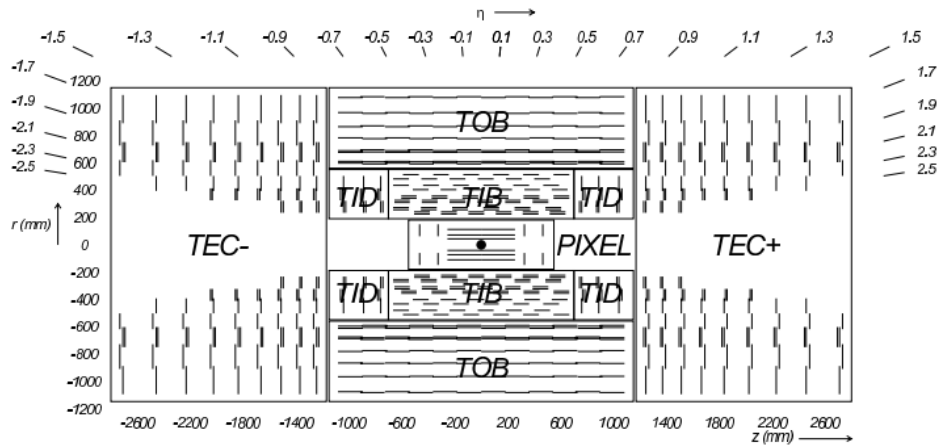


Figure 2.7. Schematic overview of the CMS tracking system [85]. The silicon pixel detector in the center is surrounded by the silicon strip detector which consists of endcaps and different barrel components.

The tracker is required to have high granularity, fast response and high radiation and age resistance. Therefore, silicon technology was used for the construction of the tracker. The

tracker was designed to operate without loss of efficiency up to an integrated luminosity of  $500 \text{ fb}^{-1}$ . The solenoid magnet covers fully the tracker, whose total sensitivity area is  $200 \text{ m}^2$  and its acceptance expands up to  $|\eta| < 2.5$ .

The tracker consists of five parts as depicted by Figure 2.7:

1. Pixel Detector: 4 concentric barrel layers of  $285 \mu\text{m}$  thick sensors at  $r = 2.9, 6.8, 10.9$  and  $16.0 \text{ cm}$ , covering up to  $|z| < 27 \text{ cm}$  and three disks,  $300 \mu\text{m}$  thick each at distances of  $|z| = 29.1, 39.6$ , and  $51.6 \text{ cm}$ .
2. Tracker Inner Barrel (TIB): 4 barrel layers of  $320 \mu\text{m}$  thick sensors, covering up to  $|z| < 65 \text{ cm}$  and  $20 < r < 55 \text{ cm}$ , configured parallel to the beam line.
3. Tracker Inner Disks (TID): 3 disks at each end covering  $65 < |z| < 120 \text{ cm}$  and  $20 < r < 55 \text{ cm}$ . Each micro-strip sensor is  $320 \mu\text{m}$  thick, configured radially.
4. Tracker Outer Barrel (TOB): 6 barrel layers of sensors,  $500 \mu\text{m}$  thick. Extends in radius from  $55 < r < 116 \text{ cm}$  and withing  $|z| < 118 \text{ cm}$ , surrounding the TIB/TID.
5. Tracker End Caps (TEC): Each TEC is composed of 9 disks,  $320 - 500 \mu\text{m}$  thick. They are configured in the radial direction, covering the region  $124 < |z| < 282 \text{ cm}$  and  $22.5 < |r| < 116 \text{ cm}$ .

All parts apart from the Pixel Detector are made out of silicon microstrips. The tracker transverse momentum resolution for high momentum tracks ( $100 \text{ GeV}$ ) in the central region ( $|\eta| < 1.6$ ) is 1-2% and degrades at higher  $\eta$ . For lower momentum tracks the transverse momentum resolution of the tracker is dominated by multiple scattering. The transverse and longitudinal impact parameter resolution is  $10 \mu\text{m}$  for high momentum tracks while it reduces at lower momentum due to multiple scattering.

## Silicon pixel detector

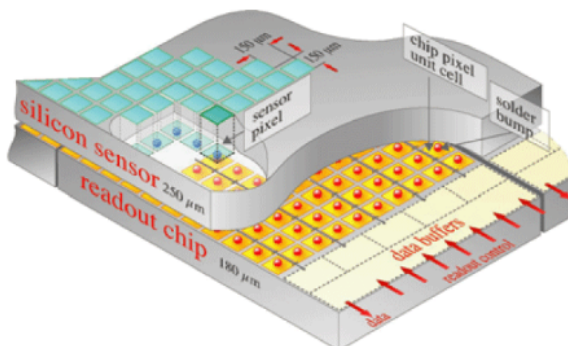


Figure 2.8. Sketch of a typical pixel sensor used in the pixel detector [100]

The Pixel Detector contains 124 million pixels and allows the tracks reconstruction with extreme accuracy. After the end of 2016 data taking period the pixel detector was replaced with an upgraded version called CMS Phase-1 pixel detector [101, 102]. The layout of the CMS Phase-1 pixel detector is optimized to have four-hit coverage over the pseudorapidity range  $|\eta| < 2.5$ , improved pattern recognition and track reconstruction, and added redundancy to cope with hit losses.

Each of the four layers is composed of individual silicon modules, splitted into little silicon sensors, the pixels (Figure 2.8). Each of these silicon pixels is  $100 \mu\text{m} \times 150 \mu\text{m}$ , about two hairs widths. When a charged particle passes through a pixel, it gives enough energy to eject the electrons from silicon atoms, thus creating electron-hole pairs. A voltage applied to the sensor allows collecting these charges as a small electric signal, which is amplified by an electronic readout chip (for a total of 16 chips per module). Knowing which two-dimensional pixels and in which layer has been touched allows us to deduce the three-dimensional particle's trajectory.

## Silicon strip detector

Covering an area of  $223 \text{ m}^2$  with axial range of 20 to 116 cm, the tracker houses 10 million Strip Silicon Detectors. It contains 15,200 modules, read by 80,000 microelectronic chips, designed to withstand radiation at  $-20^\circ\text{C}$ . While pixels focus on recording precise three-dimensional particle trajectory data, strip trackers capture more rough two-dimensional information across multiple surfaces, enhancing momentum measurement accuracy.

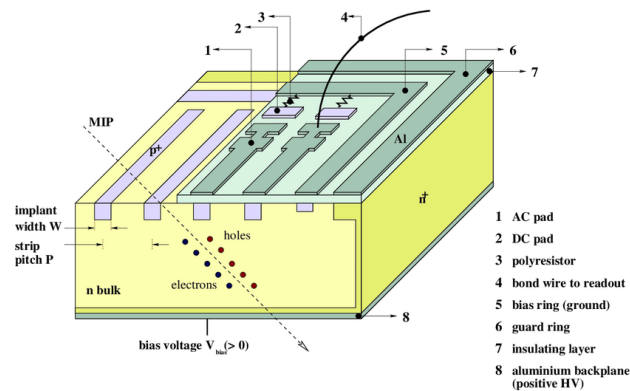


Figure 2.9. Schematic structure of a CMS silicon microstrip sensor [103].

As mentioned above, the strip tracker, is formed by four sub-modules forming a ten-layered silicon strip detector, extending to a radius of 116 cm. The silicon detectors work in much the same way as the pixels: as a charged particle crosses the material it knocks electrons from atoms giving a very small pulse of current lasting a few nanoseconds. Analogue Pipeline Voltage (APV25) chips amplify this small amount of charge, giving us “hits” when a particle passes,

which allow for the reconstruction of its path [104]. Signals are processed, converted into infrared pulses, and transmitted for analysis via fiber optic links.

## 2.2.4 Electromagnetic Calorimeter

The ECAL is almost a hermetic homogeneous<sup>5</sup> detector layer that surrounds the tracker [96, 105–108]. It is composed of 75848 lead tungstate ( $\text{PbWO}_4$ ) crystals designed to measure the energy of the particles that interact primarily via the electromagnetic interaction, i.e. electrons and photons. Electrons emit numerous Bremsstrahlung photons due to electromagnetic interactions, while photons engage with matter via the photoelectric effect, Compton scattering, and pair production.

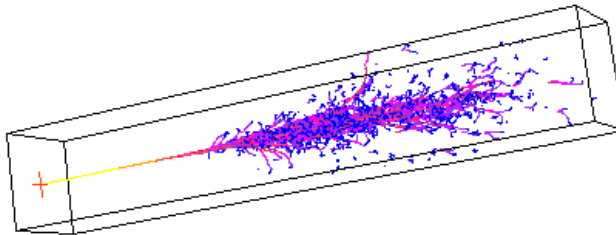


Figure 2.10. Simulated cascades inside electromagnetic crystals [109].

When a particle arrives, it interacts, generating numerous softer particles with reduced energy levels successively. This cycle continues, resulting in the creation of multiple low-energy particles, forming what is known as a cascade shower. This progression halts when the generated particles lose adequate energy and are absorbed by the material they traverse. The Molière radius is a characteristic constant of a material giving the scale of the transverse dimension of the fully contained electromagnetic showers initiated by an incident high energy electron or photon. Molière radius,  $R_M$ , is given by [12]

$$R_M = X_0 \frac{E_s}{E_C} \quad (2.10)$$

where  $E_s = 21 \text{ MeV}$  and  $E_C$  is the critical energy at which the ionization and bremsstrahlung rates are equal.  $X_0$ <sup>6</sup>, is another characteristic constant of the materials, the radiation length. The radiation length, defines the average length an electron has to travel to reduce its initial energy by  $1/e$  or the  $7/9$  of the mean free path of a photon. The shower's depth depends on the initial particle's energy as:

$$X = X_0 \frac{\ln(E_0/E_C)}{\ln 2} \quad (2.11)$$

---

<sup>5</sup>The entire volume is sensitive and contributes a signal

<sup>6</sup> $X_0$  is usually measured in  $\text{g} \cdot \text{cm}^2$

where  $E_0$  is the initial particle energy. If the energy of the shower is smaller than the critical energy, the shower stops. Both the radiation length and the Molière radius depend on the detector's material and need to be low enough in order to achieve compact calorimeters.

Lead tungstate crystal is chosen to be the active material, i.e. where all the electromagnetic processes take place, since it satisfies all of the above prerequisites. It is highly dense ( $8.28\text{g}/\text{cm}^3$ ), it has a short radiation length ( $X_0 = 0.89\text{cm}$ ) and a small Molière radius ( $R_M = 2.2\text{cm}$ ). It is also very fast responding, about 80% of the scintillation light in the crystals is emitted within 25 ns, the LHC bunch crossing time. The crystals are also radiation-hard, with the ability to maintain a good ECAL performance throughout LHC operations.

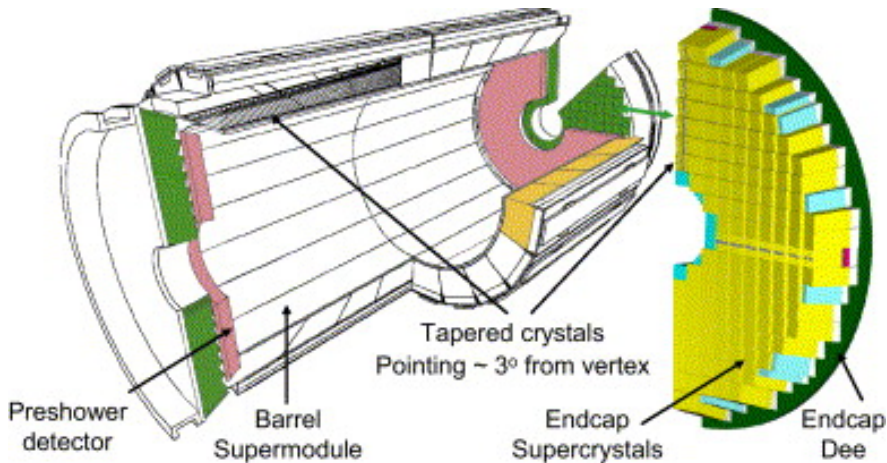


Figure 2.11. A schematic view of the CMS Electromagnetic calorimeters [107].

As electrons and photons pass through the ECAL, their electromagnetic shower results in cascades giving rise to scintillation in the crystals. Avalanche photodiodes (APDs) are used as photodetectors in the barrel and Vacuum phototriods are used in the endcaps (VPT). The lateral size of the crystals is  $\sim 1R_M$  and hence 90% of the EM shower can be contained within a single crystal. The number of scintillation photons that will be emitted by the crystals and the amplification of the photodetectors depend on the temperature. A cooling system is used to keep the temperature of the system constant.

Figure 2.11 shows the structure of ECAL. It consists of the barrel region, ECAL Barrel (EB), and the endcap region, ECAL Endcaps (EE). The EB is located at a radial distance between 129 and 175 cm, covers up to  $|\eta| < 1.479$  and contains 61200 crystals. Each crystal has a length of 23cm and a radiation length of  $25.8X_0$ . The crystals are formed into 36 “supermodules”, each weighing around three tonnes and containing 1700 crystals. The EE are located  $\pm 317\text{cm}$  from the nominal collision point, covering an interval of  $1.479 < |\eta| < 3.0$  and containing 7324 crystals, each 22 cm long. In front of these crystals, there is the ECAL Preshower (ES) detector, covering an area of  $1.653 < |\eta| < 2.6$ . It has a total width of 20 cm and consists of two lead plates and two silicon plates, arranged alternately. It is used to distinguish between

photons and the neutral pions  $\pi^0$ . These short-lived particles are produced at a very high rate during proton collisions and decay mainly into two lower energy photons which are spatially close together. For this reason, the detection strips of the preshower detector have a width of only 2 mm, thus offering higher resolution and higher precision than other calorimeter systems, making it possible to distinguish the two photons from the decay of neutral pions.

The energy resolution of the ECAL has been measured in test beams to be [85]:

$$\left(\frac{\sigma}{E}\right)^2 = \left(\frac{2.8\%}{\sqrt{E}}\right)^2 + \left(\frac{12.0\%}{E}\right)^2 + (0.3\%)^2 \quad (2.12)$$

with E measured in GeV. The first term in Eq. 2.12 is the stochastic term and parameterizes the intrinsic energy fluctuations of the shower. The second term is the noise term and accounts for electronic and digitization noise or energy fluctuations from external to the shower sources. The last term is the constant term and accounts for calibration errors or leakage of the EM shower. Since it is a homogeneous calorimeter, the effect of the very small stochastic and noise term become negligible at 50 GeV. The real challenge for the ECAL energy resolution at high energy is the constant term [110].

## 2.2.5 Hadronic Calorimeter

The HCAL [111] is a sampling calorimeter<sup>7</sup> that consists of alternating layers of brass or stainless steel as absorber and plastic scintillator or quartz fiber tiles as sensitive material that measures the energy deposit. Its main purpose is the absorption and energy measurement of strongly interacting particles. These particles create hadronic showers in the brass layer and induce detectable light in the scintillator which is guided by embedded wavelength-shifting fiber to readout electronics [112, 113].

In contrast with the electromagnetic cascades, the physical processes leading to the formation of hadron showers are different. Hadron production, nuclear deexcitation and meson decays predominate in these showers. Approximately one-third of the produced pions are neutral whose energy is dissipated in the form of electromagnetic showers. It is very often that a hadronic shower has also an electromagnetic component which sometimes can be a bit displaced from the hadronic one because of the magnetic field.

Additionally, hadronic showers differ in their development duration compared to electromagnetic ones. This can be seen by comparing the number of particles present versus depth for pion and electron initiated showers. The longitudinal development of hadronic showers scales with the interaction length. For this reason hadronic calorimeters are longer and bigger than the electromagnetic calorimeters, in order to include the whole cascade and avoid as much

---

<sup>7</sup>The material that produces the particle shower is distinct from the material that measures the deposited energy

as possible energy and particles losses from the back parts of the alternating layers of active material and absorber plates.

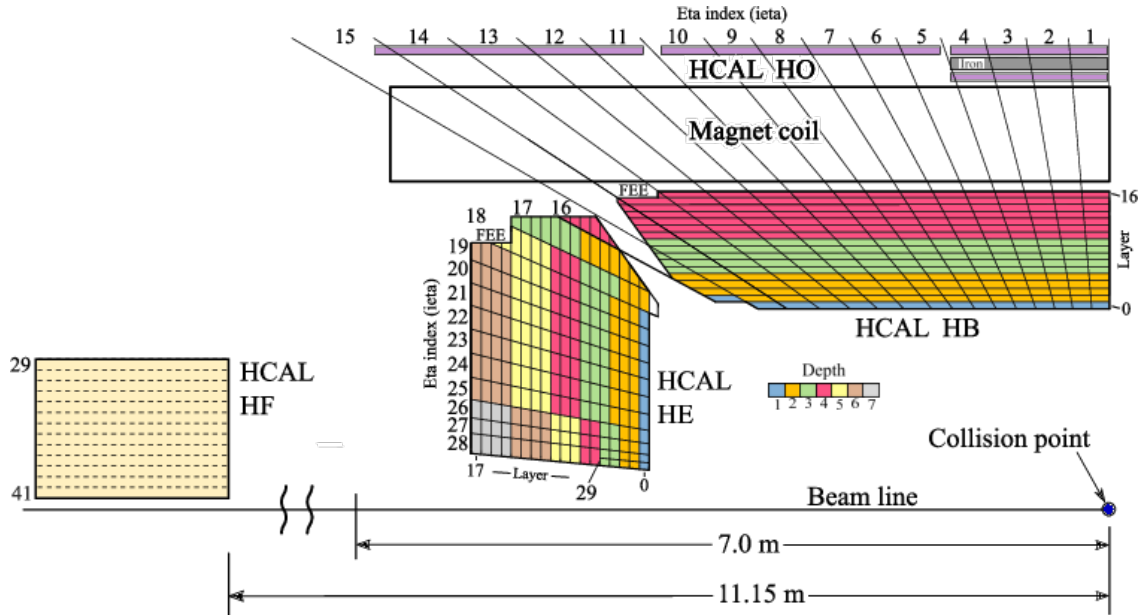


Figure 2.12. A quadrant of the CMS hadronic calorimeter [114].

The HCAL consists of four parts arranged in the layout shown in Figure 2.12. The Hadronic Barrel (HB) and the Hadronic Endcaps (HE) calorimeters surround the ECAL and are located inside the superconducting solenoid. The Hadronic Outer (HO) calorimeter is placed just outside the solenoid complementing the HB and the Hadronic Forward (HF) calorimeter is located 11.15 m away from the interaction point. The angle coverage of HCAL reaches up to  $|\eta| < 5.2$ .

The design of the HCAL was significantly influenced by the choice of magnetic parameters, since the detector array, with the exception of the HO section, is located within the solenoid magnet. Thus, brass was chosen for the absorber material as it has a relatively short interaction length and is non-magnetic, while plastic scintillator plates were used as the active material.

The combined energy resolution of the CMS HCAL+ECAL for pions that was measured during a test-beam analysis is (after correction) [110]:

$$\left(\frac{\sigma}{E}\right)^2 = \left(\frac{84.7\%}{\sqrt{E}}\right)^2 + (7.4\%)^2 \quad (2.13)$$

The noise term is found to be negligible. Similar energy resolution was found also in the endcaps. Comparing the stochastic term of the Equation 2.13 with the corresponding one from the ECAL (Eq. 2.12), we notice that this term, in the case of the HCAL, is bigger. This happens because the HCAL is a sampling calorimeter and not homogeneous. The HF energy resolution

from test beam [115] is:

$$\left(\frac{\sigma}{E}\right)^2 = \left(\frac{280\%}{\sqrt{E}}\right)^2 + (11\%)^2 \quad (2.14)$$

## 2.2.6 The magnet

Immediately after the hadronic calorimeter we find the superconducting solenoid [116–120]. The purpose of this powerful magnet is to curve the trajectories of the electrically charged particles generated during the collision as they move away from the collision point. Indeed, the bending of the particle trajectories serves two purposes. First, it helps to identify the charge of a particle. Charges, depending on their sign (positive or negative), bend in opposite directions in the same magnetic field. Second, it allows us to calculate the momentum of the charged particle as the trajectory of particles with high momentum curves less than the trajectory of those with lower momentum.

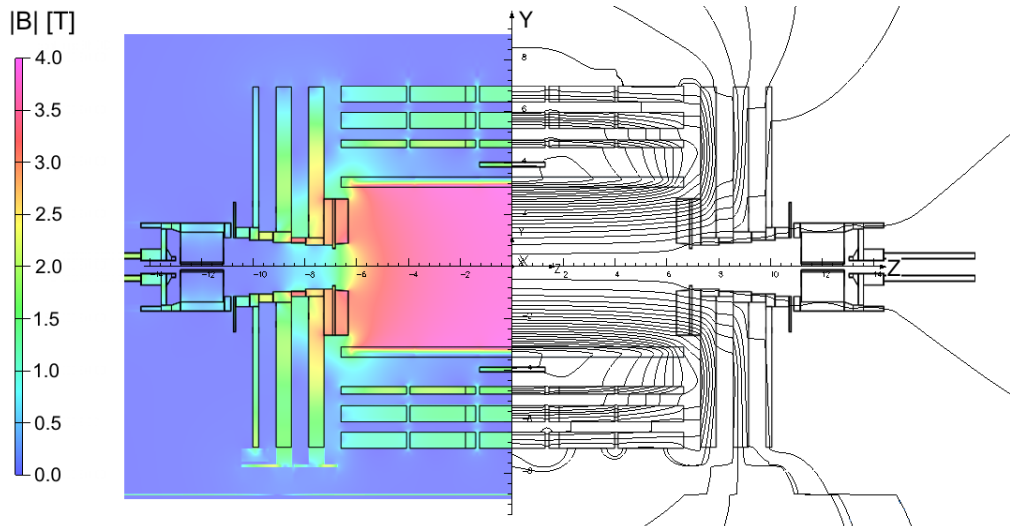


Figure 2.13. Value of  $|B|$  (left) and field lines (right) predicted on a longitudinal section of the CMS detector, for the underground model at a central magnetic flux density of 3.8T. Each fieldline represents a magnetic flux increment of 6 Wb [105].

Regarding the magnet, it is the largest solenoid superconducting magnet in the world. It consists of a cylinder 12.9 meters long, with an inner radius of 5.9 meters and an outer radius of 6.5 meters, which is wrapped with wire 2168 times [121]. The electric current flowing through the wire creates a magnetic field of  $3.8\text{ T}$ <sup>8</sup> (homogeneous inside the solenoid, see Figure 2.13), about 100,000 times that of the Earth, while the total stored energy of the field reaches  $2.3\text{ GJ}$ , energy equivalent to about half a ton of TNT. To create a magnetic field of such a high intensity, an electric current of  $18.164\text{ kA}$  is required, and to avoid the development

<sup>8</sup>Originally the solenoid was intended to produce a magnetic field of  $4\text{ T}$  but in order to maximize its longevity, the operating field was reduced to  $3.8\text{ T}$  [122]

of enormous temperatures due to this current intensity, the wire must be superconducting. In order to achieve superconductivity of the wire, it must be cooled to  $-269^{\circ}\text{C}$ .

It is worth noting that the solenoid magnet is enclosed within 12-sided iron yokes 14 metres in diameter, which close the dynamic lines of the magnetic field coming out of the caps (so the magnetic field in the muon detector is in the opposite direction to that in the silicon detectors and calorimeters). The magnet together with the yokes weigh a total of 12500 tons making it the heaviest subsystem in the whole detector assembly.

The magnetic field along the beam axis is parameterised as:

$$B_z(0, z) = \frac{1}{2} B_0 \sqrt{1 + \bar{a}} \cdot [f(u) + f(v)] \quad (2.15)$$

where

$$\begin{aligned} u &= (1 - \bar{z})/\bar{a}, \quad v = (1 + \bar{z})/\bar{a} \\ \bar{z} &= 2z/L, \quad \bar{a} = 2a/L \\ f(x) &= x/\sqrt{1 + x^2} \end{aligned}$$

with  $a$  being the solenoid radius and  $L$  its length. Inside the solenoid region, the two components of the magnetic field (along the  $z$  axis and the radial one respectively) are parameterised as:

$$B_z(r, z) = \sum_{\nu=0}^{\infty} \frac{(-1)^{\nu}}{(\nu!)^2} \frac{\partial^{2\nu}}{\partial z^{2\nu}} B_z(0, z) \left(\frac{r}{2}\right)^{2\nu} \quad (2.16)$$

$$B_r(r, z) = \sum_{\nu=0}^{\infty} \frac{(-1)^{\nu}}{\nu!(\nu-1)!} \frac{\partial^{2\nu-1}}{\partial z^{2\nu-1}} B_z(0, z) \left(\frac{r}{2}\right)^{2\nu-1} \quad (2.17)$$

## 2.2.7 The muon system

The muon system [123, 124] is located outside the solenoid magnet and comprises the outermost layer of the CMS detector. The objectives of the CMS muon system are to identify muons, measure their momenta, and provide signals for triggering on them. These goals are achieved with four complementary detector systems arranged in the steel flux-return yoke of the CMS solenoid. These subsystems are: the drift tubes (DTs), the cathode strip chambers (CSCs), the resistive-plate chambers (RPCs), and the recently added gas electron multiplier (GEM) detector. Altogether, the CMS muon detectors comprise almost one million electronic channels [114].

The physical arrangement of the muon detectors is shown in Fig. 2.14. The central section is configured in a barrel geometry with four roughly cylindrical stations at different radii from the beam axis. The endcap section is arranged in four planar stations in  $z$  in each endcap.

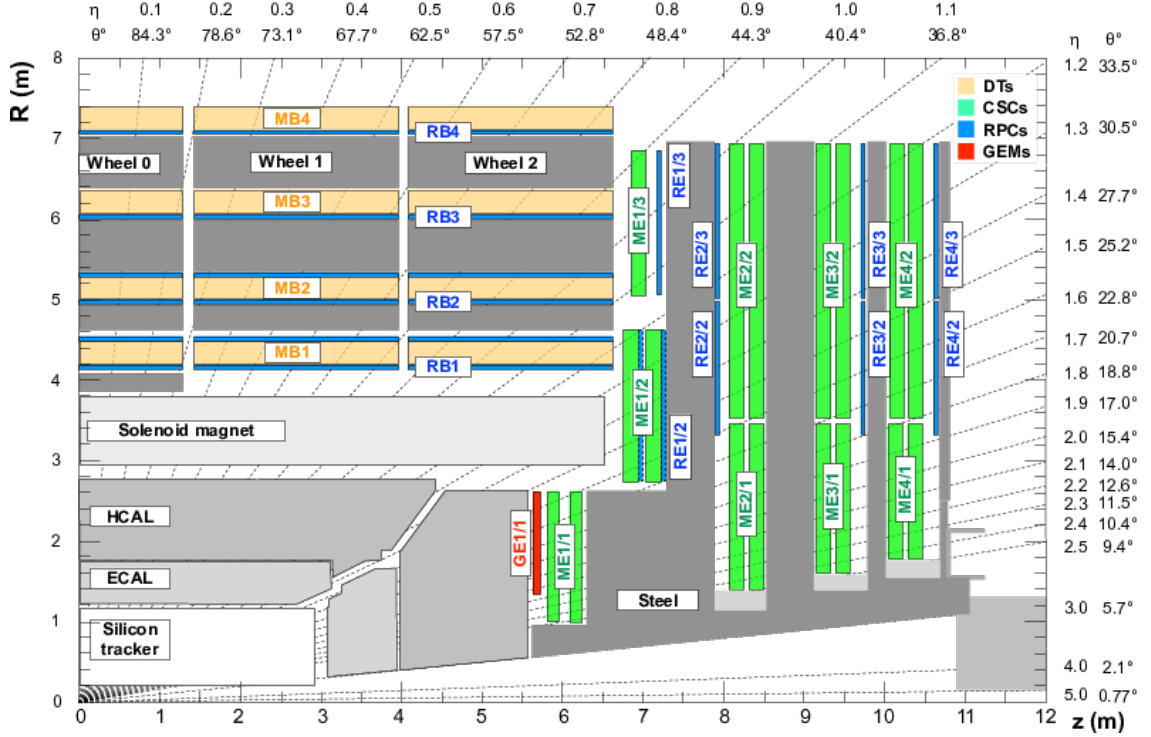


Figure 2.14. Schematic view in the  $r - z$  plane of a CMS detector quadrant [123].

## Drift Tubes

The drift tube (DT) system in the barrel covers (fully)  $|\eta| < 1.2$  (0.83) and is composed of chambers formed by multiple layers of long rectangular tubes that are filled with an Ar and CO<sub>2</sub> gas mixture. An anode wire is located at the center of each tube, whereas cathode and field-shaping strips are positioned on its borders. They create an electric field that induces an almost uniform drift of ionization electrons produced by charged particles traversing the gas. The charged-particle trajectory is determined from the arrival time of the currents generated on the anode wires.

## Cathode Strip Chambers

The cathode strip chamber (CSC) system in the endcap comprises multiwire proportional chambers having cathode strips with an  $R - \phi$  geometry and covering (fully) the region  $0.9(1.24) < |\eta| < 2.4$ . The CSCs are operated with a gas mixture of Ar, CO<sub>2</sub>, and CF<sub>4</sub>. Signals are generated on both anode wires and cathode strips. The finely segmented cathode strips and fast readout electronics provide good timing and spatial resolution to trigger on and identify muons. Because of the higher flux of particles in the endcap region, the CSCs are designed to have a faster response time than the DTs.

## Resistive Plate Chambers

The RPCs are located in both the barrel and endcap regions, and they complement the DTs and CSCs with a very fast response time that can be used to unambiguously identify the bunch crossing corresponding to a muon trigger candidate. The RPCs comprise two detecting layers of high-pressure laminate plates that are separated by a thin gap filled with a gas mixture of  $\text{C}_2\text{H}_2\text{F}_4$ , i-C<sub>4</sub>H<sub>10</sub>, and SF<sub>6</sub>. The electronic readout strips are located between the two layers, and the high voltage is applied to high-conductivity electrodes coated on each plate. The detectors are operated in avalanche mode to cope with the high background rates.

## Gas Electron Multiplier

To enhance the track reconstruction and trigger capabilities of the endcap muon spectrometer, large-area triple-layer gas electron multiplier (GEM) detectors [125] were installed in the region covering  $1.55 < |\eta| < 2.18$  of the CMS detector for the Run 3. The first station, denoted GE1/1, was installed at the very start of Run 3 while the second station, GE2/1 was added during the Year End Technical Stop (YETS) in 2024.

The key feature of the GEM is a foil consisting of a perforated insulating polymer surrounded on the top and bottom by conductors. A voltage difference is applied on the foils producing a strong electric field in the holes. The GEM is operated with a gas mixture of Ar and CO<sub>2</sub>. When the gas volume is ionized, electrons are accelerated through the holes and read out on thinly separated strips. This structure allows for high amplification factors with modest voltages that provide good timing and spatial resolution, and can be operated at high rates.

### 2.2.8 Forward detectors

#### CASTOR Calorimeter

The CASTOR (Centauro And Strange Object Research) calorimeter [126–128], is located 14.37 m from the CMS interaction point and extends the forward rapidity coverage to the region  $-6.6 < \eta < -5.2$ <sup>9</sup>. CASTOR is a sampling electromagnetic and hadronic calorimeter and presents a sandwich structure of tungsten (W) absorber plates and quartz plates as active material. The collection of the signal is based on the production of Cerenkov photons which are transmitted to photomultiplier tubes through aircore lightguides. The tungsten and quartz plates are inclined by 45° with respect to the beam axis to optimize the photon yield (Figure 2.15).

---

<sup>9</sup>Only on the negative longitudinal side of CMS

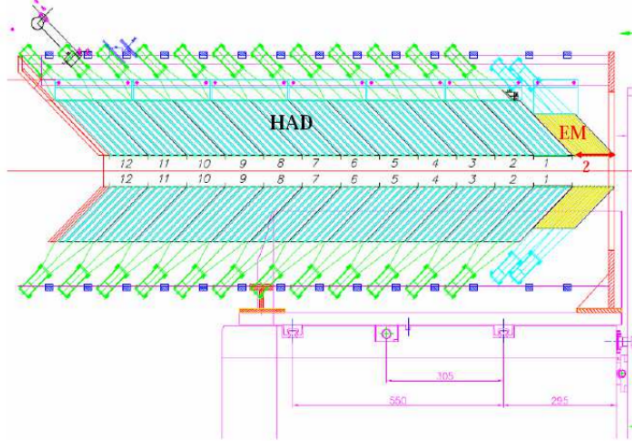


Figure 2.15. The CASTOR calorimeter [127].

## Zero Degree Calorimeter

The Zero Degree Calorimeter (ZDC) [127] detects neutral particles in  $|\eta| > 8.5$  region. These detectors are located at  $z = \pm 140\text{m}$  from the interaction point. The CMS ZDC is able to measure the spectator neutron multiplicity distribution. Its fibres are made up of quartz, its effective material is tungsten, and its technology is similar with that of the CASTOR calorimeter.

### 2.2.9 Triggering system

The LHC collides proton bunches at a rate of 40 MHz, spaced 25 ns apart. Considering a storage size of  $\sim 1\text{ MB}$  per bunch crossing event, the LHC collision frequency would result to data output of 40 TB per second, which is unfeasible to be recorded. However, not all collision events hold pertinent information for physics investigations. Hence, a meticulous selection process is necessary to isolate events of interest while discarding the rest. To accomplish this, the CMS employs a sophisticated two-tiered trigger system: the Level-1 Trigger (L1 Trigger), implemented in hardware and the High-Level Trigger (HLT), implemented in software.

#### Level-1 Trigger

The L1 Trigger system is instrumented with custom-designed hardware processors, and runs event selection algorithms using information from the CMS subdetectors. It takes a decision within  $3.8\ \mu\text{s}$  and selects up to 110 kHz of interesting events, out of the 40 MHz rate it receives.

The L1 Trigger consists of two primary components: the L1 calorimeter trigger and the L1 muon trigger. The output of the two subsystems is collected by the Global Trigger (GT) which takes the final decision on the event. The decision is made based on approximately 500 event selection algorithms that depend on kinematic quantities, position, isolation and quality of the

event's objects. The selection algorithms, also referred to as L1 Trigger seeds, are executed in parallel for the final trigger decision. A schematic representation of the CMS L1 Trigger structure is depicted in Figure 2.16.

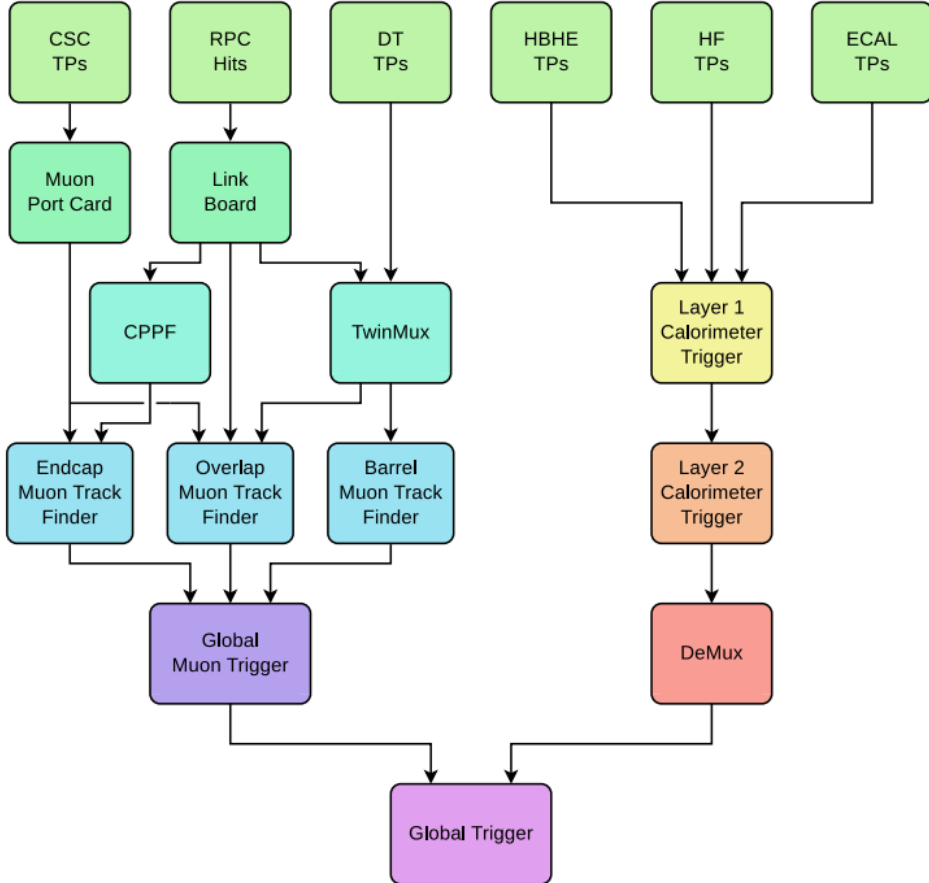


Figure 2.16. Diagram of the CMS L1 Trigger system [129]

The L1 Calorimeter Trigger consists of two layers. The Layer-1 receives, calibrates and sorts the local energy deposits, which are called "trigger primitives" (TP) and are sent from ECAL, HCAL and HF. The Layer-2 uses the TPs to reconstruct physics objects. The input to Layer-1 is organized into trigger towers (TT) that correspond to  $\Delta\eta \times \Delta\phi$  of  $0.087 \times 0.087$  each. Every TT encodes energy deposits at a specific position in the calorimeters. A Time Multiplexed Trigger (TMT) architecture is used and allows for the information of all the TT in the event to be received by the Layer-2. There are no regional boundaries in the object reconstruction and the full granularity is exploited when the energy deposits are computed. The output of the TMT nodes are collected in the de-multiplexing (DeMux) node, sorted and sent to GT [130]. The calorimeter trigger creates two different types of trigger object, reflecting the two fundamental types of energy deposition in the calorimeter; electron/photon candidates and jets. The former are spatially-compact objects mainly confined to the ECAL, while the latter

are larger and primarily in the HCAL. In addition, algorithms have been developed aiming at reconstructing efficiently hadronically decaying  $\tau$  leptons using the combination of the ECAL and HCAL energies, thus creating possible  $\tau$  candidates [131].

The L1 muon trigger consists of three regional muon reconstructing algorithms [132, 133]:

- The Barrel Muon Track Finder (BMTF) receives DT TPs and RPC hits from  $|\eta| < 0.83$ . The TPs and hits are combined in “superprimitives” in TwinMux
- The Overlap Muon Track Finder (OMTF) receives uncombined DT TPs and RPC hits transmitted from TwinMux, together with CSC TPs. The TPs and hits delivered to the OMTF cover the range from  $0.83 < |\eta| < 1.24$
- The Endcap Muon Track Finder (EMTF): takes as input CSC TPs and RPC hits from the forward pseudorapidity regions of  $1.24 < |\eta| < 2.4$ , through CPPF (Concentration Pre-processing and Fan-out).

The muon track finder algorithms measure the charge, transverse momentum and bending angle of the L1 muon candidates, and assign to them a quality bit based on the reconstruction fit. Upon receiving up to 36 L1 muon candidates from each track finder, the GMT undertakes several tasks to refine the selection. Firstly, it sorts the candidates by transverse momentum and assesses their quality based on parameters such as pT resolution and hit count, while eliminating duplicate entries. Furthermore, the GMT incorporates spatial coordinates from the muon stations, extrapolating each candidate’s track back to the interaction point. The extrapolation corrections are derived from simulation as a function of  $p_T, \eta, \phi$  and charge and are stored in look up tables (LUT). The corrected coordinates are propagated to the GT and improve the performance of the L1 trigger seeds that rely on the invariant mass or the spatial coordinate difference between multiple muons.

A maximum of 8 muon candidates are chosen based on a combination of quality and transverse momentum metric and are sent to the GT for the final L1 Trigger decision. The GT collects L1 muons and calorimeter objects and executes every selection algorithm in parallel in order to make the final trigger decision.

## High Level Trigger and Data Acquisition

The HLT task is to further reduce the event rate to 1 kHz. To achieve this, all events that pass the L1 Trigger are sent to a computer farm of approximately 30k CPU cores, known as the Event Filter Farm. This is located in a dedicated room at the surface of the CMS cavern. The HLT has access to the full detector readout, including the tracker information, and runs a lighter version of the offline event reconstruction.

An important concept of the HLT data processing is the "path", which is a set of algorithm steps, running in predefined order, both for reconstruction of physics objects and for selection. Each path is a sequence of steps of increasing complexity. If an event is accepted by at least one path it is stored, otherwise it is discarded.

Events accepted by the HLT are transferred to another software process called the storage manager, under the supervision of the Data Acquisition system (DAQ). The data events are first stored locally on disk, into multiple primary datasets (PD). Each PD is fed by a number of logically coherent trigger paths. When operating, CMS records about 80 TB of data every day, which corresponds to approximately  $80 \times 120 \sim 9.6$  PB per run period. The recorded events are reconstructed with offline algorithms and the post-processing results are stored in NanoAOD format based on the ROOT framework [134]. A world wide computing farm with three-tier structure is used for the processing and storage of the data.

## 2.3 The L1 muon trigger performance

The most important metric of a triggering system is its efficiency, i.e. the fraction of events the trigger was supposed to collect to the fraction of events which is really collected. In order to perform an efficiency measurement without using a separate reference trigger, leading to almost unbiased estimates, a technique called tag-and-probe is used [135]. In this method, both the "tag" muon and the "probe" muon are selected using the same strict criteria, with the exception that the tag muon is specifically required to have fired the HLT. This ensures that the selection applied to the probe muon does not introduce bias into the efficiency measurement. The fraction of probe muons that passes the selection under study gives an estimate of its efficiency.

$$\epsilon_{\text{probe}} = \frac{N_{\text{pass}}^{\text{tag \& probe}}}{N_{\text{pass}}^{\text{tag}}} \quad (2.18)$$

Basically, the tag muon always fires the trigger, independently of the probe, while the probe muon fires the trigger only in some cases, thus giving us the unbiased trigger efficiency.

The efficiency of the L1 muon trigger was measured in data with this tag-and-probe technique using offline reconstructed muons from  $Z \rightarrow \mu\mu$  events. Figures 2.17a and 2.17b show the efficiency as a function of the reconstructed probe muon  $p_T$ , for a L1  $p_T$  threshold of 22 GeV, for the four different  $\eta$  regions: BMTF, OMTF, EMTF as well as the inclusive region, GMT. The inclusive in  $\eta$  efficiency is higher than 90% for the specific L1  $p_T$  threshold and it reaches 93% at the plateau.

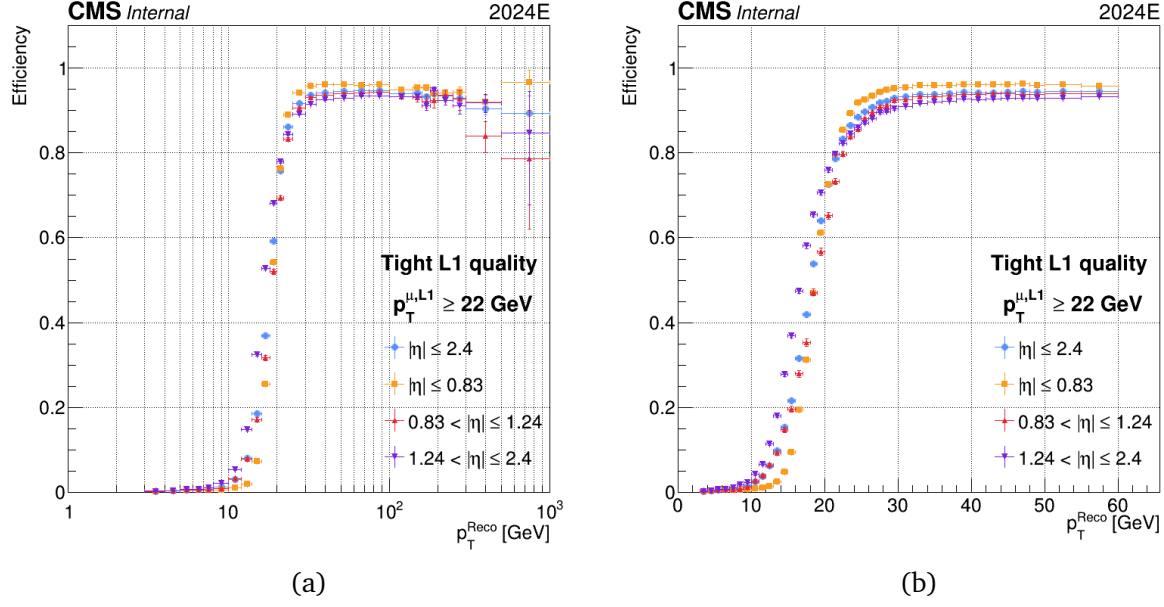


Figure 2.17. The single-muon L1 Trigger efficiency for 2024 data as a function of probe muon  $p_T$

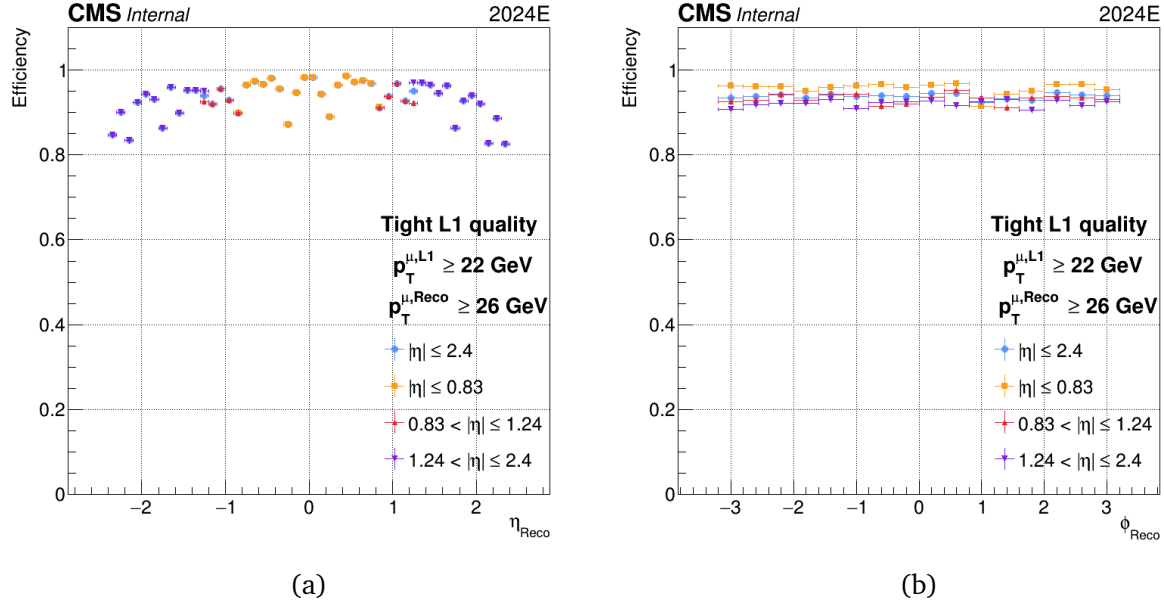


Figure 2.18. The single-muon L1 Trigger efficiency for 2024 data as a function of probe muon (a)  $\eta$  and (b)  $\phi$

Among the three regional track finders, it is easy to see that the BMTF has the best efficiency, while EMTF has the worst. This can be seen better in Figure 2.18a where the efficiency as a function of the reconstructed probe muon  $\eta$  is illustrated. From this plot, it is obvious that, the efficiency is consistently above 95%, with the exception of two points. These drops are due to the gaps between the central DT "wheel" (Wheel 0) and the neighboring wheels (Wheels 1 &

-1), where muons passing through these gaps do not leave enough hits in the DTs and thus they are often not reconstructed (see Figure 2.14). As far as the EMTF, we can see that while we go outwards, towards bigger  $|\eta|$  the efficiency drops significantly, reaching as low as 80%. This efficiency drop, originates from the inhomogenous and weaker magnetic field (CSCs are located outside the magnet) and the higher occupancy of the chambers in the forward directions.

For completeness, in Figure 2.18b the efficiency as a function of the reconstructed probe muon  $\phi$  is presented. We can see that for the region around  $\phi = 1$  there is a small drop in efficiency for all  $\eta$  regions. This is caused by the so-called "chimney", the vertical-pit where readout fibers go from the detector to the surface and opens a hole in the DT (and GMT) system. The EMTF and OMTF efficiencies should not have this feature. This effect is better illustrated in Figure 2.19, where a two dimensional plot representing the efficiency in the whole coverage of the detector is presented.

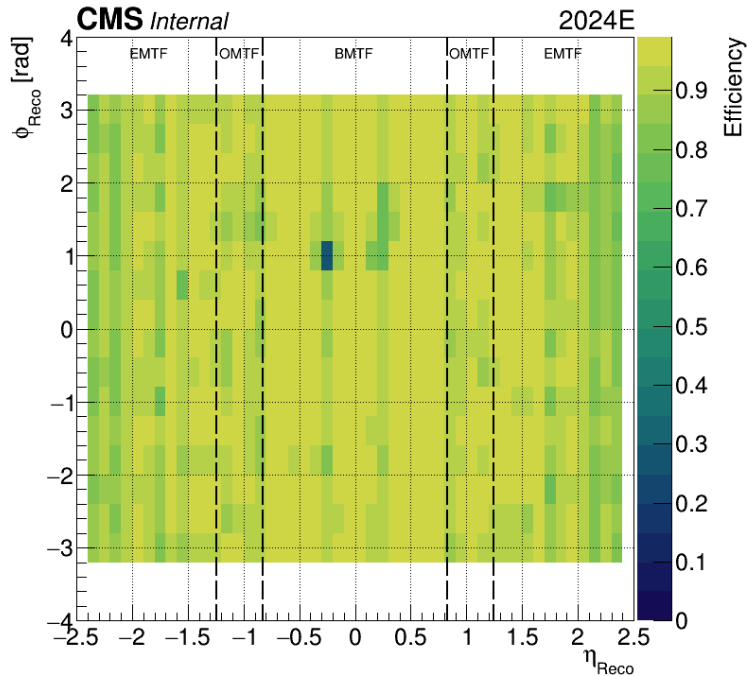


Figure 2.19. Heatmap of the single-muon L1 Trigger efficiency for 2024 data

Another important metric of the triggering system is the charge misidentification probability. This basically, indicates, how good the reconstruction is between the L1 and offline muons. In contrast with the calculation of the efficiency, for the charge misidentification probability we do not use the tag-and-probe method, but we simply match the L1 muons with the corresponding reconstructed muons and compare the charges between the two. The results are shown in Figure 2.20 as a function of the reconstructed probe muon  $p_T$ , for a L1  $p_T$  threshold of 22 GeV, for the four different  $\eta$  regions. In Figure 2.21, the two dimensional plot representing the

charge misidentification probability in the whole coverage of the detector is presented.

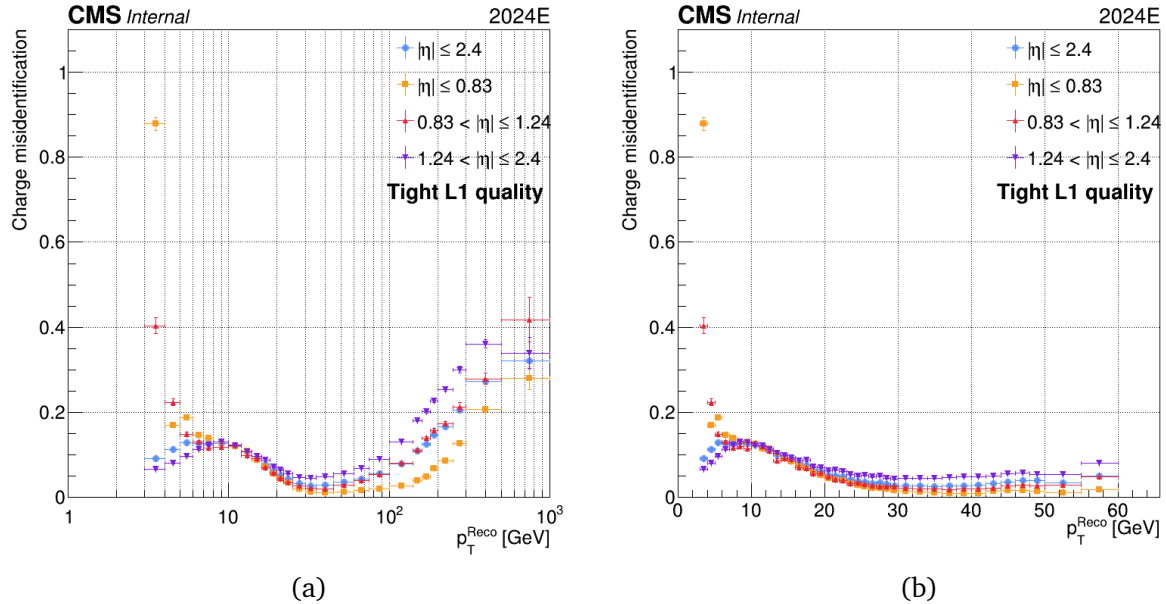


Figure 2.20. The charge misidentification for 2024 data as a function of the reconstructed muon  $p_T$

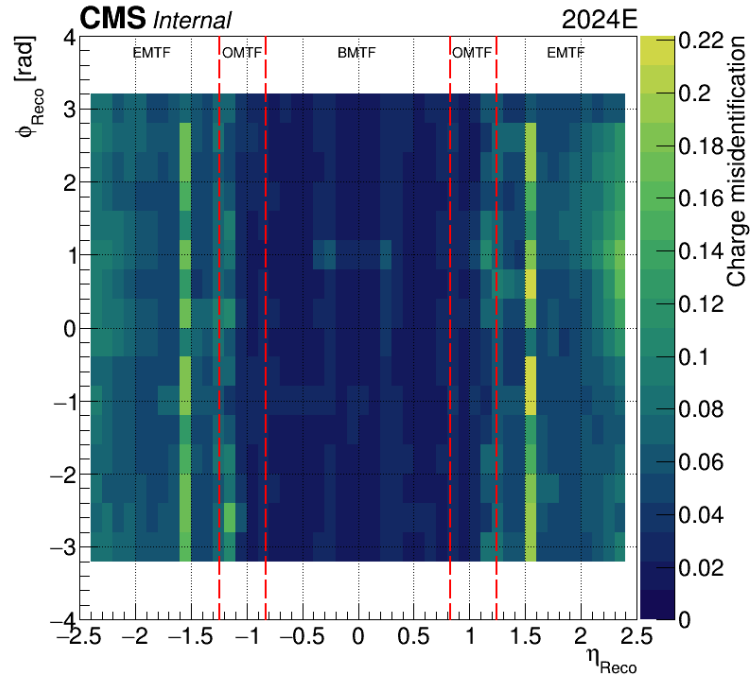


Figure 2.21. Heatmap of the charge misidentification for 2024 data



# 3 Event Simulation

In order to compare the data to predictions of the Standard Model (or of some other theory), samples are simulated using the Monte Carlo (MC) method to represent the stochastic effects and the probabilistic nature of the underlying theory. For this reason the simulated samples are often called Monte Carlo samples and the tools used to produce them are MC event generators.

Their production is a complicated process, divided into two major steps. First, the underlying collision needs to be described, starting with the two protons in the initial state and their interaction and ending with stable particles in the final state. In the second stage, the propagation of particles from the first stage, through the detector and simulation of detector response needs to be performed. Each collision and its subsequent products constitute a single event and the production of the MC samples can be called an event simulation or generation.

The simulation starts at small distances, where the colliding protons can be viewed as collections of partons (quarks and gluons). An interaction of these partons can lead to a hard-scattering, represented by a matrix element of the process. This is described in Section 3.1. In Section 3.1.2 a brief overview of next-to-leading-order calculations is presented while in Section 3.2 the basics of parton showers are emphasized. These two complementary approaches for calculating higher orders can be combined into a common framework (NLO+PS). This is described in Section 3.3. In Section 3.4 a short summary of the Monte Carlo methods used by the generators is presented. Finally, in Section 3.5 the structure of a simulated event in a proton-proton collision is described.

## 3.1 Matrix element calculations in perturbative QCD

The principal task of QCD calculations for collider experiments is to relate the incoming state to the outgoing state. This is accomplished by the scattering matrix, which relates asymptotic incoming  $\psi_{in}(\alpha)$  and outgoing states  $\psi_{out}(\beta)$ , described by the set of momenta and quantum numbers  $\alpha$  and  $\beta$ , through the relation

$$S_{\beta\alpha} \equiv \langle \psi_{out}(\beta) | \psi_{in}(\alpha) \rangle \quad (3.1)$$

In QCD,  $\psi_{in}$  and  $\psi_{out}$  would in principle correspond to incoming and outgoing quarks and gluons, however complications arise due to the confining nature of the strong force. This complication is overcome via the factorization theorem that will be discussed in Section 3.1.1. For the moment we can pretend that the fields appearing in Equation (3.1) are the fundamental degrees of freedom of the theory, i.e. quarks and gluons.

The  $S$  matrix comprises of a trivial part (no interaction) and a non-trivial part

$$S_{\beta\alpha} = \delta_{\beta\alpha} + iT_{\beta\alpha} = \delta_{\beta\alpha} + (2\pi)^4 \delta^{(4)} \left( \sum_i p_i - \sum_f p_f \right) i \mathcal{M}_{\beta\alpha} \quad (3.2)$$

The invariant matrix element  $\mathcal{M}$  represents the non-trivial part of the scattering matrix, i.e. it encapsulates the dynamics of the interaction. The delta function in Equation (3.2) imposes the conservation of the incoming 4-momenta  $p_i$ .

The matrix element can be calculated by perturbation theory using the QCD Feynman rules, which are derived from the QCD Lagrangian [136]. Cross-sections can then be calculated using the so-called Fermi's golden rule [137], which states that the transition probabilities from one state to another are given by the squared amplitude of the matrix element describing the transition, multiplied by the density of final states. More specifically, for a process  $p_1 p_2 \rightarrow k_1 \dots k_n$ , the cross section is given by

$$d\sigma = \frac{1}{F} |\mathcal{M}_n|^2 d\Phi_n \quad (3.3)$$

where  $F$  is the incoming particle flux and  $d\Phi_n$  is the n-particle final state phase space,

$$\begin{aligned} d\Phi_n(q; k_1, \dots, k_n) &= (2\pi)^4 \delta^{(4)} \left( q - \sum_{i=1}^n k_i \right) \prod_{i=1}^n \frac{d^3 k_i}{(2\pi)^3 2k_i^0} \\ F &= 4\sqrt{(p_1 \cdot p_2)^2 - (m_1 m_2)^2} \end{aligned} \quad (3.4)$$

### 3.1.1 Factorization and parton distribution functions

It was first proposed by Feynman [138], that lepton-hadron scattering in the limit of large momentum transfer can be explained by the parton model. In this model, the hadron is viewed as consisting of fundamental point-like constituents, which were later identified as QCD quarks and gluons. As it was further elaborated by Bjorken and Paschos [139], the essential ingredient of the parton model is to consider a class of infinite momentum frames, in which a parton  $i$  will carry a fraction  $0 < x_i < 1$  of the hadron's momentum. Consequently, the hadronic cross section  $\sigma_{pp \rightarrow X}$  could be obtained by convolving the cross-section for the hard-scattering sub-

process  $\hat{\sigma}_{ij \rightarrow X}$  with the Parton Distribution Functions (PDFs)  $f_i$ ,

$$\sigma_{pp \rightarrow X} = \sum_{ij} \int \int dx_i dx_j f_i(x_i, \mu_F^2) f_j(x_j, \mu_F^2) \hat{\sigma}_{ij \rightarrow X}(x_i, x_j, \mu_F^2, \mu_R^2) \quad (3.5)$$

The PDFs  $f_i(x, \mu_F^2)$  express the probability of finding a parton  $i$  inside the hadron, in this case inside a proton, carrying a momentum fraction  $x$ . However, the perturbative calculation is limited at a certain threshold by the energy dependence of the strong coupling constant which is growing with decreasing energy. The non-perturbative parts factorize at a characteristic energy scale  $\mu_F$  and are incorporated into the PDFs extracted from observed data. This energy scale is called the factorization scale and generally represents the smallest scale at which a physical process may be resolved and absorbed into the non-perturbative PDF. In addition, we have introduced another scale,  $\mu_R^2$ , called the renormalization scale which removes nonphysical divergences. Equation (3.5) is an example of theorems called factorization theorems [140] which essentially express the fact that in certain kinematic regimes the non-perturbative dynamics, encapsulated in the PDFs, can be separated from the perturbative dynamics, encapsulated in the partonic cross section.

However, these energy scales that we introduced are non-physical and in the case of an exact expansion of the perturbation series an observable  $\mathcal{O}$  is independent of these parameters. This is expressed via the so-called renormalization group equation (RGE)

$$\frac{\partial \mathcal{O}(x, Q^2)}{\partial \ln(\mu^2)} = \frac{\partial \mathcal{O}_{LO}}{\partial \ln(\mu^2)} + \frac{\partial \mathcal{O}_{NLO}}{\partial \ln(\mu^2)} + \sum_{k=2}^{\infty} \frac{\partial \mathcal{O}_{N^k LO}}{\partial \ln(\mu^2)} = 0 \quad (3.6)$$

In analogy with the beta function for the QCD running coupling, Equation (1.27), the RGE leads to the evolution equations for the PDFs [49], which are known as the DGLAP<sup>1</sup> equations [141–144]

$$\frac{d}{d \ln \mu_F^2} \begin{pmatrix} f_{q_i}(x, \mu_F^2) \\ f_g(x, \mu_F^2) \end{pmatrix} = \sum_j \frac{\alpha_s}{2\pi} \int_x^1 \frac{d\xi}{\xi} \begin{pmatrix} P_{q_i q_j}\left(\frac{x}{\xi}\right) & P_{q_i g}\left(\frac{x}{\xi}\right) \\ P_{g q_j}\left(\frac{x}{\xi}\right) & P_{gg}\left(\frac{x}{\xi}\right) \end{pmatrix} \begin{pmatrix} f_{q_j}(\xi, \mu_F^2) \\ f_g(\xi, \mu_F^2) \end{pmatrix} \quad (3.7)$$

The DGLAP equations express the fact that a quark or gluon with momentum fraction  $x$  can come from a quark or gluon with a larger momentum fraction  $x/\xi$  with a probability proportional to  $\alpha_s P_{ij}$ . Here,  $P_{ij}$  are the so-called splitting functions, which are calculable in perturbation theory, with the LO contributions shown in Figure 3.1.

---

<sup>1</sup>The acronym DGLAP refers to the names of its authors: Dokshitzer-Gribov-Lipatov-Altarelli-Parisi

$$\begin{aligned}
P_{gg}(z) &= 2C_A \left[ \left( \frac{z}{1-z} \right)_+ + \frac{1-z}{z} + z(1-z) \right] + \frac{11C_A - 4n_f T_f}{6} \delta(1-z) \\
P_{qq}(z) &= C_F \left( \frac{1+z^2}{[1-z]} \right)_+ \\
P_{gq}(z) &= C_F \left[ \frac{1+(1-z)^2}{z} \right] \\
P_{qg}(z) &= T_F [z^2 + (1-z)^2]
\end{aligned} \tag{3.8}$$

where  $C_F = 4/3$ ,  $C_A = 3$  and  $T_F = 1/2$ , while the notation  $_+$  indicates that we treat the splitting functions at  $z = 1$  as distribution functions.

$$F(z)_+ = F(z) - \delta(1-z) \int_0^1 d\zeta F(\zeta) \tag{3.9}$$

Physically, this corresponds to the fact that as the momentum scale of the interaction is increased, the sea of quark-antiquark pairs and gluons that surround the original parton are resolved. We note that although the DGLAP equations determine the evolution of the PDFs with the energy transfer, the  $x$ -dependence, shown in Figure 3.2 for an example PDF set, can only be determined by data.

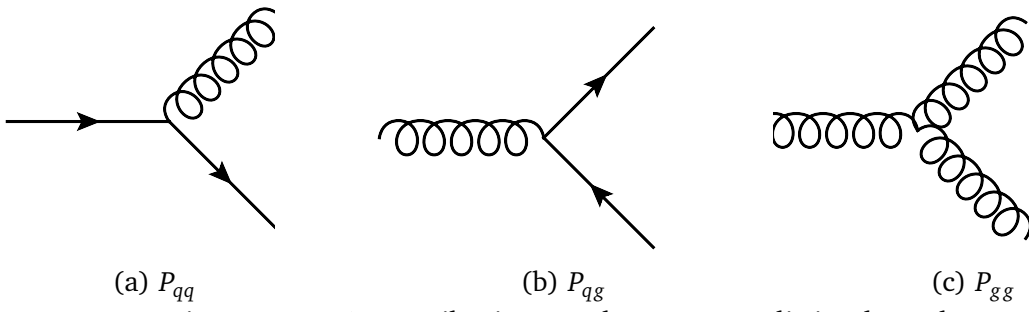


Figure 3.1. LO contributions to the DGLAP splitting kernels

Since an exact calculation is not possible, observables are usually calculated at leading-order (LO), next-to-leading-order (NLO) or next-to-next-to-leading-order (NNLO). The renormalization scale is normally chosen to be equal to the scale of the hard scattering process and is calculated individually for each event. The factorization scale is usually set to the same value as the renormalization scale.

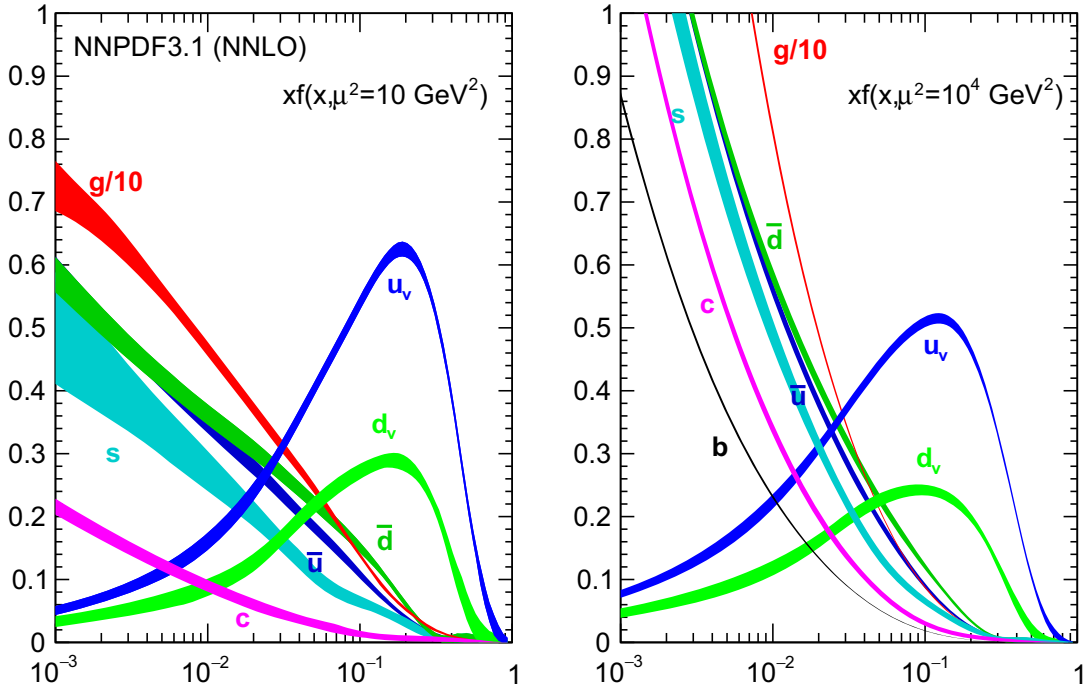


Figure 3.2. NNPDF3.1 NNLO pdf as a function of the momentum fraction  $x$  of partons in a proton. The NNPDF3.1 NNLO pdf set is evaluated at two different scales  $\mu_F^2$ . On the left at lower energy scale  $\mu_F^2 = 10 \text{ GeV}^2$  and on the right at higher energy scale  $\mu_F^2 = 10^4 \text{ GeV}^2$ . The gluon pdfs (red) are scaled by a factor of 1/10 as their contribution is by far dominant at low momentum fraction  $x$  [145].

### 3.1.2 Higher order QCD calculations

The matrix element in Equation (3.3) has a perturbative expansion in  $\alpha_s$ . Going beyond the lowest order contributing to a given process corresponds to the emission or emission and re-absorption of gluons, as shown in Figure 3.3. In the usual nomenclature, the tree-level contributions, i.e. containing no loops, are referred to as Born contributions, while  $N^k LO$  contributions correspond to adding  $k$  gluons to the LO contribution.

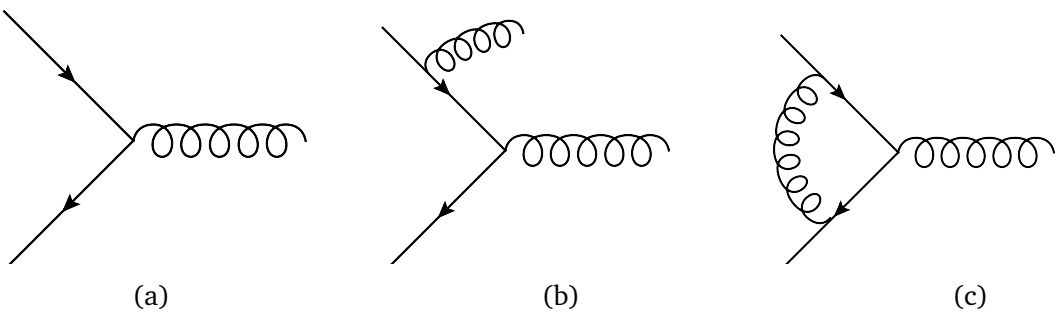


Figure 3.3. Example of (a) Born, (b) Real and (c) Virtual Feynman diagrams

One can symbolically write the parton-level cross-section at NLO accuracy as

$$\sigma^{NLO} = \int_n d\sigma^B + \int_{n+1} d\sigma^R + \int_n d\sigma^V \quad (3.10)$$

with  $d\sigma^B, d\sigma^R, d\sigma^V$  representing the Born (LO), Real and Virtual contributions respectively while the integration subscripts represent the number of partons in the final state. The exclusive cross sections  $d\sigma^R$  and  $d\sigma^V$  have the same structure as the Born-level cross section in Equation (3.3), apart from the replacements  $|\mathcal{M}_n|^2 \rightarrow |\mathcal{M}_{n+1}|^2$ ,  $d\Phi_n \rightarrow d\Phi_{n+1}$  and  $|\mathcal{M}_n|^2 \rightarrow |\mathcal{M}_n|_{(1-loop)}^2$ . Here  $|\mathcal{M}_n|_{(1-loop)}^2$  denotes the QCD amplitude to produce  $n$  final state partons evaluated in the one-loop approximation.

Expressing the Born cross section as  $Bd\Phi_B$  and the real cross section as  $Rd\Phi_R$  we can write the differential NLO cross section schematically as

$$d\sigma^{NLO} = [B(\Phi_B) + \hat{V}(\Phi_B)]d\Phi_B + R(\Phi_R)d\Phi_R \quad (3.11)$$

where we have also assumed that all phase space Jacobians needed to reproduce the Lorentz invariant phase space are absorbed into the definition of  $B$ ,  $\hat{V}$  and  $R$ . In addition, we write  $d\Phi_R = d\Phi_B d\Phi_{rad}$  where  $\Phi_{rad}$  is the radiation phase space.

However, the calculation of these integrals, leads to the so-called ultraviolet, infrared (soft) and collinear divergences. Ultraviolet divergences arise from the  $p \rightarrow \infty$  limit of the loop integral, i.e. the virtual cross section. Infrared divergences come from the the  $p \rightarrow 0$  limit of loop diagrams and the emission of soft gluons in the real contributions while the collinear divergences are from real emission diagrams which involve branchings between three massless partons. These divergences are not physical but signal the breakdown of perturbation theory. The ultraviolet divergences can be handled in a simple way within the loop corrections by carrying out the renormalization procedure, introducing  $\mu_R$ . Thus, we can assume that the virtual cross section in Equation (3.10) is given it terms of the renormalized matrix element and the ultraviolet divergences have been removed. On the other hand, infrared and collinear divergences lead to the main problem. Due to the Kinoshita-Lee-Nauenberg theorem [146, 147], by adding the real and virtual contributions, must mutually cancel for an inclusive cross section calculation. However, this cancellation does not take place at the integrand level.

The cancellation of soft and collinear divergences in NLO calculations is usually dealt with using the subtraction method [148]. The general idea of the subtraction method is to introduce an auxiliary counter-term  $C(\Phi_R)$  which is required to coincide with the real squared amplitude  $R$  in the soft and collinear limit:

$$d\sigma^{NLO} = [B(\Phi_B) + \hat{V}(\Phi_B)]d\Phi_B + [R(\Phi_R) - C(\Phi_R)]d\Phi_R + C(\Phi_R)d\Phi_R \quad (3.12)$$

Assuming that we want to compute an infrared safe observable  $\mathcal{O}$ , the infrared safety requires that, in the soft or the collinear limit:

$$\mathcal{O}(\Phi_R(\Phi_B, \Phi_{rad})) \rightarrow \mathcal{O}(\Phi_B) \quad (3.13)$$

Thus, we can write

$$\begin{aligned} \langle \mathcal{O} \rangle &= \int d\sigma \mathcal{O} = \int d\Phi_B [B(\Phi_B) + \hat{V}(\Phi_B)] \mathcal{O}(\Phi_B) + \int d\Phi_R R(\Phi_R) \mathcal{O}(\Phi_R) \\ &= \int d\Phi_B [B(\Phi_B) + V(\Phi_B)] \mathcal{O}(\Phi_B) + \int d\Phi_R [R(\Phi_R) \mathcal{O}(\Phi_R) - C(\Phi_R) \mathcal{O}(\Phi_B)] \end{aligned} \quad (3.14)$$

where

$$V(\Phi_B) = \hat{V}(\Phi_B) + \int d\Phi_{rad} C(\Phi_R(\Phi_B, \Phi_{rad})) \quad (3.15)$$

The above equations represent schematically the subtraction method in QCD. By suitable choice of the counter-term  $C$ , the integral of the radiation variables in Equation (3.15) can be performed analytically. The soft and collinear divergent terms arising from this integration cancel against those of the virtual term  $\hat{V}$  yielding a finite result  $V$ . At the same time in Equation (3.14) the soft and collinear divergences in  $R$  cancel, because in the soft or collinear limit  $\mathcal{O}(\Phi_R) = \mathcal{O}(\Phi_B)$  and  $C$  has the same singularity structure as  $R$  [149].

## 3.2 The Parton Shower approach

Additional radiation can be described by the perturbative QCD framework up to the hadronization scale  $\Lambda_{QCD}$ , where the value of  $\alpha_s$  becomes larger than one. However, due to an increasing number of contributing processes, current generators usually provide only a matrix element at the leading order or the NLO. Parton showers (PS) offer a way to generate the additional soft and collinear emissions, which dominate the production of additional particles. They are divided into the Initial State Radiation (ISR), connected to the initial parton from the proton before the hard scattering, and Final State Radiation (FSR), which describes emission from the particles produced by the hard scattering.

We consider first the leading collinear region in which an extra parton is emitted at a small angle by one of the outgoing lines of an n-parton process (FSR). Here the cross section approximately factorizes in the form

$$d\sigma_{n+1}(\Phi_{n+1}) = \mathcal{P}(\Phi_{rad}) d\sigma_n(\Phi_n) d\Phi_{rad} \quad (3.16)$$

and  $d\Phi_{n+1} = d\Phi_n d\Phi_{rad}$ . The function  $\mathcal{P}$  depends on the type of emitting and emitted partons. In the notation of the previous Section, if the n-parton process is the Born process, we have  $\Phi_n = \Phi_B$ ,  $\Phi_{n+1} = \Phi_R$  and  $\mathcal{P}(\Phi_{rad})B(\Phi_B) \equiv R^{(MC)}(\Phi_R)$  is an approximation to  $R(\Phi_R)$  in the near-collinear region. In this region it is convenient to parameterize the phase space  $\Phi_{rad}$  in terms of a hardness scale  $q$ , for example the transverse momentum  $p_T$  or the angle  $\theta$  relative to the emitter, the fraction of longitudinal momentum  $z$  of the emitter after the emission and the azimuthial angle of splitting,  $\phi$ . Then,

$$\mathcal{P}(\Phi_{rad})d\Phi_{rad} \approx \frac{\alpha_s(q)}{\pi} \frac{dq}{q} P(z, \phi) dz \frac{d\phi}{2\pi} \quad (3.17)$$

where  $P(z, \phi)$  is the relevant splitting function, Equation (3.8), which in practise is averaged over the azimuthial angle and simply written as  $P(z)$ . The collinear divergence is regulated with a cutoff,  $q > Q_0$ . Emissions with  $q < Q_0$  are said to be unresolvable. Emissions with small momentum fractions  $z$  are also unresolvable. Depending on the definition of the scale  $q$ , the cutoff on  $z$  is some function  $z_0(q, Q_0)$ .

Equations (3.16) and (3.17) provide the basis of an iterative scheme for summing collinear-enhanced contributions to all orders. Each parton participating in a hard process can emit at scales  $q$  up to order  $Q$ . The probability of an emission in an interval between  $q + dq$  and  $q$  is given by Equation (3.17). It follows that the probability of no resolvable emission between scales  $q_1$  and  $q_2 < q_1$  is given by

$$\Delta_s(q_1, q_2) = \exp \left[ - \int_{q_2}^{q_1} \frac{\alpha_s(q)}{\pi} \frac{dq}{q} \int_{z_0}^1 P(z) dz \right] \quad (3.18)$$

This function is known as the Sudakov form factor [150, 151].

The parton shower is generated in the following way: for each particle  $i$  at a scale  $q$ , a uniform random number  $r$  between 0 and 1 is generated. One then finds a new scale  $q_1$  by solving an equation  $r = \Delta_s(q, q_1)$ . If  $q_1 > Q_0$ , a new emission is introduced at the scale  $q_1$  otherwise the particle is considered to be a final state parton. This procedure is repeated until all partons are final state, producing new particles with a lower virtuality down to  $Q_0$ .

A similar method is used also for the ISR [152]. The only difference is that the initial partons have to be connected to the proton PDF leading to the formula:

$$\mathcal{P}^{(ISR)}(\Phi_{rad})d\Phi_{rad} \approx \frac{\alpha_s(q)}{\pi} \frac{dq}{q} P(z) \frac{f(x/z, q)}{f(x, q)} dz \frac{d\phi}{2\pi} \quad (3.19)$$

This obviously leads to a different form of the Sudakov form-factor:

$$\Delta_s^{(ISR)}(q_1, q_2) = \exp \left[ - \int_{q_2}^{q_1} \frac{a_s(q)}{\pi} \frac{dq}{q} \int_{z_0}^1 P(z) dz \frac{f(x/z, q)}{f(x, q)} \right] \quad (3.20)$$

## 3.3 Matching NLO calculations with PS

Based on our earlier discussion, it's evident that there are two different approaches for the calculation of observables in hadron collisions: the matrix element approach which relies on perturbative calculations performed at a given fixed order and the parton shower approach which includes all-order contributions in the collinear limit. The two approaches are complementary in the sense that in the soft/collinear region, where the parton shower approach is valid, the matrix-element calculation breaks down due to the appearance of large logarithms, while in the hard/wide-angle emission region, where the matrix-element calculation provides a good description, the approximations involved in the parton shower approach become invalid.

There are two methods for matching NLO matrix elements with parton showers, dubbed MC@NLO [153] and POWHEG [154, 155]. In both of these methods, the emission with the highest  $p_T$  is taken from the NLO matrix element (with the shower approximation subtracted) and the following emissions are taken from the parton shower and are thus only reliable in the collinear limit.

### 3.3.1 The POWHEG method

The basic idea in POWHEG<sup>2</sup> is to generate the hardest radiation first, and then feed the event to any shower generator for subsequent, softer radiation. In shower generators ordered in transverse momenta, the hardest emission is always the first, and in this case POWHEG simply replaces the hardest emission with its own, NLO accurate emission. In angular ordered showers, the hardest radiation may not be the first, and the inclusion of so-called "truncated showers" is needed to restore soft coherence in these cases.

The generation of the first emission in the shower approximation is given by

$$d\sigma = d\Phi_B B \left[ \Delta_S(Q_0) + \Delta(p_T) \frac{R}{B} d\Phi_{rad} \right] \quad (3.21)$$

---

<sup>2</sup>The acronym stands for Positive Weight Hardest Emission Generator

where,

$$\Delta(p_T) = \exp\left[-\int \frac{R}{B} d\Phi_{rad} \Theta(p_T(\Phi_{rad}) - p_T)\right] \quad (3.22)$$

According to the POWHEG procedure [156], the Equation (3.21) can achieve NLO accuracy by replacing the differential cross section  $d\Phi_B B$  with an expression that integrates to the full NLO cross section. This is achieved by the substitution

$$d\Phi_B B \rightarrow d\Phi_B \bar{B}^S \quad (3.23)$$

with  $\bar{B}^S$  being:

$$\bar{B}^S = B + V + \int d\Phi_{rad} R^S \quad (3.24)$$

Here we have split the real cross section  $R$  into two components

$$R = R^S + R^F \quad (3.25)$$

where  $R^F$  is regular in the small  $p_T$  region and  $R^S$  embodies all the singularities. A simple way to achieve the  $R^S - R^F$  separation is to choose

$$R^S = \frac{h^2}{h^2 + p_T^2}, \quad R^F = \frac{p_T^2}{h^2 + p_T^2} \quad (3.26)$$

With these changes, the equation for the generation of the hardest emission becomes

$$d\sigma = d\Phi_B \hat{B}^S \left[ \Delta_S(Q_0) + \Delta_S(p_T) \frac{R^S}{B} d\Phi_{rad} \right] + R^F d\Phi_R \quad (3.27)$$

with

$$\Delta_S(p_T) = \exp\left[-\int \frac{R^S}{B} d\Phi_{rad} \Theta(p_T(\Phi_{rad}) - p_T)\right] \quad (3.28)$$

We can see that, taking  $h \rightarrow \infty$ ,  $R^F$  vanishes, resulting back in Equation (3.21). Using the POWHEG formula, Equation (3.27), an infrared-safe observable  $\mathcal{O}$  with NLO matrix element calculation accuracy is given by

$$\langle \mathcal{O} \rangle = \frac{1}{\sigma} \left\{ \int d\Phi_B \bar{B}^S \left[ \mathcal{O}(\Phi_B) \Delta_S(Q_0) + \int d\Phi_{rad} \Delta_S(p_T) \frac{R^S}{B} \mathcal{O}(\Phi_R) \right] + \int d\Phi_R \mathcal{O}(\Phi_R) R^F \right\} \quad (3.29)$$

In the way we defined the  $\bar{B}$  function in Equation 3.24, for each  $\Phi_B$  phase space point, we would need a 3D integral in  $d\Phi_{rad}$ . This is too demanding if we want to generate  $\Phi_B$  by a hit-or-miss

technique (described in the following Section). We thus define a function

$$\tilde{B} = B(\Phi_B) + V(\Phi_B) + R(\Phi_B, \Phi_{rad}) \quad (3.30)$$

where we assume that the  $\Phi_{rad}$  phase space has been mapped to the unit cube, so that  $\int d\Phi_{rad} = 1$ . Thus

$$\bar{B} = \int d\Phi_{rad} \tilde{B} \quad (3.31)$$

## 3.4 The Monte-Carlo method for event generation

Hadron collisions typically involve the production of multi-particle final states, therefore the computation of observables for hadron collider experiments involves multi-dimensional integrations over the final-state phase space. These integrals are almost always impossible to compute analytically and one has to resort to numerical methods. One of the the most popular methods is the Monte-Carlo technique [157]. The Monte-Carlo technique is based on the approximation of an integral as follows

$$I = \int_{x_1}^{x_2} dx f(x) = (x_2 - x_1) \langle f(x) \rangle \approx (x_2 - x_1) \frac{1}{N} \sum_{i=1}^N f(x_i) \quad (3.32)$$

The approximate equality becomes exact in the limit  $N \rightarrow \infty$ . Using this approximation for the cross-section one gets

$$\sigma = \int_0^1 dx \frac{d\sigma}{dx} \approx \frac{1}{N} \sum_{i=1}^N \left. \frac{d\sigma}{dx} \right|_i \quad (3.33)$$

where  $x$  is an arbitrary parametrization of the phase space chosen so that the boundaries lie at  $x = 0, 1$ . The differential cross section  $\left. \frac{d\sigma}{dx} \right|_i$  is called the weight of the event parameterized by  $x_i$ . After calculating the cross section for a process, one wants to go one step further and simulate physical events as they occur in nature, i.e. generate a set of 4-momenta distributed according to the dynamical laws governing the process under study. This step is called event generation. In a mathematical language the event generation amounts to choosing a value  $x \in [x_{min}, x_{max}]$  distributed according to  $f(x)$  or equivalently to selecting uniformly  $(x, y)$  in  $x_{min} < x < x_{max}$ ,  $0 < y < f(x)$ . In the case where the primitive  $F$  of  $f$  is known, the problem can be solved analytically by noting that

$$\int_{x_{min}}^x dx' f(x') = R \int_{x_{min}}^{x_{max}} dx' f(x') \quad (3.34)$$

Then

$$x = F^{-1}[F(x_{min}) + RA_{tot}] \quad (3.35)$$

where  $A_{tot} = \int_{x_{min}}^{x_{max}} dx f(x)$ . In most of the cases,  $F$  is unknown and the problem is tackled using the hit-or-miss-technique. The hit-or-miss algorithm proceeds as follows

1. generate two random numbers  $R, R'$  uniformly distributed in  $(0,1)$
2. calculate  $x = x_{min} + R(x_{max} - x_{min})$  and  $y = R'f_{max}$
3. if  $y < f(x)$  accept the event (hit), else go to step 1

One can write

$$I = \frac{\int_{x_{min}}^{x_{max}} dx f(x)}{f_{max}(x_{max} - x_{min})} \Omega = \frac{N_{hit}}{N_{try}} \Omega \quad (3.36)$$

where  $\Omega = f_{max}(x_{max} - x_{min})$  and  $N_{hit}, N_{try}$  are the number of hits and number of total tries respectively. Then the integral of a function can be computed by

$$\int_{x_{min}}^{x_{max}} dx f(x) = f_{max}(x_{max} - x_{min}) \frac{N_{hit}}{N_{try}} \quad (3.37)$$

Thus the probability of a hit is proportional to  $f / f_{max}$ . Performing the hit-or-miss technique on a sample of events generated with a uniform sampling over the phase space (weighted events) gives a final sample of events which occur with the same probability as in nature (unweighted events). The probability for an event to be accepted by the hit-or-miss technique is  $\frac{(d\sigma/dx)_i}{(d\sigma/dx)_{max}}$  while the unweighting efficiency is given by  $\frac{(d\sigma/dx)_{ave}}{(d\sigma/dx)_{max}}$ .

In certain scenarios, standard Monte Carlo sampling may be inefficient due to the variance of the function  $f(x)$  over the integration range. Importance sampling aims to improve efficiency by focusing sampling efforts on regions where  $f(x)$  contributes significantly to the integral [158]. The idea is to introduce a new probability distribution  $g(x)$  that closely matches  $f(x)$  where  $f(x)$  is large. The integral  $I$  can then be rewritten as:

$$I = \int_{x_{min}}^{x_{max}} dx f(x) = \int_{x_{min}}^{x_{max}} dx \frac{f(x)}{g(x)} g(x) \quad (3.38)$$

By introducing  $g(x)$  as a sampling distribution, where  $g(x)$  is chosen such that  $f(x)/g(x)$  is relatively constant and not too large or too small across the integration range, we can approximate the integral more efficiently. The importance sampling estimate of  $I$  becomes:

$$I \approx \frac{1}{N} \sum_{i=1}^N \frac{f(x_i)}{g(x_i)} \quad (3.39)$$

where  $x_i$  are samples drawn from  $g(x)$ . Importance sampling can significantly reduce the variance of Monte Carlo estimates when  $f(x)$  varies widely, making it a powerful technique for improving the efficiency of simulations in high-dimensional phase spaces encountered in hadron collider experiments.

## 3.5 Structure of a simulated pp collision

The simulation of a proton-proton collision in Monte Carlo event generators involves multiple stages, as illustrated in Figure 3.4. The simulation starts from the calculation of the matrix element for the process of interest, referred to as the hard scattering, based on the perturbative QCD techniques that was described in Section 3.1.

The incoming and outgoing partons involved in the hard scattering process are produced with energies which are usually much higher than the hadronization scale  $Q_{had} \approx 1$  GeV. After the simulation of the hard scattering process, the phase-space from the scale of the hard scattering down to a cut-off scale  $Q_0 \approx Q_{had}$  is filled with partons mostly from soft and collinear parton branchings, simulated by the initial and final state parton shower algorithms, as discussed in Section 3.2.

After the parton showers have evolved the partons from the hard scattering process down to the cut-off scale, the strong coupling constant becomes so large that perturbation theory is no longer valid. Consequently, the subsequent step of the confinement of the partons into colorless hadrons, called hadronization must be based on phenomenological models. One such model is the Lund string model [159]. In this model, gluons, as the carriers of the strong interaction, form flux tubes between color-charged particles. As the distance between these particles increases, the energy contained in the flux tubes increases due to their linear potential. If the potential energy is high enough, a new quark-antiquark pair is created which forms new flux tubes with the other particles. This hadronization model is utilized for example in the PYTHIA general-purpose event generator [160]. A different model, the cluster hadronization model, is used for example by the HERWIG event generator [161]. In this model quarks and gluons are combined into color-neutral clusters which are iteratively fragmented into smaller clusters until stable hadrons are formed.

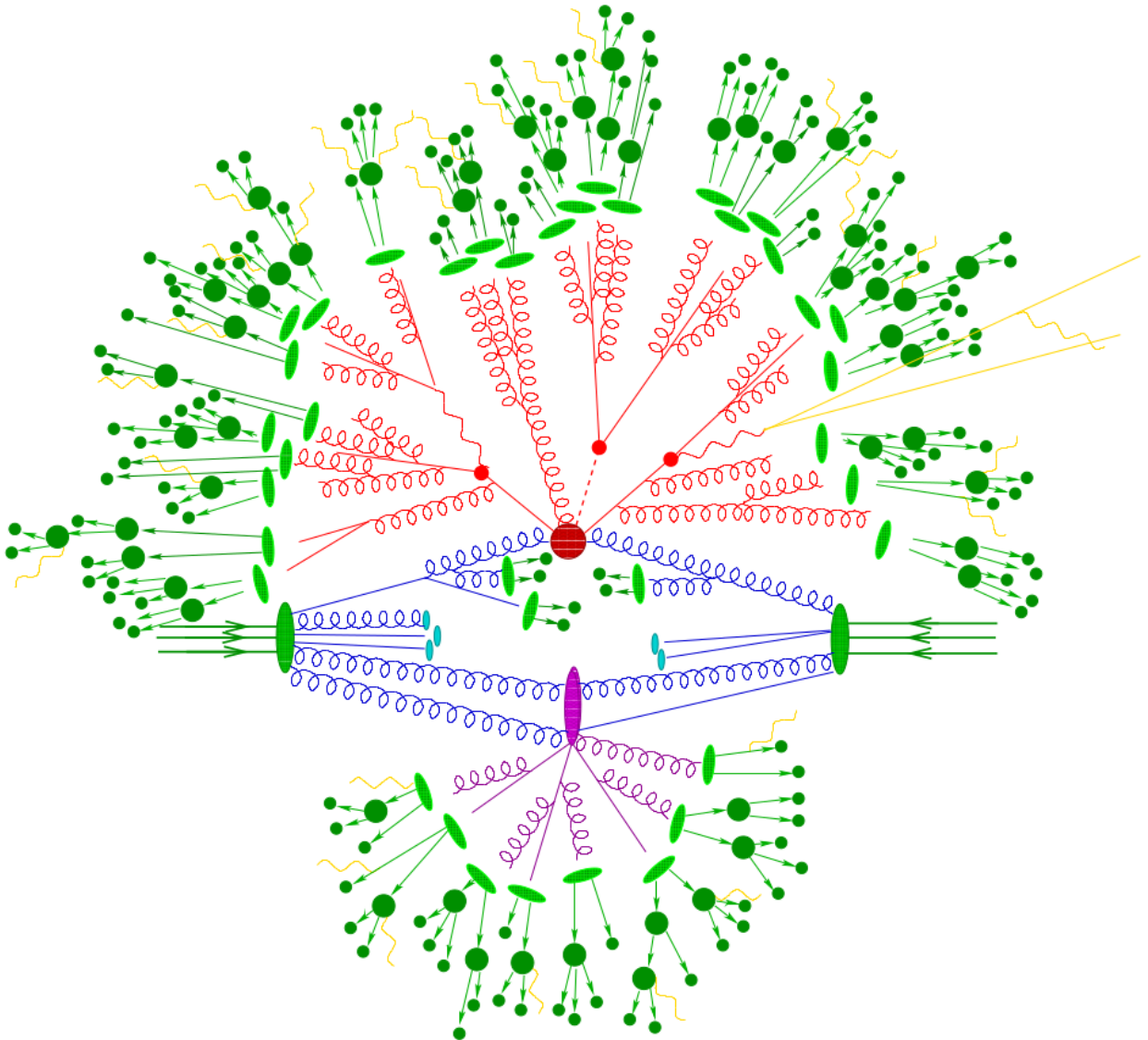


Figure 3.4. The simulation chain for a typical process at hadron colliders. The red blob in the center represents the hard collision, surrounded by a tree-like structure representing Bremsstrahlung as simulated by parton showers. The purple blob indicates a secondary hard scattering event. Parton-to-hadron transitions are represented by light green blobs, dark green blobs indicate hadron decays, while yellow lines signal soft photon radiation [162].

# 4 $t\bar{t} + hf$ jets Analysis

One of the next major physics priorities of the LHC is to establish interactions with second generation fermions, particularly focusing on second-generation quarks. To this end our focus is on the search for H boson decay to a charm quark-antiquark pair ( $c\bar{c}$ ). The corresponding Yukawa coupling  $y_c$ , can be significantly modified by physics beyond the SM (BSM). However, the SM-predicted branching fraction is small, around 3%, and the high production rate of quark and gluon jets at the LHC, coupled with the challenges in identifying charm jets in a hadronic environment due to their properties lying between lighter quark and bottom quark jets, makes this a challenging measurement. Although  $t\bar{t}H$  production has a smaller cross-section than other production mechanisms, as described in Section 1.4, the presence of W bosons and top quarks in the decay chain can, if effectively utilized, provide strong discriminative power to suppress SM background processes. Achieving this requires innovation in all aspects of the analysis. We adapt the state-of-the-art ParticleNet algorithm for AK4 jets and the Particle Transformer (ParT) architecture to effectively capture correlations among physics objects, providing strong discrimination of the  $H \rightarrow c\bar{c}$  signal from backgrounds. Furthermore, a sophisticated strategy is developed to estimate the complex backgrounds, mainly from the associated production of top-antitop quark pair ( $t\bar{t}$ ) with additional bottom or charm quarks.

This chapter begins with a brief summary of the  $t\bar{t}H$  analysis strategy in Section 4.1. Sections 4.1.1 and 4.1.2 provide an overview of the innovative machine learning algorithms, ParticleNet and Particle Transformer, employed in the analysis. The primary focus of this thesis, the Monte Carlo generator study for modeling the  $t\bar{t}+b\bar{b}$  background process, is detailed in Section 4.2. Section 4.2.1 discusses the motivation for this study, followed by a description of the specific generator configuration used in the analysis in Section 4.2.2. Finally, the results for the three channels, DL, SL, and FH, are presented in Sections 4.2.4, 4.2.5, and 4.2.6, respectively.

## 4.1 Analysis strategy for $t\bar{t}H$

The production of a Higgs boson in association with a top-quark-antiquark pair is particularly interesting for testing the SM and the Higgs mechanism. Although the main focus of this mea-

surement is the Yukawa coupling of the Higgs boson with the charm quark, both  $H \rightarrow b\bar{b}$  and  $H \rightarrow c\bar{c}$  decay modes are relevant. This is because managing the  $t\bar{t}H(b\bar{b})$  background, is improved by measuring it simultaneously with  $t\bar{t}H(c\bar{c})$ . As the top quark decays almost exclusively into a W boson and a bottom quark, the decay modes of the W boson into quarks or into a lepton and a neutrino identify the decay modes of the  $t\bar{t}$  system, as discussed in Section 1.3.

The offline event selection targets events from the production of a Higgs boson in association with  $t\bar{t}$  events, where the Higgs boson decays into  $c\bar{c}$ . All three  $t\bar{t}$  decay channels are considered: fully-hadronic (FH), semi-leptonic (SL), and dilepton (DL) decays. These signatures imply the presence of zero, one, or two isolated charged loose leptons ( $e, \mu$ ), missing transverse momentum due to the neutrinos from W boson leptonic decays, and jets with typical transverse momenta of several tens of GeV or more originating from the final-state quarks, several of which originate from b or c quarks. Hadronically decaying tau leptons are not reconstructed in this analysis, while tau leptons decaying to an electron or muon plus neutrinos can enter the selection in the SL and DL channels

One of the most challenging task of the whole analysis lies in discriminating jets originated from the hadronization of c-quarks from all other jets. Because of the intermediate properties of c-quark with respect to b- and light-quarks in terms of invariant mass, multiplicity of tracks inside the jet and average displacement of the secondary vertexes, tagging c-jets turns out to be more complicated than tagging b-jets versus other jet flavors. In order to perform our jet tagging, the output of ParticleNet [163] tagger, described in Section 4.1.1, is used.

Dominant background contributions arise from QCD multijet production (referred to as “QCD background”) in the FH channel and from  $t\bar{t} + \text{jets}$  production in all channels. The latter includes in particular  $t\bar{t}+b\bar{b}/c\bar{c}$  production, where additional b quarks can arise from QCD radiation or loop-induced QCD processes. The  $t\bar{t}+b\bar{b}/c\bar{c}$  background remains almost irreducible with respect to  $t\bar{t}H$ ,  $H \rightarrow b\bar{b}/c\bar{c}$ , with both processes having the same quarks in the final state, and constitutes the critical background to the analysis. The remaining backgrounds each make up a small fraction of the total, with  $t\bar{t}Z(Z \rightarrow q\bar{q})$  being the most notable due to its kinematic similarity with  $t\bar{t}H$ . These large and complex backgrounds in this analysis make the need for a powerful event classifier clear, a role which is filled by a Particle Transformer [164] model, described in 4.1.2.

### 4.1.1 Jet tagging with ParticleNet

ParticleNet is a state of the art Neural Network (NN) based on the Dynamic Graph Convolutional Neural Network (DGCNN) [165], developed for jet tagging purposes. The main aspect of this NN is the way it treats its candidates, i.e. the jets. Unlike other taggers, such as DeepJet [166], which organize jets’ constituent particles into an ordered structure (e.g. sequence or a

tree), ParticleNet, in a more natural representation, treats all candidates inside an object as an unordered, permutation-invariant set of particles called particle cloud.

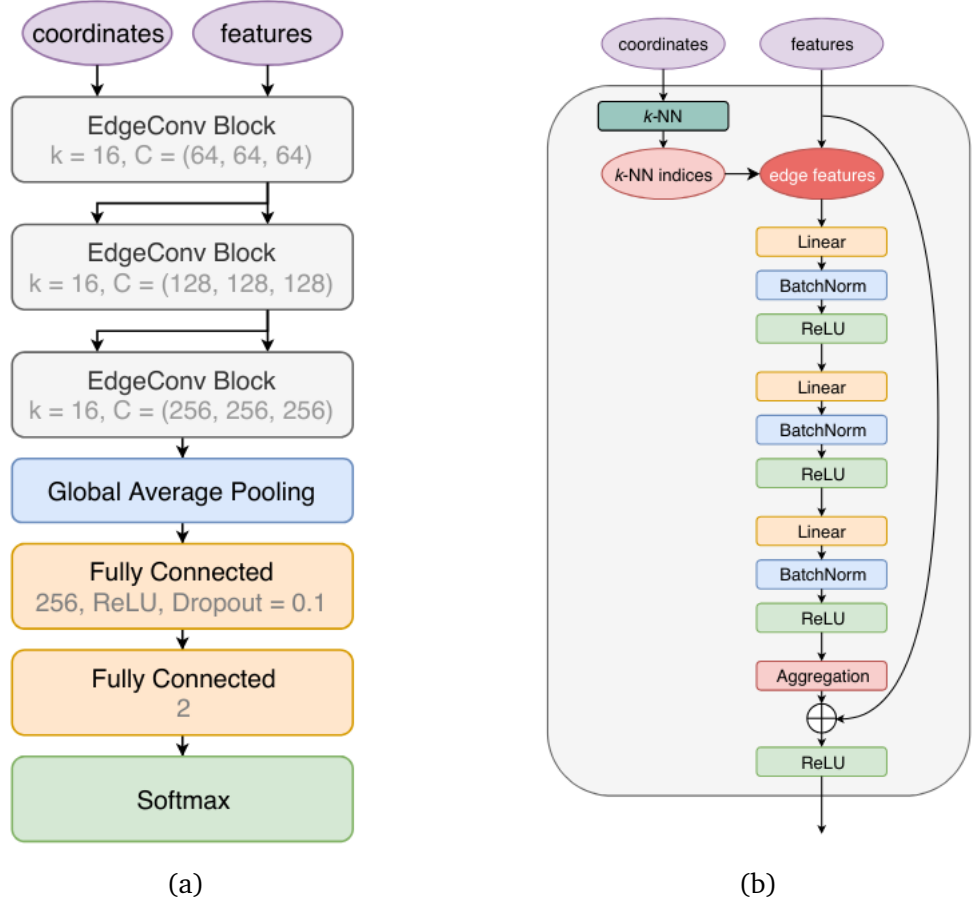


Figure 4.1. (a) The architecture of the ParticleNet. (b) The structure of the EdgeConv block [163]

The core concept of ParticleNet is the edge convolution operation, referred to as EdgeConv. The EdgeConv is a convolution-like operation for point clouds or in our case, particle clouds, which is realized by applying feature aggregation for each particle and its  $k$  nearest particles in the jet. ParticleNet's architecture consists of three EdgeConv blocks as illustrated in Figure 4.1a. The specific process of each EdgeConv block is depicted in the Figure 4.1b. It starts by finding the  $k$ -nearest neighbors for each particle within the jet. The edge between each particle and its  $k$ -nearest neighbors is determined using the input features of each particle. The EdgeConv operation is implemented as a three-layer multilayer perceptron (MLP). Each layer consists of a linear transformation, followed by a batch normalization and then a rectified linear unit (ReLU). Apart from the number of neighbors, an EdgeConv block is also characterized by the number of channels,  $C = (C_1, C_2, C_3)$ , corresponding to the number of units in each linear transformation layer. In the first EdgeConv block, the spatial coordinates ( $\Delta\eta$ ,  $\Delta\phi$ ) of the particles in the pseudorapidity-azimuth space are used to compute the edge of each pair of

particles, while the subsequent EdgeConv blocks use the learned feature vectors as coordinates. The input features, differ from one task to another but generally include kinematic variables constructed with the 4-momentum of each particle, the PID information, the charge, and some impact parameters.

After the EdgeConv blocks, a channel-wise global average pooling operation is applied to aggregate the learned features over all particles in the cloud. This is followed by a fully connected layer with 256 units and the ReLU activation. A dropout layer with a drop probability of 0.1 is included to prevent overfitting. A fully connected layer with two units, followed by a softmax function<sup>1</sup>, is used to generate the output for the classification task. We then use this output, which is in the form of scores, corresponding to the cases listed in Table 4.1.

Table 4.1. Classes definition for jet tagging

class	jets, at generator level, ...	Definition
bb	with two or more b hadrons	$nBHadrons > 1$
b	with exactly one b hadron	$nBHadrons = 1$
cc	with two or more c, but no b hadrons	$nBHadrons = 0 \ \& \ nCHadrons > 1$
c	with exactly one c, but no b hadrons	$nBHadrons = 0 \ \& \ nCHadrons = 1$
uds	induced by u, d, or s partons	$hadronflavor = 0 \ \& \  partonflavor  \in \{1, 2, 3\}$
g	induced by g partons	$hadronflavor = 0 \ \& \ partonflavor = 21$

From this, we establish two discriminating scores. One differentiates between heavy flavor (HF) jets (type bb, b, cc or c) and light flavor (LF) jets (type uds or type g):

$$\text{score[HF vs. LF]} = \frac{\text{score[bb]} + \text{score[b]} + \text{score[cc]} + \text{score[c]}}{\text{score[bb]} + \text{score[b]} + \text{score[cc]} + \text{score[c]} + \text{score[uds]} + \text{score[g]}}$$

The second differentiates between charm and bottom induced jets

$$\text{score[b vs. c]} = \frac{\text{score[bb]} + \text{score[b]}}{\text{score[cc]} + \text{score[c]} + \text{score[bb]} + \text{score[b]}}$$

Instead of using the entire score output in our analysis, we divide the two-dimensional plane defined by these two scores into categories enriched in either LF, c, or b jets. These categories are illustrated in Figure 4.2. Each category is labeled with a letter L, C, or B, representing the dominant flavor (LF, c, or b jets) in that category. The subsequent index increases with higher purity of the corresponding flavor. Additionally, we define a loose, medium, and tight working point, starting at index 0, 1, and 2, respectively.

---

<sup>1</sup>The softmax function converts a vector of  $K$  real numbers into a probability distribution of  $K$  possible outcomes. The softmax function is often used as the last activation function of a neural network to normalize the output of a network to a probability distribution over predicted output classes.

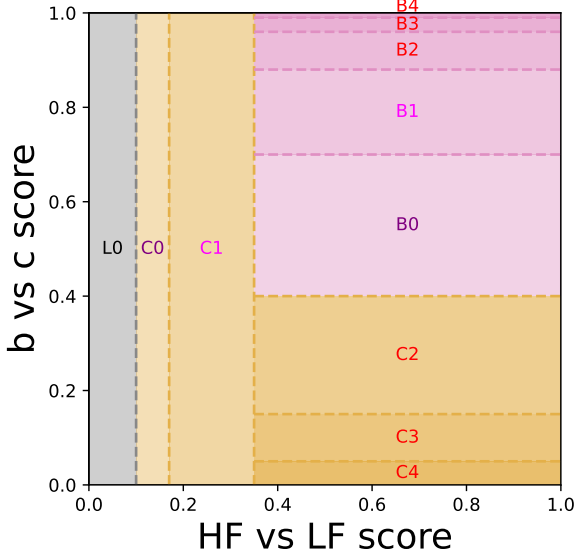


Figure 4.2. Jet tagging categories used in the analysis. The C and B categories with indices 2 or higher are considered tightly tagged (red), one or higher medium (magenta + red), zero and higher loose (purple + magenta + red).

#### 4.1.2 Event classification with Particle Transformer

Like ParticleNet, Particle Transformer is a Deep Neural Network (DNN) designed to be invariant under permutations of its input particles. However, there are two main differences between them. First, as its name suggests, Particle Transformer is based on a transformer architecture, whereas ParticleNet, discussed in the previous section, employs a convolutional architecture. Second, while ParticleNet does not explicitly focus on pairwise interactions between particles, Particle Transformer does, and is therefore more sensitive to correlations between them.

An overview of the Particle Transformer’s architecture is presented in Figure 4.3a. As a Transformer architecture, its fundamental layer is called Attention. In our case, it is specifically the Particle Attention Block, which is illustrated in Figure 4.3b. It consists of two stages. The first stage features a multi-head attention (MHA) module, with a LayerNorm (LN) layer both preceding and following it. The second stage includes a 2-layer MLP with an LN before each linear layer and a Gaussian Error Linear Unit (GELU)<sup>2</sup> nonlinearity in between. A stack of  $L$  of these particle attention blocks is employed. Following this, two class attention blocks and a global class token  $x_{\text{class}}$  are utilized. The class attention block, depicted in Figure 4.3c, has a similar structure as the particle attention block. In this block, the attention between  $x_{\text{class}}$  and all the particles is computed using the standard MHA. The class token is then passed through a single-layer MLP followed by a softmax function, to generate the final classification scores.

<sup>2</sup>The Gaussian Error Linear Unit (GELU) is a neural network activation function that provides a smoother alternative to ReLU.

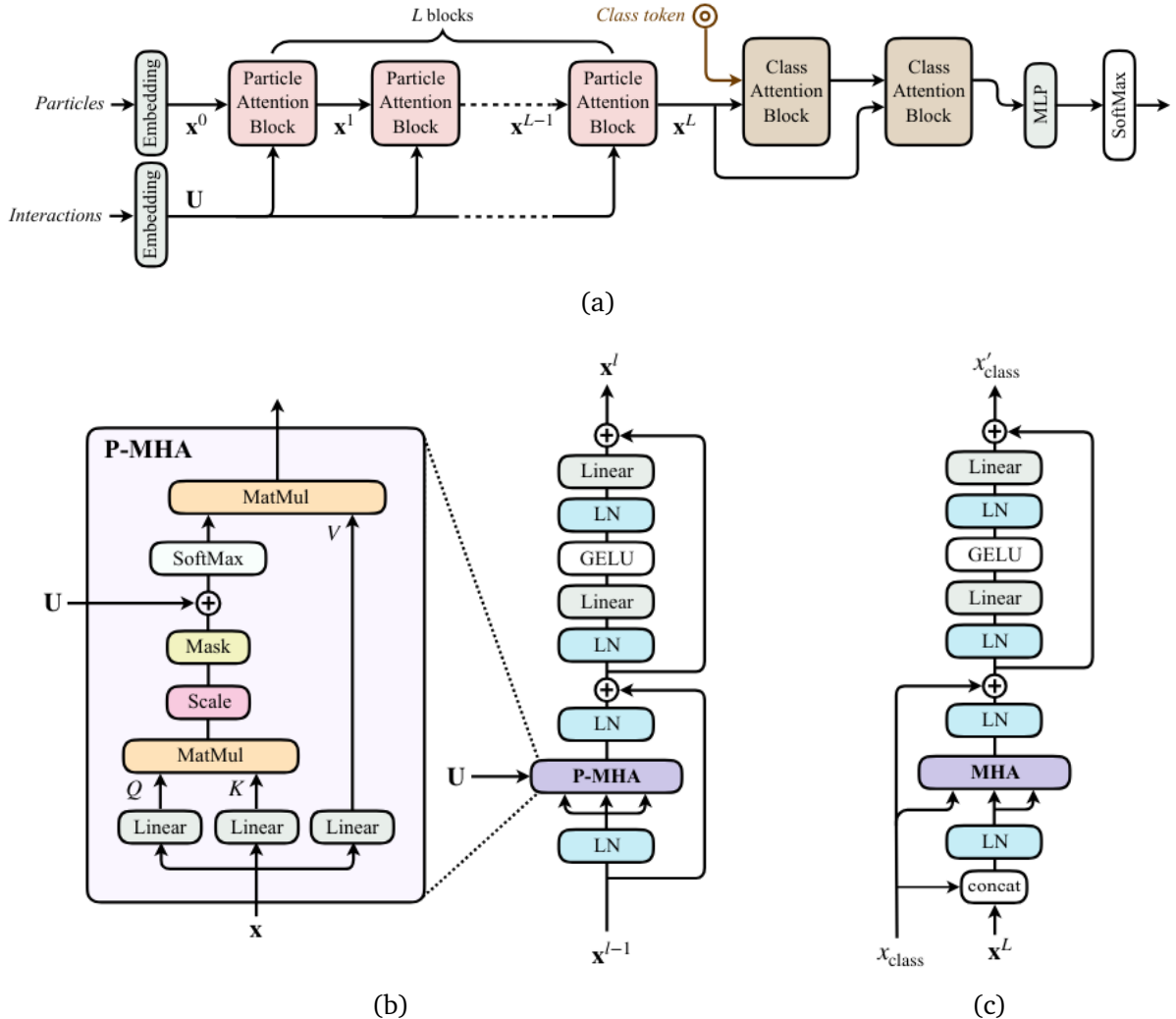


Figure 4.3. The architecture of (a) Particle Transformer (b) Particle Attention Block (c) Class Attention Block [164]

The Particle Transformer model takes  $\ln p_T$ ,  $\ln E$ ,  $\eta$ , and  $\phi$  for each lepton and jet, as well as  $\ln E_{\text{MET}}$ . Additionally, each lepton is given an "isEl/isMu" flag to enable the Particle Transformer to differentiate between the electron and muon streams more effectively. For each event used during training, all highest  $p_T$  jets are used up to a channel dependent maximum: 10 for full-hadronic, 8 for single leptonic, and finally 6 for the dilepton channel. Each jet is paired with eight flags indicating which ParticleNet b- and c-tagging score thresholds the jet passes. Events in the training sample are weighted by cross-section, then renormalized such that the sum of the weights in each category is the same.

In the single-lepton and dilepton channels, a total of ten event categories are used during the training, one for each of the following processes: The five  $t\bar{t}$  backgrounds  $t\bar{t}+bb$ ,  $t\bar{t}+bj$ ,  $t\bar{t}+cc$ ,  $t\bar{t}+cj$  and  $t\bar{t}+lf$ ; the three Z backgrounds  $t\bar{t}Z(Z \rightarrow c\bar{c})$ ,  $t\bar{t}Z(Z \rightarrow b\bar{b})$ , and  $t\bar{t}Z(Z \rightarrow q\bar{q})$ ; the  $t\bar{t}H(H \rightarrow b\bar{b})$  background and finally the  $t\bar{t}H(H \rightarrow c\bar{c})$  signal process. The trained model assigns

ten scores that reflect the probability of an event falling into each category, but since the scores must sum to 1, the result is nine independent Particle Transformer scores. The fully hadronic channel uses the same set-up, but adds an additional category for QCD events, bringing the total event category up to eleven and the number of independent scores to 10. The natural next step is to categorize all events based on their Particle Transformer scores by sorting each event into the category corresponding to its largest score. A cut of  $(ttH_{cc} + ttH_{bb} + ttZ_{bb} + ttZ_{cc})/(1 - ttZ_{qq}) > 0.85$  in these scores, defines the search region of our analysis. In Figure 4.4 an example of the Particle Transformer’s output is presented for the  $t\bar{t}Z$  and  $t\bar{t}H$  categories in case of the FH channel, while the corresponding output for the  $t\bar{t}+jets$  categories is shown in Figure 4.5.

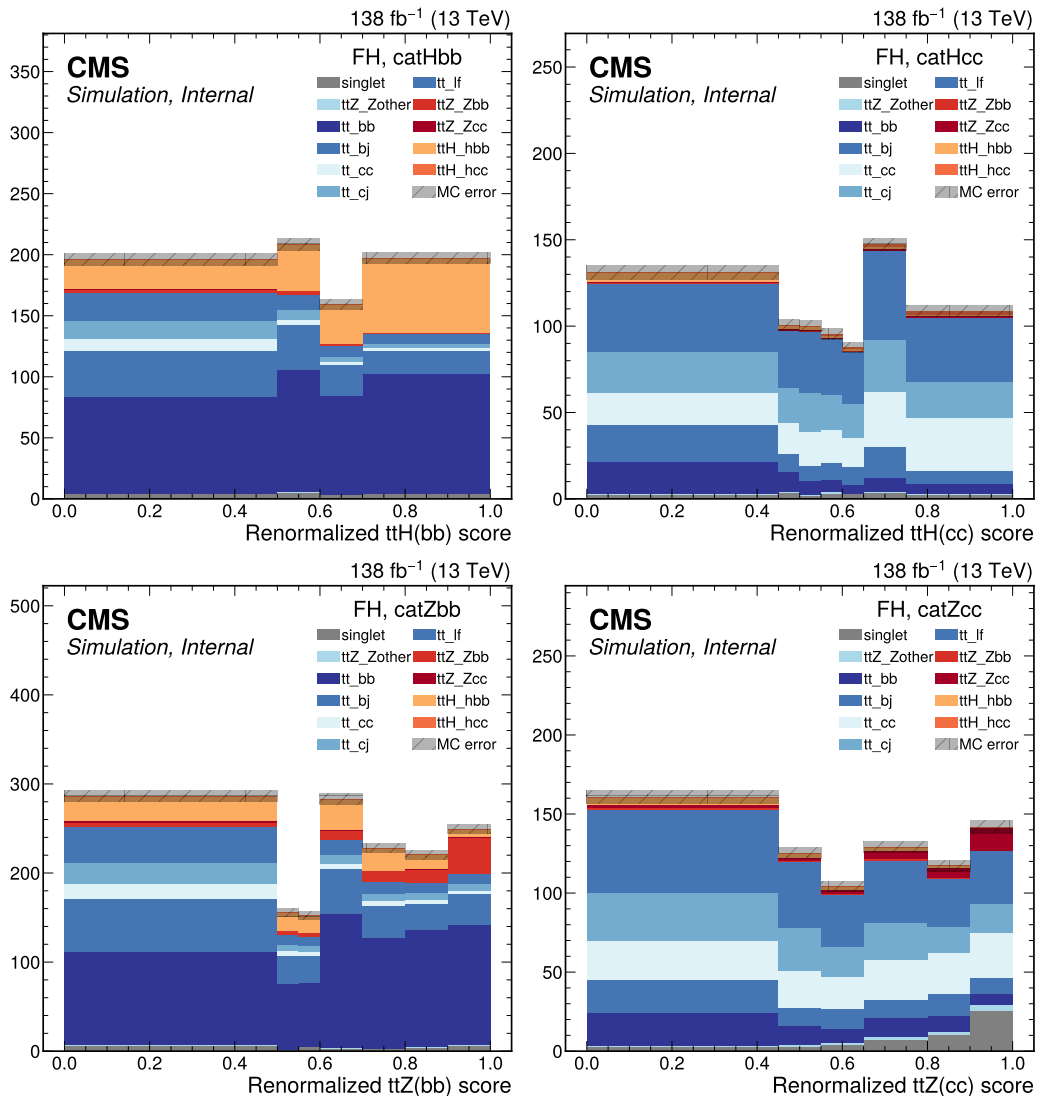


Figure 4.4. Renormalized scores in the search region with all years combined for the  $t\bar{t}H$  categories (top) and the  $t\bar{t}Z$  categories (bottom) in the FH channel. Data points are not included because the analysis is blinded.

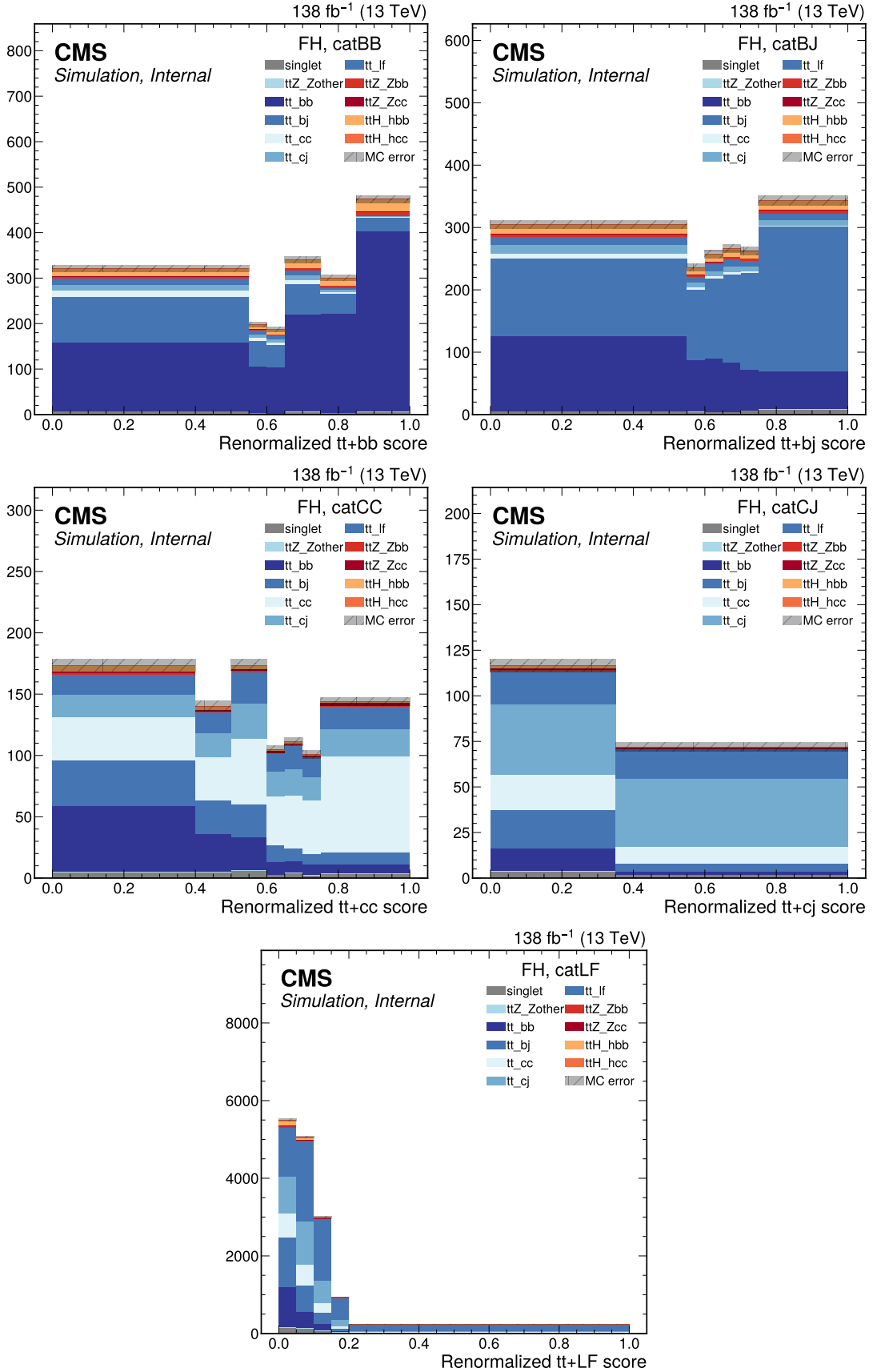


Figure 4.5. Renormalized scores in the search region with all years combined for  $t\bar{t}+jets$  categories in the FH channel. Data points are not included because the analysis is blinded.

## 4.2 $t\bar{t}+b\bar{b}$ simulation

Many measurements performed at pp collider experiments rely on accurate simulation to estimate background processes with similar signatures in the detectors compared to the process of interest (signal process). In such measurements, a subset of events is selected that contain a large fraction of events stemming from the signal process. In order to determine the contribution of the signal process to a set of selected events, an estimation of known SM-like processes can be performed via simulation of the known processes. As we saw in the previous section, the main background process, in our case, is  $t\bar{t}+b\bar{b}$ . Therefore better understanding of the  $t\bar{t}+b\bar{b}$  process is important, as an accurate and reliable description of the  $t\bar{t}+b\bar{b}$  process will allow for a measurement of our signal process with higher accuracy.

A detailed study of the  $t\bar{t}+b\bar{b}$  process is also of interest due to the challenging modeling of the process. In summary, the  $t\bar{t}+b\bar{b}$  process is difficult to model accurately as it contains  $b$  quarks with low but non-negligible masses, and, by comparison, heavy top quarks. Hence, finding appropriate energy scales for the calculation of  $t\bar{t}+b\bar{b}$  MEs and interfacing the MEs with PS and PDF calculations is a difficulty. Uncertainties related to the choice of renormalization and factorization scales can, in ME calculations at NLO in QCD, lead to uncertainties of up to 50% in fiducial and differential cross section predictions of  $t\bar{t}+b\bar{b}$  [167]. Improved knowledge in this process via fiducial and differential measurements of  $t\bar{t}+b\bar{b}$  is therefore of prime interest in order to validate or discard scale choices made for state-of-the-art simulations.

### 4.2.1 Motivation

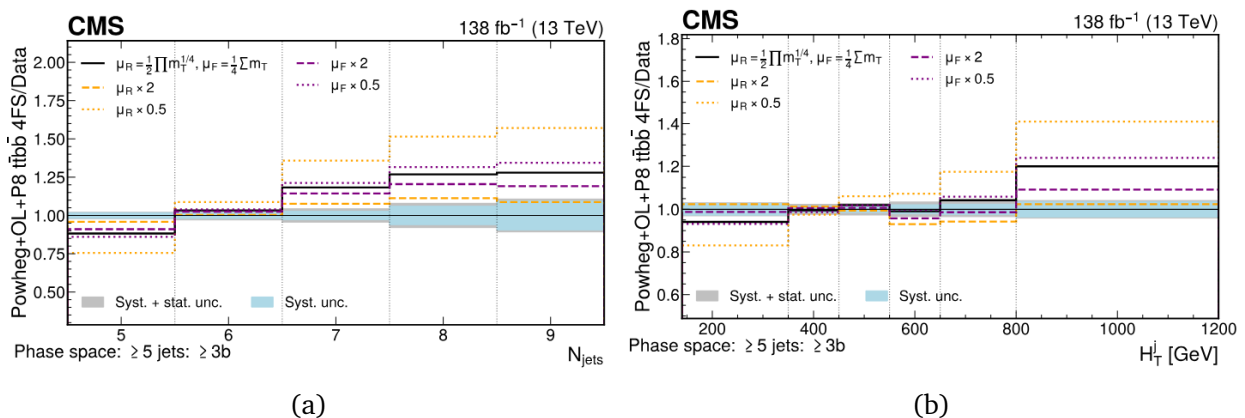


Figure 4.6. Ratio of normalized differential cross section predictions of the POWHEG+OL+P8  $t\bar{t}+bb$  4FS modeling approach with different  $\mu_R$  and  $\mu_F$  scale settings relative to the measured normalized differential cross sections for (a) the number of jets and (b)  $H_T$  of jets in the  $\geq 5$  jets:  $\geq 3b$  phase space [168]

Previous analyses by the CMS Collaboration [168] studied some variations of the  $t\bar{t}+b\bar{b}$   $\mu_R$  and  $\mu_F$  scales in order to check their compatibility with the data compared to the nominal model. The results are shown in Figures 4.6, 4.7. For these results, the  $t\bar{t}+b\bar{b}$  matrix element was calculated using POWHEG and OPENLOOPS (OL) at NLO in QCD, utilizing the four-flavor-scheme (4FS), where b quarks are not part of the proton PDF, and matched with PYTHIA-8 (P8) for parton showering and hadronization. From these results, it is clear that the  $\mu_R \times 2$  and  $\mu_F \times 2$  variations improve the description. In addition, a measurement of the fiducial  $t\bar{t}+b\bar{b}$  cross sections was performed [169]. In this study, as it is illustrated in 4.8, we can see that  $\mu_R \times 2$  and  $\mu_F \times 2$  variations decrease the fiducial cross section predictions, with  $\mu_R \times 2$  decreasing too much, beyond what we measure in data, while  $\mu_F \times 2$  is compatible. Motivated by these results, our study in this thesis, focuses mainly on the  $\mu_F \times 2$  variation, compared with the nominal, within the context of our  $t\bar{t}H$  analysis.

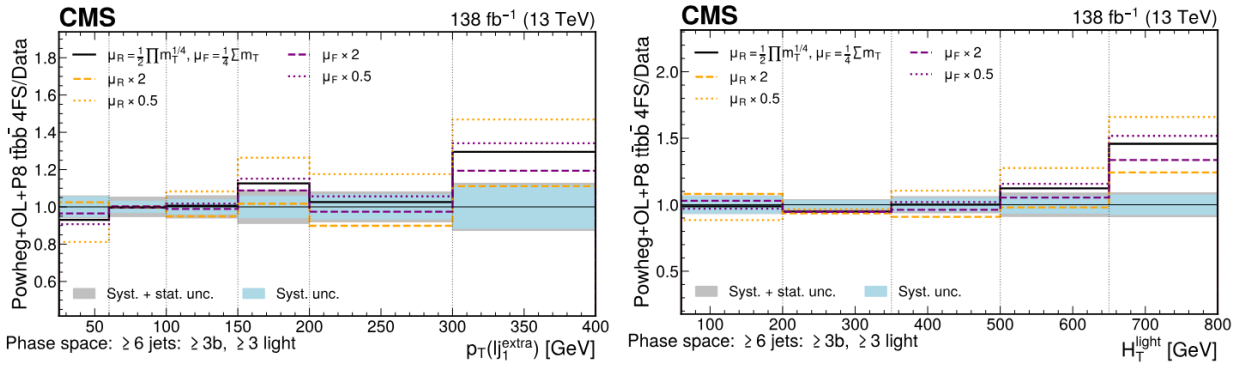


Figure 4.7. Ratio of normalized differential cross section predictions of the Powheg+OL+P8  $t\bar{t}+b\bar{b}$  4FS modeling approach with different  $\mu_R$  and  $\mu_F$  scale settings relative to the measured normalized differential cross sections for (a) the extra light jet and (b)  $H_T$  of light jets in the  $\geq 6$  jets:  $\geq 3b$ ,  $\geq 3$  light phase space [168]

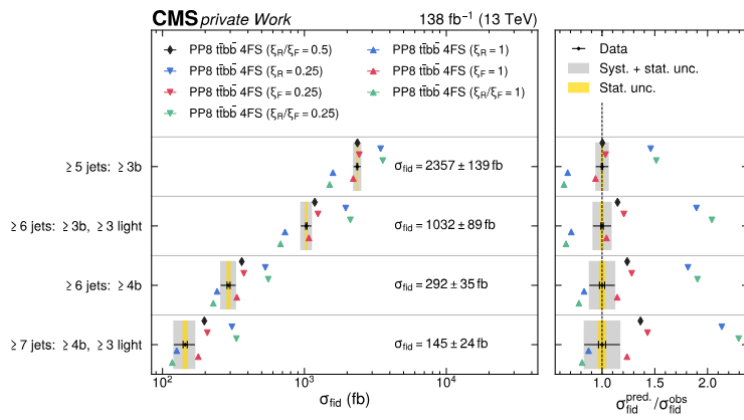


Figure 4.8. Fiducial cross sections measurement compared to the Powheg+OL+P8 4FS signal model and alternative  $\mu_R$  and  $\mu_F$  scale choices. Variations of the  $\mu_R$  and  $\mu_F$  scales by factors of two up and down are indicated via triangles. The nominal values for  $\mu_F$  and  $\mu_R$  correspond to  $\xi_F = 0.5$ ,  $\xi_R = 0.5$  respectively [169].

## 4.2.2 Generator configuration

POWHEG BOX RES [170] is the main tool used for event simulation of  $t\bar{t}+b\bar{b}$  events in the scope of this thesis. The generator uses the POWHEG method for interfacing PS generators with NLO QCD computations as described in Section 3.3.1. POWHEG BOX RES requires an input file, in which different variables, dependent on the process, are defined. An example of an input file for the  $t\bar{t}+b\bar{b}$  package can be found in the Appendix A. The output of the generator is a Les Houches Event (LHE) File [171], containing the input file as a header, followed by the initialization and state of the Random Number Generator (RNG) and the event data. The information is wrapped in XML<sup>3</sup> structure [172].

POWHEG BOX RES generates events through a linear process consisting of four stages. These stages can be executed on a single core or parallelized across multiple cores, which is particularly useful for simulating complex processes or at next-to-leading order (NLO). In this thesis, only the parallelized mode is considered. The main advantage of parallelization in POWHEG BOX RES is to increase statistical accuracy rather than reduce runtime. This means that the total computational effort is not distributed across multiple parallel runs but is the result of multiplying the computations of a single run by the number of parallel runs. Each parallel run uses a different random seed, ensuring statistical independence, and their results can be combined.

In parallel execution mode, the next stage starts only after all parallel computations for the current stage are completed. The output from these computations is written in a file and combined at the beginning of the next stage, ensuring all parallel runs start with the same data. As the necessary information is stored after each stage, the simulation can be resumed at any point.

The four stages of computations in a POWHEG BOX RES simulation are the following:

1. **Importance sampling grids.** As discussed in Section 3.4, MC integration can be improved by importance sampling. POWHEG BOX RES implements this method by generating points in a d-dimensional ( $[0, 1] \times [0, 1]$ )-plane, mapped to the actual integral that needs to be estimated. These points constitute the importance sampling grids, in the following simply referred to as sampling grids. The shape of the sampling grids represents their quality. It can be examined in visualizations accessible through a .top<sup>4</sup> file which is only created when the parallel executed computations have been combined either in a next iteration of the first stage or by execution of the second stage. If the shape of the visualized sampling grid is not smooth, this hints at insufficient statistics which then leads

---

<sup>3</sup>XML stands for Extensible Markup Language

<sup>4</sup>The name extension .top, indicates that the file format is appropriate for the portable TOP DRAWER graphics package

to unusable samples as the integral kernel cannot be accurately estimated. POWHEG BOX RES provides options to increase the number of sampled phase space points. This can be done directly by increasing the number of parallel runs, by running the first stage multiple times, or by a combination of both. Each iteration of the first stage is treated as a distinct stage, meaning all parallel computations of one iteration must be completed before the next iteration can begin, with results from the previous iteration combined.

2. **Cross section computations.** Once the previously constructed sampling grids are combined and the associated .top file is created, a multidimensional step function is calculated and stored on the sampling grid. This function acts as an upper bound on the integrand, aiding in the integral estimation. The number of calls for these computations can be directly set and increased by either running more parallel executions or performing multiple iterations of this stage.
3. **Generation of radiation.** In addition to combining the stage 2 computations, additional files are generated, containing all the information from the previous two stages. A human-readable text file with details on the cross section is also created. Subsequently, the upper bounding factors for radiation generation are calculated. These factors are used for simulating the hardest emission at NLO, following the POWHEG method. While the number of calls to the relevant functions can be configured by the user, this stage cannot be repeated for multiple iterations.
4. **Event generation.** At this stage, the program loads the previously generated files to produce events, which are then saved in an LHE file. The user determines the number of events, and this number can be increased later by re-executing this stage with new seeds.

## Input parameters

As it was mentioned in the previous section, POWHEG BOX RES requires an input file, with different variables. Here we present some of the most important ones. First, heavy-quark mass effects are included throughout using

$$m_t = 172.5 \text{ GeV} \quad \text{and} \quad m_b = 4.75 \text{ GeV} \quad (4.1)$$

All other quarks are treated as massless in the perturbative part of the calculations. Since we use massive b-quarks, for the PDF evolution and the running of  $\alpha_s$  we adopt the four-flavor-scheme (4FS). Thus, for consistency, we renormalise  $\alpha_s$  in the decoupling scheme, where top- and bottom-quark loops are subtracted at zero momentum transfer. In this way, heavyquark loop contributions to the evolution of the strong coupling are effectively described at first order

in  $\alpha_s$  through the virtual corrections.

For the calculation of hard cross sections at NLO, as well as for the generation of the first POWHEG emission, we use the NNPDF31\_nnlo\_as\_0118\_nf\_4 parton distributions [173] as implemented in the LHAPDFs [174] and the corresponding  $\alpha_s^{(4F)}$ .

## Scale choices

Because of its strong interaction origin, the  $t\bar{t}+b\bar{b}$  cross section scales with  $\alpha_s^4$ , and is therefore highly sensitive to the choice of renormalization scale  $\mu_R$  (see Section 3.1.1). As the  $t\bar{t}+b\bar{b}$  process incorporates a top quark and a b quark, in Ref. [167] choices of the renormalization scale for an ME-level simulation are recommended as

$$\mu_R = \frac{1}{2} \sqrt{\mu_{t\bar{t}} \mu_{b\bar{b}}} \quad (4.2)$$

where  $\mu_{t\bar{t}}$  and  $\mu_{b\bar{b}}$  are defined as the geometric average of the transverse masses of the  $t\bar{t}$  and  $b\bar{b}$  systems,

$$\mu_{t\bar{t}} = \sqrt{m_T(t)m_T(\bar{t})} \quad \text{and} \quad \mu_{b\bar{b}} = \sqrt{m_T(b)m_T(\bar{b})} \quad (4.3)$$

resulting in

$$\mu_R = \frac{1}{2} \left[ m_T(t) \cdot m_T(\bar{t}) \cdot m_T(b) \cdot m_T(\bar{b}) \right]^{1/4} \quad (4.4)$$

Here, the transverse mass is defined as  $m_T(i) = \sqrt{m^2(i) + p_T^2(i)}$ . For the factorization scale  $\mu_F$ , recommended choice is

$$\mu_F = \frac{1}{4} \left[ m_T(t) + m_T(\bar{t}) + m_T(b) + m_T(\bar{b}) + m_T(g) \right] \quad (4.5)$$

## Damping parameter

As we saw in Section 3.3.1, the master formula for the description of NLO radiation in the POWHEG approach consists of two contributions which arise from the splitting of real emission into singular (S) and finite (F) parts as described by Equation (3.25). For the splitting of these two parts, we introduced a parameter  $h$ , or as it is usually called,  $h_{damp}$ . This freely adjustable parameter in POWHEG represents the matching scale between the ME calculation and the PS. Basically,  $h_{damp}$  describes the damping of radiation with a high transverse momentum. It separates the low and the high transverse momentum regions and controls the hardest radiation.

In the context of the  $t\bar{t}+b\bar{b}$  simulation, we define this parameter as,

$$h_{damp} = \sqrt{\frac{1}{2} (m_T(t) + m_T(\bar{t})) \cdot \text{dynhdampPF}} \quad (4.6)$$

Therefore, any variation in this damping parameter is introduced through the `dynhdampPF` variable. The nominal value of this variable is set to `dynhdampPF = 0.5`. For our study we introduce two variations which we will refer to as *hdampUP* and *hdampDOWN* where the `dynhdampPF` variable is set to 0.835 and 0.317 respectively. In Table 4.2 the number of events generated for each one of these variations across the three channels is presented. Specifically, the total number of events generated for the purpose of this thesis is 205 million, since we generate the events presented in Table 4.2 for both  $\mu F \times 1$  and  $\mu F \times 2$ . The distribution of the events, of course, is not random but mirrors the number of events of the Run 2 samples used in the  $t\bar{t}H$  analysis.

Table 4.2. Number of events generated for each damping parameter across the three channels

	DL	SL	FH
<code>dynhdampPF = 0.5</code>	12 M	25 M	19 M
<code>dynhdampPF = 0.835</code>	8 M	10 M	7 M
<code>dynhdampPF = 0.317</code>	7 M	10 M	7 M

### 4.2.3 Observables

To investigate the effect of different parameter choices, one needs to perform tests on observables which are sensitive to these parameters. For this MC generator study, all three channels are analyzed. Depending on the channel we have different number of jets in the final state according to the W boson decays. For all channels, we have four  $b/\bar{b}$  quarks, two from the initial process which will refer to as *prompt* and two from the  $t/\bar{t}$  decay.

The renormalization scale, factorization scale and the  $h_{damp}$  are parameters affecting the kinematics of the hadrons in the system. Observables related to hadron momentum or momentum of a system consisting of two hadrons are sensitive to these parameters. The observables studied are shown in the Table 4.3. In the following sections, only a few selected observables will be presented, while the rest of them can be found in Appendix B.

### 4.2.4 Dileptonic channel

As it was discussed in Chapter 1, the dileptonic (DL) channel involves four leptons in the final state, two charged and two neutral, originating from the two W boson decays. It is the easiest channel to model amongst the others due to the lower number of jets. The only jets that appear in the final state are from the four  $b/\bar{b}$  quarks, as it was mentioned in the previous section, as well as the extra emission that is generated for the NLO calculation.

Table 4.3. Description of all measured observables for each of the three channels

	Observable	DL	SL	FH
<b>Global observables</b>				
$m(t\bar{t} + b\bar{b})$	Invariant mass of $t\bar{t}+b\bar{b}$ system	✓	✓	✓
$H_T(t\bar{t} + b\bar{b})$	Scalar sum of transverse momentum of $t\bar{t}+b\bar{b}$ system	✓	✓	✓
<b>Observables related to top quarks</b>				
$E(t, \bar{t})$	Energy of $t/\bar{t}$ quarks	✓	✓	✓
$p_T(t, \bar{t})$	Transverse momentum of $t/\bar{t}$ quarks	✓	✓	✓
$m^{reco}(t, \bar{t})$	Reconstructed mass of $t/\bar{t}$ quarks	✓	✓	✓
$y(t, \bar{t})$	Rapidity of $t/\bar{t}$ quarks	✓	✓	✓
$\phi(t, \bar{t})$	Azimuthial angle of $t/\bar{t}$ quarks	✓	✓	✓
$\Delta R(t\bar{t})$	Angular separation of $t\bar{t}$ system	✓	✓	✓
$H_T(t\bar{t})$	Scalar sum of transverse momentum of $t\bar{t}$ system	✓	✓	✓
$m(t\bar{t})$	Invariant mass of $t\bar{t}$ system	✓	✓	✓
$y(t\bar{t})$	Rapidity of $t\bar{t}$ system	✓	✓	✓
$p_T(t\bar{t})$	Transverse momentum of $t\bar{t}$ system	✓	✓	✓
<b>Observables considering all pairs of b jets</b>				
$E(b, \bar{b}^{all})$	Energy of $b/\bar{b}$ quarks	✓	✓	✓
$p_T(b, \bar{b}^{all})$	Transverse momentum of $b/\bar{b}$ quarks	✓	✓	✓
$\eta(b, \bar{b}^{all})$	Pseudorapidity of $b/\bar{b}$ quarks	✓	✓	✓
$\phi(b, \bar{b}^{all})$	Azimuthial angle of $b/\bar{b}$ quarks	✓	✓	✓
<b>Observables related to the pair of b jets from <math>t\bar{t}</math> decay</b>				
$\Delta R(b\bar{b})$	Angular separation of $b\bar{b}$ system	✓	✓	✓
$H_T(b\bar{b})$	Scalar sum of transverse momentum of $b\bar{b}$ system	✓	✓	✓
$m(b\bar{b})$	Invariant mass of $b\bar{b}$ system	✓	✓	✓
$y(b\bar{b})$	Rapidity of $b\bar{b}$ system	✓	✓	✓
$p_T(b\bar{b})$	Transverse momentum of $b\bar{b}$ system	✓	✓	✓
<b>Observables related to the pair of b jets not from <math>t\bar{t}</math> decay (<math>b^{\text{prompt}}</math>)</b>				
$\Delta R(b\bar{b}^{\text{prompt}})$	Angular separation of prompt $b\bar{b}$ system	✓	✓	✓
$H_T(b\bar{b}^{\text{prompt}})$	Scalar sum of transverse momentum of prompt $b\bar{b}$ system	✓	✓	✓
$m(b\bar{b}^{\text{prompt}})$	Invariant mass of prompt $b\bar{b}$ system	✓	✓	✓
$y(b\bar{b}^{\text{prompt}})$	Rapidity of prompt $b\bar{b}$ system	✓	✓	✓
$p_T(b\bar{b}^{\text{prompt}})$	Transverse momentum of prompt $b\bar{b}$ system	✓	✓	✓
<b>Observables related to light jets from W decay</b>				
$E(q_{lf})$	Energy of lf-quarks	✓	✓	
$p_T(q_{lf})$	Transverse momentum of lf-quarks	✓	✓	
$\eta(q_{lf})$	Pseudorapidity of lf-quarks	✓	✓	
$\phi(q_{lf})$	Azimuthial angle of lf-quarks	✓	✓	
$\Delta R(q'\bar{q})$	Angular separation of lf-quarks system	✓	✓	
$H_T(q'\bar{q})$	Scalar sum of transverse momentum of lf-quarks system	✓	✓	
$m(q'\bar{q})$	Invariant mass of lf-quarks system	✓	✓	
$\eta(q'\bar{q})$	Pseudorapidity of lf-quarks system	✓	✓	
<b>Observables related to leptons from W decay</b>				
$E(l, \nu_l)$	Energy of leptons (charged or neutral)	✓	✓	
$p_T(l, \nu_l)$	Transverse momentum of leptons (charged or neutral)	✓	✓	
$\eta(l, \nu_l)$	Pseudorapidity of leptons (charged or neutral)	✓	✓	
$\phi(l, \nu_l)$	Azimuthial angle of leptons (charged or neutral)	✓	✓	
$\Delta R(l^-l^+)$	Angular separation of charged leptons system	✓		
$H_T(l^-l^+)$	Scalar sum of transverse momentum of charged leptons system	✓		
$m(l^-l^+)$	Invariant mass of charged leptons system	✓		
$\eta(l^-l^+)$	Pseudorapidity of charge leptons system	✓		
<b>Observables related to extra light jets</b>				
$E(l_j^{\text{extra}})$	Energy of extra light jet	✓	✓	✓
$p_T(l_j^{\text{extra}})$	Transverse momentum of extra light jet	✓	✓	✓
$\eta(l_j^{\text{extra}})$	Pseudorapidity of extra light jet	✓	✓	✓
$\phi(l_j^{\text{extra}})$	Azimuthial angle of extra light jet	✓	✓	✓

As expected, the observables that were found to be most sensitive to the different parameters used in our simulation, are the ones related to the transverse momentum. Specifically, in Figure 4.9, the distributions of the transverse momentum for the  $t/\bar{t}$  (4.9a) and the  $b/\bar{b}$  (4.9b) quarks are presented. It is easy to see from the ratio plots, that the most significant parameter change is the different factorization scale. As the transverse momentum increases, the ratio of the  $\mu_F \times 1$  sample over the  $\mu_F \times 2$  sample for the nominal damping parameter, also increases for both  $t/\bar{t}$  and  $b/\bar{b}$  quarks. This effect is stronger in the case of  $t/\bar{t}$ , reaching up to 10% difference. On the low  $p_T$  spectrum, in case of the  $t/\bar{t}$  quarks, we can see a very small drop in the ratio plot, indicating again, that for  $\mu_F \times 2$ , the  $t/\bar{t}$  quarks are simulated to be less energetic.

As for the  $h_{\text{damp}}$  variations, it is obvious, that they basically have no effect. The results for both  $h_{\text{dampUP}}$  and  $h_{\text{dampDOWN}}$  variations are identical to the nominal selection for both  $\mu_F \times 1$  and  $\mu_F \times 2$  samples.

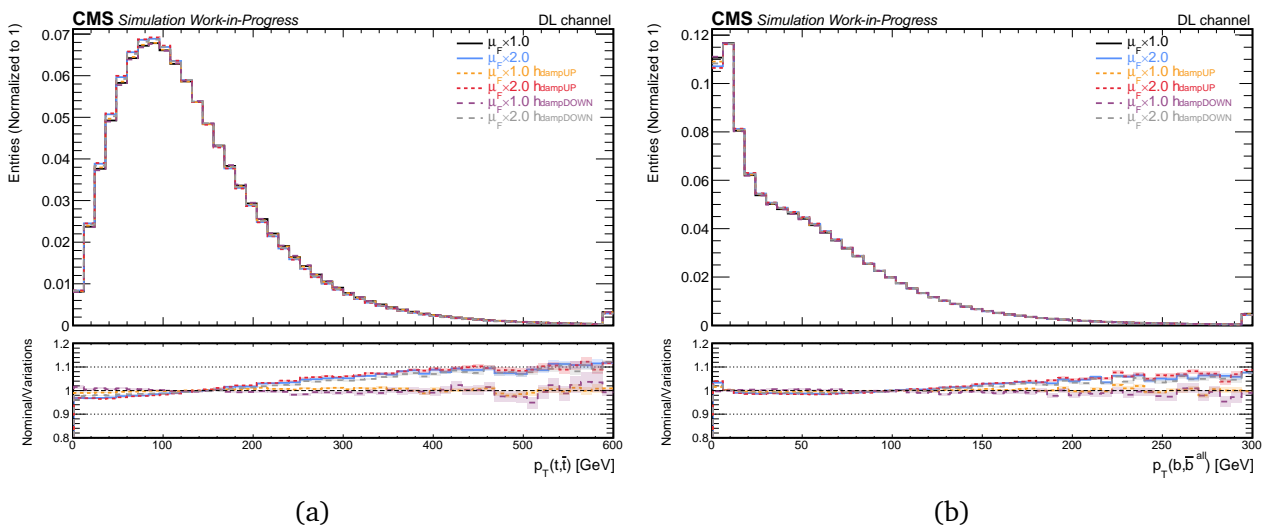


Figure 4.9. Distribution of the transverse momentum of (a) the  $t/\bar{t}$  and (b) the  $b/\bar{b}$  quarks for the six different settings used in the simulation. The lower panel shows the ratio of the nominal setting to the variations. The shaded bands represent statistical uncertainties. The last bins contain the overflow events.

Of course, since the transverse momentum is very sensitive to the different factorization scale selection, as we saw from the previous plots, we expect similar results from the  $H_T$  variable. In Figure 4.10, the results for the different  $t\bar{t}$  and  $b\bar{b}$  systems are presented. Obviously, the  $b$  quarks have been separated into the two different categories, depending on the mother particles that originate from.

As expected, in Fig. 4.10a, one can see again the same trend as before for the  $H_T$  of the  $t\bar{t}$  system. As for the  $b\bar{b}$  system originating from the top quarks, it is clear that they inherit the same behavior. This, however, is not the case for the prompt  $b\bar{b}$  system (Fig. 4.10b).

The prompt  $b$  quarks, are generated from the initial particles alongside the top quarks.

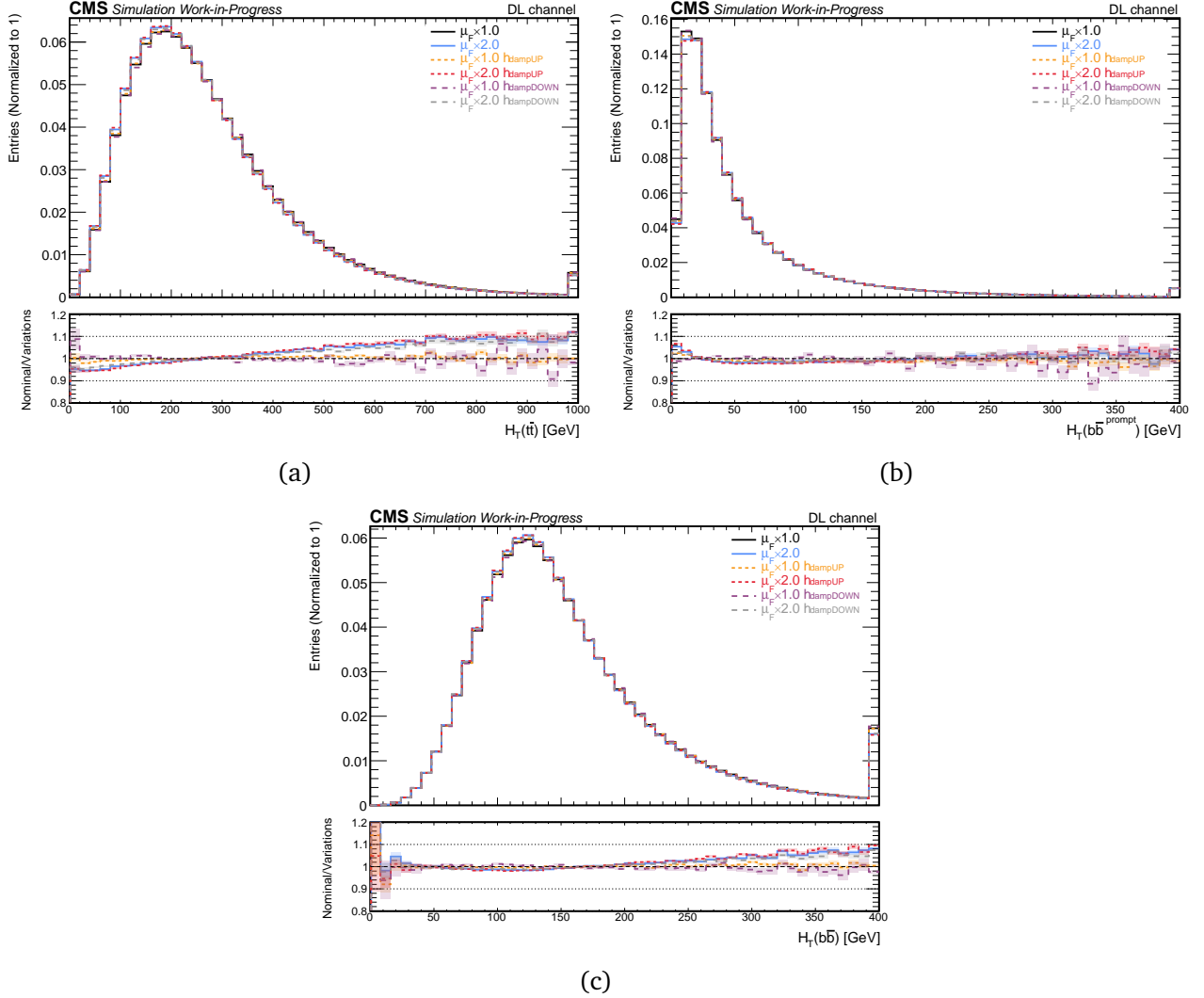


Figure 4.10. Distribution of  $H_T$  for (a)  $t\bar{t}$ , (b) prompt  $b\bar{b}$  and (c)  $b\bar{b}$ , originating from top quarks, systems for the six different settings used in the simulation. The lower panel shows the ratio of the nominal setting to the variations. The shaded bands represent statistical uncertainties. The last bins contain the overflow events.

Therefore, due to the larger mass, the top quarks are more boosted, resulting in significantly less energy and transverse momentum for the remaining b quarks. Since the different settings affect the higher values of  $p_T$  and  $H_T$ , it is normal to not see any change for the different settings.

This difference in the features of the two systems can be seen in Figure 4.11, where the angular separation is presented. More specifically, as we can see from Fig. 4.11a, there is a peak in the distribution of the angular separation of the  $t\bar{t}$  system which represents that the two top quarks are predominantly produced centrally ( $\Delta\eta \sim 0$ ) and back-to-back ( $\Delta\phi \sim \pi$ ). This of course happens, due to the fact that, the two top quarks carry most of the momentum transferred from the initial to the final state. On the other hand, the angular separation of prompt  $b\bar{b}$  system, presented in 4.11b, shows that most of the b quarks are close to each other due to

the low momentum with only a small fraction of them being generated to be back-to-back.

As far as the different settings, we can see that angular separation as well as all the angle related variables, are insensitive to them. We can only see a really small trend in Fig. 4.11a, towards higher values of  $\Delta R$  but nothing significant. The same can also be said for the prompt  $b\bar{b}$  system in Figure 4.11b, but the fluctuations are large due to low statistics.

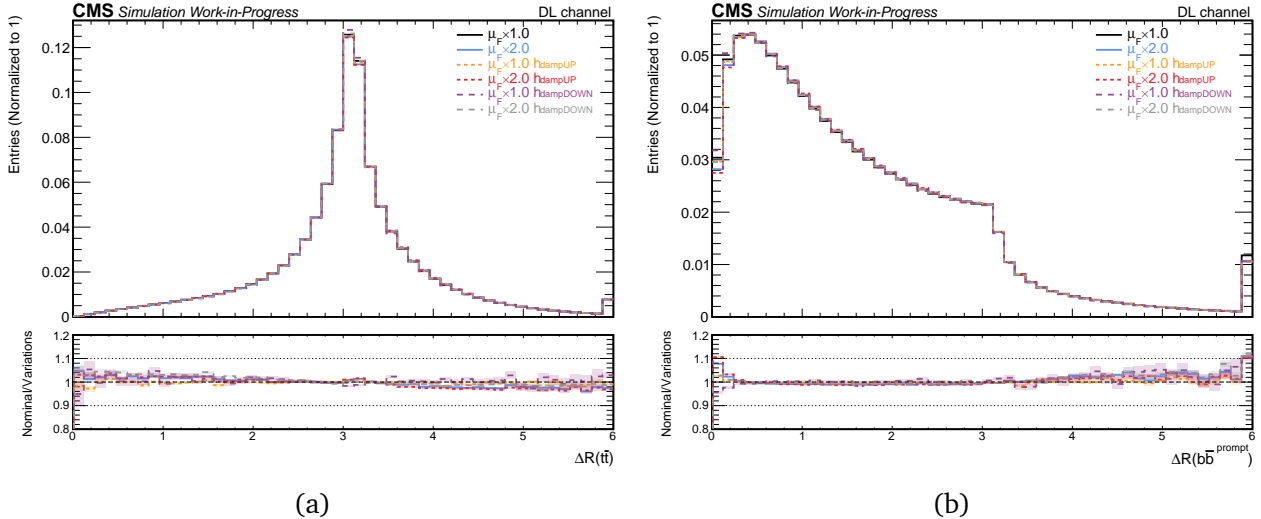


Figure 4.11. Distribution of the angular separation of (a)  $t\bar{t}$  and (b) prompt  $b\bar{b}$  systems for the six different settings used in the simulation. The lower panel shows the ratio of the nominal setting to the variations. The shaded bands represent statistical uncertainties. The last bins contain the overflow events.

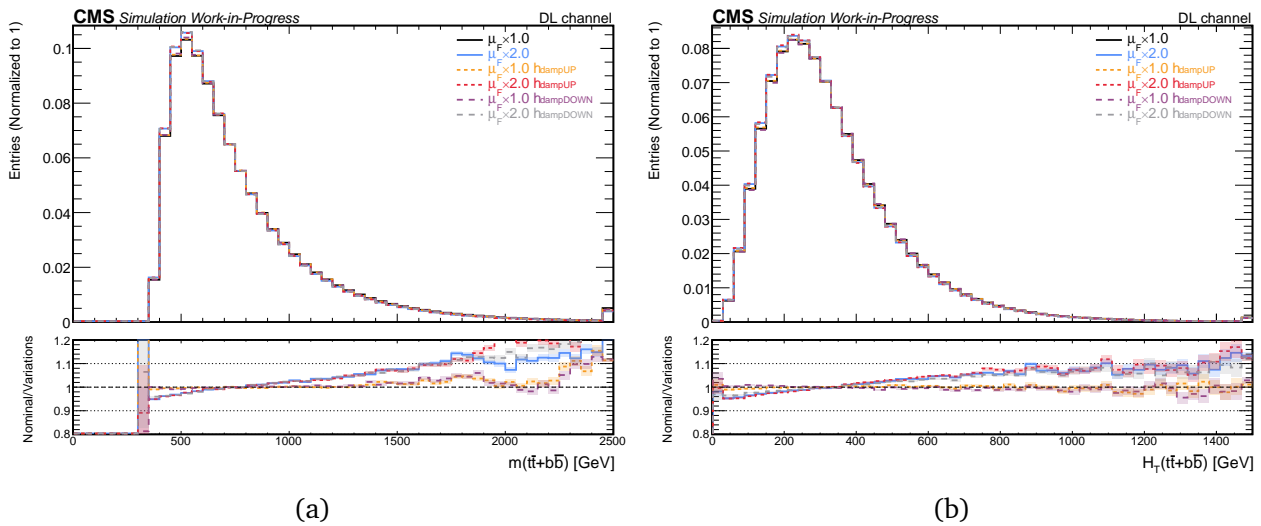


Figure 4.12. Distributions of (a) invariant mass and (b)  $H_T$  of the  $t\bar{t} + b\bar{b}$  system for the six different settings used in the simulation. The lower panel shows the ratio of the nominal setting to the variations. The shaded bands represent statistical uncertainties. The last bins contain the overflow events.

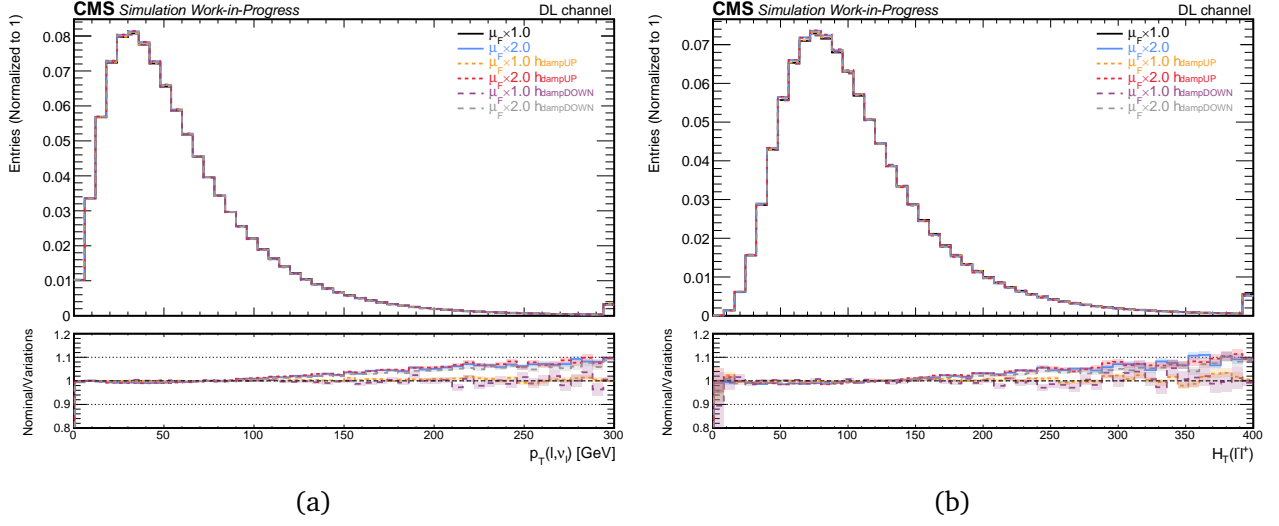


Figure 4.13. Distribution of (a) the transverse momentum of all the leptons (charged and neutral) and (b) the  $H_T$  of  $\ell^-\ell^+$  system for the six different settings used in the simulation. The lower panel shows the ratio of the nominal setting to the variations. The shaded bands represent statistical uncertainties. The last bins contain the overflow events.

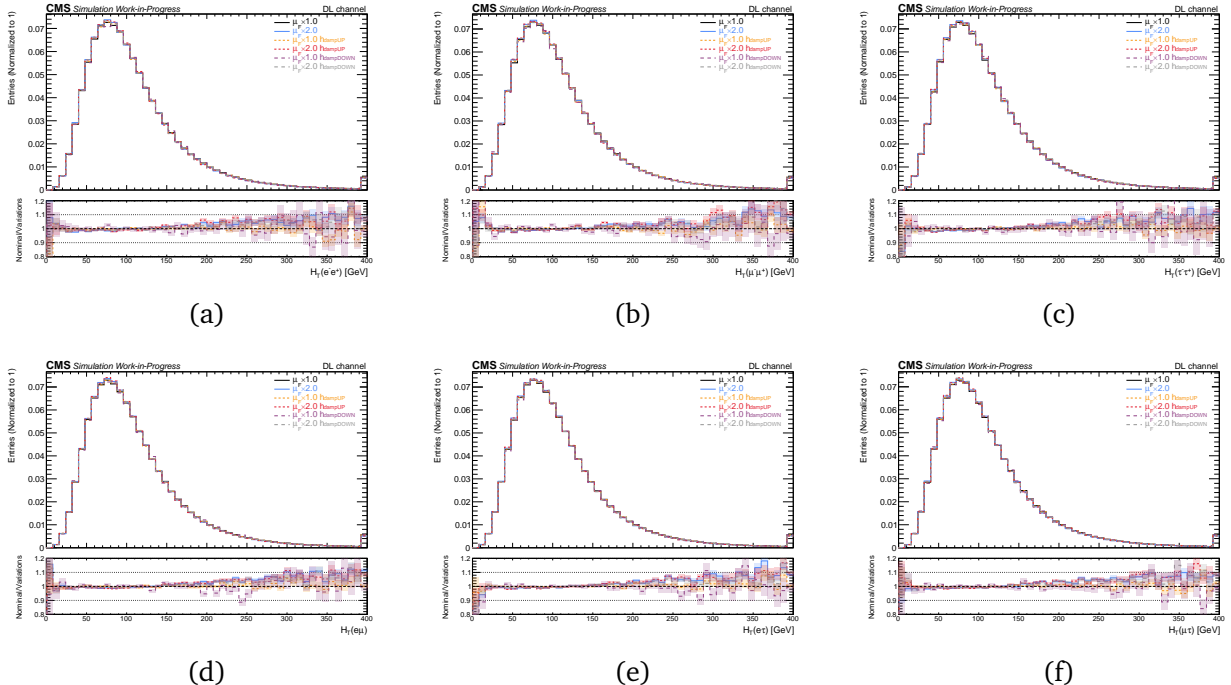


Figure 4.14. Distribution of  $H_T$  for (a)  $e^-e^+$ , (b)  $\mu^-\mu^+$ , (c)  $\tau^-\tau^+$ , (d)  $e\mu$  (e)  $e\tau$  and (f)  $\mu\tau$  systems for the six different settings used in the simulation. The lower panel shows the ratio of the nominal setting to the variations. The shaded bands represent statistical uncertainties.

The results, for the combination of the two separate systems, i.e. the  $t\bar{t}$  and the prompt  $b\bar{b}$  systems, are shown in Figure 4.12. It is clear that, the effect of the factorization scale remains the same in the distribution of  $H_T$  for the inclusive  $t\bar{t}+b\bar{b}$  system. The same can be said, also,

for its invariant mass, with the effect, even being, stronger for values above 2000 GeV. In fact, for these high values of the invariant mass, there is also a separation between the different damping settings, reaching up to 20% difference for the sample with hdampDOWN and  $\mu_F \times 2$  settings.

As for the other final state particles, which in this case are leptons, the results are shown in Figure 4.13. Similarly to the previous results from the quarks, both the transverse momentum of leptons (4.13a) and  $H_T$  of the  $\ell^-\ell^+$  system (4.13b) are sensitive to the change of the factorization scale.

For completeness, the distributions of the  $H_T$  variable for the six different leptons combinations are presented in Figure 4.14. The results are similar with the combination of all, but due to this separation, there is low statistics in high  $H_T$  values, resulting in some bigger fluctuations.

Finally, the last particle of interest is the hardest emission generated from the POWHEG method. We would expect that this extra light jet will be the most sensitive particle to the choice of  $h_{damp}$ , since it regulates the hardness of this radiation. As it is shown in Figure 4.15, this is true for the hdampDOWN variation. For both factorization scales, the hdampDOWN variation is consistently above, in the ratio plot. To be more specific, this effect appears to be larger in case of the  $\mu_F \times 1$ , reaching up to 8 % difference in the high  $p_T$  spectrum. Of course, the change of the factorization scale again affects significantly the distribution for high  $p_T$  values, where with the combination of the hdampDOWN, we observe almost 12 % difference.

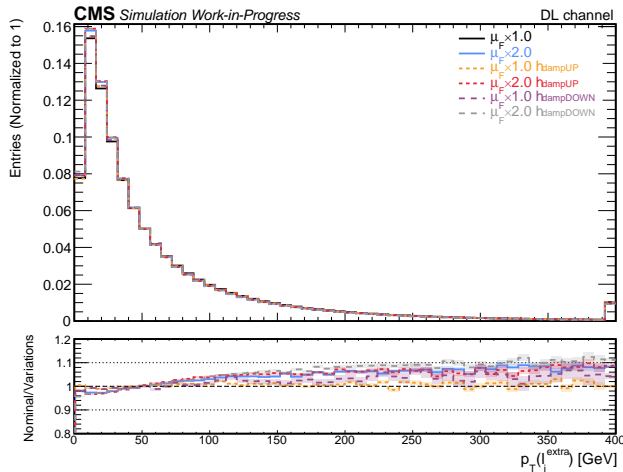


Figure 4.15. Distribution of the transverse momentum of the extra light jet for the six different settings used in the simulation. The lower panel shows the ratio of the nominal setting to the variations. The shaded bands represent statistical uncertainties. The last bins contain the overflow events.

## 4.2.5 Semileptonic channel

In the semileptonic channel, as the name suggests, only one W boson decays into leptons with the other decaying hadronically. The appearance of more jets in the final state makes this channel a little more challenging to model in comparison with the DL channel, but due to the significantly larger branching ratio, it is more promising for the search of the Yukawa coupling.

As was the case for the DL, the observables that were found to be more sensitive to the choice of the different settings are the transverse momentum and  $H_T$ . In Figure 4.16, the distributions of  $H_T$  for the  $t\bar{t}$  and the two different  $b\bar{b}$  systems are presented, while in Figure 4.17, the transverse momentum for  $t/\bar{t}$  and the  $b/\bar{b}$  quarks is presented.

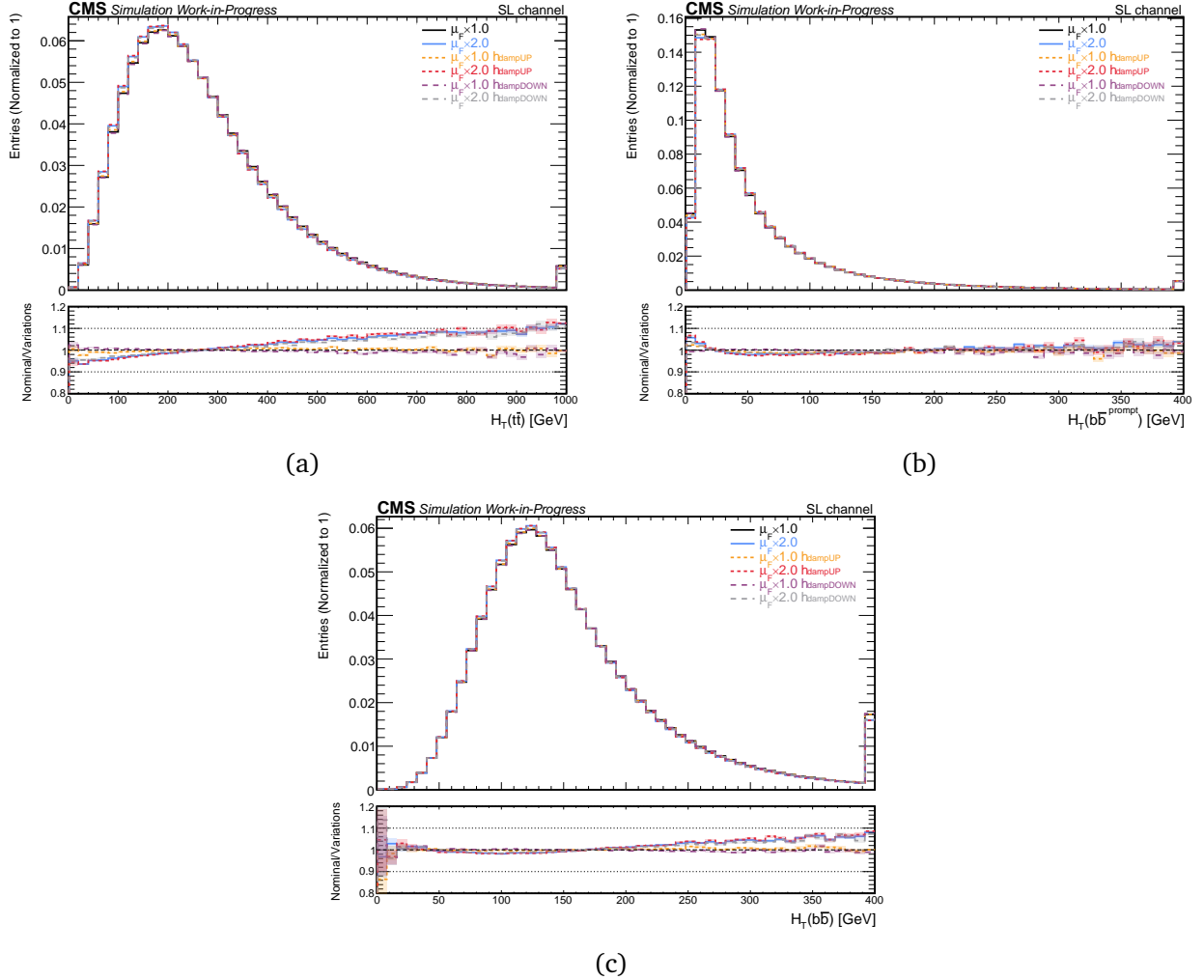


Figure 4.16. Distribution of  $H_T$  for (a)  $t\bar{t}$ , (b) prompt  $b\bar{b}$  and (c)  $b\bar{b}$ , originating from top quarks, systems for the six different settings used in the simulation. The lower panel shows the ratio of the nominal setting to the variations. The shaded bands represent statistical uncertainties. The last bins contain the overflow events.

With no surprise the results are identical to the ones in the DL channel. There is a strong trend in the high  $p_T$  spectrum for the  $\mu_F \times 2$  setting, especially for the  $t/\bar{t}$  quarks in Figure 4.17a. The same can be said for the  $H_T$  distributions for the quark-antiquark systems with the exception of the prompt  $b\bar{b}$  system in Fig. 4.16b. There are little to no deviations for the different  $h_{\text{damp}}$  parameters for the two different factorization scales.

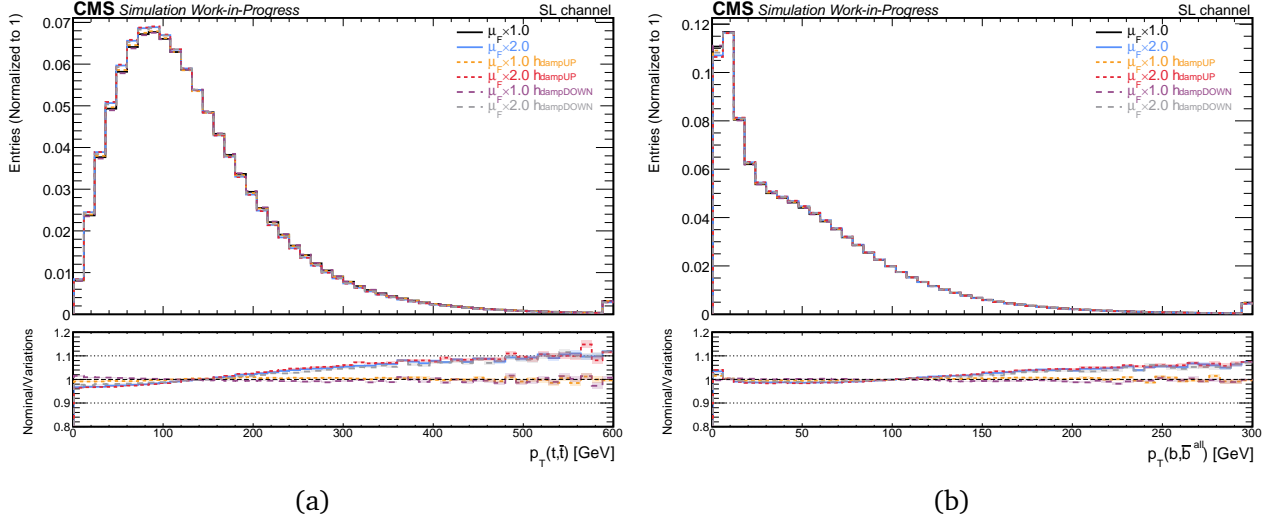


Figure 4.17. Distribution of the transverse momentum of (a) the  $t/\bar{t}$  and (b) the  $b/\bar{b}$  quarks for the six different settings used in the simulation. The lower panel shows the ratio of the nominal setting to the variations. The shaded bands represent statistical uncertainties. The last bins contain the overflow events.

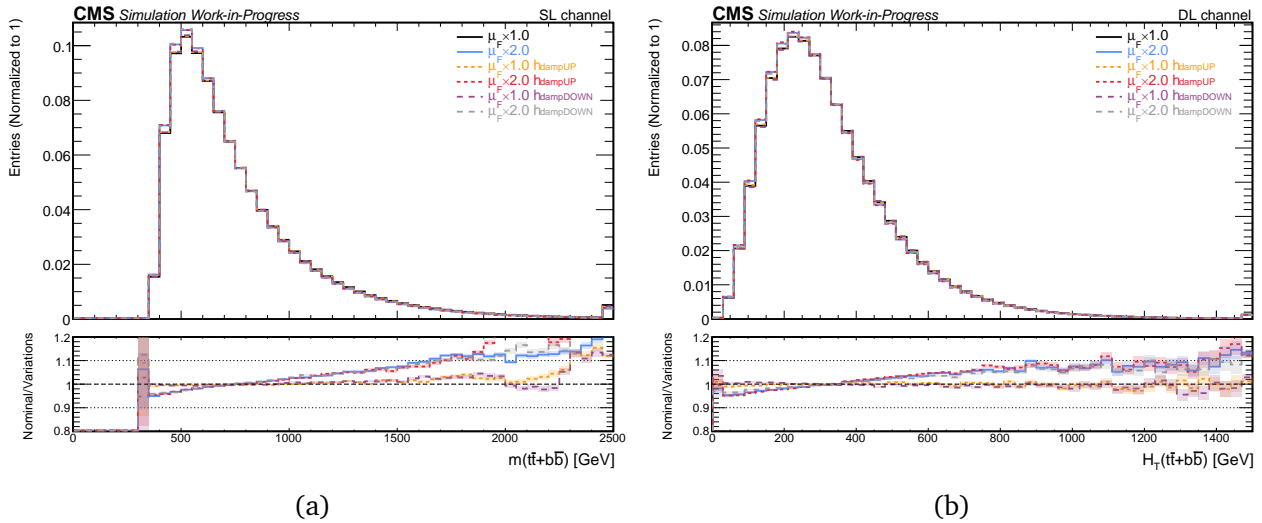


Figure 4.18. Distribution of (a) invariant mass and (b)  $H_T$  for the  $t\bar{t} + b\bar{b}$  system for the six different settings used in the simulation. The lower panel shows the ratio of the nominal setting to the variations. The shaded bands represent statistical uncertainties. The last bins contain the overflow events.

In Figure 4.18, the distributions of the invariant mass and the  $H_T$  for the  $t\bar{t}+bb$  system are shown. There is a strong effect for the samples with  $\mu_F \times 2$  for both distributions, as was the case in the DL channel. As for the different damping parameters, there is basically no difference between them for the  $H_T$ . However, this is not the case for the invariant mass where, there are some significant deviations at very high values, especially in the case of the hdampDOWN setting

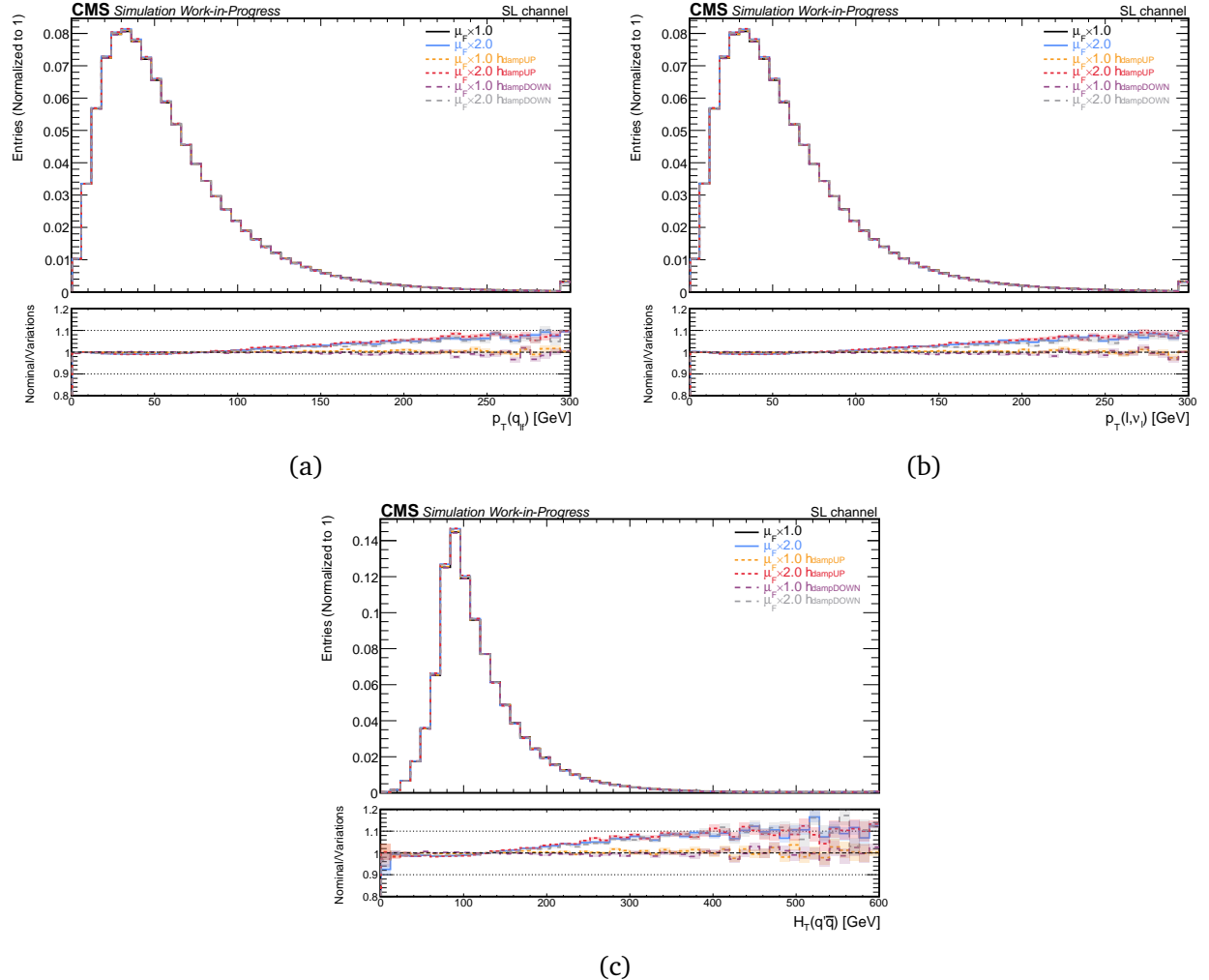


Figure 4.19. Distribution of the transverse momentum of (a) light flavor quarks and (b) leptons, and (c) the  $H_T$  of  $q\bar{q}'$  system for the six different settings used in the simulation. The lower panel shows the ratio of the nominal setting to the variations. The shaded bands represent statistical uncertainties. The last bins contain the overflow events.

The difference from the DL channel, lies in the final state particles, whose variables of interest are illustrated in Figure 4.19. Specifically, in Figure 4.19a the distribution of the transverse momentum of the light flavor quarks originating from W boson decays is presented, whereas in Figure 4.19b the corresponding plot for the leptons is shown. In both figures, we observe the same behavior as before, significant difference towards higher  $p_T$  values for  $\mu_F \times 2$  with very

small deviations from the different  $h_{\text{damp}}$  settings. The same can be said also for the  $H_T$  of the  $\bar{q}q'$  systems originating from the hadronic W decay presented in Figure 4.19c. The separation of this plot into the four different quark-antiquark pairs combinations is depicted in Figure 4.20. It is obvious, that the two Cabibbo suppressed quark-antiquark pairs, in the two bottom plots (4.20c, 4.20d), have very low statistics, resulting in constant fluctuations. The other two plots (4.20a, 4.20b), as it is expected have the same trend as the aggregated plot.

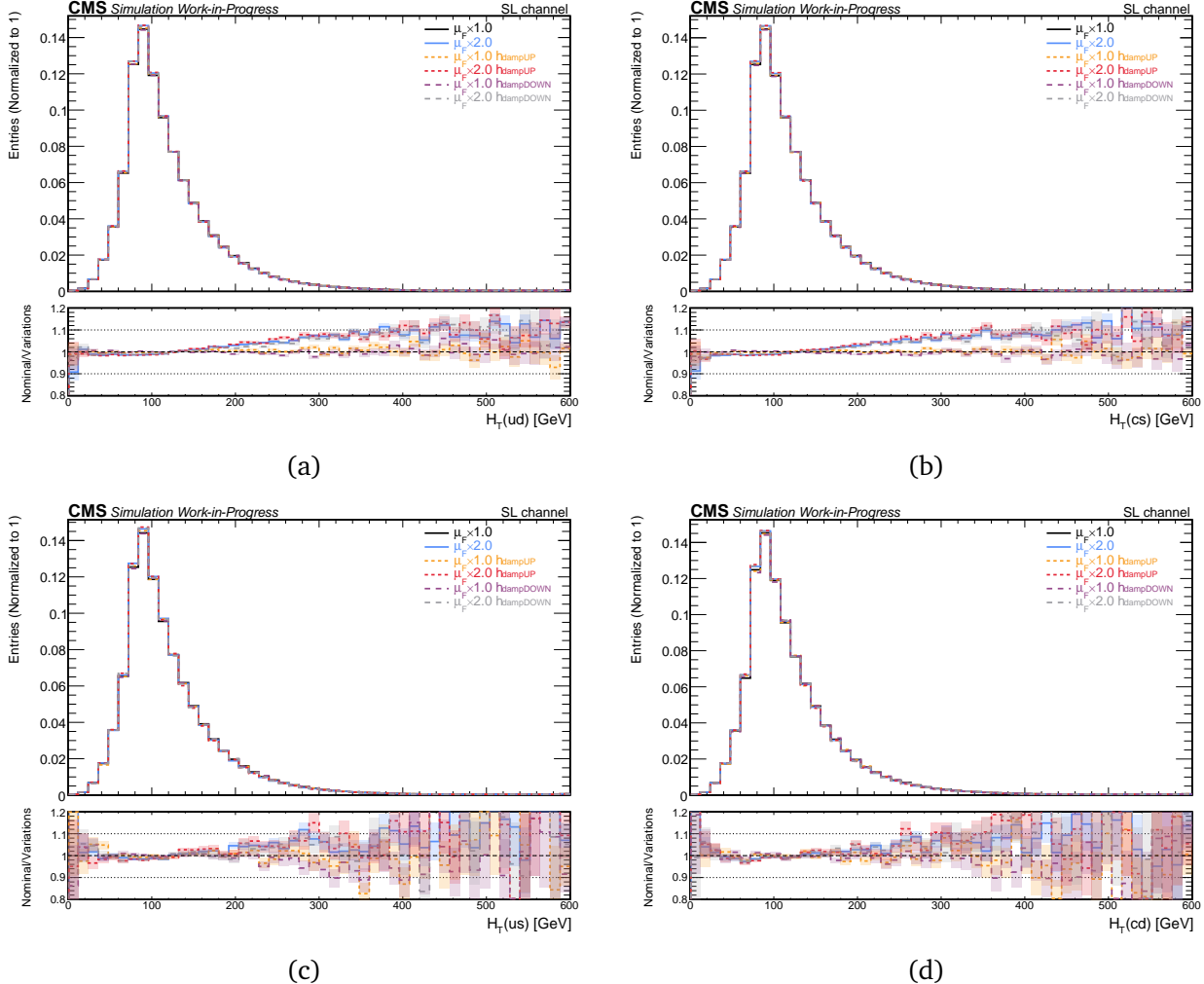


Figure 4.20. Distribution of  $H_T$  for (a) ud (b) cs (c) us and (d) cd systems for the six different settings used in the simulation. The lower panel shows the ratio of the nominal setting to the variations. The shaded bands represent statistical uncertainties. The last bins contain the overflow events.

As for the extra light jet that is being emitted, similar to the DL channel, it is the most sensitive particle to the different  $h_{\text{damp}}$  variations and in particular the  $hdampDOWN$  variation as it can be seen from Figure 4.21. As for the factorization scale, we observe again the same increase towards high  $p_T$  values.

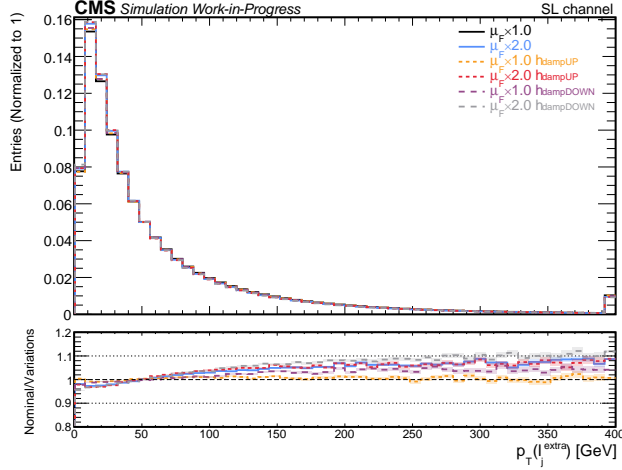


Figure 4.21. Distribution of the transverse momentum of the extra light jet for the six different settings used in the simulation. The lower panel shows the ratio of the nominal setting to the variations. The shaded bands represent statistical uncertainties. The last bin contains the overflow events.

#### 4.2.6 Fully hadronic channel

For the fully hadronic channel, the final state comprises of four light flavor jets originating from the W boson decays, one extra emission of a light flavor jet from the initial particles as well as the standard four b quarks. This jet enriched final state is obviously the most difficult to model amongst the three channels.

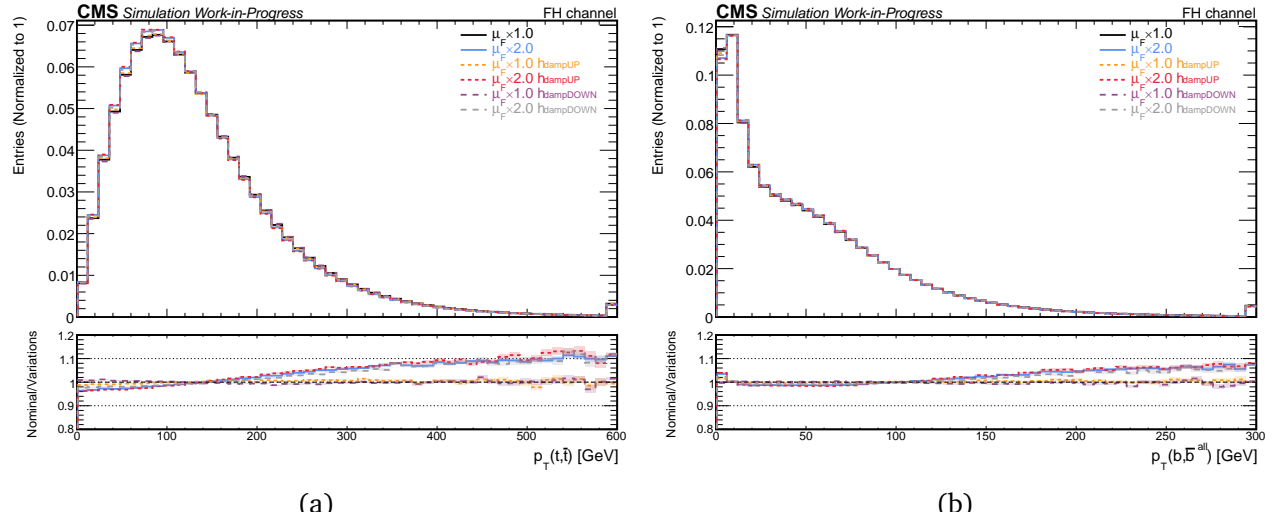


Figure 4.22. Distribution of the transverse momentum of (a) the  $t/\bar{t}$  and (b) the  $b/\bar{b}$  quarks for the six different settings used in the simulation. The lower panel shows the ratio of the nominal setting to the variations. The shaded bands represent statistical uncertainties. The last bins contain the overflow events.

Naturally, as in the previous channels, here too the interesting observables are the transverse momentum and  $H_T$ . The results for these variables for the heavy quarks in the event are presented in Figures 4.22 and 4.23. Again, the most significant parameter change is the factorization scale. We can see that for both  $t/\bar{t}$  and  $b/\bar{b}$  quarks, the ratio is increasing as the transverse momentum increases. This basically indicates that by increasing the factorization scale, the heavy quarks are generated less energetic in comparison to the nominal setting.

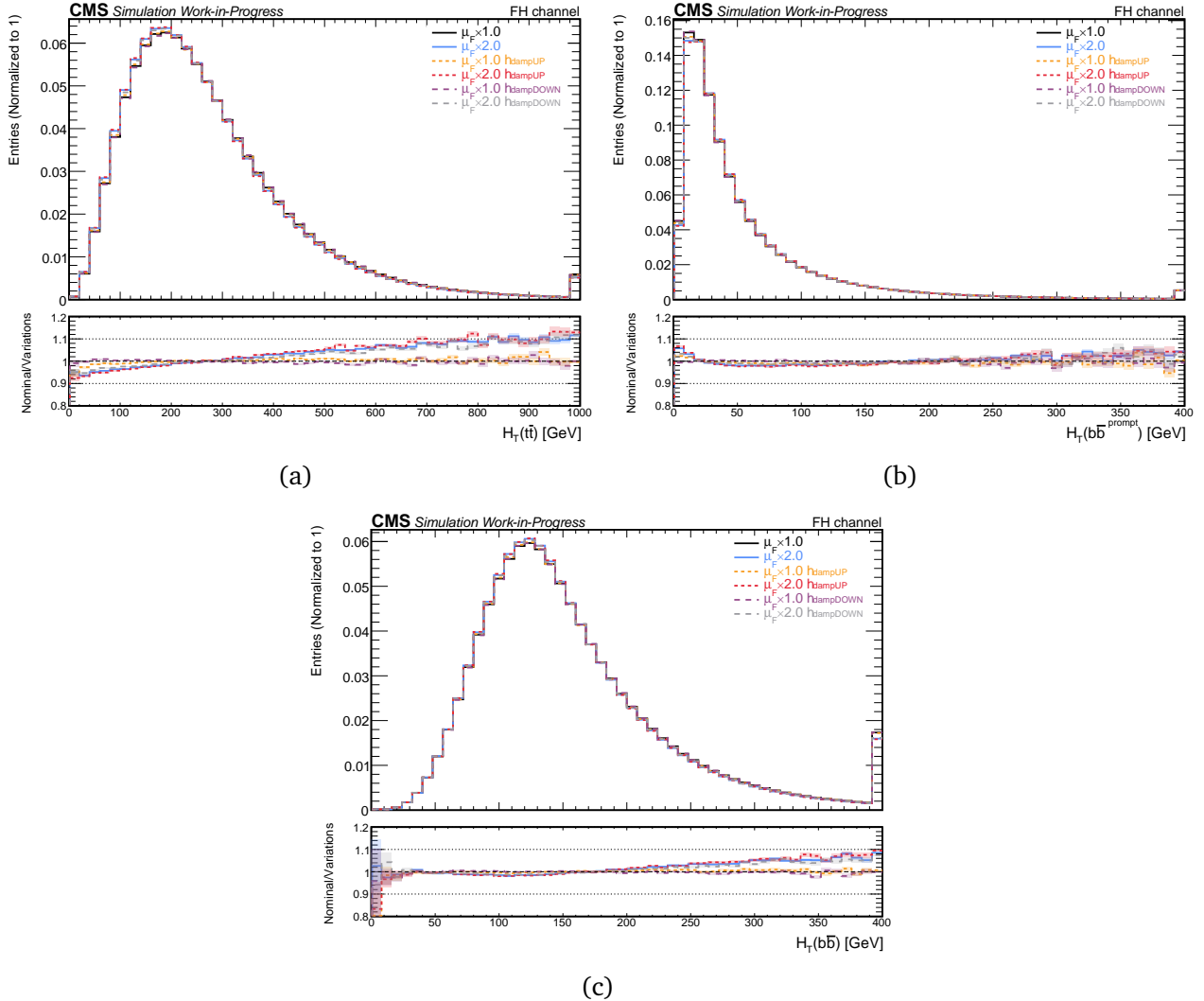


Figure 4.23. Distribution of  $H_T$  for (a)  $t\bar{t}$ , (b) prompt  $b\bar{b}$  and (c)  $b\bar{b}$ , originating from top quarks, systems for the six different settings used in the simulation. The lower panel shows the ratio of the nominal setting to the variations. The shaded bands represent statistical uncertainties. The last bins contain the overflow events.

The same can also be said for the  $H_T$  of the particle systems,  $t\bar{t}$  and the subsequent  $b\bar{b}$  system from the top decays. For the  $t\bar{t}$  system especially, we observe a small drop at the ratio plot in the low  $H_T$  values that reaches up to 8 % difference and slowly moving up, reaching the other end of the  $H_T$  spectrum with an up to 10 % difference, this time above the line corresponding to the

nominal setting. The  $b\bar{b}$  system that comes from the top quarks, exhibit the same behavior but to a lesser extent. The results for the prompt  $b\bar{b}$  system are again different. This system seems to be almost unaffected by any different setting. Only a small deviation at very low  $H_T$  values is observed for the different factorization scale settings, while the rest of the spectrum seems to be consistent with the nominal settings with only small differences of 2% being observed.

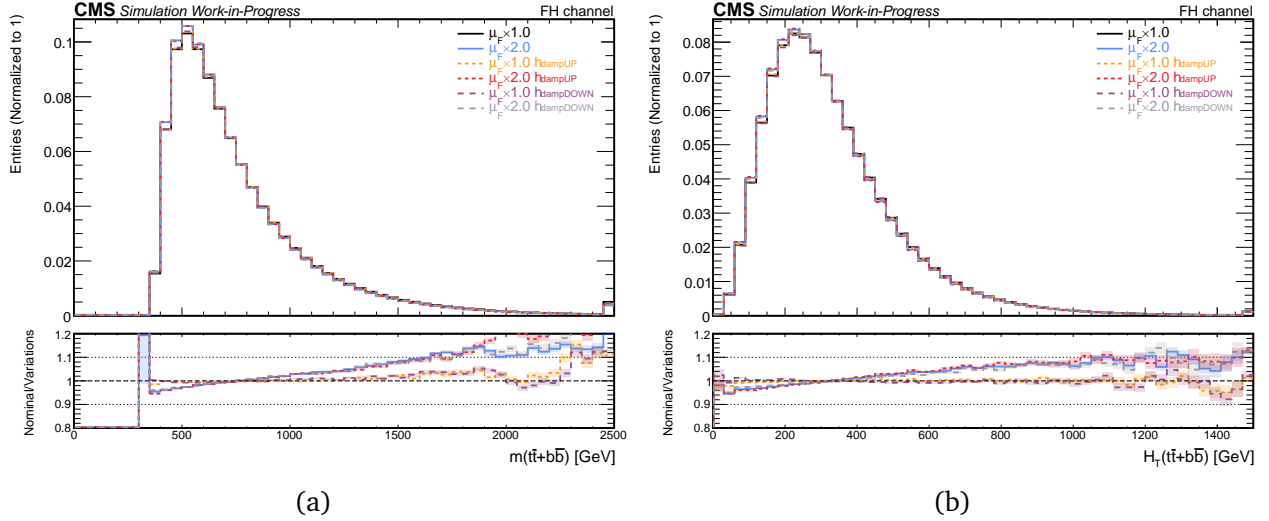


Figure 4.24. Distribution of (a) invariant mass and (b)  $H_T$  for the  $t\bar{t}+b\bar{b}$  system for the six different settings used in the simulation. The lower panel shows the ratio of the nominal setting to the variations. The shaded bands represent statistical uncertainties. The last bins contain the overflow events.

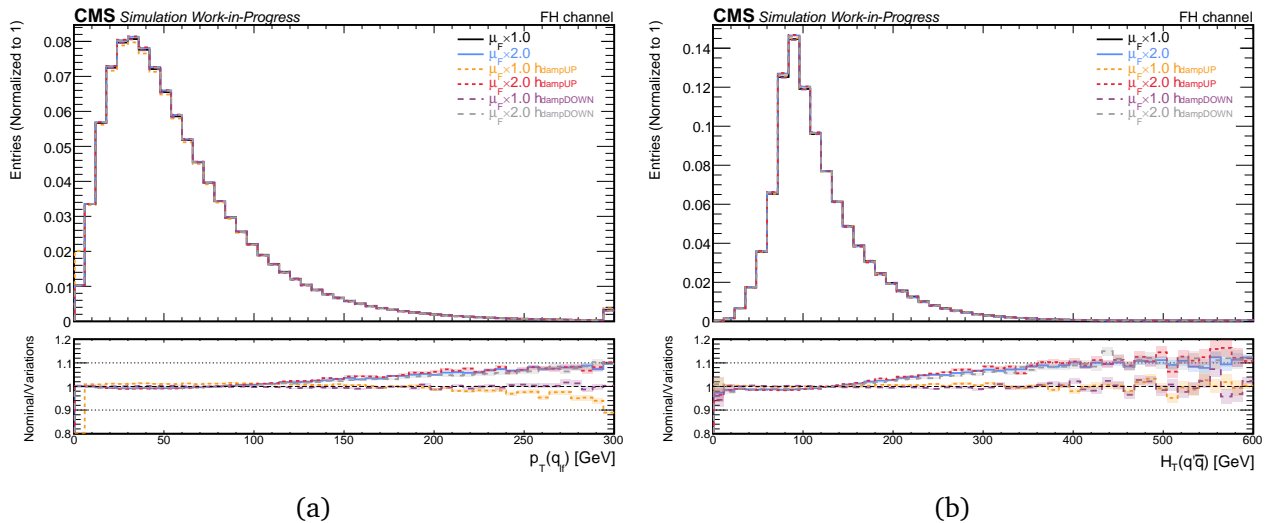


Figure 4.25. Distribution of (a) the transverse momentum of all the quarks and (b) the  $H_T$  of  $q\bar{q}$  system for the six different settings used in the simulation. The lower panel shows the ratio of the nominal setting to the variations. The shaded bands represent statistical uncertainties. The last bins contain the overflow events.

Figure 4.24, illustrates the distributions of the invariant mass and the HT for the  $t\bar{t}+b\bar{b}$  system. The samples with  $\mu_F \times 2$  exhibit a significant impact on both distributions, similar to what was observed in the other two channels. Regarding the various damping parameters, there is virtually no difference among them for HT. However, this consistency does not hold for the invariant mass, which shows notable deviations at very high values, particularly in the hdamp-DOWN setting.

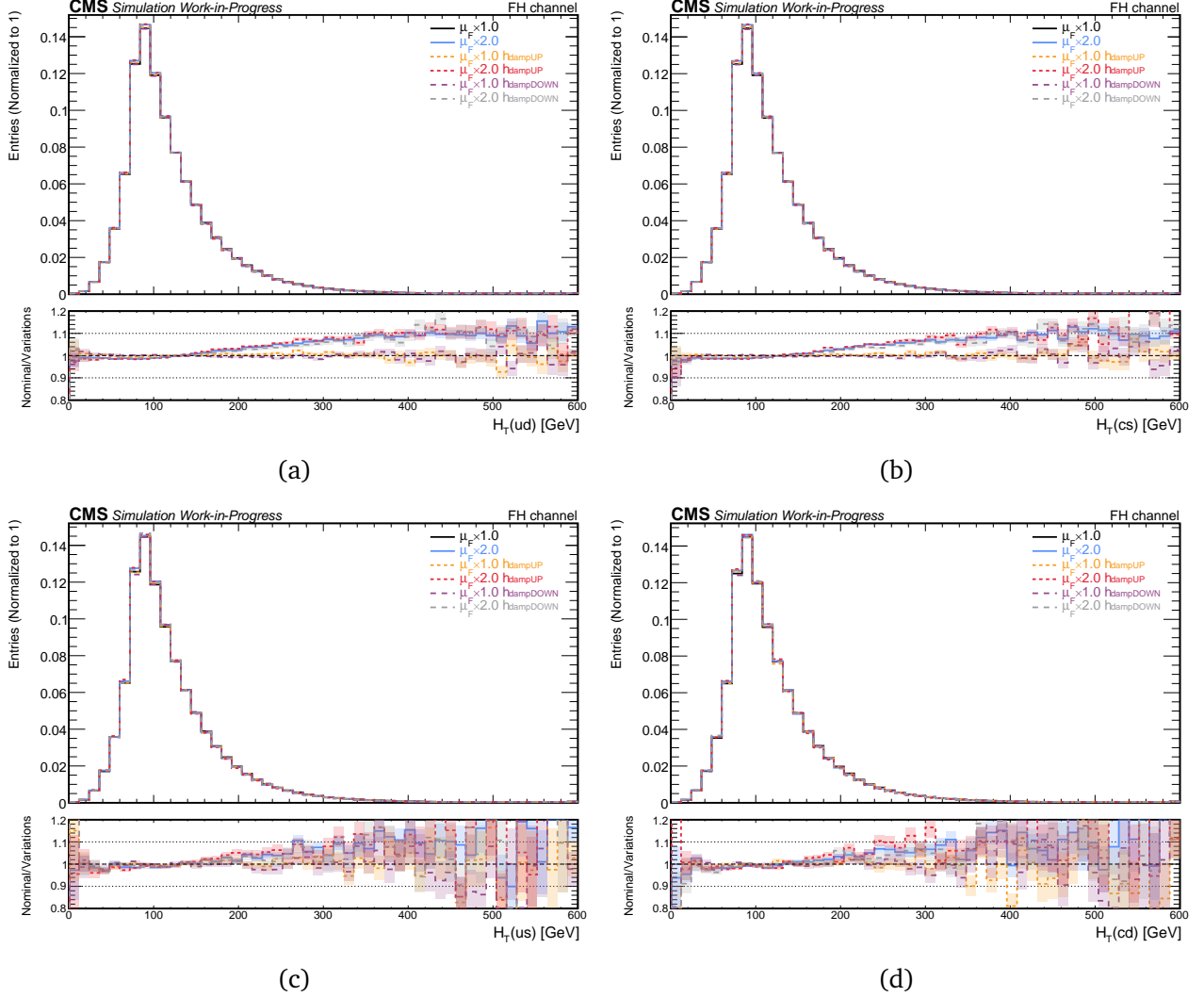


Figure 4.26. Distribution of  $H_T$  for (a) ud (b) cs (c) us and (d) cd systems for the six different settings used in the simulation. The lower panel shows the ratio of the nominal setting to the variations. The shaded bands represent statistical uncertainties. The last bins contain the overflow events.

As for the light flavor quarks, the distributions for the transverse momentum and the  $H_T$  are illustrated in Figures 4.25a and 4.25b respectively. As expected, the trend observed in these plots is similar to the heavier quarks. In particular, there is a strong deviation to the change

of the factorization scale, while again, the different  $h_{damp}$  variations do not affect in significant manner the distributions. As for the different quark-antiquark combinations, the distribution of their  $H_T$  is presented in Figure 4.26. Similar to the SL channel, the results from the two Cabibbo suppressed pairs us (4.26c) and cd (4.26d), due to low statistics have significant fluctuations, while the other two, favored quark-antiquark pairs, ud (4.26a) and cs (4.26b), obviously exhibit the same behavior with the aggregated plot.

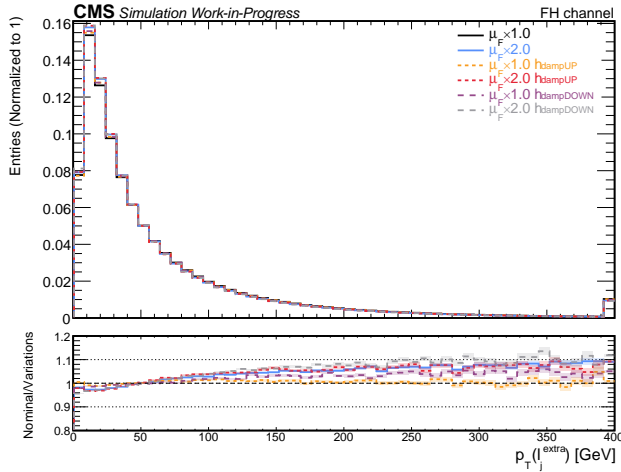


Figure 4.27. Distribution of the transverse momentum of the extra light jet for the six different settings used in the simulation. The lower panel shows the ratio of the nominal setting to the variations. The shaded bands represent statistical uncertainties. The last bins contain the overflow events.

Finally, for the extra radiated particle, as we can see from 4.27, it displays similar results to the other two channels. Specifically, for this particle's transverse momentum, there is a strong trend not only in the selection of the factorization scale but also in the  $h_{dampDOWN}$  variation. In fact, the  $h_{dampDOWN}$  variation with  $\mu_F \times 1$ , has similar deviations as the  $\mu_F \times 2$ . As for the  $h_{dampUP}$  variations, again, there isn't a significant deviation from the nominal settings.

## 4.3 Summary

The objective of this thesis was to optimize the simulation of  $t\bar{t}+b\bar{b}$  production, which as we saw, is a critical background in numerous experimental searches such as the  $t\bar{t}H(b\bar{b}/c\bar{c})$ . In particular, the sensitivity of events on the MC generator free parameter  $h_{damp}$ , and the factorisation scale was studied. Several sets of samples were generated with different settings using the POWHEG BOX RES package, for all three decay channels. The results presented in the previous sections show that different  $h_{damp}$  choices have very small deviations. On the other hand, the increase of the factorization scale by a factor of two impacts the distribution of the

$p_T$ -dependent variables significantly.

Throughout this thesis, all presented results are at the parton level. Consequently, additional processes such as showering and hadronization remain necessary. Moving forward, the next stages involve integrating the new datasets into the current analysis. This integration could involve replacing existing samples or adjusting the Run 3 Monte Carlo samples.

# Bibliography

- [1] Y. Fukuda *et al.* “Evidence for Oscillation of Atmospheric Neutrinos”. In: *Physical Review Letters* 81.8 (Aug. 1998), pp. 1562–1567. ISSN: 1079-7114. DOI: [10.1103/physrevlett.81.1562](https://doi.org/10.1103/physrevlett.81.1562).
- [2] Q. R. Ahmad *et al.* “Direct Evidence for Neutrino Flavor Transformation from Neutral-Current Interactions in the Sudbury Neutrino Observatory”. In: *Physical Review Letters* 89.1 (June 2002). ISSN: 1079-7114. DOI: [10.1103/physrevlett.89.011301](https://doi.org/10.1103/physrevlett.89.011301).
- [3] N. Agafonova *et al.* “Final results of the OPERA experiment on  $\nu_\tau$  appearance in the CNGS beam”. In: *Physical Review Letters* 120.21 (May 2018). ISSN: 1079-7114. DOI: [10.1103/physrevlett.120.211801](https://doi.org/10.1103/physrevlett.120.211801).
- [4] CMS Collaboration. “Observation of a new boson at a mass of 125 GeV with the CMS experiment at the LHC”. In: *Physics Letters B* 716.1 (Sept. 2012), pp. 30–61. DOI: [10.1016/j.physletb.2012.08.021](https://doi.org/10.1016/j.physletb.2012.08.021).
- [5] ATLAS Collaboration. “Observation of a new particle in the search for the Standard Model Higgs boson with the ATLAS detector at the LHC”. In: *Physics Letters B* 716.1 (Sept. 2012), pp. 1–29. DOI: [10.1016/j.physletb.2012.08.020](https://doi.org/10.1016/j.physletb.2012.08.020).
- [6] ATLAS and CMS Collaborations. “Combined Measurement of the Higgs Boson Mass in pp Collisions at  $\sqrt{s} = 7$  and 8 TeV with the ATLAS and CMS Experiments”. In: *Physical Review Letters* 114.19 (May 2015). DOI: [10.1103/physrevlett.114.191803](https://doi.org/10.1103/physrevlett.114.191803).
- [7] Paul Adrien Maurice Dirac. “On the theory of Quantum Mechanics”. In: *Proceedings of the Royal Society of London. Series A, Containing Papers of a Mathematical and Physical Character* 112.762 (Oct. 1926), pp. 661–677. DOI: [10.1098/rspa.1926.0133](https://doi.org/10.1098/rspa.1926.0133).
- [8] Alberto Zannoni. *On the Quantization of the Monoatomic Ideal Gas*. 1999. arXiv: [cond-mat/9912229 \[cond-mat.stat-mech\]](https://arxiv.org/abs/cond-mat/9912229).
- [9] W. Pauli. “Über den Zusammenhang des abschlusses der elektronengruppen im atom mit der komplexstruktur der spektren”. In: *Zeitschrift für Physik* 31.1 (Feb. 1925), pp. 765–783. DOI: [10.1007/bf02980631](https://doi.org/10.1007/bf02980631).
- [10] Bose. “Plancks gesetz und lichtquantenhypothese”. In: *Zeitschrift fur Physik* 26.1 (Dec. 1924), pp. 178–181. DOI: [10.1007/bf01327326](https://doi.org/10.1007/bf01327326).
- [11] A. Einstein. “Quantentheorie des Einatomigen idealen gases”. In: *Albert Einstein: Akademie Vorträge* (Dec. 2005), pp. 237–244. DOI: [10.1002/3527608958.ch27](https://doi.org/10.1002/3527608958.ch27).
- [12] R. L. Workman *et al.* “Review of Particle Physics”. In: *PTEP* 2022 (2022), p. 083C01. DOI: [10.1093/ptep/ptac097](https://doi.org/10.1093/ptep/ptac097).

- [13] G. Arnison *et al.* “Experimental observation of isolated large transverse energy electrons with associated missing energy at s=540 GeV”. In: *Physics Letters B* 122.1 (1983), pp. 103–116. ISSN: 0370-2693. DOI: [10.1016/0370-2693\(83\)91177-2](https://doi.org/10.1016/0370-2693(83)91177-2).
- [14] P. Bagnaia *et al.* “Evidence for  $Z^0 \rightarrow e^+e^-$  at the CERN pp collider”. In: *Physics Letters B* 129.1 (1983), pp. 130–140. ISSN: 0370-2693. DOI: [10.1016/0370-2693\(83\)90744-X](https://doi.org/10.1016/0370-2693(83)90744-X).
- [15] Steven Weinberg. “A Model of Leptons”. In: *Phys. Rev. Lett.* 19 (21 Nov. 1967), pp. 1264–1266. DOI: [10.1103/PhysRevLett.19.1264](https://doi.org/10.1103/PhysRevLett.19.1264).
- [16] A. Salam and J.C. Ward. “Electromagnetic and weak interactions”. In: *Physics Letters* 13.2 (1964), pp. 168–171. ISSN: 0031-9163. DOI: [10.1016/0031-9163\(64\)90711-5](https://doi.org/10.1016/0031-9163(64)90711-5).
- [17] Sheldon L. Glashow. “Partial-symmetries of weak interactions”. In: *Nuclear Physics* 22.4 (1961), pp. 579–588. ISSN: 0029-5582. DOI: [10.1016/0029-5582\(61\)90469-2](https://doi.org/10.1016/0029-5582(61)90469-2).
- [18] Yoichiro Nambu. “Quasi-Particles and Gauge Invariance in the Theory of Superconductivity”. In: *Phys. Rev.* 117 (3 Feb. 1960), pp. 648–663. DOI: [10.1103/PhysRev.117.648](https://doi.org/10.1103/PhysRev.117.648).
- [19] J. Goldstone. “Field theories with «superconductor» solutions”. In: *Il Nuovo Cimento* 19.1 (Jan. 1961), pp. 154–164. DOI: [10.1007/bf02812722](https://doi.org/10.1007/bf02812722).
- [20] Y. Nambu and G. Jona-Lasinio. “Dynamical Model of Elementary Particles Based on an Analogy with Superconductivity. I”. In: *Phys. Rev.* 122 (1 Apr. 1961), pp. 345–358. DOI: [10.1103/PhysRev.122.345](https://doi.org/10.1103/PhysRev.122.345).
- [21] Jeffrey Goldstone, Abdus Salam, and Steven Weinberg. “Broken Symmetries”. In: *Phys. Rev.* 127 (3 Aug. 1962), pp. 965–970. DOI: [10.1103/PhysRev.127.965](https://doi.org/10.1103/PhysRev.127.965).
- [22] P. W. Anderson. “Plasmons, Gauge Invariance, and Mass”. In: *Phys. Rev.* 130 (1 Apr. 1963), pp. 439–442. DOI: [10.1103/PhysRev.130.439](https://doi.org/10.1103/PhysRev.130.439).
- [23] Walter Gilbert. “Broken Symmetries and Massless Particles”. In: *Phys. Rev. Lett.* 12 (25 June 1964), pp. 713–714. DOI: [10.1103/PhysRevLett.12.713](https://doi.org/10.1103/PhysRevLett.12.713).
- [24] F. Englert and R. Brout. “Broken Symmetry and the Mass of Gauge Vector Mesons”. In: *Phys. Rev. Lett.* 13 (9 Aug. 1964), pp. 321–323. DOI: [10.1103/PhysRevLett.13.321](https://doi.org/10.1103/PhysRevLett.13.321).
- [25] P.W. Higgs. “Broken symmetries, massless particles and gauge fields”. In: *Physics Letters* 12.2 (Sept. 1964), pp. 132–133. ISSN: 0031-9163. DOI: [10.1016/0031-9163\(64\)91136-9](https://doi.org/10.1016/0031-9163(64)91136-9).
- [26] Peter W. Higgs. “Broken Symmetries and the Masses of Gauge Bosons”. In: *Phys. Rev. Lett.* 13 (16 Oct. 1964), pp. 508–509. DOI: [10.1103/PhysRevLett.13.508](https://doi.org/10.1103/PhysRevLett.13.508).
- [27] G. S. Guralnik, C. R. Hagen, and T. W. B. Kibble. “Global Conservation Laws and Massless Particles”. In: *Phys. Rev. Lett.* 13 (20 Nov. 1964), pp. 585–587. DOI: [10.1103/PhysRevLett.13.585](https://doi.org/10.1103/PhysRevLett.13.585).
- [28] Peter W. Higgs. “Spontaneous Symmetry Breakdown without Massless Bosons”. In: *Phys. Rev.* 145 (4 May 1966), pp. 1156–1163. DOI: [10.1103/PhysRev.145.1156](https://doi.org/10.1103/PhysRev.145.1156).

- [29] Alexander A. Migdal and Alexander M. Polyakov. “Spontaneous Breakdown of Strong Interaction Symmetry and the Absence of Massless Particles”. In: *Zh. Eksp. Teor. Fiz.* 51 (1966), pp. 135–146.
- [30] T. W. B. Kibble. “Symmetry Breaking in Non-Abelian Gauge Theories”. In: *Phys. Rev.* 155 (5 Mar. 1967), pp. 1554–1561. DOI: [10.1103/PhysRev.155.1554](https://doi.org/10.1103/PhysRev.155.1554).
- [31] S. Tomonaga. “On a Relativistically Invariant Formulation of the Quantum Theory of Wave Fields\*”. In: *Progress of Theoretical Physics* 1.2 (Aug. 1946), pp. 27–42. ISSN: 0033-068X. DOI: [10.1143/PTP.1.27](https://doi.org/10.1143/PTP.1.27).
- [32] Julian Schwinger. “On Quantum-Electrodynamics and the Magnetic Moment of the Electron”. In: *Phys. Rev.* 73 (4 Feb. 1948), pp. 416–417. DOI: [10.1103/PhysRev.73.416](https://doi.org/10.1103/PhysRev.73.416).
- [33] Julian Schwinger. “Quantum Electrodynamics. I. A Covariant Formulation”. In: *Phys. Rev.* 74 (10 Nov. 1948), pp. 1439–1461. DOI: [10.1103/PhysRev.74.1439](https://doi.org/10.1103/PhysRev.74.1439).
- [34] R. P. Feynman. “Space-Time Approach to Quantum Electrodynamics”. In: *Phys. Rev.* 76 (6 Sept. 1949), pp. 769–789. DOI: [10.1103/PhysRev.76.769](https://doi.org/10.1103/PhysRev.76.769).
- [35] R. P. Feynman. “The Theory of Positrons”. In: *Phys. Rev.* 76 (6 Sept. 1949), pp. 749–759. DOI: [10.1103/PhysRev.76.749](https://doi.org/10.1103/PhysRev.76.749).
- [36] R. P. Feynman. “Mathematical Formulation of the Quantum Theory of Electromagnetic Interaction”. In: *Phys. Rev.* 80 (3 Nov. 1950), pp. 440–457. DOI: [10.1103/PhysRev.80.440](https://doi.org/10.1103/PhysRev.80.440).
- [37] F. J. Dyson. “The Radiation Theories of Tomonaga, Schwinger, and Feynman”. In: *Phys. Rev.* 75 (3 Feb. 1949), pp. 486–502. DOI: [10.1103/PhysRev.75.486](https://doi.org/10.1103/PhysRev.75.486).
- [38] F. J. Dyson. “The S Matrix in Quantum Electrodynamics”. In: *Phys. Rev.* 75 (11 June 1949), pp. 1736–1755. DOI: [10.1103/PhysRev.75.1736](https://doi.org/10.1103/PhysRev.75.1736).
- [39] Paul Adrien Maurice Dirac and Ralph Howard Fowler. “The quantum theory of the electron”. In: *Proceedings of the Royal Society of London. Series A, Containing Papers of a Mathematical and Physical Character* 117.778 (1928), pp. 610–624. DOI: [10.1098/rspa.1928.0023](https://doi.org/10.1098/rspa.1928.0023).
- [40] Emmy Noether. “Invariant variation problems”. In: *Transport Theory and Statistical Physics* 1.3 (1971), pp. 186–207. DOI: [10.1080/00411457108231446](https://doi.org/10.1080/00411457108231446).
- [41] H. Fritzsch, Murray Gell-Mann, and H. Leutwyler. “Advantages of the Color Octet Gluon Picture”. In: *Phys. Lett. B* 47 (1973), pp. 365–368. DOI: [10.1016/0370-2693\(73\)90625-4](https://doi.org/10.1016/0370-2693(73)90625-4).
- [42] Murray Gell-Mann. “Symmetries of Baryons and Mesons”. In: *Phys. Rev.* 125 (3 Feb. 1962), pp. 1067–1084. DOI: [10.1103/PhysRev.125.1067](https://doi.org/10.1103/PhysRev.125.1067).
- [43] M. Gell-Mann. “A schematic model of baryons and mesons”. In: *Physics Letters* 8.3 (1964), pp. 214–215. ISSN: 0031-9163. DOI: [10.1016/S0031-9163\(64\)92001-3](https://doi.org/10.1016/S0031-9163(64)92001-3).
- [44] G Zweig. “An  $SU_3$  model for strong interaction symmetry and its breaking; Version 2”. In: (1964). DOI: [10.17181/CERN-TH-412](https://doi.org/10.17181/CERN-TH-412).

- [45] David J. Gross and Frank Wilczek. “Ultraviolet Behavior of Non-Abelian Gauge Theories”. In: *Phys. Rev. Lett.* 30 (26 June 1973), pp. 1343–1346. DOI: [10.1103/PhysRevLett.30.1343](https://doi.org/10.1103/PhysRevLett.30.1343).
- [46] David J. Gross and Frank Wilczek. “Asymptotically Free Gauge Theories. I”. In: *Phys. Rev. D* 8 (10 Nov. 1973), pp. 3633–3652. DOI: [10.1103/PhysRevD.8.3633](https://doi.org/10.1103/PhysRevD.8.3633).
- [47] David J. Gross and Frank Wilczek. “Asymptotically free gauge theories. II”. In: *Phys. Rev. D* 9 (4 Feb. 1974), pp. 980–993. DOI: [10.1103/PhysRevD.9.980](https://doi.org/10.1103/PhysRevD.9.980).
- [48] C. S. Wu *et al.* “Experimental Test of Parity Conservation in Beta Decay”. In: *Phys. Rev.* 105 (4 Feb. 1957), pp. 1413–1415. DOI: [10.1103/PhysRev.105.1413](https://doi.org/10.1103/PhysRev.105.1413).
- [49] John Ellis. “Higgs Physics”. In: (2015), pp. 117–168. DOI: [10.5170/CERN-2015-004.117](https://doi.org/10.5170/CERN-2015-004.117). arXiv: [1312.5672](https://arxiv.org/abs/1312.5672).
- [50] D. B. Chitwood *et al.* “Improved Measurement of the Positive-Muon Lifetime and Determination of the Fermi Constant”. In: *Phys. Rev. Lett.* 99 (3 July 2007), p. 032001. DOI: [10.1103/PhysRevLett.99.032001](https://doi.org/10.1103/PhysRevLett.99.032001).
- [51] Hideki Yukawa. “On the Interaction of Elementary Particles. I”. In: *Progress of Theoretical Physics Supplement* 1 (Jan. 1955), pp. 1–10. ISSN: 0375-9687. DOI: [10.1143/PTPS.1.1](https://doi.org/10.1143/PTPS.1.1).
- [52] A. Tumasyan *et al.* “A portrait of the Higgs boson by the CMS experiment ten years after the discovery”. In: *Nature* 607.7917 (July 2022), pp. 60–68. ISSN: 1476-4687. DOI: [10.1038/s41586-022-04892-x](https://doi.org/10.1038/s41586-022-04892-x).
- [53] T. Matsuoka. “The CKM Matrix and Its Origin”. In: *Progress of Theoretical Physics* 100.1 (July 1998), pp. 107–122. ISSN: 1347-4081. DOI: [10.1143/ptp.100.107](https://doi.org/10.1143/ptp.100.107).
- [54] Makoto Kobayashi and Toshihide Maskawa. “CP-Violation in the Renormalizable Theory of Weak Interaction”. In: *Progress of Theoretical Physics* 49.2 (Feb. 1973), pp. 652–657. ISSN: 0033-068X. DOI: [10.1143/PTP.49.652](https://doi.org/10.1143/PTP.49.652).
- [55] Nicola Cabibbo. “Unitary Symmetry and Leptonic Decays”. In: *Phys. Rev. Lett.* 10 (12 June 1963), pp. 531–533. DOI: [10.1103/PhysRevLett.10.531](https://doi.org/10.1103/PhysRevLett.10.531).
- [56] Cristiano Alpigiani *et al.* *Unitarity Triangle Analysis in the Standard Model and Beyond*. 2017. arXiv: [1710.09644 \[hep-ph\]](https://arxiv.org/abs/1710.09644).
- [57] S. L. Glashow, J. Iliopoulos, and L. Maiani. “Weak Interactions with Lepton-Hadron Symmetry”. In: *Phys. Rev. D* 2 (7 Oct. 1970), pp. 1285–1292. DOI: [10.1103/PhysRevD.2.1285](https://doi.org/10.1103/PhysRevD.2.1285).
- [58] Ziro Maki, Masami Nakagawa, and Shoichi Sakata. “Remarks on the Unified Model of Elementary Particles”. In: *Progress of Theoretical Physics* 28.5 (Nov. 1962), pp. 870–880. DOI: [10.1143/PTP.28.870](https://doi.org/10.1143/PTP.28.870).
- [59] B. Pontecorvo. “Inverse beta processes and nonconservation of lepton charge”. In: *Zh. Eksp. Teor. Fiz.* 34 (1957), p. 247.
- [60] Rabindra N. Mohapatra and Goran Senjanović. “Neutrino Mass and Spontaneous Parity Nonconservation”. In: *Phys. Rev. Lett.* 44 (14 Apr. 1980), pp. 912–915. DOI: [10.1103/PhysRevLett.44.912](https://doi.org/10.1103/PhysRevLett.44.912).

- [61] S.M. Bilenky, J. Hošek, and S.T. Petcov. “On the oscillations of neutrinos with Dirac and Majorana masses”. In: *Physics Letters B* 94.4 (1980), pp. 495–498. ISSN: 0370-2693. DOI: [10.1016/0370-2693\(80\)90927-2](https://doi.org/10.1016/0370-2693(80)90927-2).
- [62] M. Aker *et al.* *First direct neutrino-mass measurement with sub-eV sensitivity*. 2021. arXiv: [2105.08533 \[hep-ex\]](https://arxiv.org/abs/2105.08533).
- [63] F. Abe *et al.* “Observation of Top Quark Production in  $\bar{\pi}\pi$  Collisions with the Collider Detector at Fermilab”. In: *Phys. Rev. Lett.* 74 (14 Apr. 1995), pp. 2626–2631. DOI: [10.1103/PhysRevLett.74.2626](https://doi.org/10.1103/PhysRevLett.74.2626).
- [64] S. Abachi *et al.* “Observation of the Top Quark”. In: *Phys. Rev. Lett.* 74 (14 Apr. 1995), pp. 2632–2637. DOI: [10.1103/PhysRevLett.74.2632](https://doi.org/10.1103/PhysRevLett.74.2632).
- [65] *NNLO+NNLL top-quark-pair cross sections*. URL: <https://twiki.cern.ch/twiki/bin/view/LHCPhysics/TtbarNNLO>.
- [66] A. Tumasyan *et al.* “First measurement of the top quark pair production cross section in proton-proton collisions at  $\sqrt{s} = 13.6$  TeV”. In: *Journal of High Energy Physics* 2023.8 (Aug. 2023). ISSN: 1029-8479. DOI: [10.1007/jhep08\(2023\)204](https://doi.org/10.1007/jhep08(2023)204).
- [67] Gregory Mahlon and Stephen J. Parke. “Spin correlation effects in top quark pair production at the LHC”. In: *Phys. Rev. D* 81 (7 Apr. 2010), p. 074024. DOI: [10.1103/PhysRevD.81.074024](https://doi.org/10.1103/PhysRevD.81.074024).
- [68] G. Aad *et al.* “Measurements of the Higgs boson production and decay rates and coupling strengths using pp collision data at  $\sqrt{s}=7$  and 8 TeV in the ATLAS experiment”. In: *The European Physical Journal C* 76.1 (Jan. 2016), p. 6. ISSN: 1434-6052. DOI: [10.1140/epjc/s10052-015-3769-y](https://doi.org/10.1140/epjc/s10052-015-3769-y).
- [69] V. Khachatryan *et al.* “Precise determination of the mass of the Higgs boson and tests of compatibility of its couplings with the standard model predictions using proton collisions at 7 and 8 TeV”. In: *The European Physical Journal C* 75.5 (May 2015), p. 212. ISSN: 1434-6052. DOI: [10.1140/epjc/s10052-015-3351-7](https://doi.org/10.1140/epjc/s10052-015-3351-7).
- [70] G. Aad *et al.* “Evidence for the spin-0 nature of the Higgs boson using ATLAS data”. In: *Physics Letters B* 726.1 (2013), pp. 120–144. ISSN: 0370-2693. DOI: [10.1016/j.physletb.2013.08.026](https://doi.org/10.1016/j.physletb.2013.08.026).
- [71] V. Khachatryan *et al.* “Constraints on the spin-parity and anomalous  $HVV$  couplings of the Higgs boson in proton collisions at 7 and 8 TeV”. In: *Phys. Rev. D* 92 (1 July 2015), p. 012004. DOI: [10.1103/PhysRevD.92.012004](https://doi.org/10.1103/PhysRevD.92.012004).
- [72] CERN. *CERN Yellow Reports: Monographs, Vol 2 (2017): Handbook of LHC Higgs cross sections: 4. Deciphering the nature of the Higgs sector*. en. 2017. DOI: [10.23731/CYRM-2017-002](https://doi.org/10.23731/CYRM-2017-002).
- [73] M. Aaboud *et al.* “Observation of Higgs boson production in association with a top quark pair at the LHC with the ATLAS detector”. In: *Physics Letters B* 784 (2018), pp. 173–191. ISSN: 0370-2693. DOI: [10.1016/j.physletb.2018.07.035](https://doi.org/10.1016/j.physletb.2018.07.035).
- [74] A. M. Sirunyan *et al.* “Observation of  $t\bar{t}$  Production”. In: *Physical Review Letters* 120.23 (June 2018). ISSN: 1079-7114. DOI: [10.1103/physrevlett.120.231801](https://doi.org/10.1103/physrevlett.120.231801).

- [75] M. Aaboud *et al.* “Observation of  $H \rightarrow bb^-$  decays and VH production with the ATLAS detector”. In: *Physics Letters B* 786 (2018), pp. 59–86. ISSN: 0370-2693. DOI: [10.1016/j.physletb.2018.09.013](https://doi.org/10.1016/j.physletb.2018.09.013).
- [76] A. M. Sirunyan *et al.* “Observation of Higgs Boson Decay to Bottom Quarks”. In: *Phys. Rev. Lett.* 121 (12 Sept. 2018), p. 121801. DOI: [10.1103/PhysRevLett.121.121801](https://doi.org/10.1103/PhysRevLett.121.121801).
- [77] A. M. Sirunyan *et al.* “Evidence for Higgs boson decay to a pair of muons”. In: *Journal of High Energy Physics* 2021.1 (Jan. 2021). ISSN: 1029-8479. DOI: [10.1007/jhep01\(2021\)148](https://doi.org/10.1007/jhep01(2021)148).
- [78] Oliver Sim Brüning *et al.* *LHC Design Report*. CERN Yellow Reports: Monographs. Geneva: CERN, 2004. DOI: [10.5170/CERN-2004-003-V-1](https://doi.org/10.5170/CERN-2004-003-V-1).
- [79] Lyndon Evans and Philip Bryant. “LHC Machine”. In: *Journal of Instrumentation* 3.08 (Aug. 2008), S08001. DOI: [10.1088/1748-0221/3/08/S08001](https://doi.org/10.1088/1748-0221/3/08/S08001).
- [80] CERN. URL: <https://home.cern/news/news/physics/lhc-run-3-physics-record-energy-starts-tomorrow>.
- [81] CERN. URL: <https://home.cern/science/engineering/cryogenics-low-temperatures-high-performance>.
- [82] Lene Norderhaug Drosdal. “LHC Injection Beam Quality During LHC Run I”. PhD thesis. Oslo U., Mar. 2015.
- [83] Stephanie Rädel. “On space charge driven microbunching instability in bERLinPro”. PhD thesis. Mar. 2017.
- [84] G. Aad *et al.* “The ATLAS Experiment at the CERN Large Hadron Collider”. In: *JINST* 3 (2008), S08003. DOI: [10.1088/1748-0221/3/08/S08003](https://doi.org/10.1088/1748-0221/3/08/S08003).
- [85] S. Chatrchyan *et al.* “The CMS Experiment at the CERN LHC”. In: *JINST* 3 (2008), S08004. DOI: [10.1088/1748-0221/3/08/S08004](https://doi.org/10.1088/1748-0221/3/08/S08004).
- [86] K. Aamodt *et al.* “The ALICE experiment at the CERN LHC”. In: *JINST* 3 (2008), S08002. DOI: [10.1088/1748-0221/3/08/S08002](https://doi.org/10.1088/1748-0221/3/08/S08002).
- [87] A. Augusto Alves Jr. *et al.* “The LHCb Detector at the LHC”. In: *JINST* 3 (2008), S08005. DOI: [10.1088/1748-0221/3/08/S08005](https://doi.org/10.1088/1748-0221/3/08/S08005).
- [88] Ewa Lopienska. “The CERN accelerator complex, layout in 2022. Complexe des accélérateurs du CERN en janvier 2022”. In: (2022). General Photo. URL: <https://cds.cern.ch/record/2800984>.
- [89] CERN. URL: <https://home.cern/news/news/accelerators/so-long-linac2-and-thanks-all-protons>.
- [90] K. Schindl. “The PS booster as preinjector for LHC”. In: *Part. Accel.* 58 (1997). Ed. by Oliver S. Bruning and E. Keil, pp. 63–78.
- [91] R. Cappi. “The PS in the LHC injector chain”. In: *Part. Accel.* 58 (1997). Ed. by Oliver S. Bruning and E. Keil, pp. 79–89.
- [92] T. Linnecar. “Preparing the SPS for LHC”. In: *Part. Accel.* 58 (1997). Ed. by Oliver S. Bruning and E. Keil, pp. 91–101.

- [93] John M. Jowett. “The LHC heavy-ion programme: The energy frontier of nuclear collisions”. In: *Challenges and Goals for Accelerators in the XXI Century*. Chap. Chapter 23, pp. 443–465. DOI: [10.1142/9789814436403\\_0023](https://doi.org/10.1142/9789814436403_0023).
- [94] M Chanel. “LEIR: The low energy ion ring at CERN”. In: *Nucl. Instrum. Methods Phys. Res., A* 532 (2004), pp. 137–143.
- [95] “Cumulative delivered and recorded luminosity versus time for 2010-2012, 2015-2018, and 2022-2023 (pp data only)”. In: (2023). Public CMS Luminosity Information.
- [96] G L Bayatian *et al.* *CMS Physics: Technical Design Report Volume 1: Detector Performance and Software*. Technical design report. CMS. There is an error on cover due to a technical problem for some items. Geneva: CERN, 2006. URL: <https://cds.cern.ch/record/922757>.
- [97] Julia Bauer. “Prospects for the Observation of Electroweak Top Quark Production with the CMS Experiment”. PhD thesis. KIT, Karlsruhe, Dept. Phys., 2010. DOI: [10.5445/IR/1000018393](https://doi.org/10.5445/IR/1000018393).
- [98] Matthew D. Schwartz. “Tasi Lectures on collider physics”. In: *Anticipating the Next Discoveries in Particle Physics* (May 2018). DOI: [10.1142/9789813233348\\_0002](https://doi.org/10.1142/9789813233348_0002).
- [99] David Barney. “CMS Detector Slice”. CMS Collection. 2016. URL: <https://cds.cern.ch/record/2120661>.
- [100] URL: <https://cms.cern/detector/identifying-tracks/silicon-pixels>.
- [101] W. Adam *et al.* “The CMS Phase-1 pixel detector upgrade”. In: *Journal of Instrumentation* 16.02 (Feb. 2021), P02027. DOI: [10.1088/1748-0221/16/02/P02027](https://doi.org/10.1088/1748-0221/16/02/P02027).
- [102] A Dominguez *et al.* *CMS Technical Design Report for the Pixel Detector Upgrade*. Tech. rep. 2012. URL: <http://cds.cern.ch/record/1481838>.
- [103] Markus Axer. “Development of a Test System for the Quality Assurance of Silicon Microstrip Detectors for the Inner Tracking System of the CMS Experiment”. PhD thesis. Aachen, Tech. Hochsch., 2003.
- [104] URL: <https://cms.cern/detector/identifying-tracks/silicon-strips>.
- [105] S Chatrchyan *et al.* “Precise mapping of the magnetic field in the CMS barrel yoke using cosmic rays”. In: *JINST* 5 (2010), T03021. DOI: [10.1088/1748-0221/5/03/T03021](https://doi.org/10.1088/1748-0221/5/03/T03021). arXiv: [0910.5530](https://arxiv.org/abs/0910.5530).
- [106] CMS Collaboration. “Performance and operation of the CMS electromagnetic calorimeter”. In: *Journal of Instrumentation* 5.03 (Mar. 2010), T03010–T03010. ISSN: 1748-0221. DOI: [10.1088/1748-0221/5/03/t03010](https://doi.org/10.1088/1748-0221/5/03/t03010).
- [107] R.M. Brown. “The CMS electromagnetic Calorimeter”. In: *Nuclear Instruments and Methods in Physics Research Section A: Accelerators, Spectrometers, Detectors and Associated Equipment* 572.1 (2007). Frontier Detectors for Frontier Physics, pp. 29–32. ISSN: 0168-9002. DOI: [10.1016/j.nima.2006.10.240](https://doi.org/10.1016/j.nima.2006.10.240).
- [108] *The CMS electromagnetic calorimeter project: Technical Design Report*. Technical design report. CMS. Geneva: CERN, 1997. URL: <https://cds.cern.ch/record/349375>.
- [109] Sven Menke. URL: <https://www.mpp.mpg.de/~menke/elss/home.shtml>.

- [110] Francesca Cavallari. “Performance of calorimeters at the LHC”. In: *Journal of Physics: Conference Series* 293.1 (Apr. 2011), p. 012001. DOI: [10.1088/1742-6596/293/1/012001](https://doi.org/10.1088/1742-6596/293/1/012001).
- [111] CMS Collaboration. “Performance of the CMS hadron calorimeter with cosmic ray muons and LHC beam data”. In: *Journal of Instrumentation* 5.03 (Mar. 2010), T03012–T03012. DOI: [10.1088/1748-0221/5/03/t03012](https://doi.org/10.1088/1748-0221/5/03/t03012).
- [112] *The CMS hadron calorimeter project: Technical Design Report*. Technical design report. CMS. Geneva: CERN, 1997. URL: <https://cds.cern.ch/record/357153>.
- [113] J Mans *et al.* *CMS Technical Design Report for the Phase 1 Upgrade of the Hadron Calorimeter*. Tech. rep. 2012. URL: <https://cds.cern.ch/record/1481837>.
- [114] Aram Hayrapetyan *et al.* *Development of the CMS detector for the CERN LHC Run 3*. Tech. rep. Geneva: CERN, 2023. arXiv: [2309.05466](https://arxiv.org/abs/2309.05466). URL: <https://cds.cern.ch/record/2870088>.
- [115] S. Abdullin *et al.* “Design, performance, and calibration of CMS forward calorimeter wedges”. In: *The European Physical Journal C* 53.1 (Nov. 2007), pp. 139–166. DOI: [10.1140/epjc/s10052-007-0459-4](https://doi.org/10.1140/epjc/s10052-007-0459-4).
- [116] *The CMS magnet project: Technical Design Report*. Technical design report. CMS. Geneva: CERN, 1997. DOI: [10.17181/CERN.6ZU0.V4T9](https://doi.org/10.17181/CERN.6ZU0.V4T9).
- [117] François Kircher *et al.* “Final design of the CMS solenoid cold mass”. In: *IEEE Transactions on Applied Superconductivity* 10 (2000), pp. 407–410.
- [118] A. Herve *et al.* “Status of the construction of the CMS magnet”. In: *IEEE Transactions on Applied Superconductivity* 14.2 (2004), pp. 542–547. DOI: [10.1109/TASC.2004.829715](https://doi.org/10.1109/TASC.2004.829715).
- [119] Vyacheslav Klyukhin. “Design and Description of the CMS Magnetic System Model”. In: *Symmetry* 13.6 (June 2021), p. 1052. DOI: [10.3390/sym13061052](https://doi.org/10.3390/sym13061052).
- [120] A. Herve. “The CMS detector magnet”. In: *IEEE Transactions on Applied Superconductivity* 10.1 (2000), pp. 389–394. DOI: [10.1109/77.828255](https://doi.org/10.1109/77.828255).
- [121] Daniel Froidevaux and Paris Sphicas. “General-Purpose Detectors for the Large Hadron Collider”. In: *Annual Review of Nuclear and Particle Science* 56.1 (2006), pp. 375–440. DOI: [10.1146/annurev.nucl.54.070103.181209](https://doi.org/10.1146/annurev.nucl.54.070103.181209).
- [122] CMS Collaboration. “Precise mapping of the magnetic field in the CMS barrel yoke using cosmic rays”. In: *Journal of Instrumentation* 5.03 (Mar. 2010), T03021. DOI: [10.1088/1748-0221/5/03/T03021](https://doi.org/10.1088/1748-0221/5/03/T03021).
- [123] A.M. Sirunyan *et al.* “Performance of the CMS muon detector and muon reconstruction with proton-proton collisions at  $\sqrt{s} = 13$  TeV”. In: *Journal of Instrumentation* 13.06 (June 2018), P06015. DOI: [10.1088/1748-0221/13/06/P06015](https://doi.org/10.1088/1748-0221/13/06/P06015).
- [124] J. G. Layter. *The CMS muon project: Technical Design Report*. Technical design report. CMS. Geneva: CERN, 1997. URL: <https://cds.cern.ch/record/343814>.

- [125] F. Sauli. “GEM: A new concept for electron amplification in gas detectors”. In: *Nuclear Instruments and Methods in Physics Research Section A: Accelerators, Spectrometers, Detectors and Associated Equipment* 386.2 (1997), pp. 531–534. ISSN: 0168-9002. DOI: [10.1016/S0168-9002\(96\)01172-2](https://doi.org/10.1016/S0168-9002(96)01172-2).
- [126] Paolo Gunnellini. *The CASTOR calorimeter at the CMS experiment*. 2013. arXiv: [1304.2943 \[physics.ins-det\]](https://arxiv.org/abs/1304.2943).
- [127] Benoit Roland. *Forward Physics Capabilities of CMS with the CASTOR and ZDC detectors*. 2010. arXiv: [1008.0592 \[physics.ins-det\]](https://arxiv.org/abs/1008.0592).
- [128] Vardan Khachatryan *et al.* “The very forward CASTOR calorimeter of the CMS experiment”. In: *JINST* 16.02 (2021), P02010. DOI: [10.1088/1748-0221/16/02/P02010](https://doi.org/10.1088/1748-0221/16/02/P02010). arXiv: [2011.01185 \[physics.ins-det\]](https://arxiv.org/abs/2011.01185).
- [129] A.M. Sirunyan *et al.* “Performance of the CMS Level-1 trigger in proton-proton collisions at  $\sqrt{s}=13$  TeV”. In: *Journal of Instrumentation* 15.10 (Oct. 2020), P10017. DOI: [10.1088/1748-0221/15/10/P10017](https://doi.org/10.1088/1748-0221/15/10/P10017).
- [130] M Baber *et al.* “Development and testing of an upgrade to the CMS level-1 calorimeter trigger”. In: *Journal of Instrumentation* 9.01 (Jan. 2014), p. C01006. DOI: [10.1088/1748-0221/9/01/C01006](https://doi.org/10.1088/1748-0221/9/01/C01006).
- [131] A. Zabi *et al.* “Triggering on electrons, jets and tau leptons with the CMS upgraded calorimeter trigger for the LHC RUN II”. In: *Journal of Instrumentation* 11.02 (Feb. 2016), p. C02008. DOI: [10.1088/1748-0221/11/02/C02008](https://doi.org/10.1088/1748-0221/11/02/C02008).
- [132] Jonathan Fulcher *et al.* “The New Global Muon Trigger of the CMS Experiment”. In: *IEEE Trans. Nucl. Sci.* 64.6 (2017), pp. 1467–1473. DOI: [10.1109/TNS.2017.2663442](https://doi.org/10.1109/TNS.2017.2663442).
- [133] Manfred Jeitler *et al.* “Upgrade of the CMS Global Muon Trigger”. In: *IEEE Trans. Nucl. Sci.* 62 (2015), pp. 1104–1109. DOI: [10.1109/TNS.2015.2435060](https://doi.org/10.1109/TNS.2015.2435060).
- [134] Marco Peruzzi *et al.* “The NanoAOD event data format in CMS”. In: *Journal of Physics: Conference Series* 1525.1 (Apr. 2020), p. 012038. DOI: [10.1088/1742-6596/1525/1/012038](https://doi.org/10.1088/1742-6596/1525/1/012038).
- [135] The CMS collaboration. “Performance of CMS muon reconstruction in pp collision events at  $\sqrt{s} = 7$  TeV”. In: *Journal of Instrumentation* 7.10 (Oct. 2012), P10002. DOI: [10.1088/1748-0221/7/10/P10002](https://doi.org/10.1088/1748-0221/7/10/P10002).
- [136] Raymond Brock *et al.* “Handbook of perturbative QCD: Version 1.0”. In: *Rev. Mod. Phys.* 67 (1995), pp. 157–248. DOI: [10.1103/RevModPhys.67.157](https://doi.org/10.1103/RevModPhys.67.157).
- [137] Jay Orear *et al.* *Nuclear physics: A course given by Enrico Fermi at the University of Chicago*. University of Chicago Press, 1974.
- [138] Richard P. Feynman. “Very High-Energy Collisions of Hadrons”. In: *Phys. Rev. Lett.* 23 (24 Dec. 1969), pp. 1415–1417. DOI: [10.1103/PhysRevLett.23.1415](https://doi.org/10.1103/PhysRevLett.23.1415).
- [139] James D. Bjorken and E. A. Paschos. “Inelastic Electron Proton and gamma Proton Scattering, and the Structure of the Nucleon”. In: *Physical Review* 185 (1969), pp. 1975–1982. DOI: [10.1103/PhysRev.185.1975](https://doi.org/10.1103/PhysRev.185.1975).

- [140] John C. Collins and Davison E. Soper. “The Theorems of Perturbative QCD”. In: *Ann. Rev. Nucl. Part. Sci.* 37 (1987), pp. 383–409. DOI: [10.1146/annurev.ns.37.120187.002123](https://doi.org/10.1146/annurev.ns.37.120187.002123).
- [141] V. N. Gribov and L. N. Lipatov. “Deep inelastic e p scattering in perturbation theory”. In: *Sov. J. Nucl. Phys.* 15 (1972), pp. 438–450.
- [142] L. N. Lipatov. “The parton model and perturbation theory”. In: *Yad. Fiz.* 20 (1974), pp. 181–198.
- [143] G. Altarelli and G. Parisi. “Asymptotic freedom in parton language”. In: *Nuclear Physics B* 126.2 (1977), pp. 298–318. ISSN: 0550-3213. DOI: [10.1016/0550-3213\(77\)90384-4](https://doi.org/10.1016/0550-3213(77)90384-4).
- [144] Yuri L. Dokshitzer. “Calculation of the Structure Functions for Deep Inelastic Scattering and e+ e- Annihilation by Perturbation Theory in Quantum Chromodynamics.” In: *Sov. Phys. JETP* 46 (1977), pp. 641–653.
- [145] Richard D. Ball *et al.* “Parton distributions from high-precision collider data”. In: *The European Physical Journal C* 77.10 (Oct. 2017), p. 663. ISSN: 1434-6052. DOI: [10.1140/epjc/s10052-017-5199-5](https://doi.org/10.1140/epjc/s10052-017-5199-5).
- [146] T. Kinoshita. “Mass singularities of Feynman amplitudes”. In: *J. Math. Phys.* 3 (1962), pp. 650–677. DOI: [10.1063/1.1724268](https://doi.org/10.1063/1.1724268).
- [147] T. D. Lee and M. Nauenberg. “Degenerate Systems and Mass Singularities”. In: *Phys. Rev.* 133 (6B Mar. 1964), B1549–B1562. DOI: [10.1103/PhysRev.133.B1549](https://doi.org/10.1103/PhysRev.133.B1549).
- [148] S. Catani and M.H. Seymour. “A general algorithm for calculating jet cross sections in NLO QCD”. In: *Nuclear Physics B* 485.1–2 (Feb. 1997), pp. 291–419. ISSN: 0550-3213. DOI: [10.1016/s0550-3213\(96\)00589-5](https://doi.org/10.1016/s0550-3213(96)00589-5).
- [149] Paolo Nason and Bryan Webber. “Next-to-Leading-Order Event Generators”. In: *Ann. Rev. Nucl. Part. Sci.* 62 (2012), pp. 187–213. DOI: [10.1146/annurev-nucl-102711-094928](https://doi.org/10.1146/annurev-nucl-102711-094928). arXiv: [1202.1251 \[hep-ph\]](https://arxiv.org/abs/1202.1251).
- [150] V. V. Sudakov. “Vertex parts at very high-energies in quantum electrodynamics”. In: *Sov. Phys. JETP* 3 (1956), pp. 65–71.
- [151] John C. Collins. “Sudakov form-factors”. In: *Adv. Ser. Direct. High Energy Phys.* 5 (1989), pp. 573–614. DOI: [10.1142/9789814503266\\_0006](https://doi.org/10.1142/9789814503266_0006). arXiv: [hep-ph/0312336](https://arxiv.org/abs/hep-ph/0312336).
- [152] Torbjorn Sjostrand. “A Model for Initial State Parton Showers”. In: *Phys. Lett. B* 157 (1985), pp. 321–325. DOI: [10.1016/0370-2693\(85\)90674-4](https://doi.org/10.1016/0370-2693(85)90674-4).
- [153] Stefano Frixione and Bryan R Webber. “Matching NLO QCD computations and parton shower simulations”. In: *Journal of High Energy Physics* 2002.06 (June 2002), pp. 029–029. ISSN: 1029-8479. DOI: [10.1088/1126-6708/2002/06/029](https://doi.org/10.1088/1126-6708/2002/06/029).
- [154] Simone Alioli *et al.* “A general framework for implementing NLO calculations in shower Monte Carlo programs: the POWHEG BOX”. In: *JHEP* 06 (2010), p. 043. DOI: [10.1007/JHEP06\(2010\)043](https://doi.org/10.1007/JHEP06(2010)043). arXiv: [1002.2581 \[hep-ph\]](https://arxiv.org/abs/1002.2581).
- [155] Paolo Nason. “A New method for combining NLO QCD with shower Monte Carlo algorithms”. In: *JHEP* 11 (2004), p. 040. DOI: [10.1088/1126-6708/2004/11/040](https://doi.org/10.1088/1126-6708/2004/11/040). arXiv: [hep-ph/0409146](https://arxiv.org/abs/hep-ph/0409146).

- [156] Stefano Frixione, Paolo Nason, and Carlo Oleari. “Matching NLO QCD computations with parton shower simulations: the POWHEG method”. In: *Journal of High Energy Physics* 2007.11 (Nov. 2007), p. 070. doi: [10.1088/1126-6708/2007/11/070](https://doi.org/10.1088/1126-6708/2007/11/070).
- [157] Stefan Weinzierl. *Introduction to Monte Carlo methods*. 2000. arXiv: [hep-ph/0006269 \[hep-ph\]](https://arxiv.org/abs/hep-ph/0006269).
- [158] Víctor Elvira and Luca Martino. *Advances in Importance Sampling*. 2022. arXiv: [2102.05407 \[stat.CO\]](https://arxiv.org/abs/2102.05407).
- [159] B. Andersson *et al.* “Parton fragmentation and string dynamics”. In: *Physics Reports* 97.2 (1983), pp. 31–145. ISSN: 0370-1573. doi: [10.1016/0370-1573\(83\)90080-7](https://doi.org/10.1016/0370-1573(83)90080-7).
- [160] Torbjörn Sjöstrand *et al.* “An introduction to PYTHIA 8.2”. In: *Computer Physics Communications* 191 (2015), pp. 159–177. ISSN: 0010-4655. doi: [10.1016/j.cpc.2015.01.024](https://doi.org/10.1016/j.cpc.2015.01.024).
- [161] Manuel Bähr *et al.* “Herwig++ physics and manual”. In: *The European Physical Journal C* 58.4 (Dec. 2008), pp. 639–707. ISSN: 1434-6052. doi: [10.1140/epjc/s10052-008-0798-9](https://doi.org/10.1140/epjc/s10052-008-0798-9).
- [162] Stefan Höche. *Introduction to parton-shower event generators*. 2015. arXiv: [1411.4085 \[hep-ph\]](https://arxiv.org/abs/1411.4085).
- [163] Huilin Qu and Loukas Gouskos. “ParticleNet: Jet Tagging via Particle Clouds. Jet tagging via particle clouds”. In: *Phys. Rev. D* 101.5 (2020), p. 056019. doi: [10.1103/PhysRevD.101.056019](https://doi.org/10.1103/PhysRevD.101.056019). arXiv: [1902.08570](https://arxiv.org/abs/1902.08570).
- [164] Huilin Qu, Congqiao Li, and Sitian Qian. *Particle Transformer for Jet Tagging*. 2024. arXiv: [2202.03772 \[hep-ph\]](https://arxiv.org/abs/2202.03772).
- [165] Yue Wang *et al.* *Dynamic Graph CNN for Learning on Point Clouds*. 2019. arXiv: [1801.07829 \[cs.CV\]](https://arxiv.org/abs/1801.07829).
- [166] E. Bols *et al.* “Jet flavour classification using DeepJet”. In: *Journal of Instrumentation* 15.12 (Dec. 2020), P12012–P12012. ISSN: 1748-0221. doi: [10.1088/1748-0221/15/12/p12012](https://doi.org/10.1088/1748-0221/15/12/p12012).
- [167] Tomás Jezo *et al.* “New NLOPS predictions for  $t\bar{t} + b$ -jet production at the LHC”. In: *The European Physical Journal C* 78.6 (June 2018), p. 502. ISSN: 1434-6052. doi: [10.1140/epjc/s10052-018-5956-0](https://doi.org/10.1140/epjc/s10052-018-5956-0).
- [168] CMS Collaboration. *Inclusive and differential cross section measurements of  $t\bar{t}b\bar{b}$  production in the lepton+jets channel at  $\sqrt{s} = 13$  TeV*. 2023. arXiv: [2309.14442 \[hep-ex\]](https://arxiv.org/abs/2309.14442).
- [169] Jan van der Linden. “Inclusive and differential cross section measurement of  $ttbb$  production and studies of  $tt$  production with additional jet radiation”. PhD thesis. KIT/ETP, KIT, Karlsruhe, 2023.
- [170] Tomás Ježo and Paolo Nason. “On the Treatment of Resonances in Next-to-Leading Order Calculations Matched to a Parton Shower”. In: *JHEP* 12 (2015), p. 065. doi: [10.1007/JHEP12\(2015\)065](https://doi.org/10.1007/JHEP12(2015)065). arXiv: [1509.09071 \[hep-ph\]](https://arxiv.org/abs/1509.09071).
- [171] J. Alwall *et al.* “A standard format for Les Houches Event Files”. In: *Computer Physics Communications* 176.4 (Feb. 2007), pp. 300–304. ISSN: 0010-4655. doi: [10.1016/j.cpc.2006.11.010](https://doi.org/10.1016/j.cpc.2006.11.010).

- [172] W3C. *Extensible Markup Language (XML) 1.0 (Fifth Edition)*. <https://www.w3.org/TR/xml/>. 2008.
- [173] Richard D. Ball *et al.* “Parton distributions for the LHC run II”. In: *Journal of High Energy Physics* 2015.4 (Apr. 2015). ISSN: 1029-8479. DOI: [10.1007/jhep04\(2015\)040](https://doi.org/10.1007/jhep04(2015)040).
- [174] Andy Buckley *et al.* “LHAPDF6: parton density access in the LHC precision era”. In: *The European Physical Journal C* 75.3 (Mar. 2015). ISSN: 1434-6052. DOI: [10.1140/epjc/s10052-015-3318-8](https://doi.org/10.1140/epjc/s10052-015-3318-8).

# Appendix A

## POWHEG BOX RES Configuration

### A.1 Collider setup

```
#beam1 6500d0      ! energy of beam 1
#beam2 6500d0      ! energy of beam 2
ih1    1            ! hadron 1 (1 for protons, -1 for antiprotons)
ih2    1            ! hadron 2 (1 for protons, -1 for antiprotons)
```

### A.2 Parameters for the generation of spin correlated $t\bar{t}$ decays

```
#tdec/wmass 80.4      ! W mass for top decay
#tdec/wwidth 2.141
#tdec/bmass 4.8
#tdec/twidth 1.31     ! 1.33 using PDG LO formula
#tdec/elbranching 0.108
#tdec/emass 0.00051
#tdec/mumass 0.1057
#tdec/taumass 1.777
#tdec/dmass 0.100
#tdec/umass 0.100
#tdec/smass 0.200
#tdec/cmass 1.5
#tdec/sin2cabibbo 0.051
```

## A.3 Integrator and event generator settings

```

! values below suitable for a manyseeds run with 128 cores and 3 xgriditerations
ncall1 40000 ! number of calls for initializing the integration grid
itmxi 2 ! number of iterations for initializing the integration grid
ncall2 40000 ! number of calls for computing the integral and finding upper bound
ncall2rm 80000 ! number of calls for computing the integral and finding upper bound
itmxi2 3 ! number of iterations for computing the integral and finding upper
           ! bound

foldcsi 5 ! number of folds on csi integration
foldy 5 ! number of folds on y integration
foldphi 5 ! number of folds on phi integration

nubound 10000 ! number of bbarra calls to setup norm of upper bounding function

icsimax 1 ! <= 100, number of csi subdivision when computing the upper bounds
iyymax 1 ! <= 100, number of y subdivision when computing the upper bounds
xupbound 2d0 ! increase upper bound for radiation generation
storemintupb 1 ! (powheg default 0, ttbb recommended 1)
                 ! 1 ... store st2 btilde calls to set up upper bounding envelope;
                 ! 0 ... do not
fastbtlbounds 1 ! (powheg default 0, ttbb recommended 1)
                  ! 1 ... fast calculation of the btilder upper bounding envelope;
                  ! 0 ... usual calculation of the btilder upper bounding
compress_upb 1 ! uses zlib to compress the upper bounding envelope on the fly
compress_lhe 1 ! uses zlib to compress the .lhe files, compressed .lhe files can be
                 ! inspected using zcat
use-old-grid 1 ! (powheg default 0)
                 ! 1 ... use old grid if file pwggrids.dat is present;
                 ! 0 ... regenerate, must be 1 for a manyseed run
use-old-ubound 1 ! (powheg default 0) 1 ... use norm of upper bounding function
                  ! stored in pwgubound.dat, if present;
                  ! 0 ... regenerate, must be 1 for a manyseed run

```

## A.4 Scale settings

```

runningscales 2 ! (powheg default 0, ttbb recommended 2) renormalization and
                  ! factorization scale setting
                  ! 0... mur=muf=2*mtop;
                  ! 1... mur=[mT(top)*mT(tbar)*mT(b)*mT(bbar)]**((1/4),
                  !           muf=1/2*[mT(top)+mT(tbar)+mT(b)+mT(bbar)+mT(gluon)];
                  ! 2... mur=1/2*[mT(top)*mT(tbar)*mT(b)*mT(bbar)]**((1/4),
                  !           muf=1/4*[mT(top)+mT(tbar)+mT(b)+mT(bbar)+mT(gluon)];
btlscalereal 1 ! (powheg default 0, ttbb recommended 2) let's user chose what
                  ! kinematics (real or uborn) to use for the scales in real matrix
                  ! element, by default uborn is used
btlscalect 1 ! (powheg default 0, ttbb recommended 2) let's user chose what
                  ! kinematics (real or uborn) to use for the scales in the real
                  ! counterterm, by default same as real are used

```

## A.5 Damping

```
withdamp 1           ! (powheg default 0, ttbb recommended 1) activate separation of
                     ! the real cross section into the singular and remnant
                     ! contributions through a damping with h^2/(pt2+h^2)
#hdamp 172.5       ! fixed value of h, in the expression in the withdamp entry,
                     ! not recommended for ttbb
#dynhdamp 1         ! (ttbb default 1) 1 ... calculate the on per event basis as
                     ! h = sqrt(1/2)*(E[t]+E[t~])*dynhdampPF with
                     ! E[x]=sqrt(m[x]**2+pt[x]**2),
                     ! 0 ... use static h with the value set in hdamp
#dynhdampPF 0.5    ! (ttbb default 0.5) the value of dynhdampPF from above
#hdampMassTh 5.0   ! (ttbb default 5) by default in powheg, massive emitters are not
                     ! subjected to damping, this introduces damping for massive emitters
                     ! lighter than hdampMassTh (focusing in particular on bottom quarks)
#bornzerodampcut 2 ! (powheg default 5, ttbb default 2) points in which the real matrix
                     ! element is larger than bornzerodampcut x
                     ! [its collinear approximation] are considered remnant
```

## A.6 Scale and PDF reweighting

```
rwl_file 'pwg-rwl.dat' ! If set to '-' read the xml reweighting info
                     ! from this same file. Otherwise, it specifies
                     ! the xml file with weight information
#<initrwgt>
#<weight id='1'>default</weight> ! Default weight, necessary when using
                     ! for reweighting 1, in order to save the
                     ! weight including the virtual corrections
#<weight id='2'>renscfact=2d0 facscfact=2d0 </weight>
#<weight id='3'>renscfact=0.5d0 facscfact=0.5d0 </weight>
#<weight id='4'>renscfact=1d0 facscfact=2d0 </weight>
#<weight id='5'>renscfact=1d0 facscfact=0.5d0 </weight>
#<weight id='6'>renscfact=2d0 facscfact=1d0 </weight>
#<weight id='7'>renscfact=0.5d0 facscfact=1d0 </weight>
#</initrwgt>
rwl_group_events 1000 ! (powheg default 1000) it keeps 1000 events in
                     ! memory, reprocessing them together for reweighting

manyseeds 1
```

## A.7 Parallel runs settings

```
manyseeds 1          ! (default 0) 1 ... perform a manyseeds run
#xgriditeration 1 ! this controls xgriditeration in stage 1 manyseeds runs, modify
                  ! correspondingly throughout the run either here or via a command
                  ! line argument as ./pwhg_main xgriditeration=1
#parallelstage 1 ! this controls stage in manyseeds run, modify either here
                  ! correspondingly throughout the run or via a command line
                  ! argument as ./pwhg_main parallelstage=1
maxseeds 1000       ! maximum number of cores to consider
```

## A.8 Other settings

```
clobberlhe 1          ! 1 ... delete the event file if it exists,
                      ! 0 ... exit if it exists
olverbose 1           ! set the OpenLoops verbosity level (see OL manual)
alphas_from_lhapdf 1 ! (powheg default 0, ttbb recommended 1) use the LHAPDF routine
                      ! for alphaS running instead of the powheg internal routine
                      ! (everywhere, except for in the Sudakov form factor)

for_reweighting 0     ! (powheg default 0, ttbb recommended 0)
                      ! 1... calculate with virtual corrections switched off throughout
                      ! and then reweight with virtual corrections switched on
                      ! (useful for when virtual corrections are costly to calculate).
                      ! Note that the events will have two weights, the first an
                      ! intermediate weight (not to be used), and the second one
                      ! including all the contributions

!!!!!!!!!!!!!!!!!!!!!!!!!!!!!!!!!!!!!!!!!!!!!!!!!!!!!!!!!!!!!!!!!!!!!!!!!!!!!!!
! Physics constants
!!!!!!!!!!!!!!!!!!!!!!!!!!!!!!!!!!!!!!!!!!!!!!!!!!!!!!!!!!!!!!!!!!!!!!!
#tmass 172.5d0        ! (ttbb default 172.5)
#bmass 4.75d0         ! (ttbb default 4.75) bottom quark mass, setting it to zero
                      ! introduces a singularity in the born matrix element, make
                      ! sure to adjust hdampMassTh correspondingly if using value
                      ! larger than 5.0
```

# Appendix B

## Supplemental Material

### B.1 DL channel

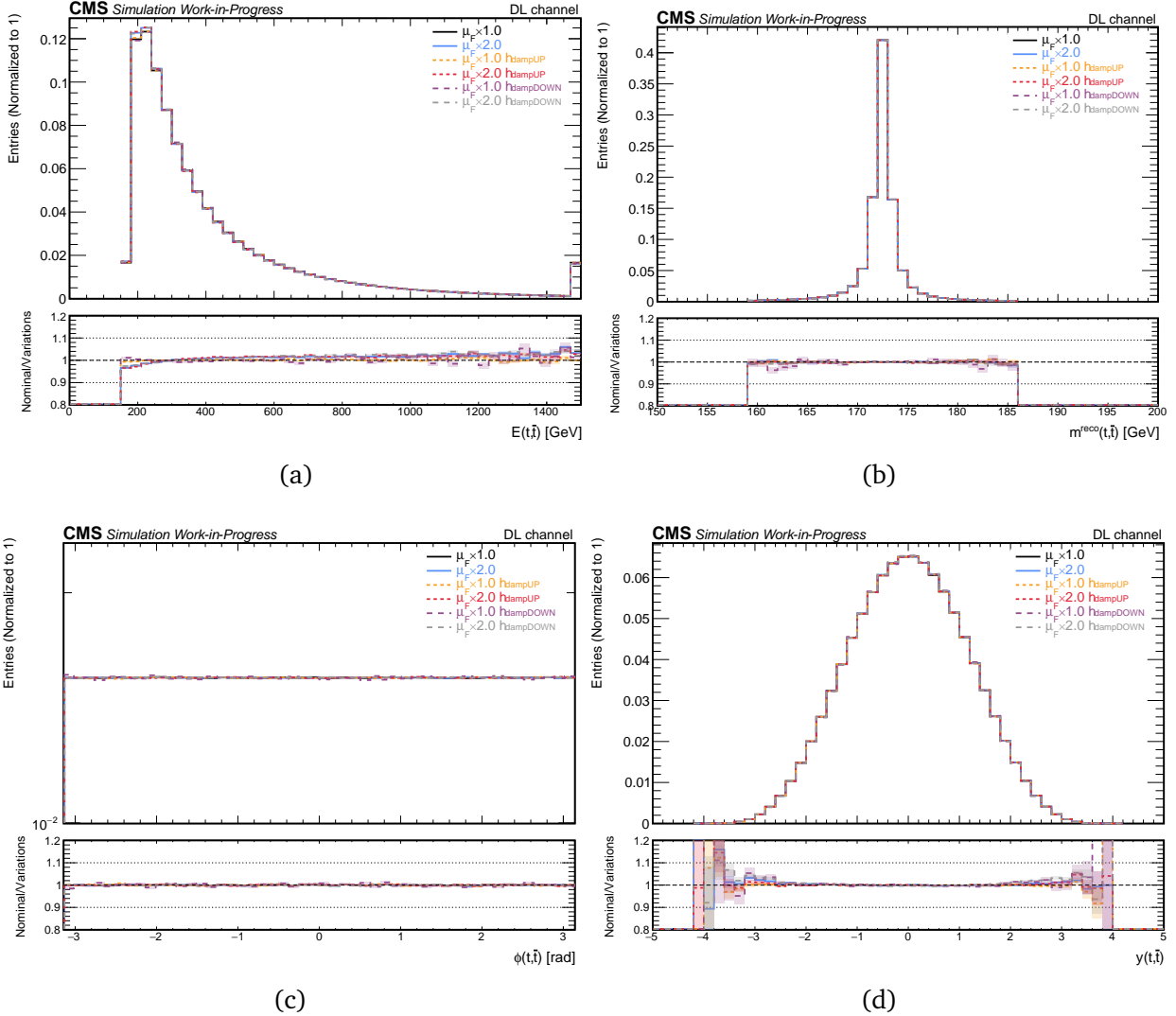


Figure B.1. Distributions of (a) energy, (b) reconstructed mass, (c) azimuthal angle and (d) rapidity of the  $t/\bar{t}$  quarks for the six different settings used in the simulation. The lower panel shows the ratio of the nominal setting to the variations. The shaded bands represent statistical uncertainties. The last bins contain the overflow events.

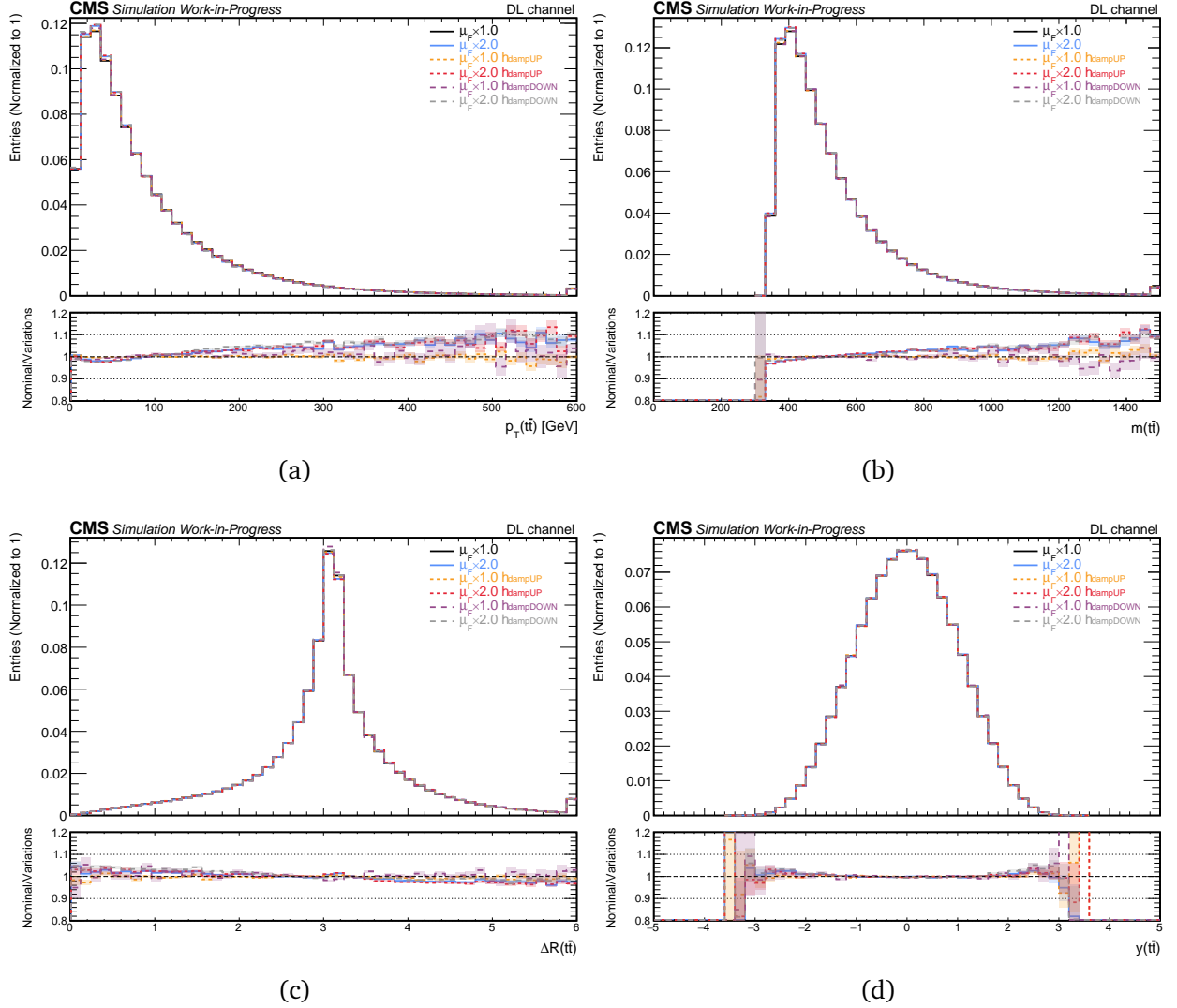


Figure B.2. Distributions of (a) transverse momentum, (b) invariant mass, (c) angular separation and (d) rapidity of the  $t\bar{t}$  system for the six different settings used in the simulation. The lower panel shows the ratio of the nominal setting to the variations. The shaded bands represent statistical uncertainties. The last bins contain the overflow events.

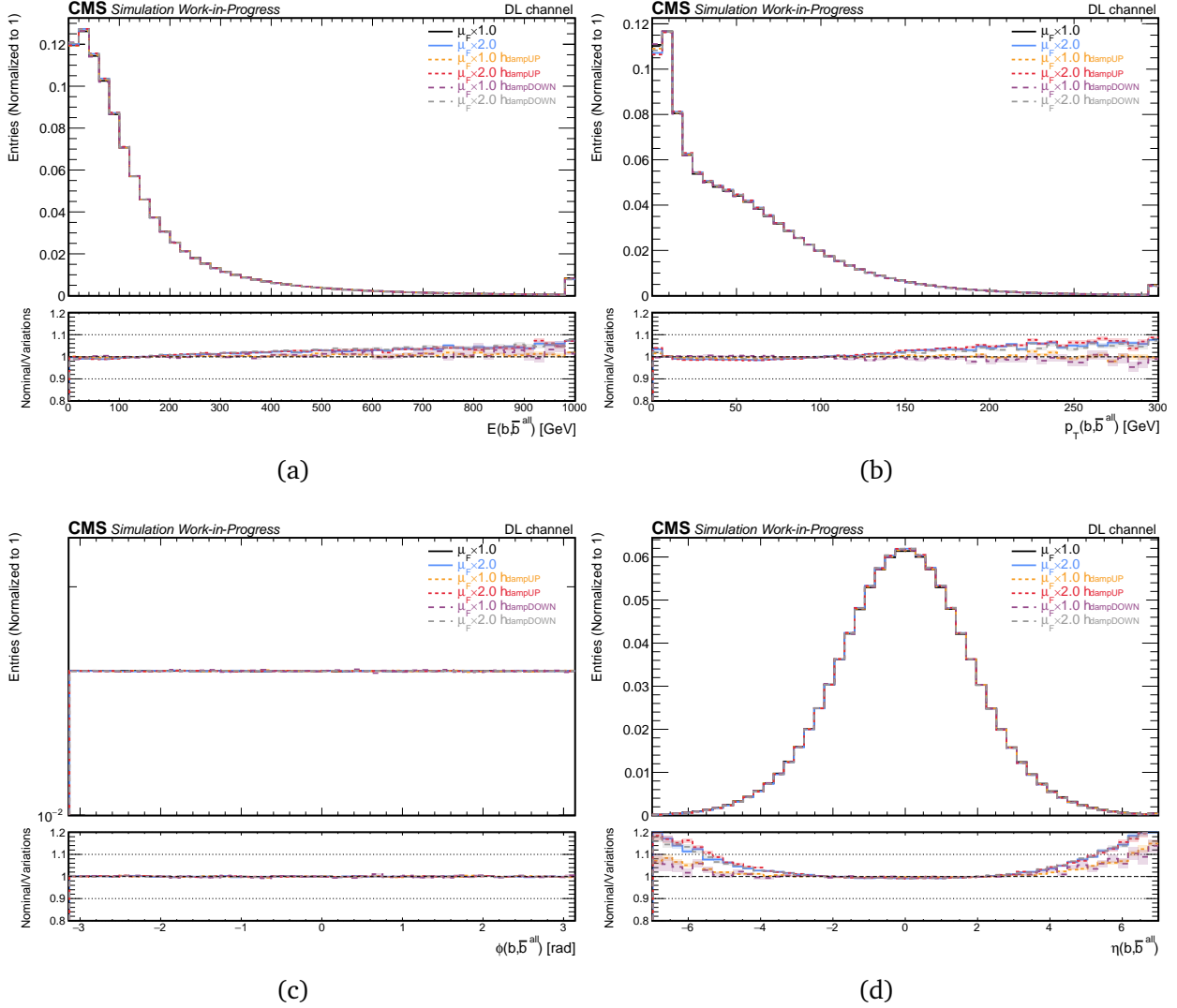


Figure B.3. Distributions of (a) energy, (b) transverse momentum, (c) azimuthal angle and (d) pseudorapidity of all the  $b/\bar{b}$  quarks for the six different settings used in the simulation. The lower panel shows the ratio of the nominal setting to the variations. The shaded bands represent statistical uncertainties. The last bins contain the overflow events.

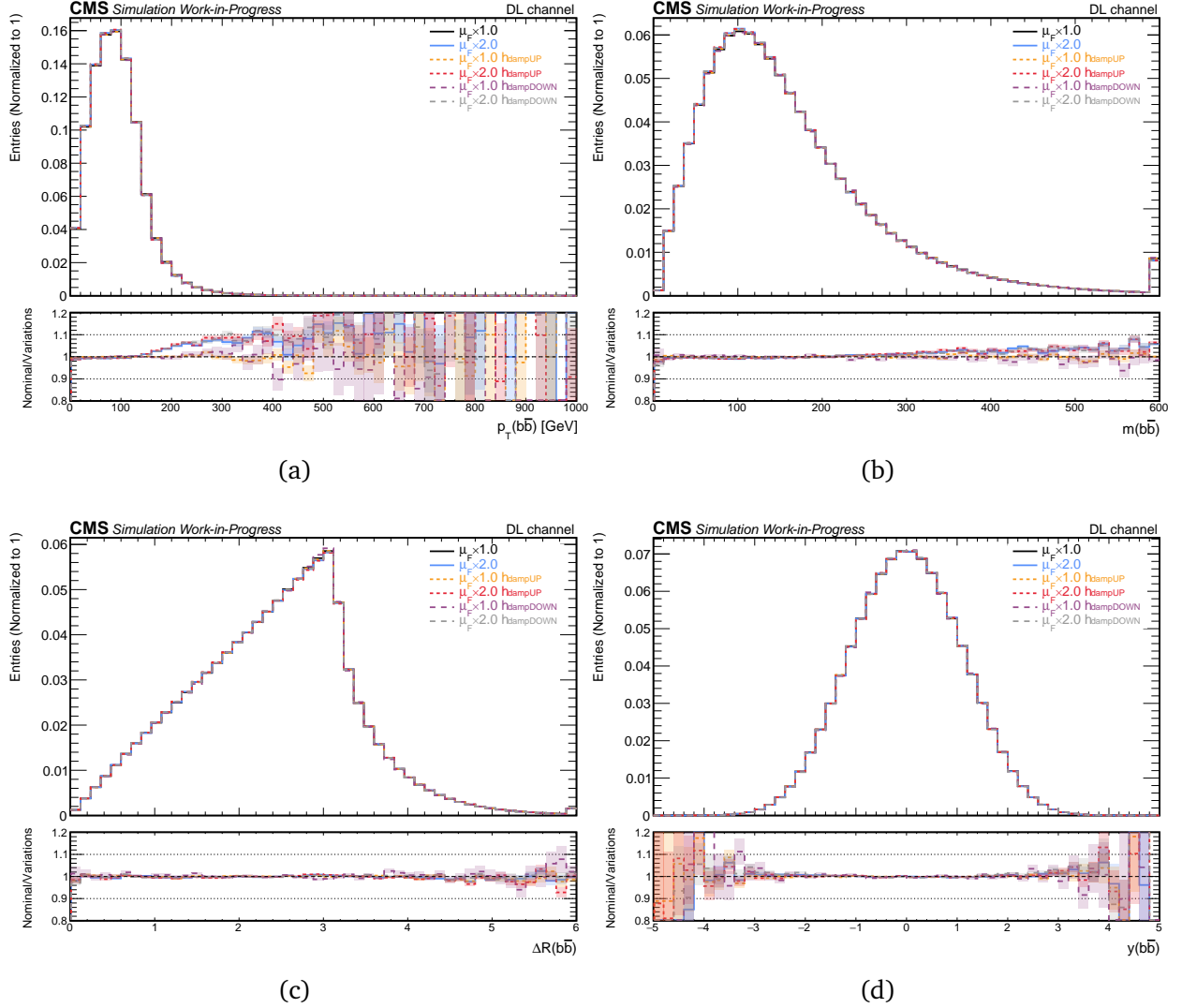


Figure B.4. Distributions of (a) transverse momentum, (b) invariant mass, (c) angular separation and (d) rapidity of the  $b\bar{b}$  system, related to top quarks, for the six different settings used in the simulation. The lower panel shows the ratio of the nominal setting to the variations. The shaded bands represent statistical uncertainties. The last bins contain the overflow events.

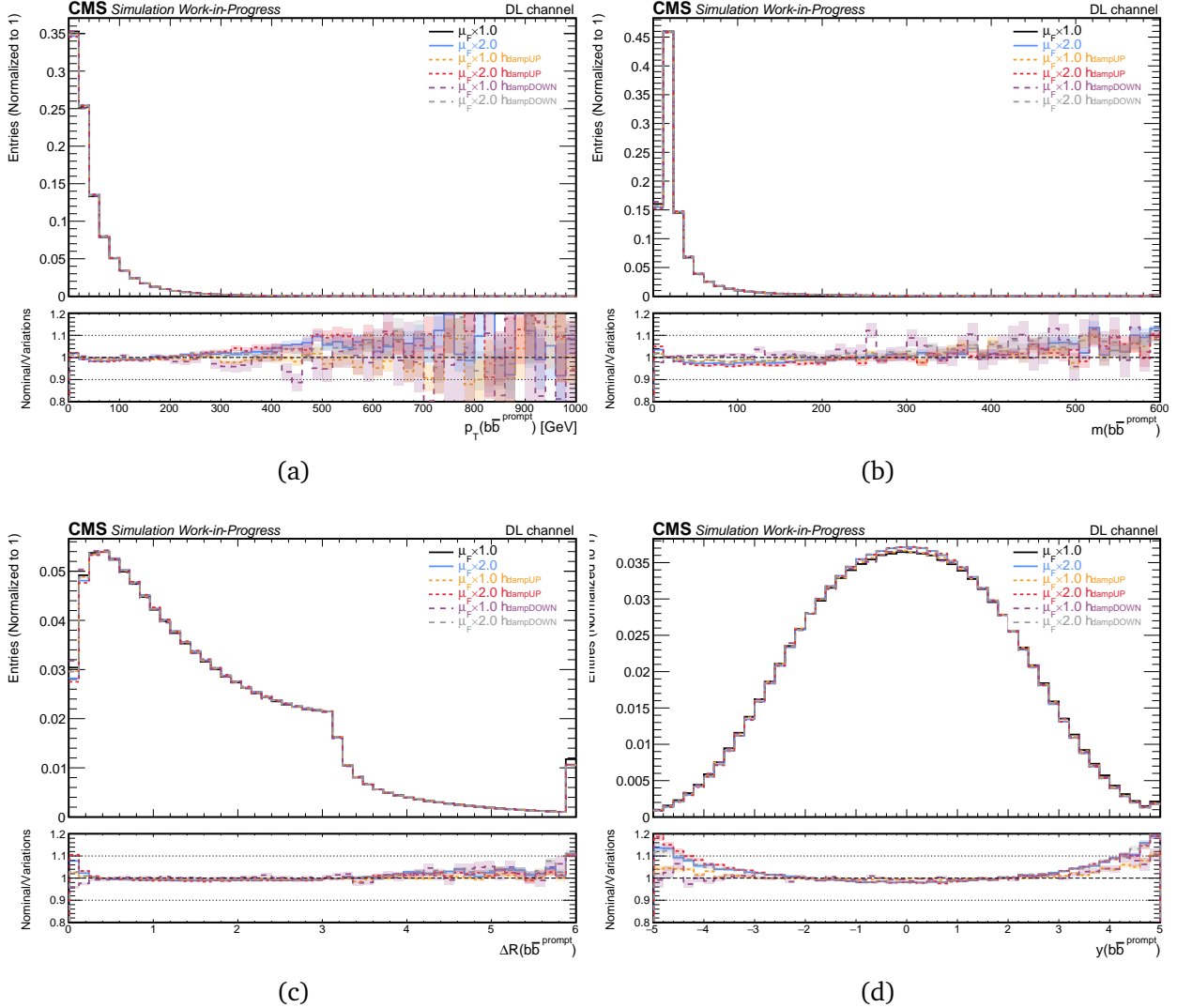


Figure B.5. Distributions of (a) transverse momentum, (b) invariant mass, (c) angular separation and (d) rapidity of the prompt  $b\bar{b}$  system for the six different settings used in the simulation. The lower panel shows the ratio of the nominal setting to the variations. The shaded bands represent statistical uncertainties. The last bins contain the overflow events.

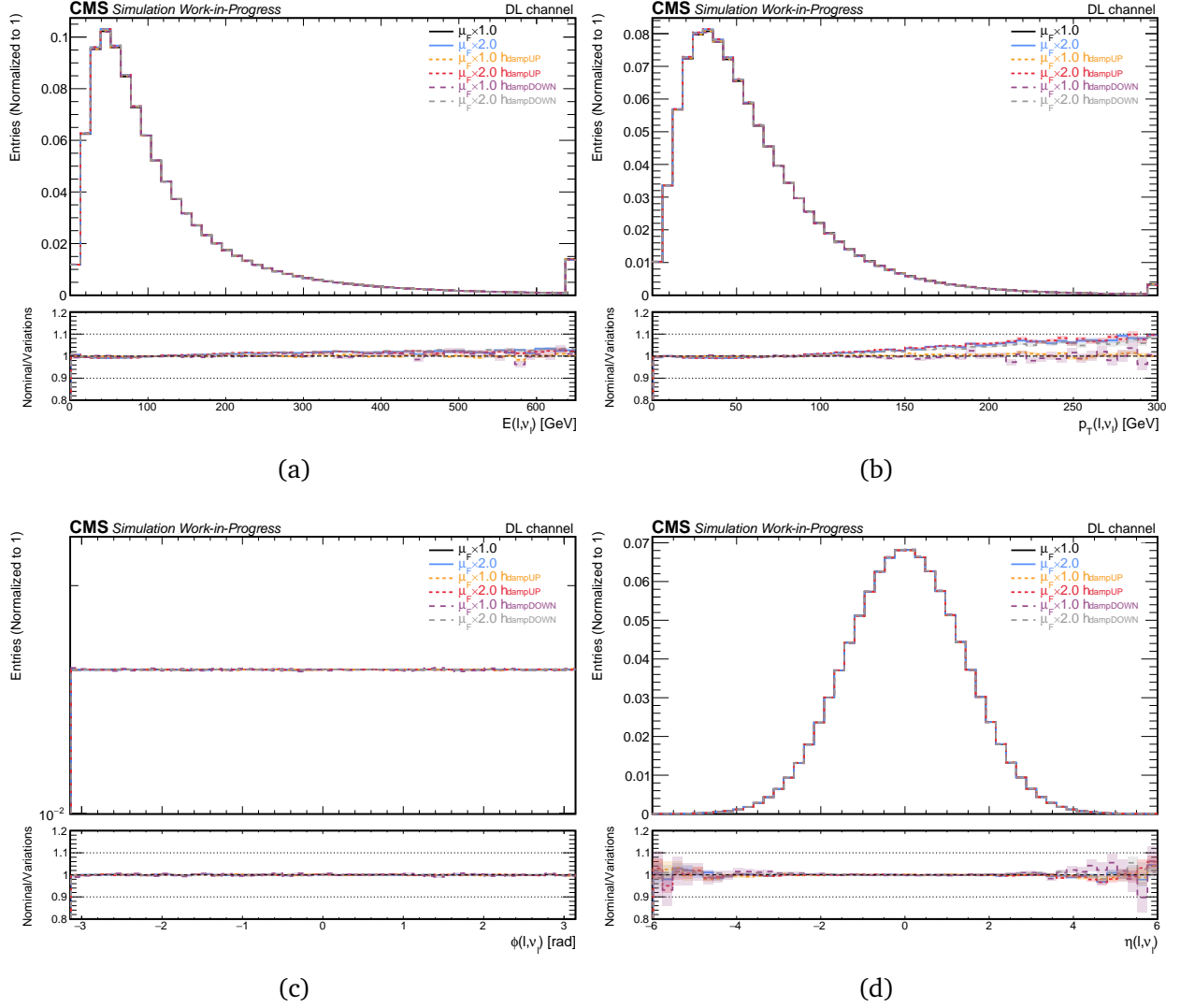


Figure B.6. Distributions of (a) energy, (b) transverse momentum, (c) azimuthal angle and (d) pseudorapidity of all the leptons (charged and neutral) for the six different settings used in the simulation. The lower panel shows the ratio of the nominal setting to the variations. The shaded bands represent statistical uncertainties. The last bins contain the overflow events.

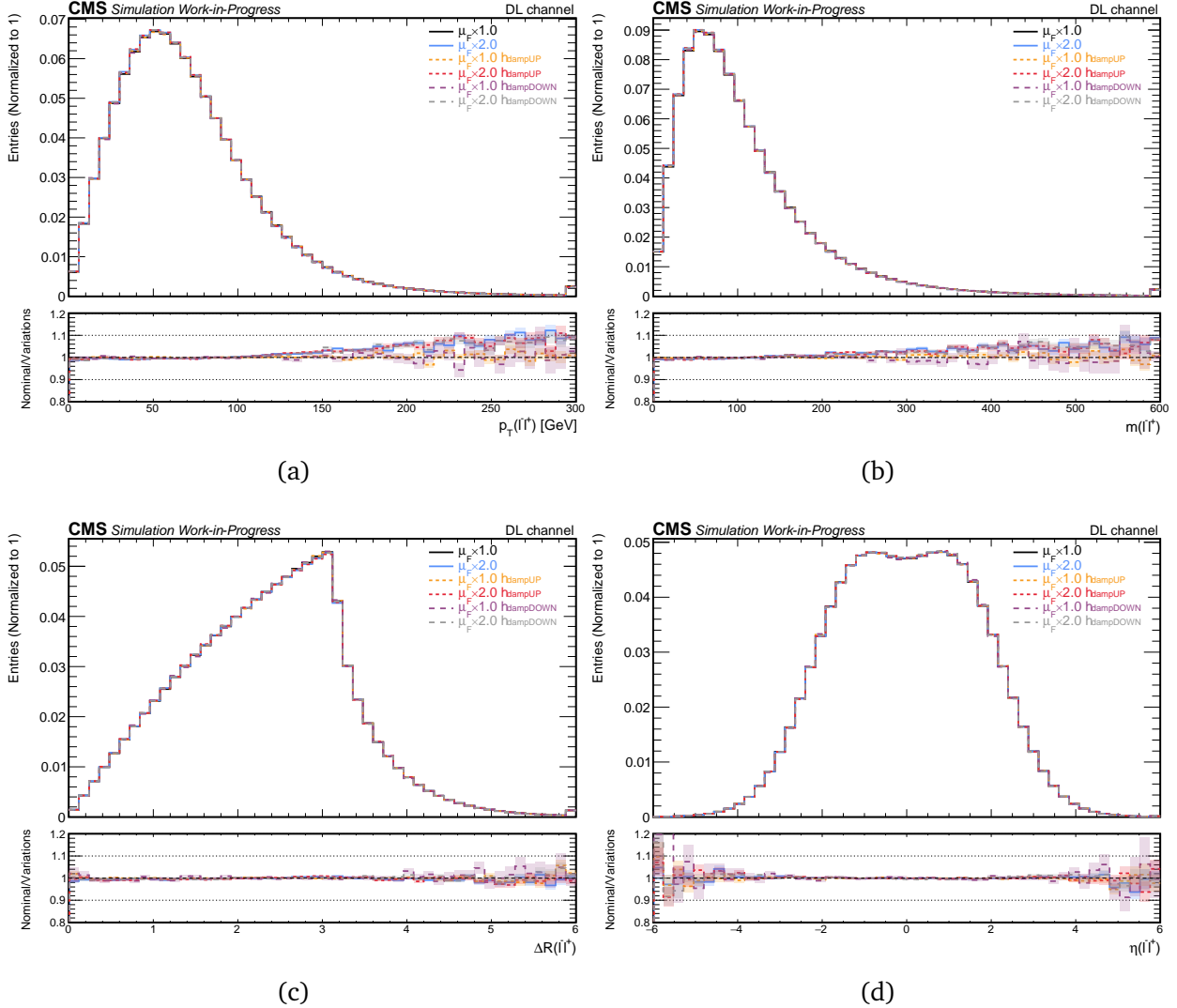


Figure B.7. Distributions of (a) transverse momentum, (b) invariant mass, (c) angular separation and (d) rapidity of the  $\ell^- \ell^+$  system for the six different settings used in the simulation. The lower panel shows the ratio of the nominal setting to the variations. The shaded bands represent statistical uncertainties. The last bins contain the overflow events.

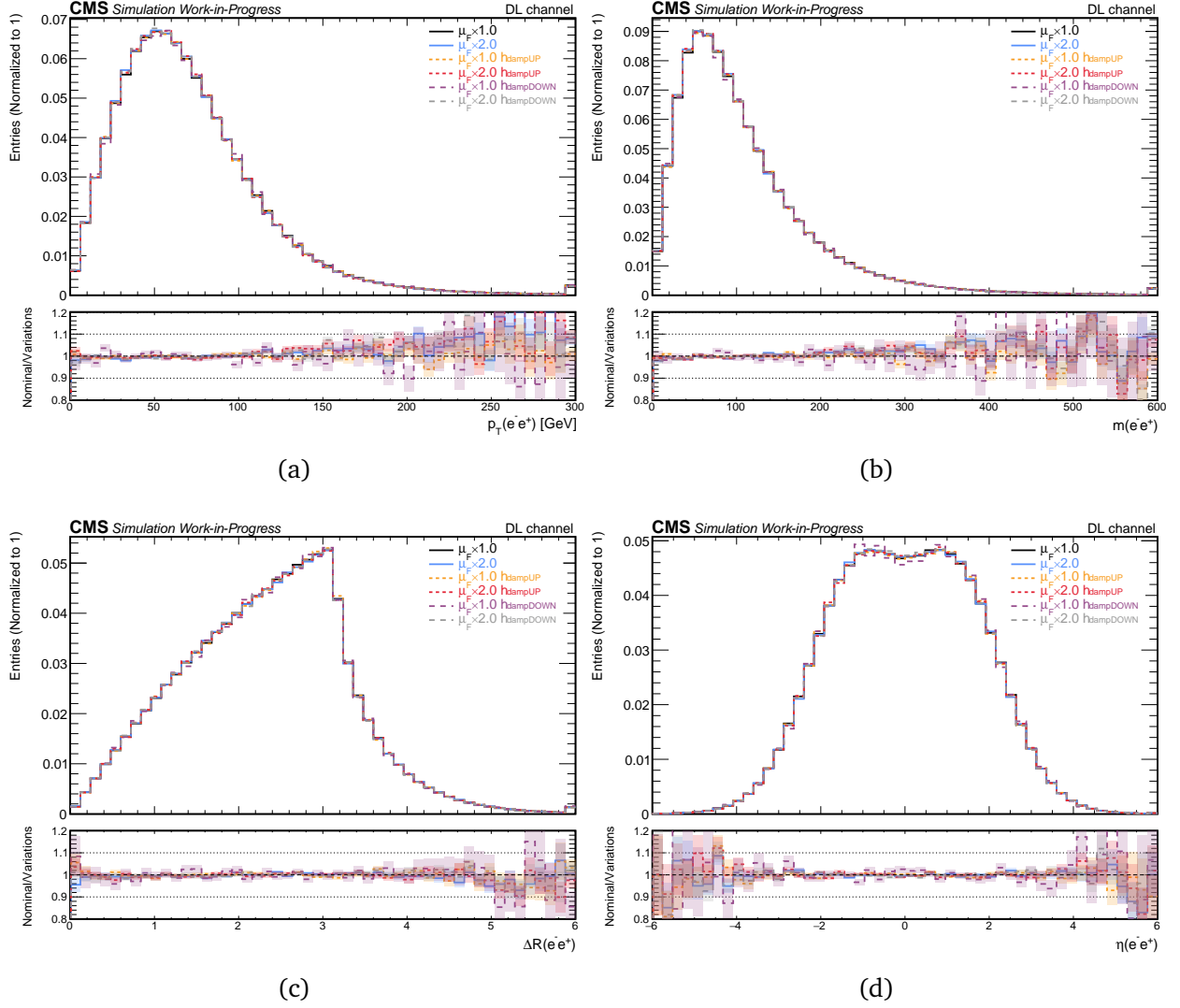


Figure B.8. Distributions of (a) transverse momentum, (b) invariant mass, (c) angular separation and (d) rapidity of the  $e^-e^+$  system for the six different settings used in the simulation. The lower panel shows the ratio of the nominal setting to the variations. The shaded bands represent statistical uncertainties. The last bins contain the overflow events.

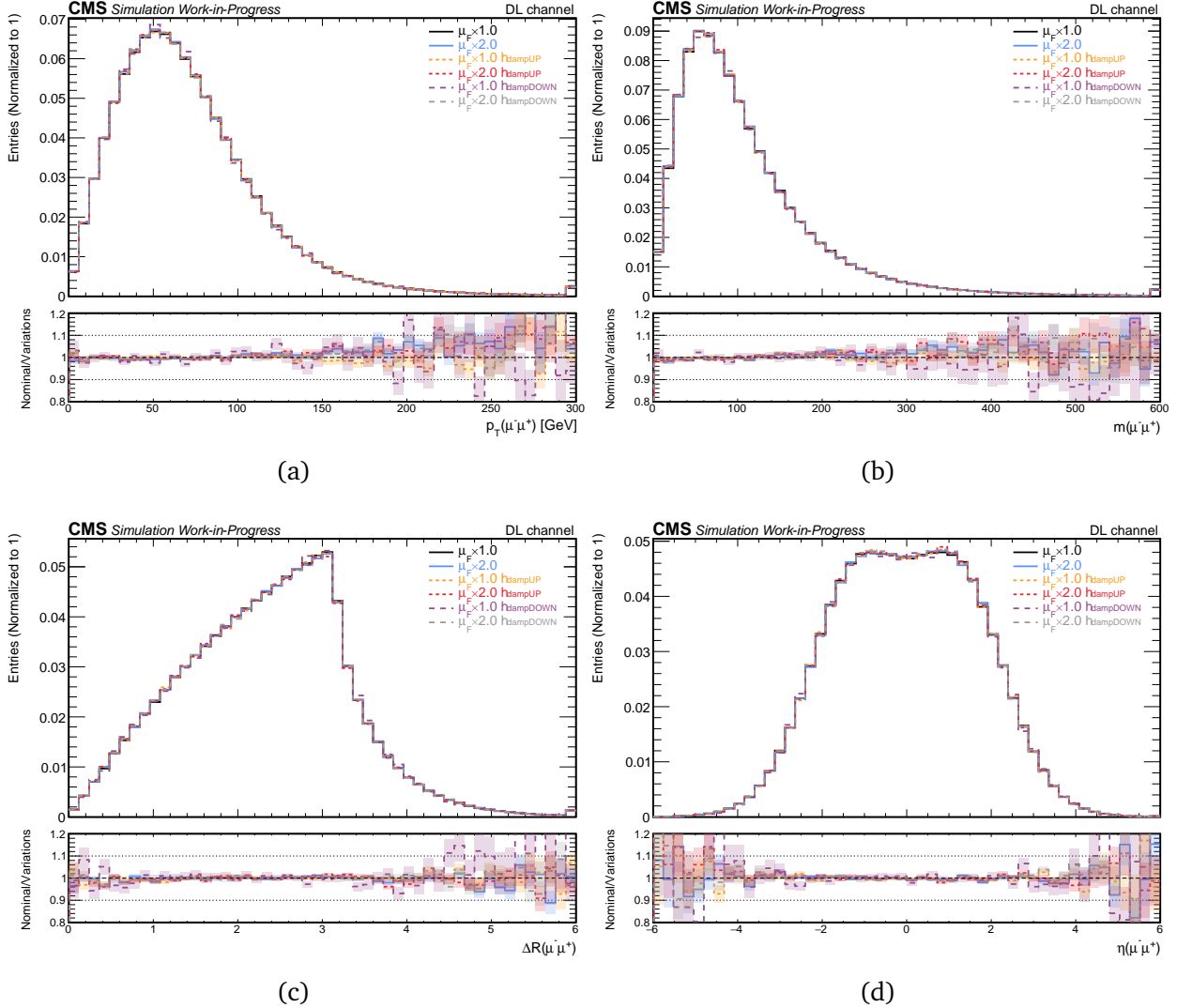


Figure B.9. Distributions of (a) transverse momentum, (b) invariant mass, (c) angular separation and (d) rapidity of the  $\mu^-\mu^+$  system for the six different settings used in the simulation. The lower panel shows the ratio of the nominal setting to the variations. The shaded bands represent statistical uncertainties. The last bins contain the overflow events.

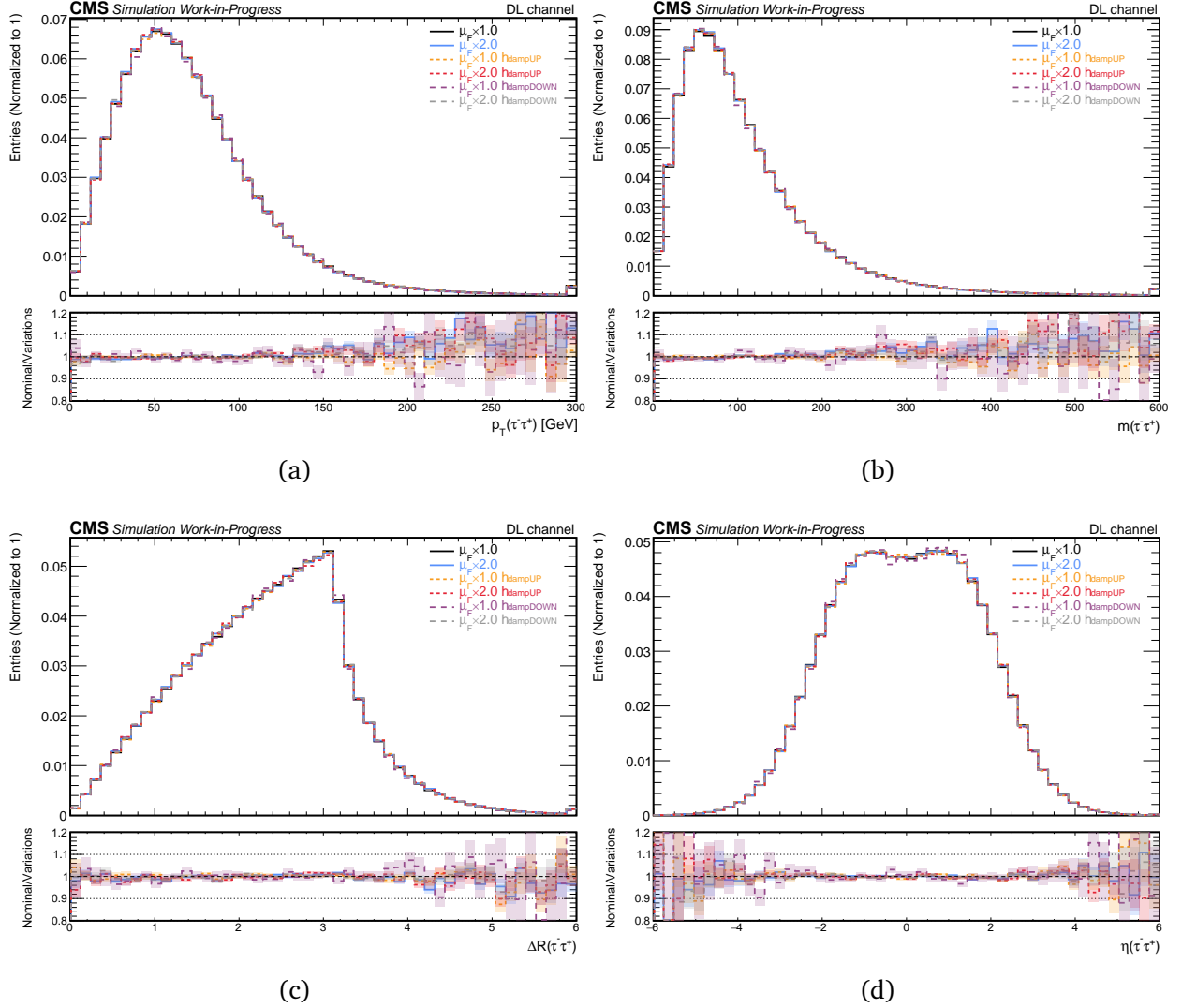


Figure B.10. Distributions of (a) transverse momentum, (b) invariant mass, (c) angular separation and (d) rapidity of the  $\tau^-\tau^+$  system for the six different settings used in the simulation. The lower panel shows the ratio of the nominal setting to the variations. The shaded bands represent statistical uncertainties. The last bins contain the overflow events.

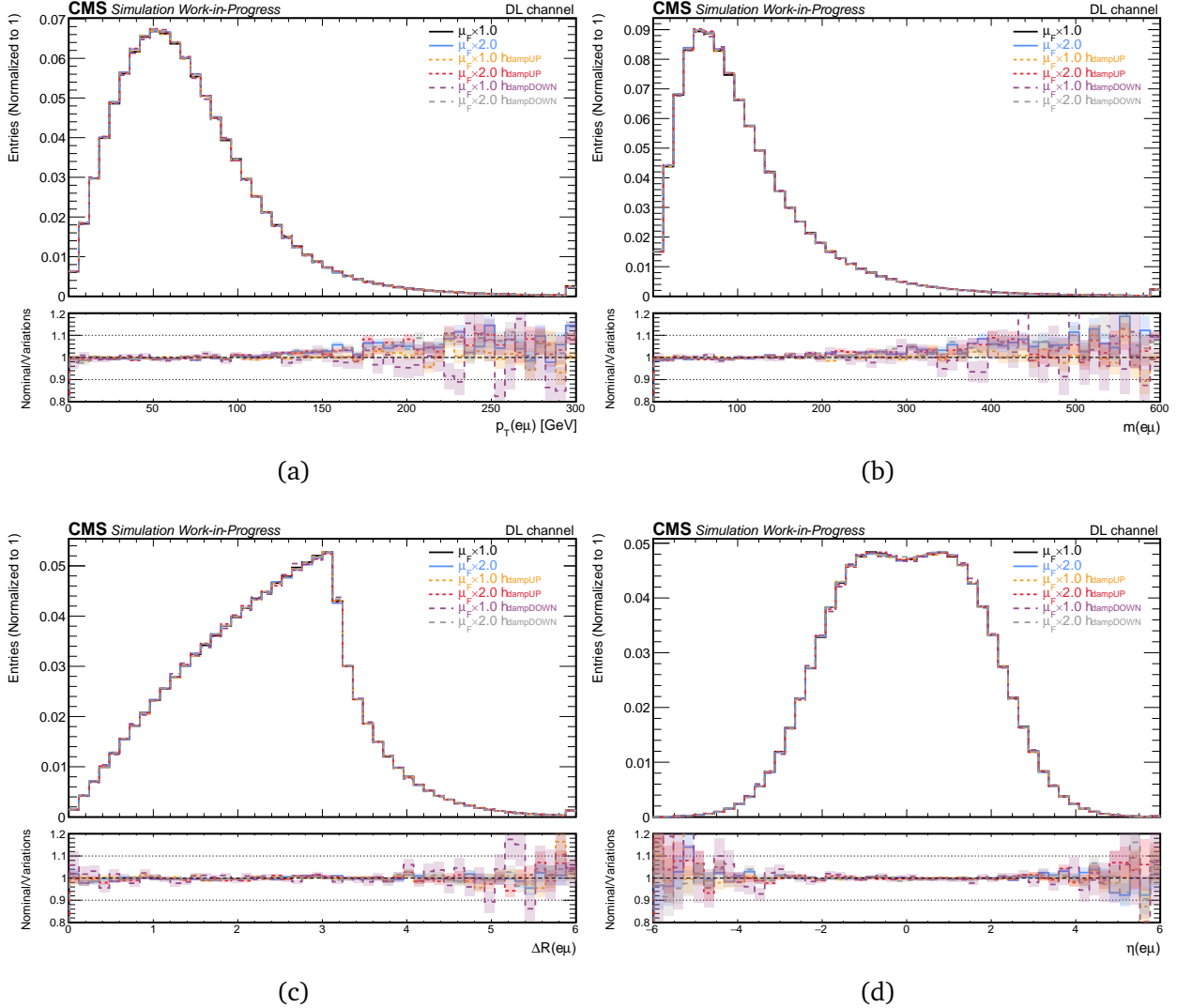


Figure B.11. Distributions of (a) transverse momentum, (b) invariant mass, (c) angular separation and (d) rapidity of the  $e\mu$  system for the six different settings used in the simulation. The lower panel shows the ratio of the nominal setting to the variations. The shaded bands represent statistical uncertainties. The last bins contain the overflow events.

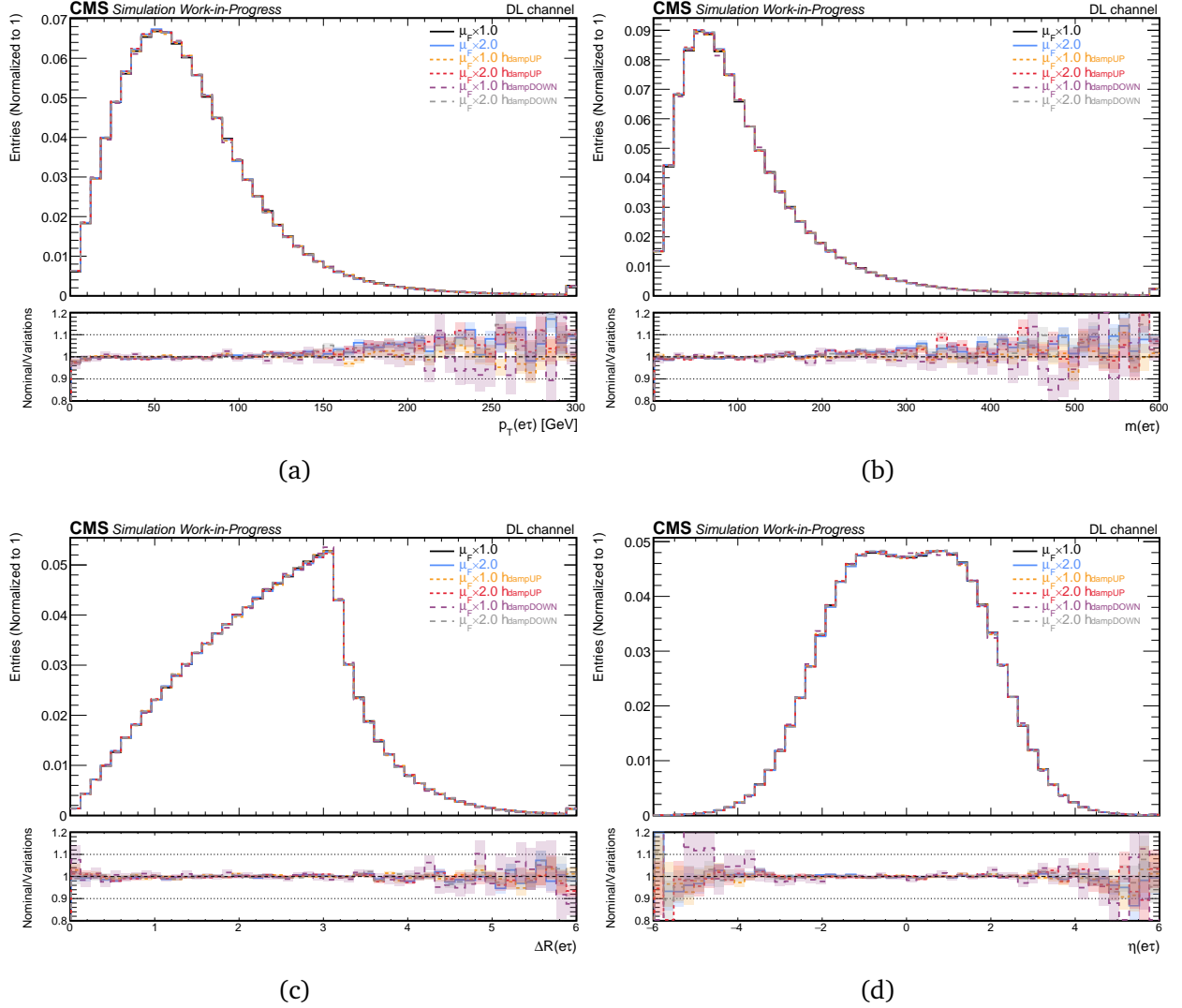


Figure B.12. Distributions of (a) transverse momentum, (b) invariant mass, (c) angular separation and (d) rapidity of the  $e\tau$  system for the six different settings used in the simulation. The lower panel shows the ratio of the nominal setting to the variations. The shaded bands represent statistical uncertainties. The last bins contain the overflow events.

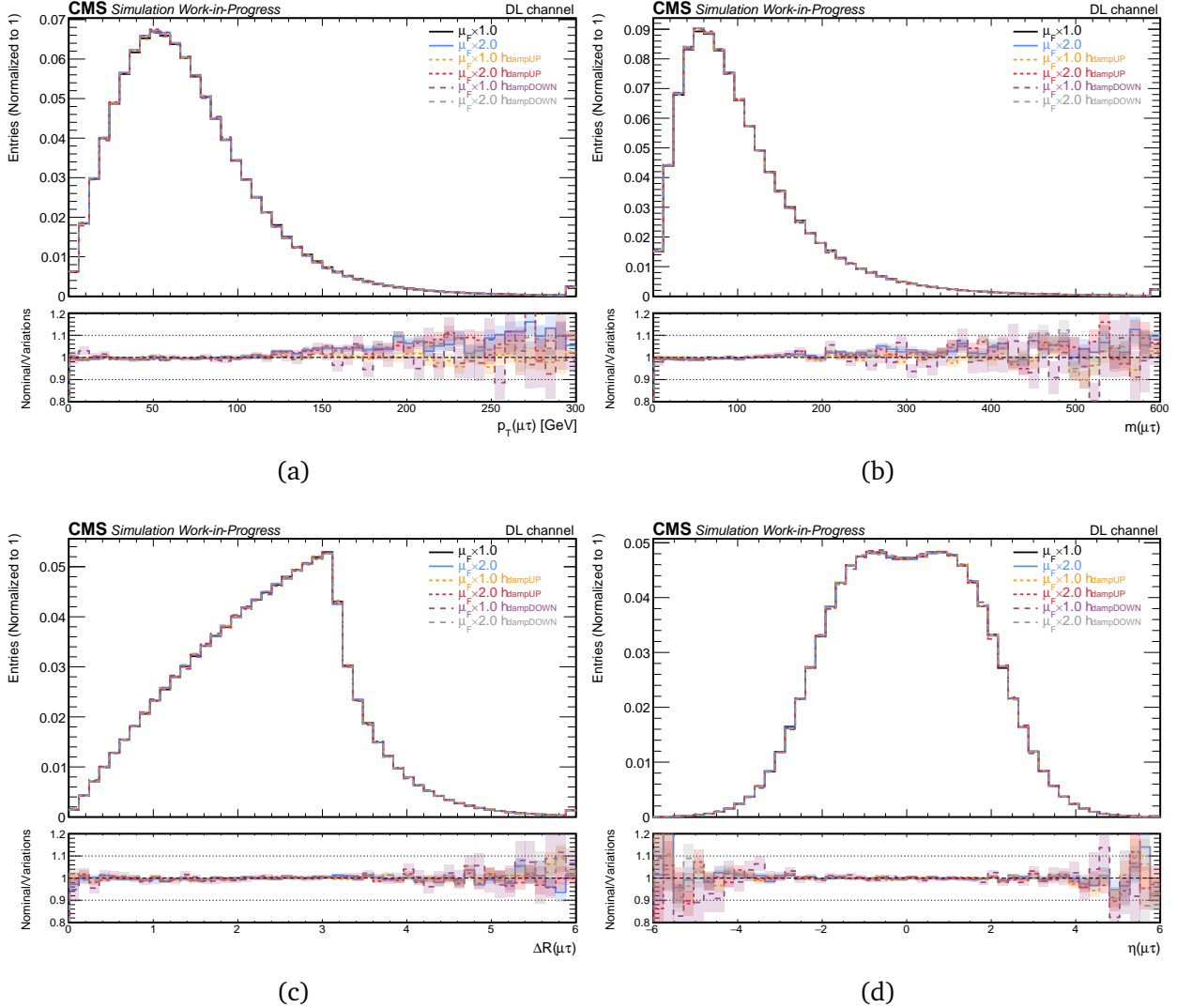


Figure B.13. Distributions of (a) transverse momentum, (b) invariant mass, (c) angular separation and (d) rapidity of the  $\mu\tau$  system for the six different settings used in the simulation. The lower panel shows the ratio of the nominal setting to the variations. The shaded bands represent statistical uncertainties. The last bins contain the overflow events.

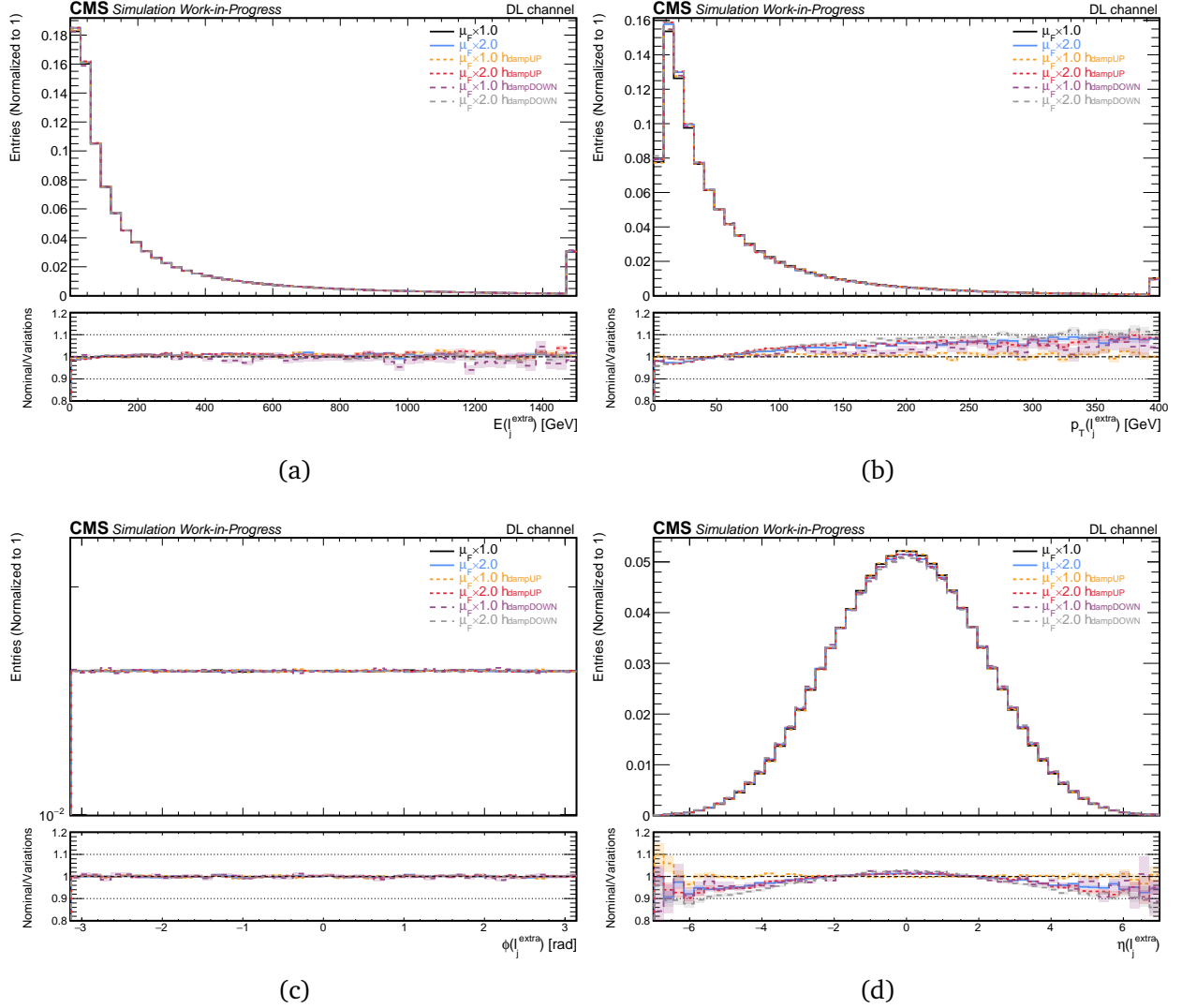


Figure B.14. Distributions of (a) energy, (b) transverse momentum, (c) azimuthal angle and (d) pseudorapidity of the extra light jet for the six different settings used in the simulation. The lower panel shows the ratio of the nominal setting to the variations. The shaded bands represent statistical uncertainties. The last bins contain the overflow events.

## B.2 SL channel

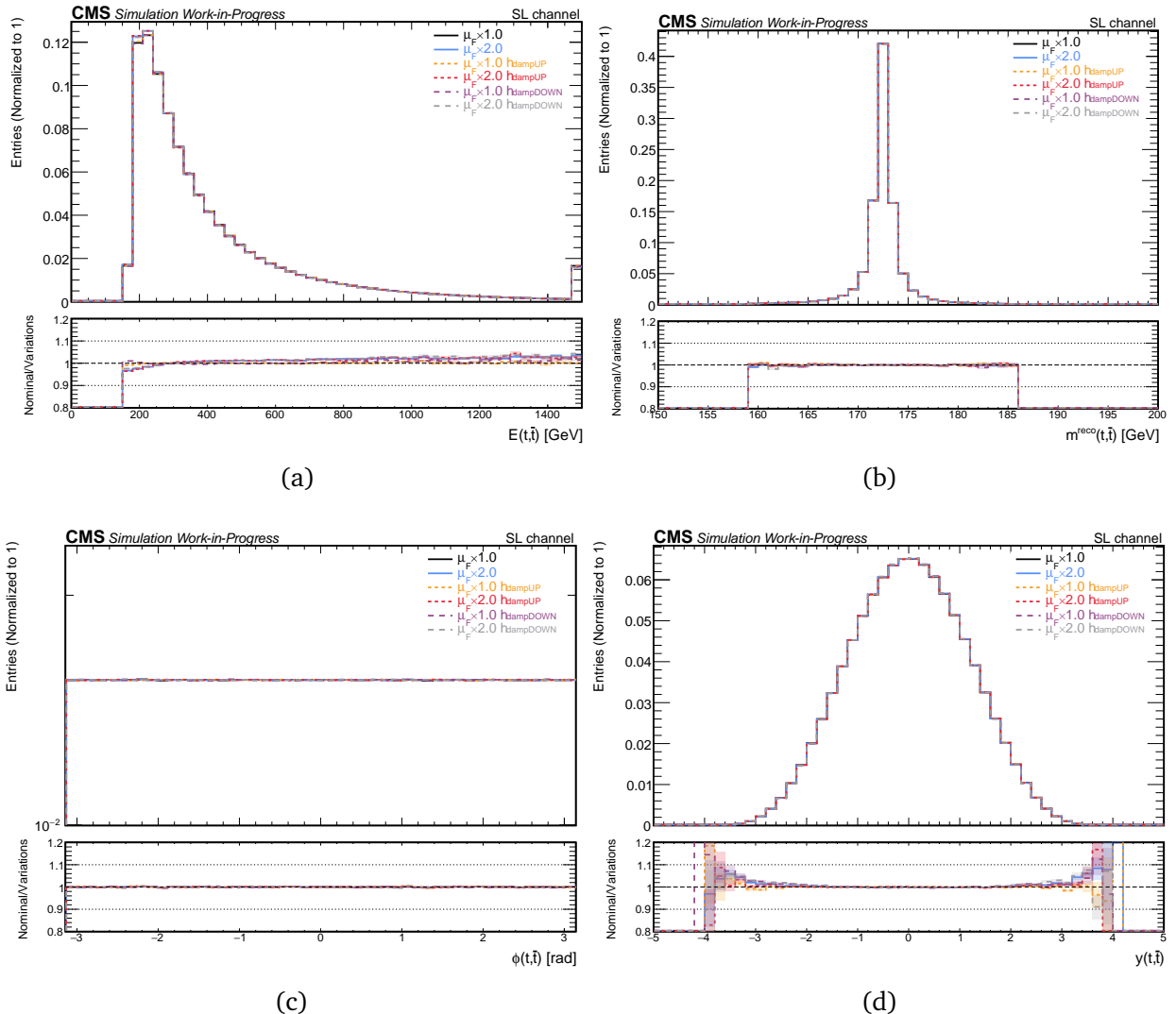


Figure B.15. Distributions of (a) energy, (b) reconstructed mass, (c) azimuthal angle and (d) rapidity of the  $t/\bar{t}$  quarks for the six different settings used in the simulation. The lower panel shows the ratio of the nominal setting to the variations. The shaded bands represent statistical uncertainties. The last bins contain the overflow events.

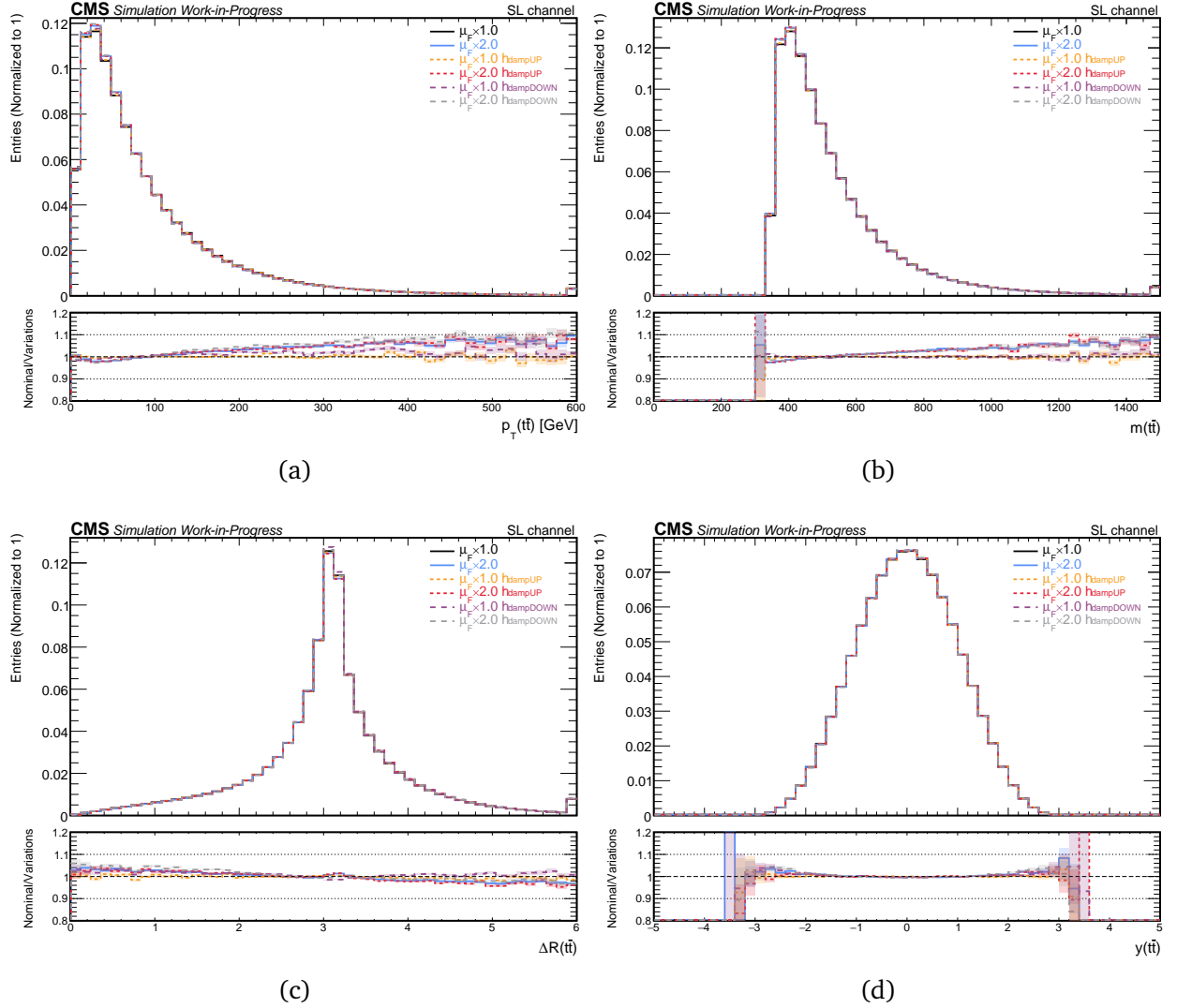


Figure B.16. Distributions of (a) transverse momentum, (b) invariant mass, (c) angular separation and (d) rapidity of the  $t\bar{t}$  system for the six different settings used in the simulation. The lower panel shows the ratio of the nominal setting to the variations. The shaded bands represent statistical uncertainties. The last bins contain the overflow events.

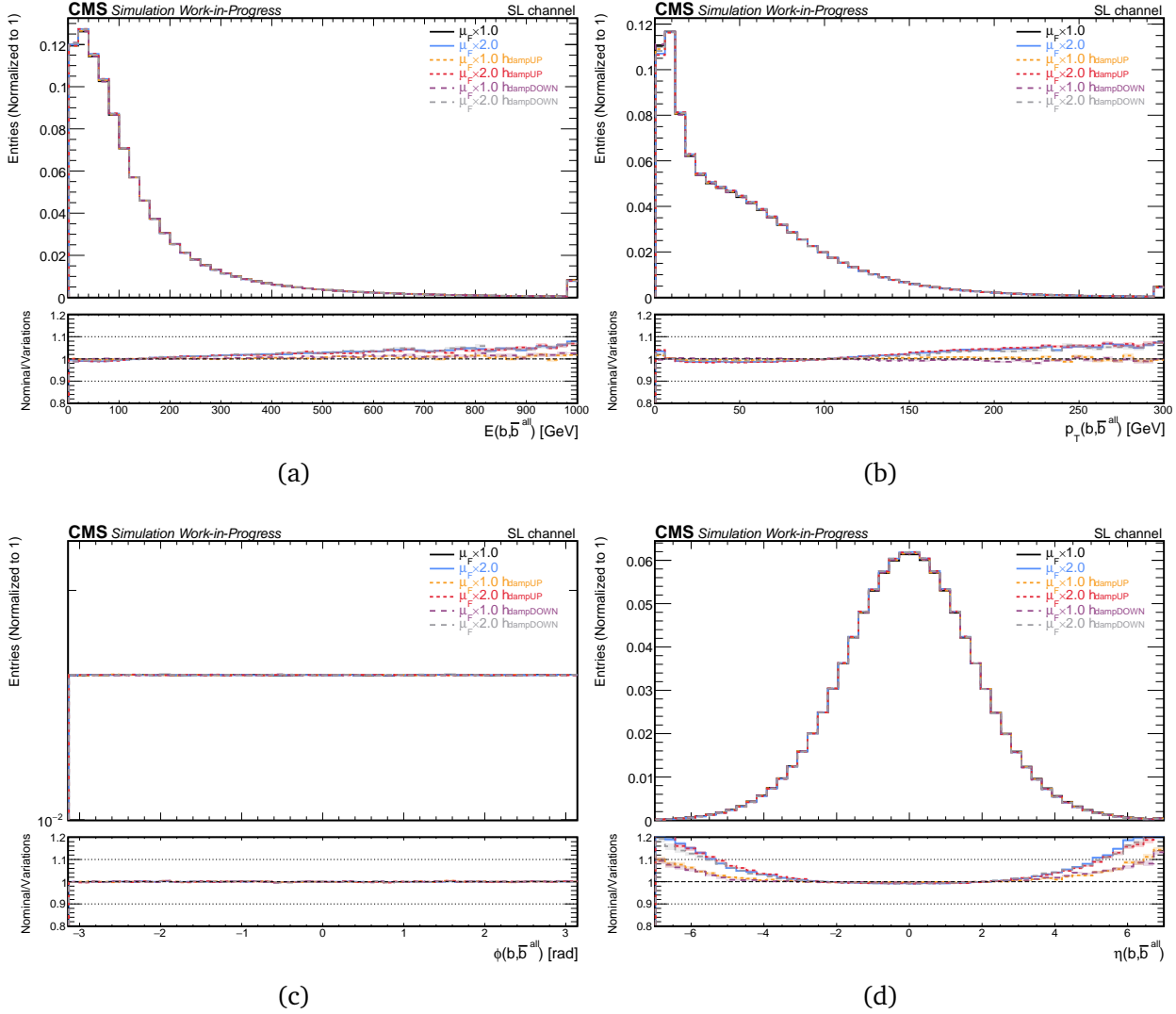


Figure B.17. Distributions of (a) energy, (b) transverse momentum, (c) azimuthal angle and (d) pseudorapidity of all the  $b/\bar{b}$  quarks for the six different settings used in the simulation. The lower panel shows the ratio of the nominal setting to the variations. The shaded bands represent statistical uncertainties. The last bins contain the overflow events.

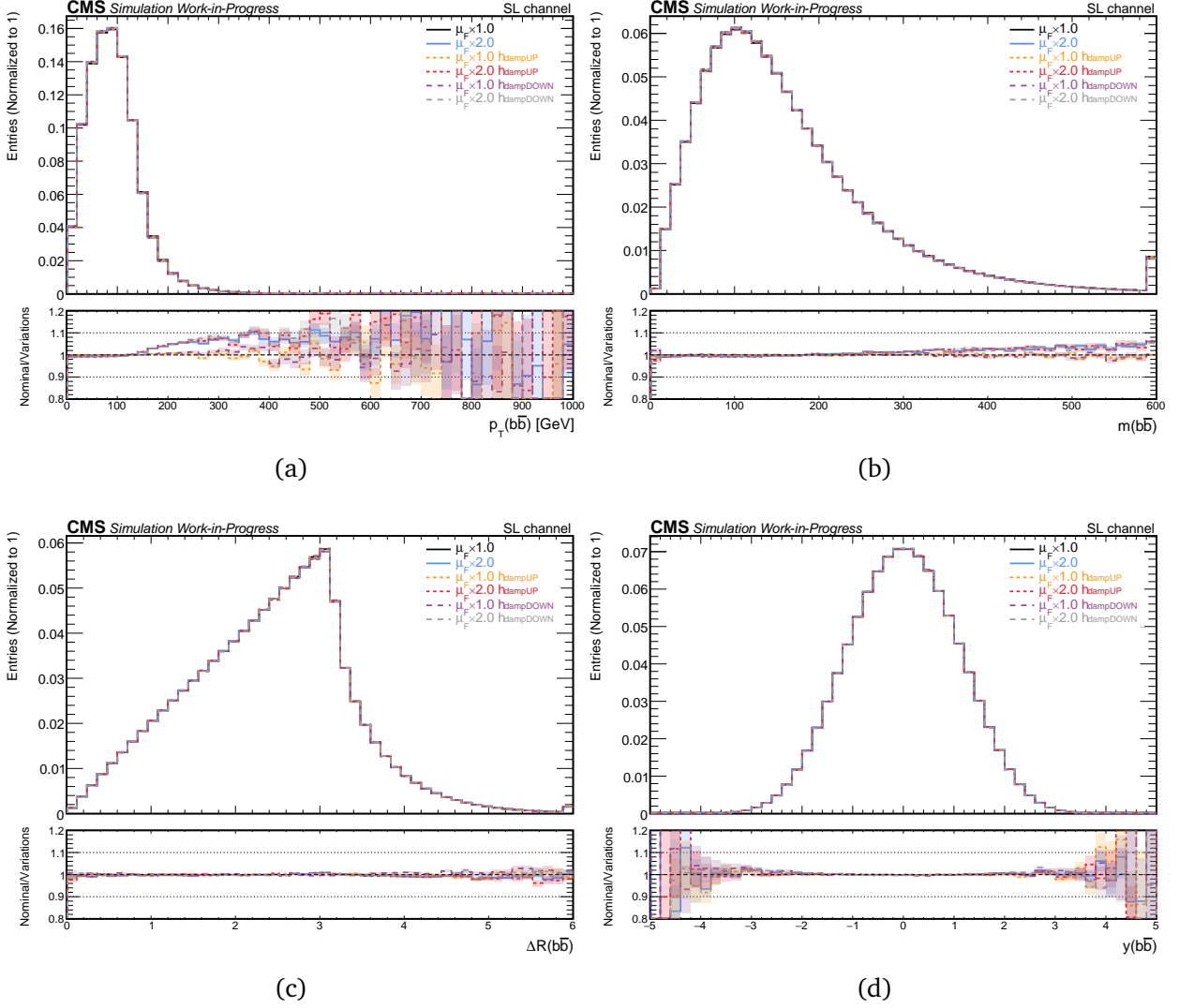


Figure B.18. Distributions of (a) transverse momentum, (b) invariant mass, (c) angular separation and (d) rapidity of the  $b\bar{b}$  system, related to top quarks, for the six different settings used in the simulation. The lower panel shows the ratio of the nominal setting to the variations. The shaded bands represent statistical uncertainties. The last bins contain the overflow events.

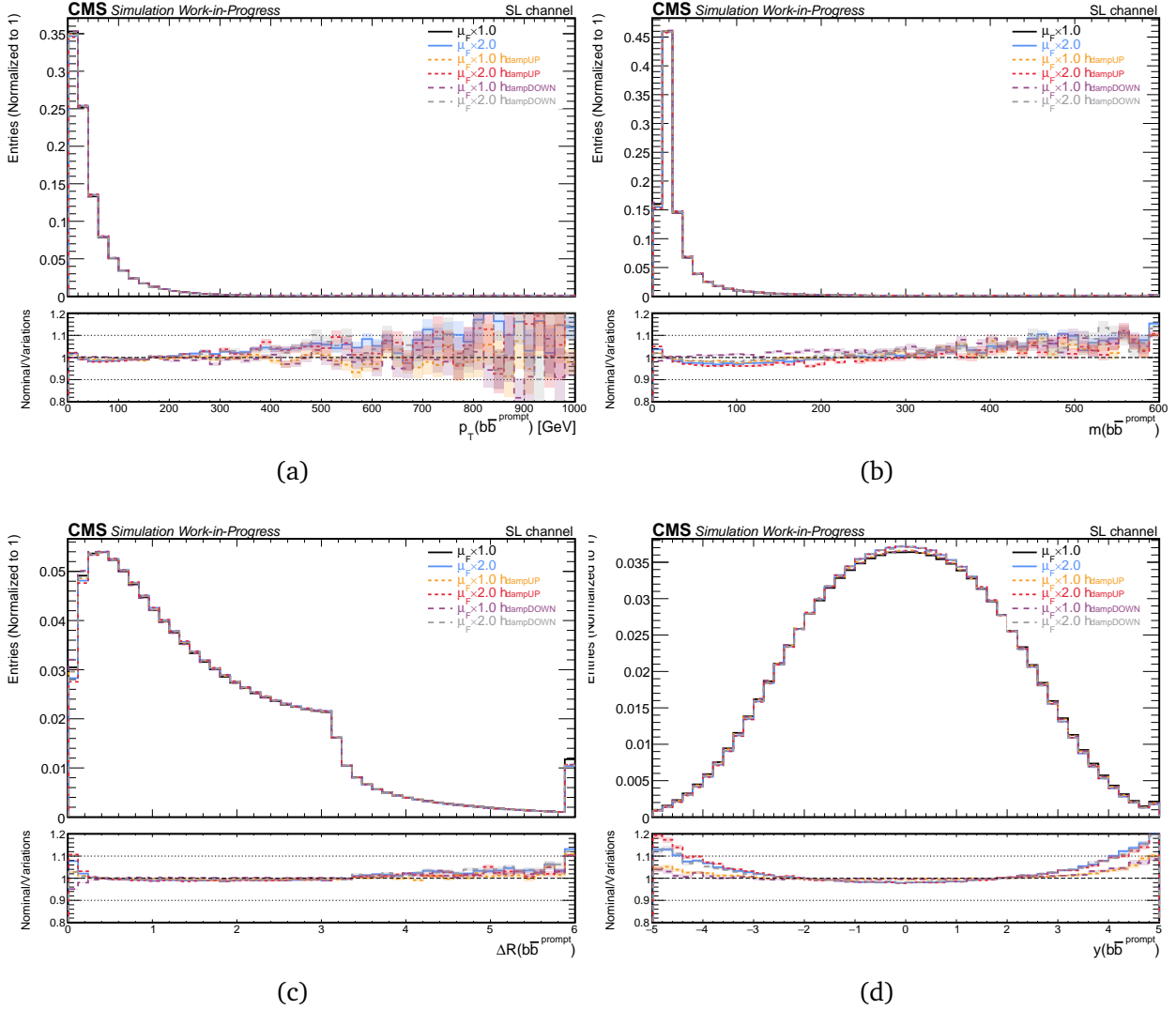


Figure B.19. Distributions of (a) transverse momentum, (b) invariant mass, (c) angular separation and (d) rapidity of the prompt  $b\bar{b}$  system for the six different settings used in the simulation. The lower panel shows the ratio of the nominal setting to the variations. The shaded bands represent statistical uncertainties. The last bins contain the overflow events.

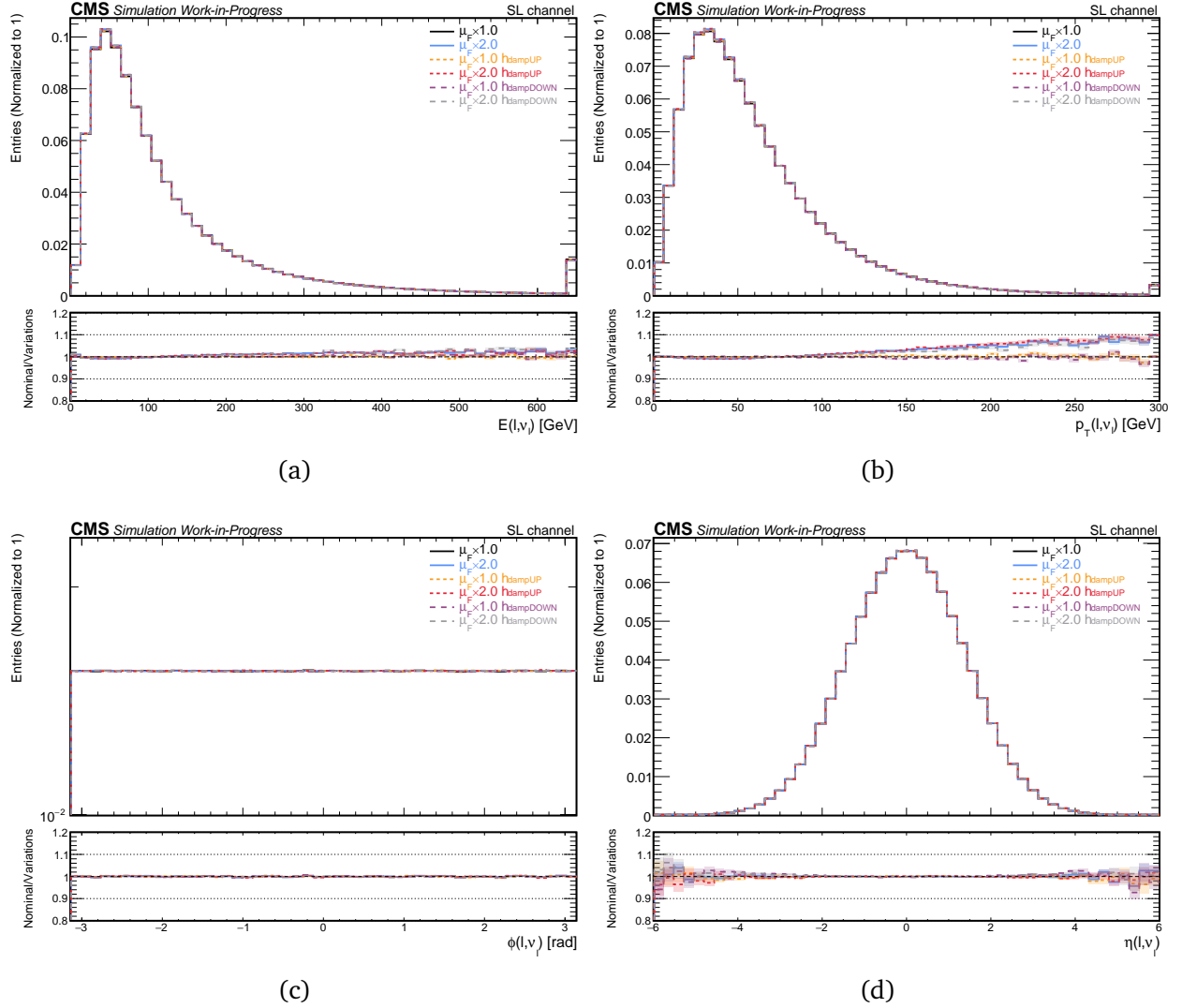


Figure B.20. Distributions of (a) energy, (b) transverse momentum, (c) azimuthal angle and (d) pseudorapidity of all the leptons (charged and neutral) for the six different settings used in the simulation. The lower panel shows the ratio of the nominal setting to the variations. The shaded bands represent statistical uncertainties. The last bins contain the overflow events.

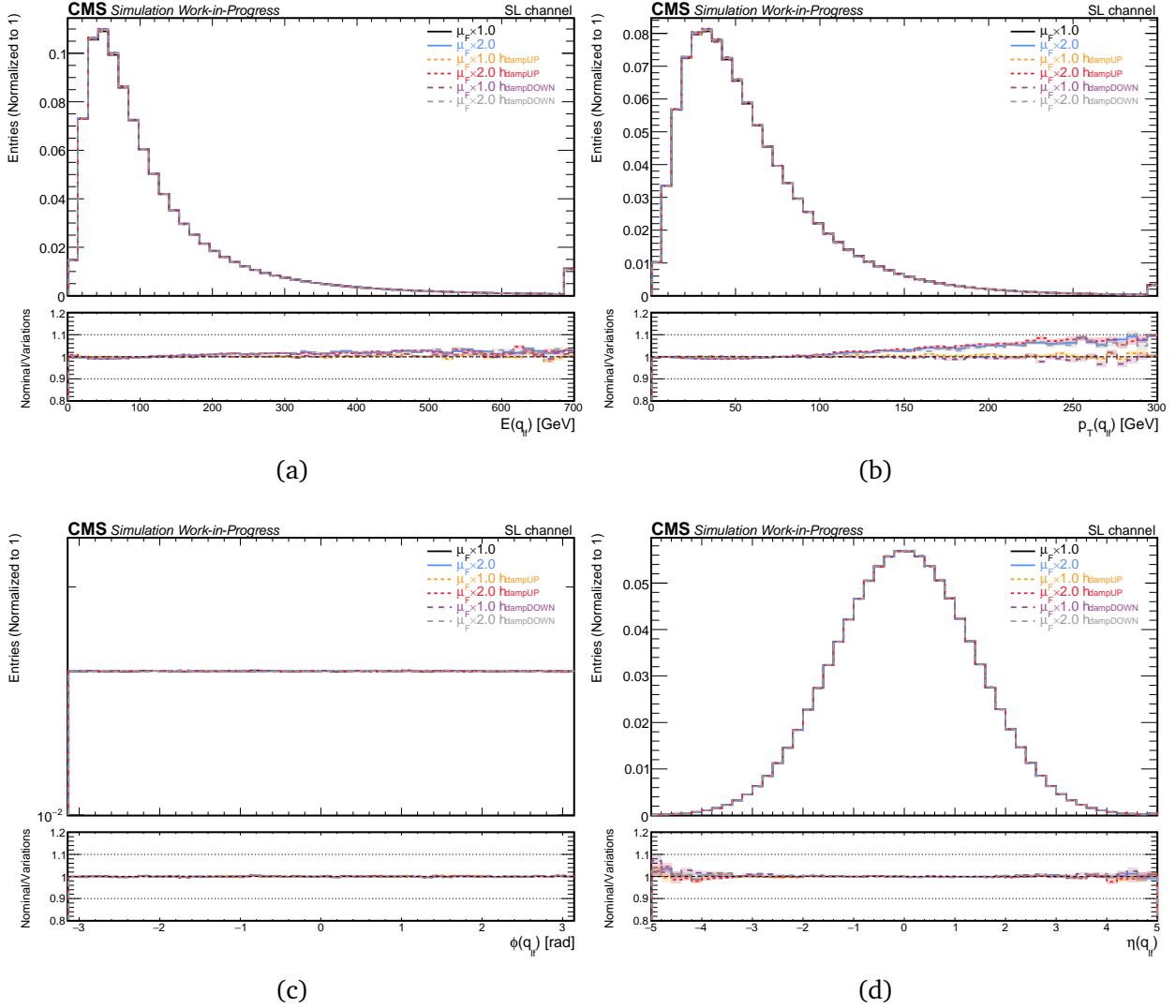


Figure B.21. Distributions of (a) energy, (b) transverse momentum, (c) azimuthal angle and (d) pseudorapidity of the light flavor quarks, related to W bosons, for the six different settings used in the simulation. The lower panel shows the ratio of the nominal setting to the variations. The shaded bands represent statistical uncertainties. The last bins contain the overflow events.

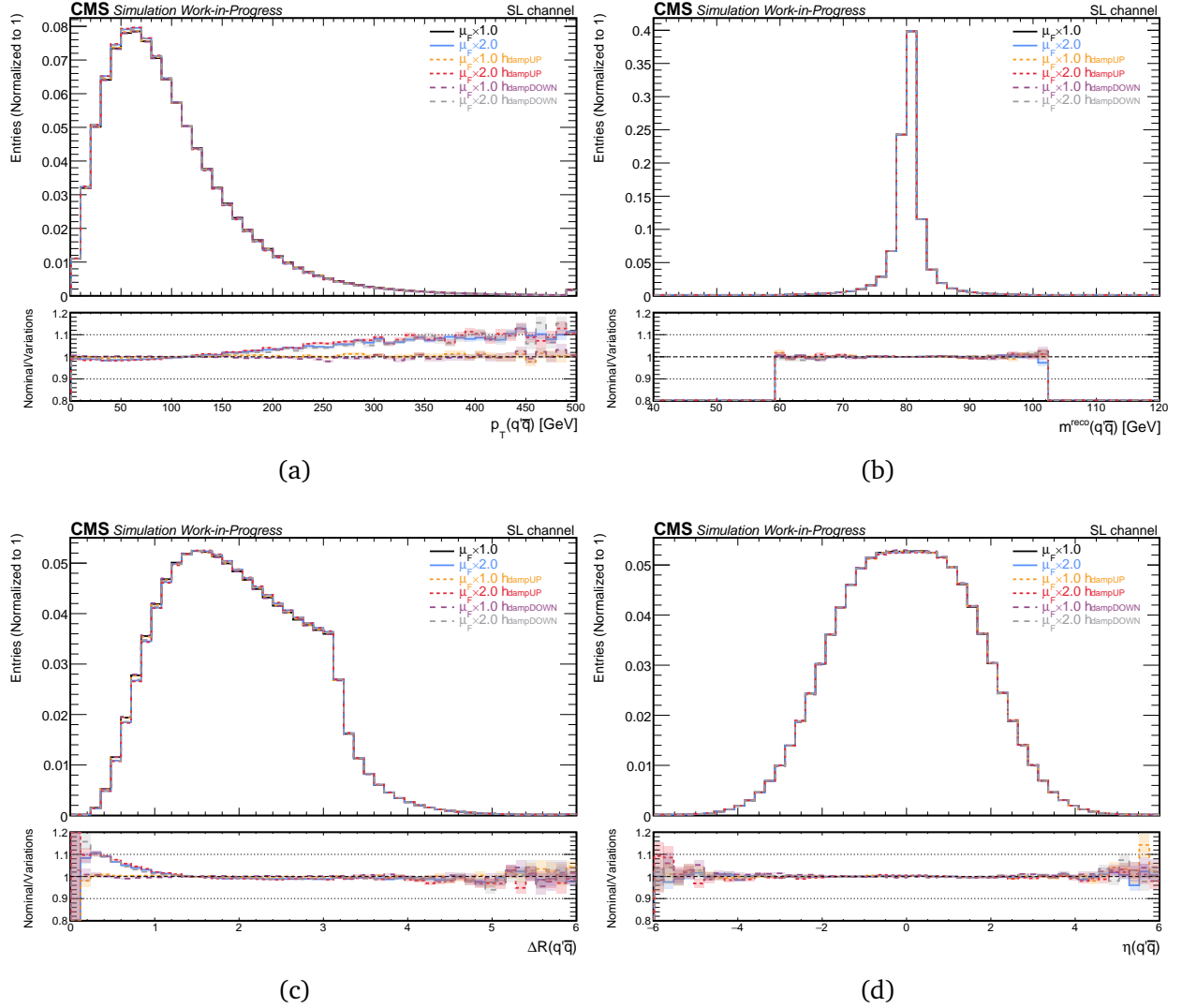


Figure B.22. Distributions of (a) transverse momentum, (b) invariant mass, (c) angular separation and (d) rapidity of the  $q\bar{q}$  system for the six different settings used in the simulation. The lower panel shows the ratio of the nominal setting to the variations. The shaded bands represent statistical uncertainties. The last bins contain the overflow events.

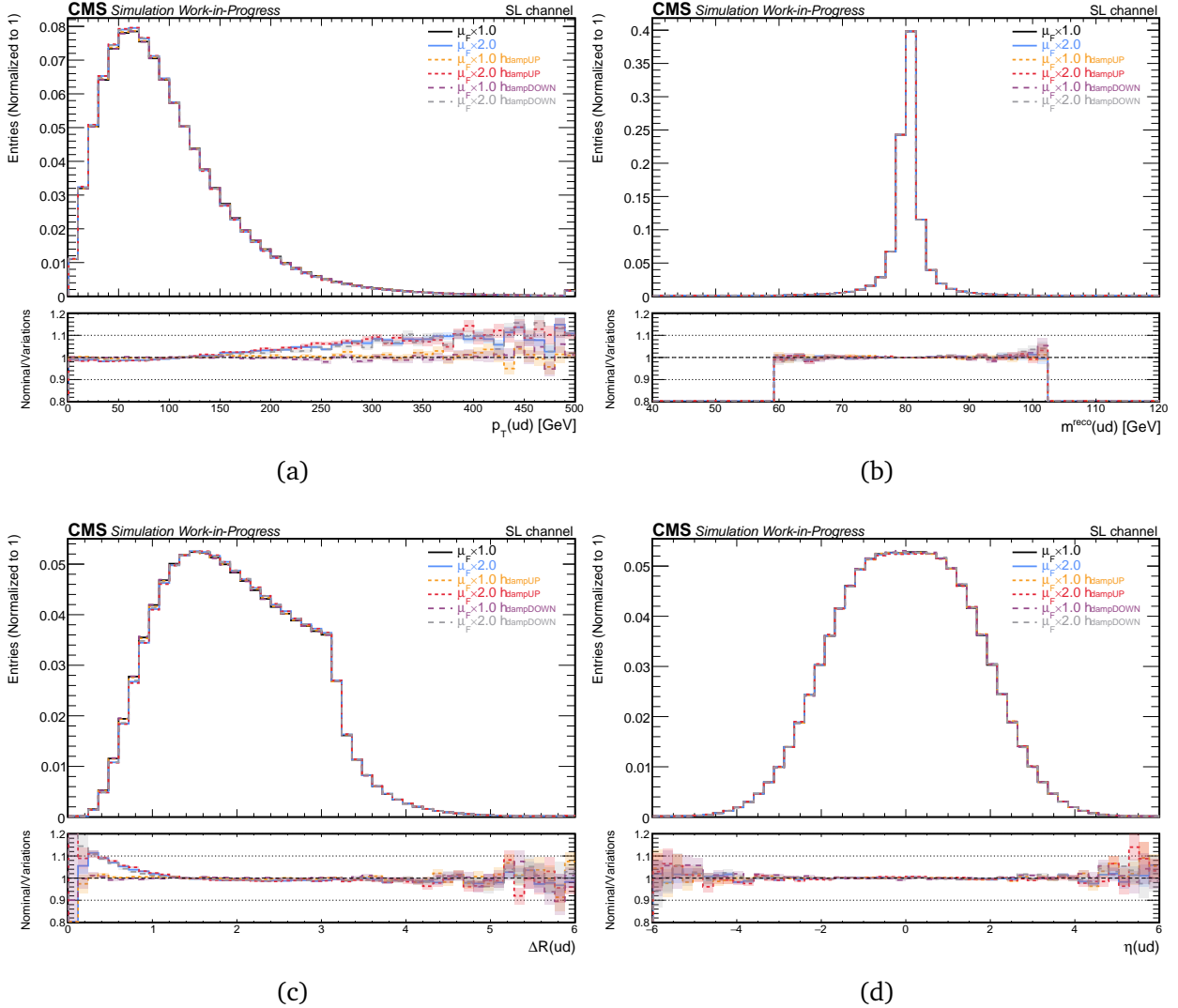


Figure B.23. Distributions of (a) transverse momentum, (b) invariant mass, (c) angular separation and (d) rapidity of the ud system for the six different settings used in the simulation. The lower panel shows the ratio of the nominal setting to the variations. The shaded bands represent statistical uncertainties. The last bins contain the overflow events.

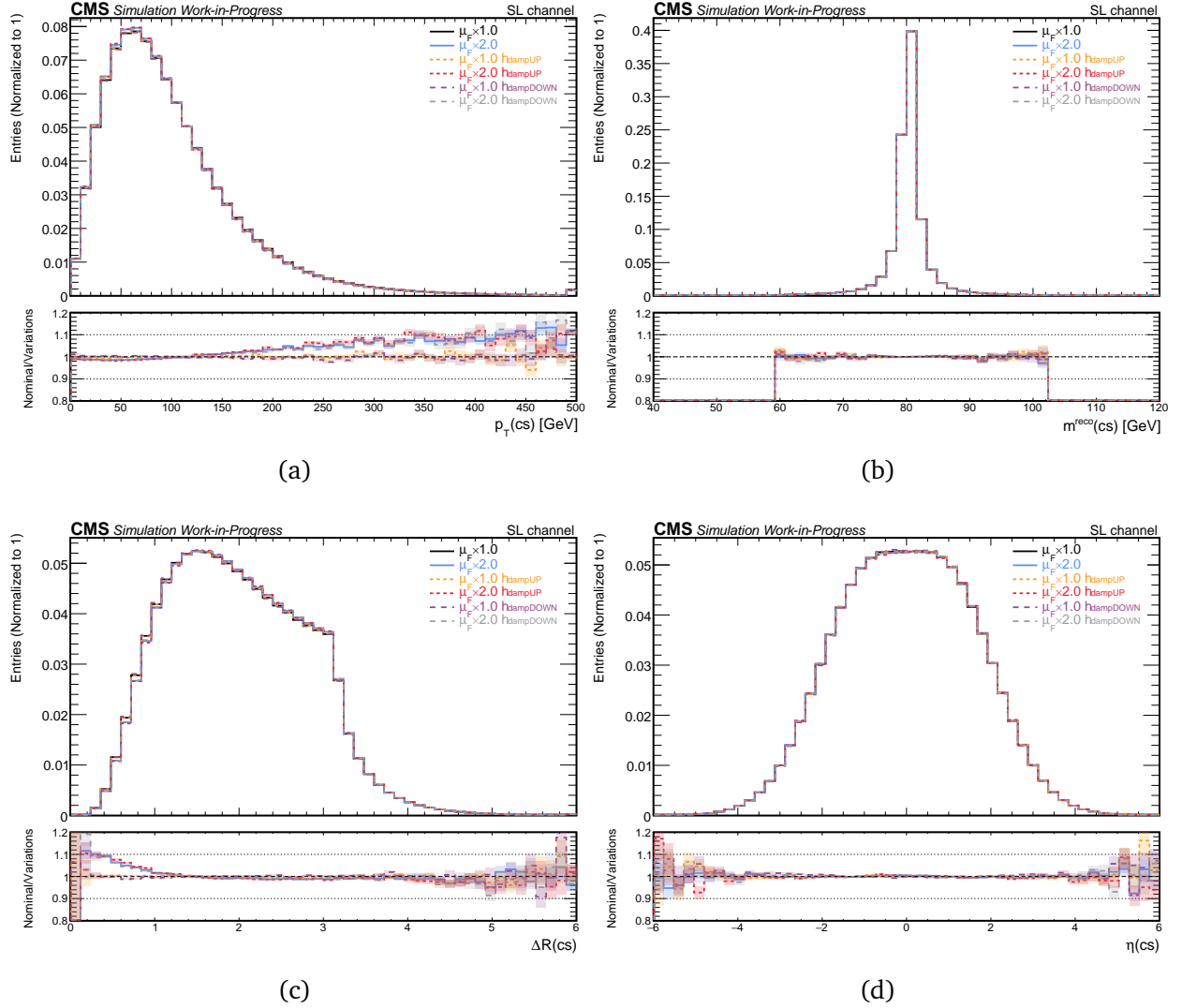


Figure B.24. Distributions of (a) transverse momentum, (b) invariant mass, (c) angular separation and (d) rapidity of the cs system for the six different settings used in the simulation. The lower panel shows the ratio of the nominal setting to the variations. The shaded bands represent statistical uncertainties. The last bins contain the overflow events.

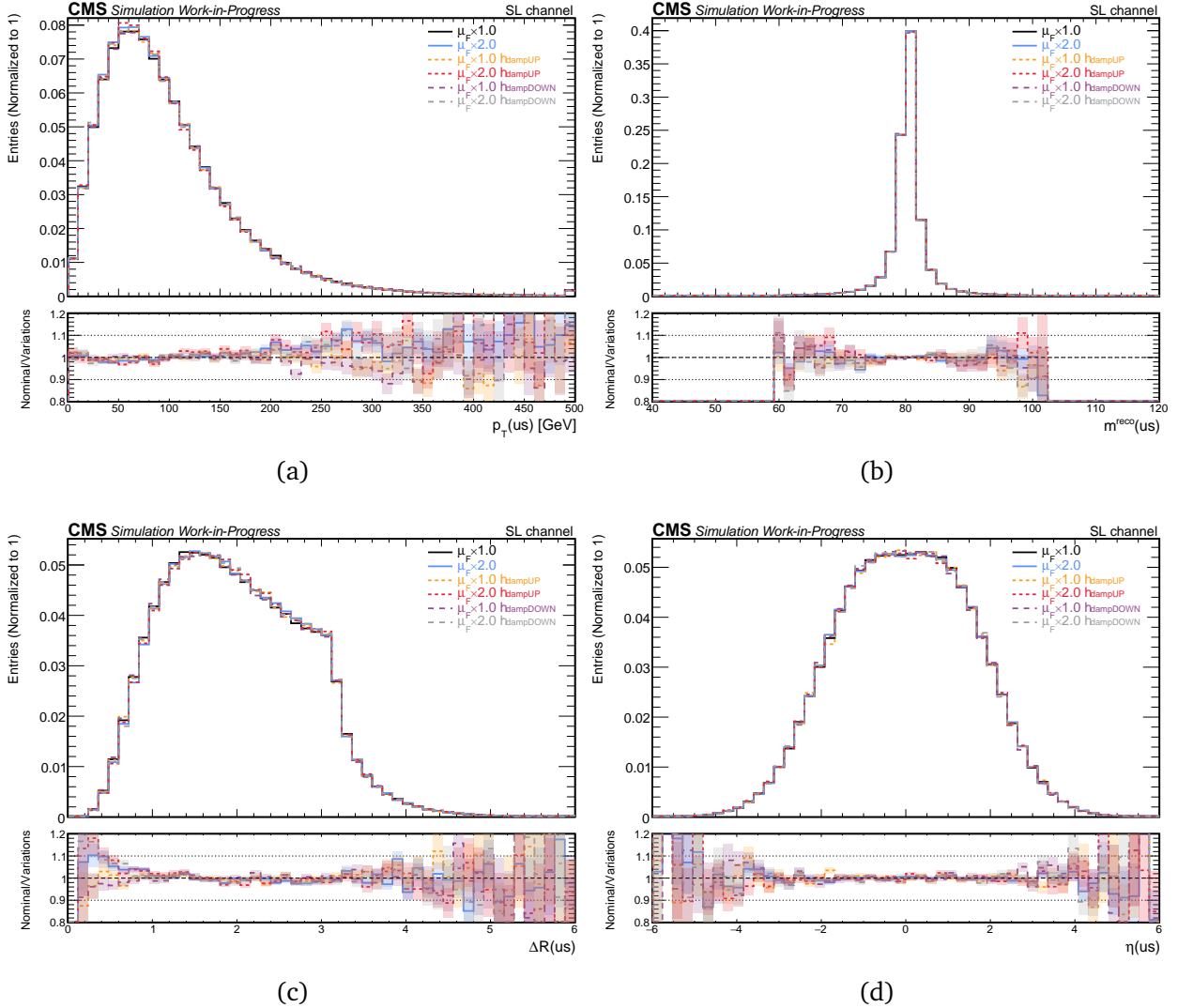


Figure B.25. Distributions of (a) transverse momentum, (b) invariant mass, (c) angular separation and (d) rapidity of the us system for the six different settings used in the simulation. The lower panel shows the ratio of the nominal setting to the variations. The shaded bands represent statistical uncertainties. The last bins contain the overflow events.

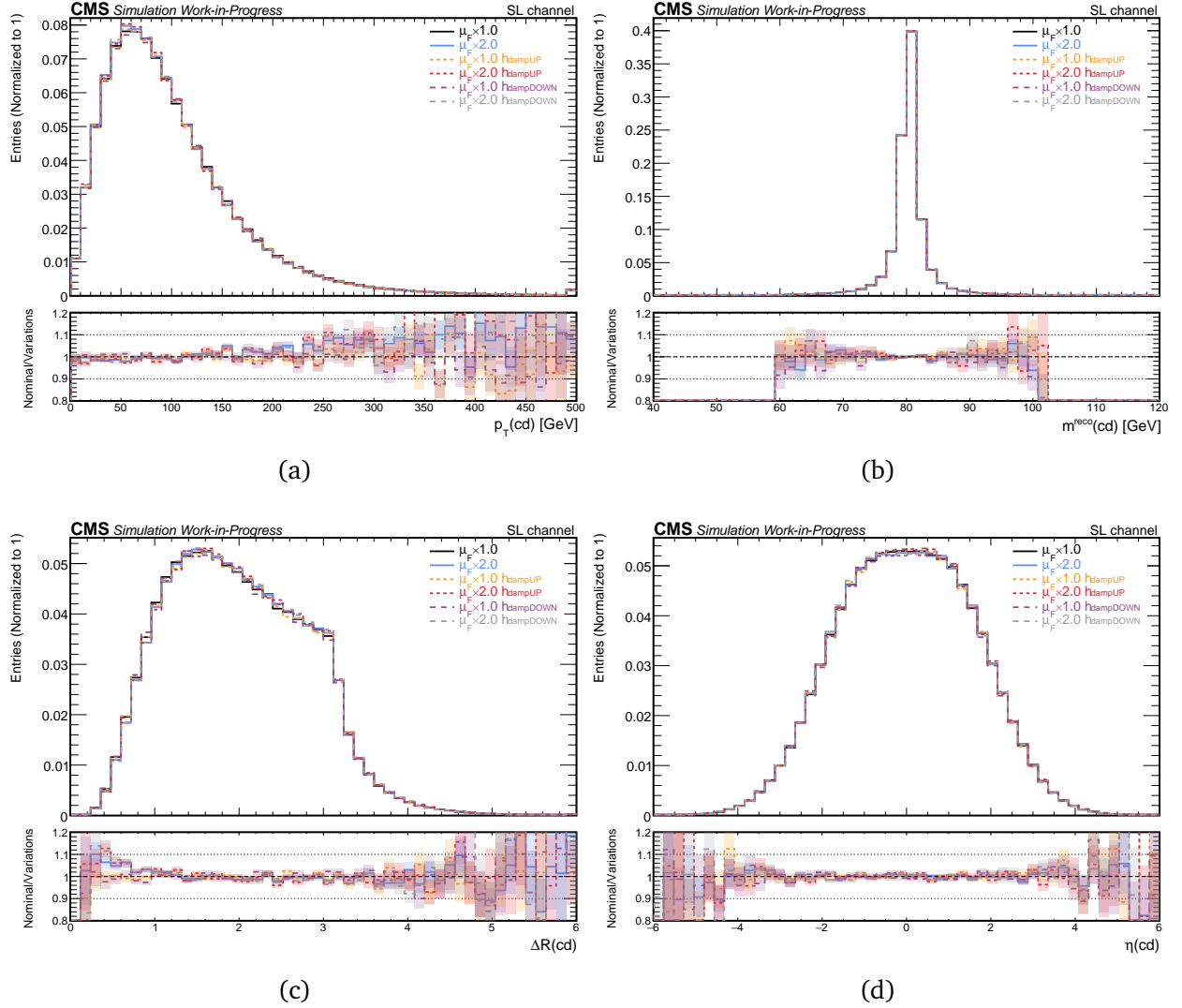


Figure B.26. Distributions of (a) transverse momentum, (b) invariant mass, (c) angular separation and (d) rapidity of the cd system for the six different settings used in the simulation. The lower panel shows the ratio of the nominal setting to the variations. The shaded bands represent statistical uncertainties. The last bins contain the overflow events.

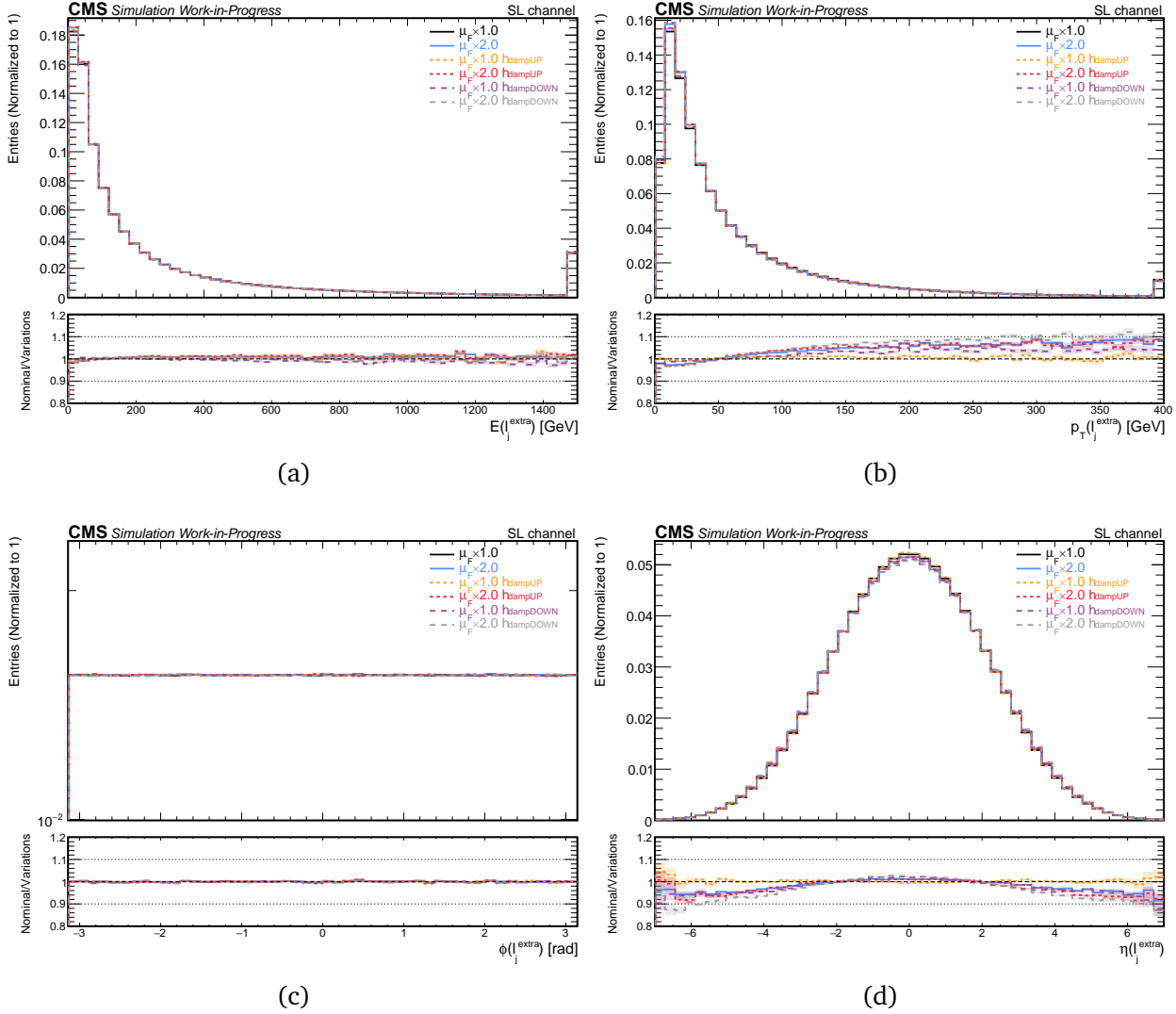


Figure B.27. Distributions of (a) energy, (b) transverse momentum, (c) azimuthal angle and (d) pseudorapidity of the extra light jet for the six different settings used in the simulation. The lower panel shows the ratio of the nominal setting to the variations. The shaded bands represent statistical uncertainties. The last bins contain the overflow events.

### B.3 FH channel

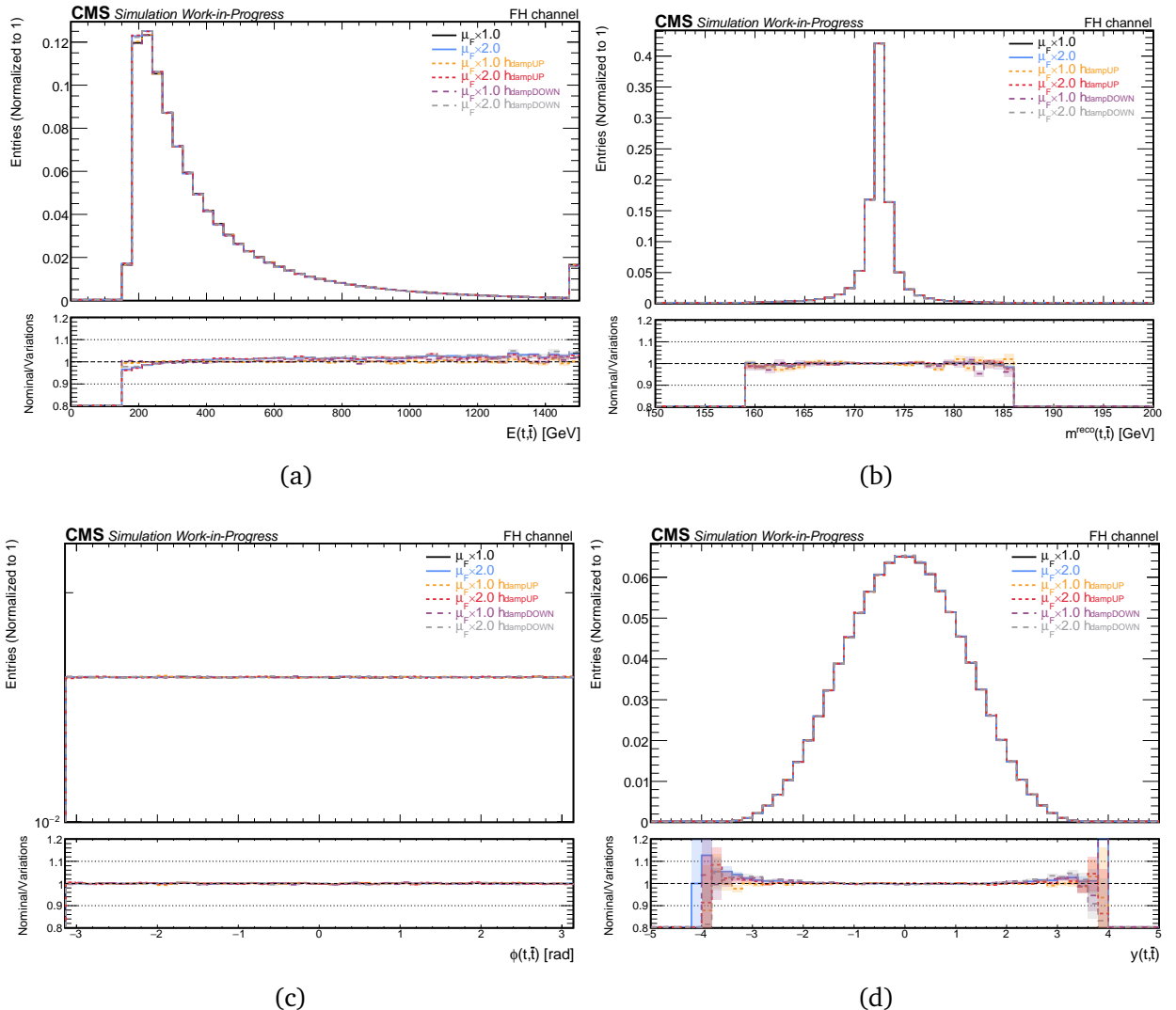


Figure B.28. Distributions of (a) energy, (b) reconstructed mass, (c) azimuthal angle and (d) rapidity of the  $t/\bar{t}$  quarks for the six different settings used in the simulation. The lower panel shows the ratio of the nominal setting to the variations. The shaded bands represent statistical uncertainties. The last bins contain the overflow events.

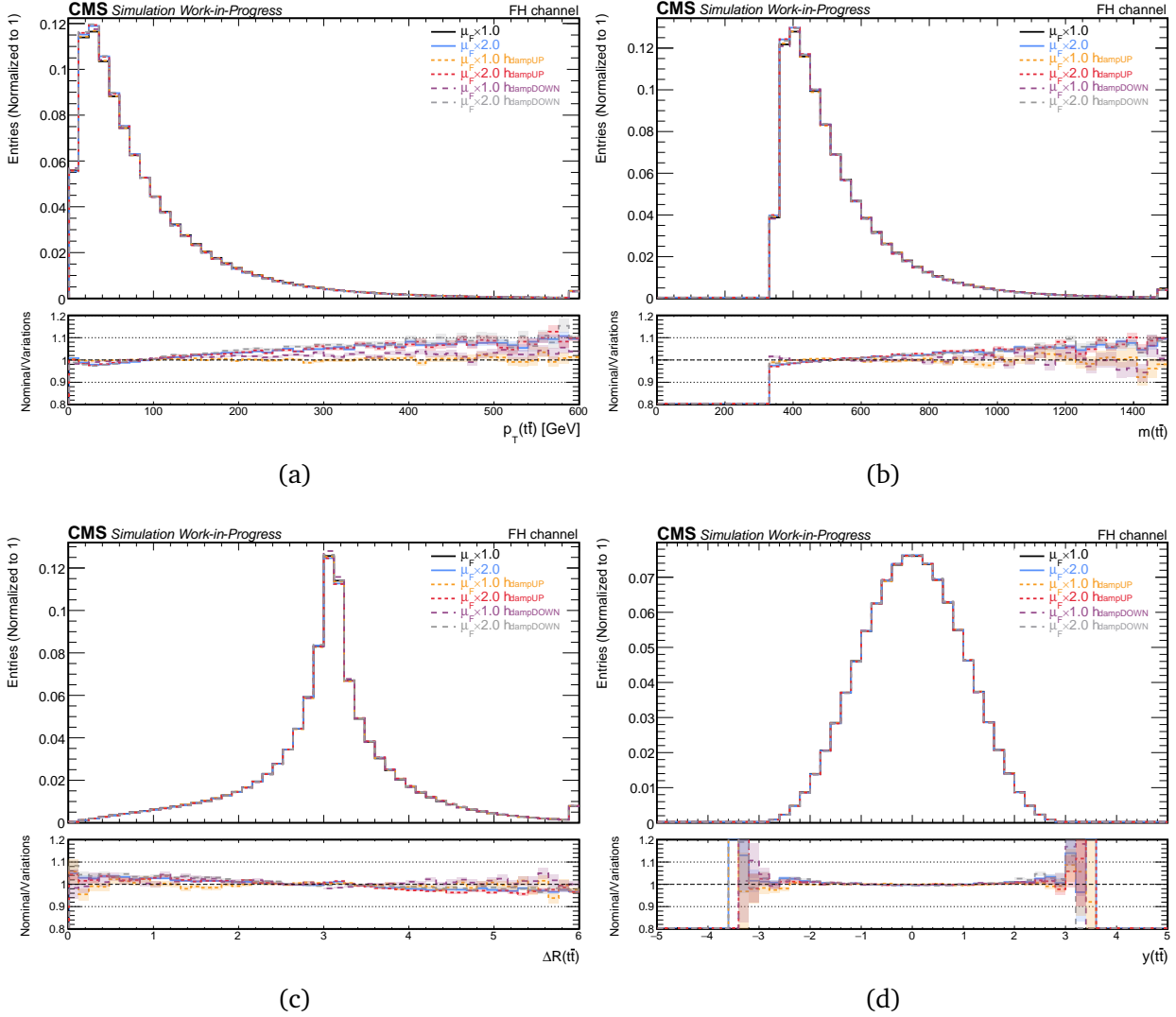


Figure B.29. Distributions of (a) transverse momentum, (b) invariant mass, (c) angular separation and (d) rapidity of the  $t\bar{t}$  system for the six different settings used in the simulation. The lower panel shows the ratio of the nominal setting to the variations. The shaded bands represent statistical uncertainties. The last bins contain the overflow events.

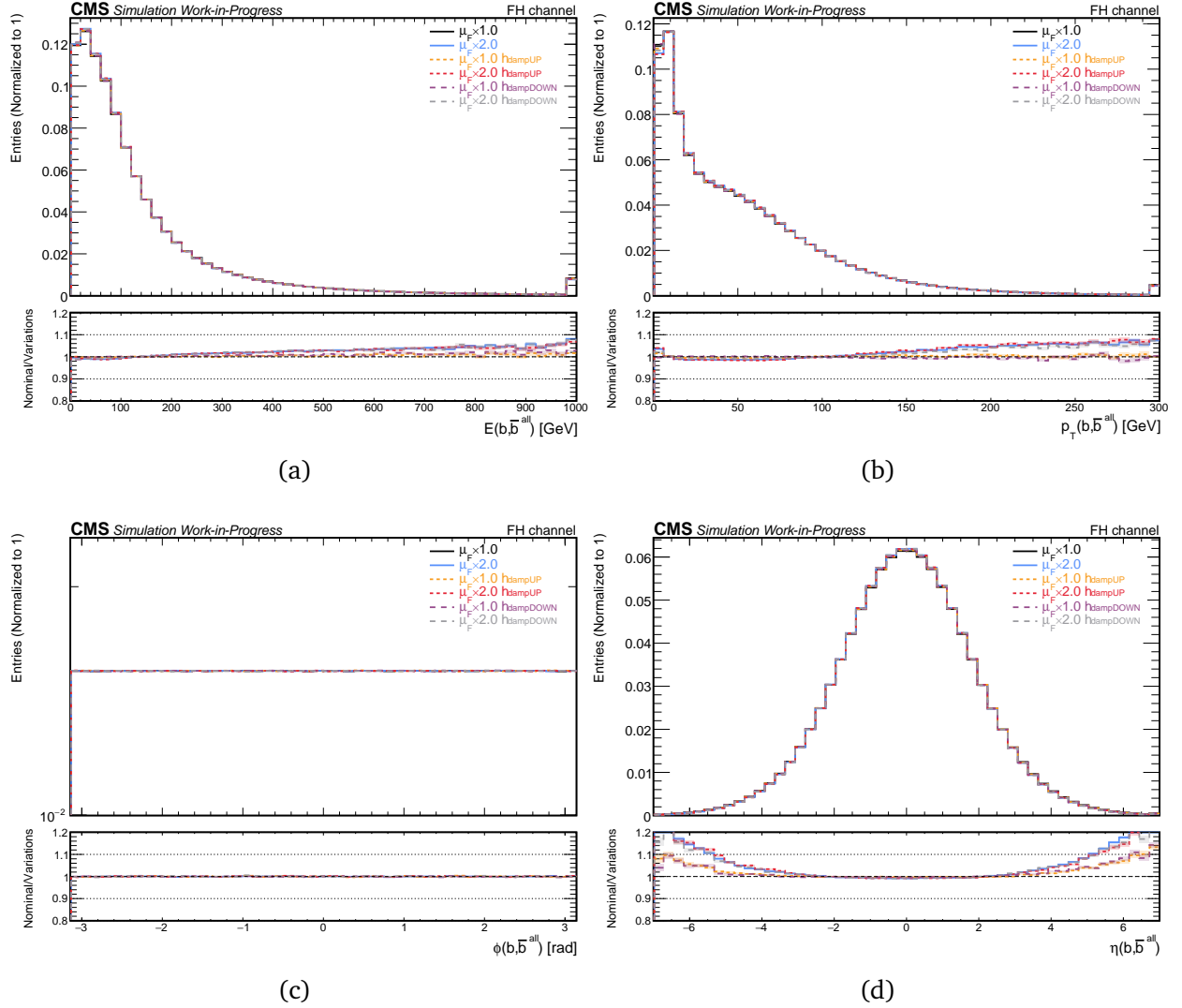


Figure B.30. Distributions of (a) energy, (b) transverse momentum, (c) azimuthal angle and (d) pseudorapidity of all the  $b/\bar{b}$  quarks for the six different settings used in the simulation. The lower panel shows the ratio of the nominal setting to the variations. The shaded bands represent statistical uncertainties. The last bins contain the overflow events.

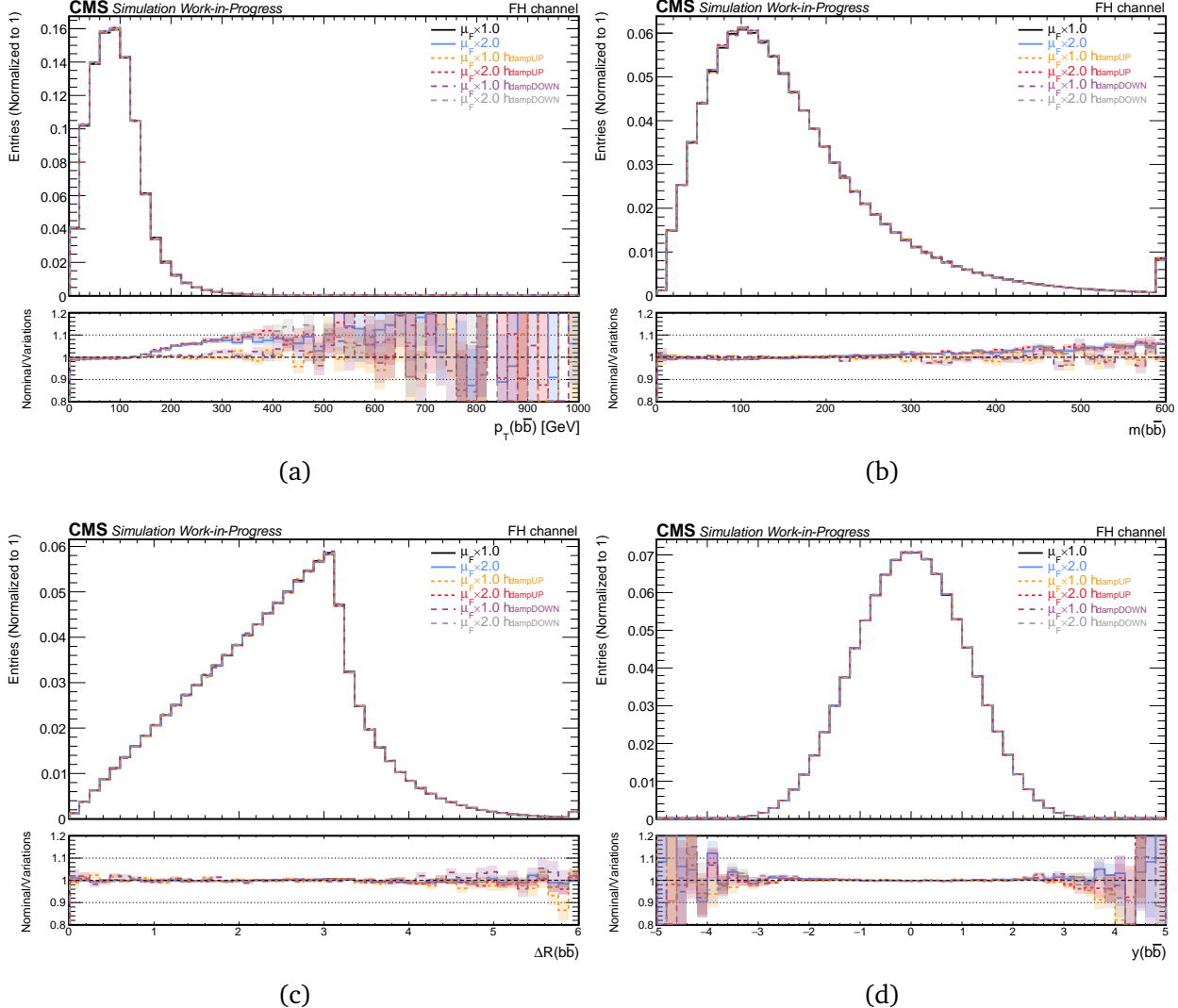


Figure B.31. Distributions of (a) transverse momentum, (b) invariant mass, (c) angular separation and (d) rapidity of the  $b\bar{b}$  system, related to top quarks, for the six different settings used in the simulation. The lower panel shows the ratio of the nominal setting to the variations. The shaded bands represent statistical uncertainties. The last bins contain the overflow events.

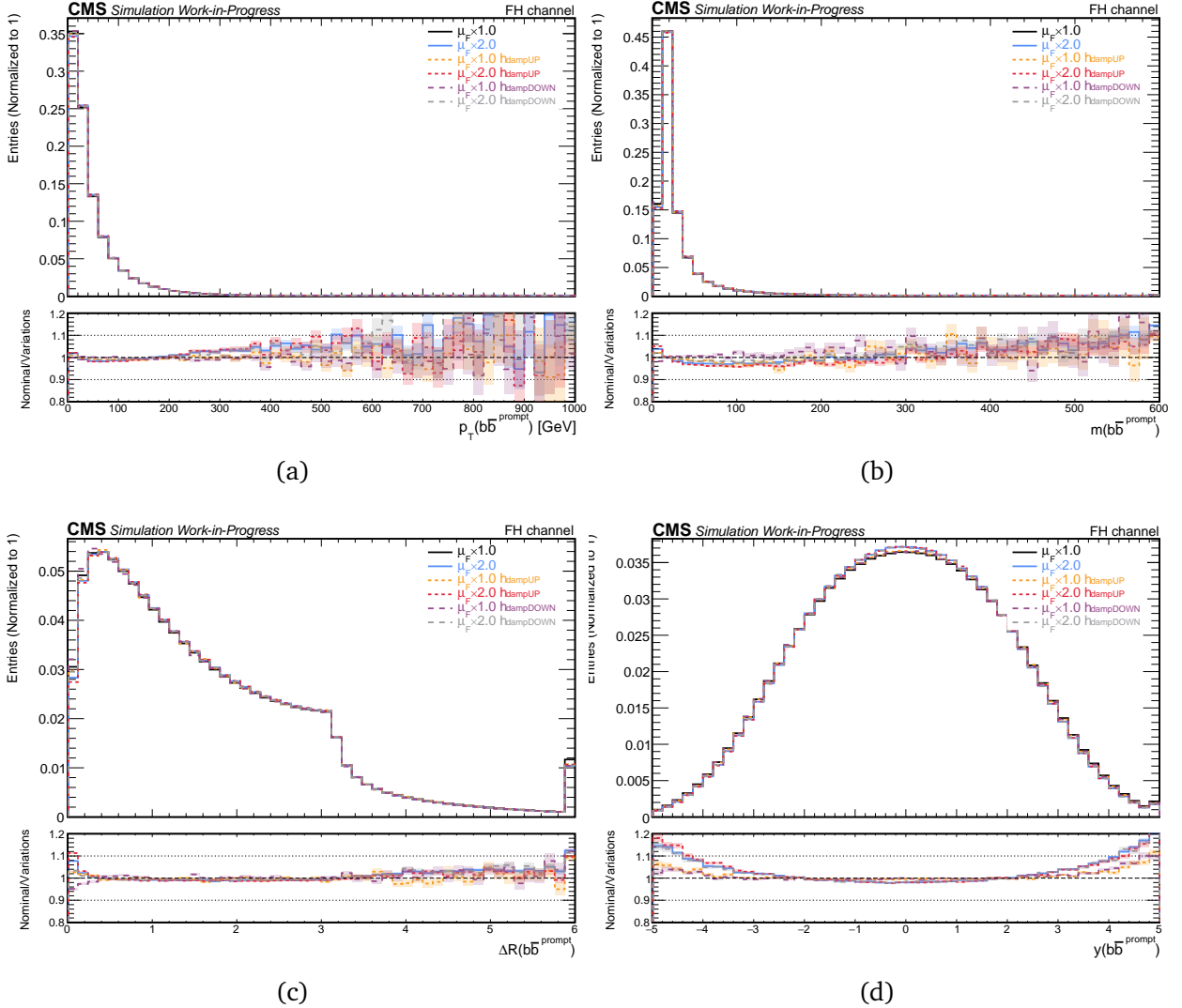


Figure B.32. Distributions of (a) transverse momentum, (b) invariant mass, (c) angular separation and (d) rapidity of the prompt  $b\bar{b}$  system for the six different settings used in the simulation. The lower panel shows the ratio of the nominal setting to the variations. The shaded bands represent statistical uncertainties. The last bins contain the overflow events.

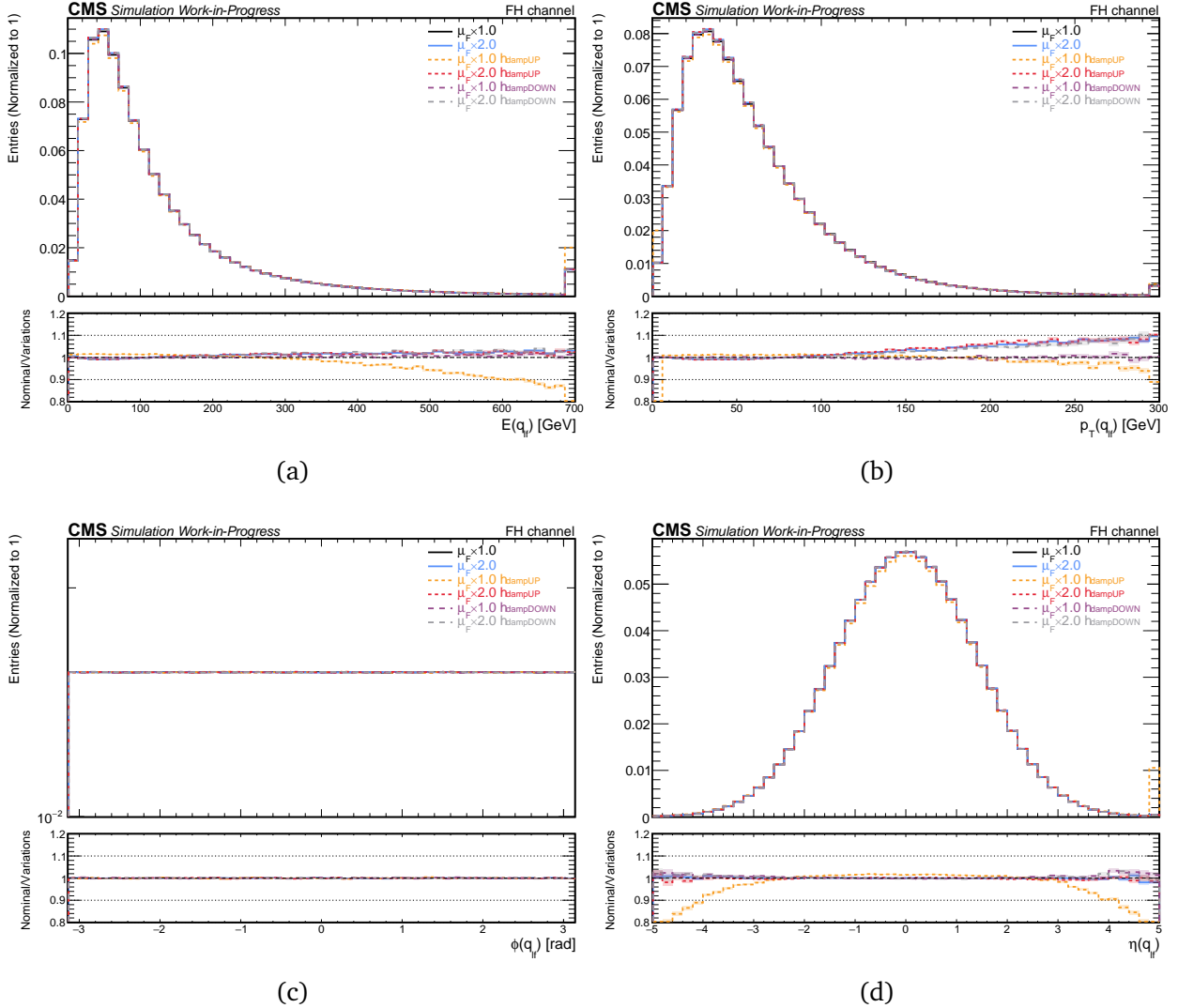


Figure B.33. Distributions of (a) energy, (b) transverse momentum, (c) azimuthal angle and (d) pseudorapidity of the light flavor quarks, related to W bosons, for the six different settings used in the simulation. The lower panel shows the ratio of the nominal setting to the variations. The shaded bands represent statistical uncertainties. The last bins contain the overflow events.

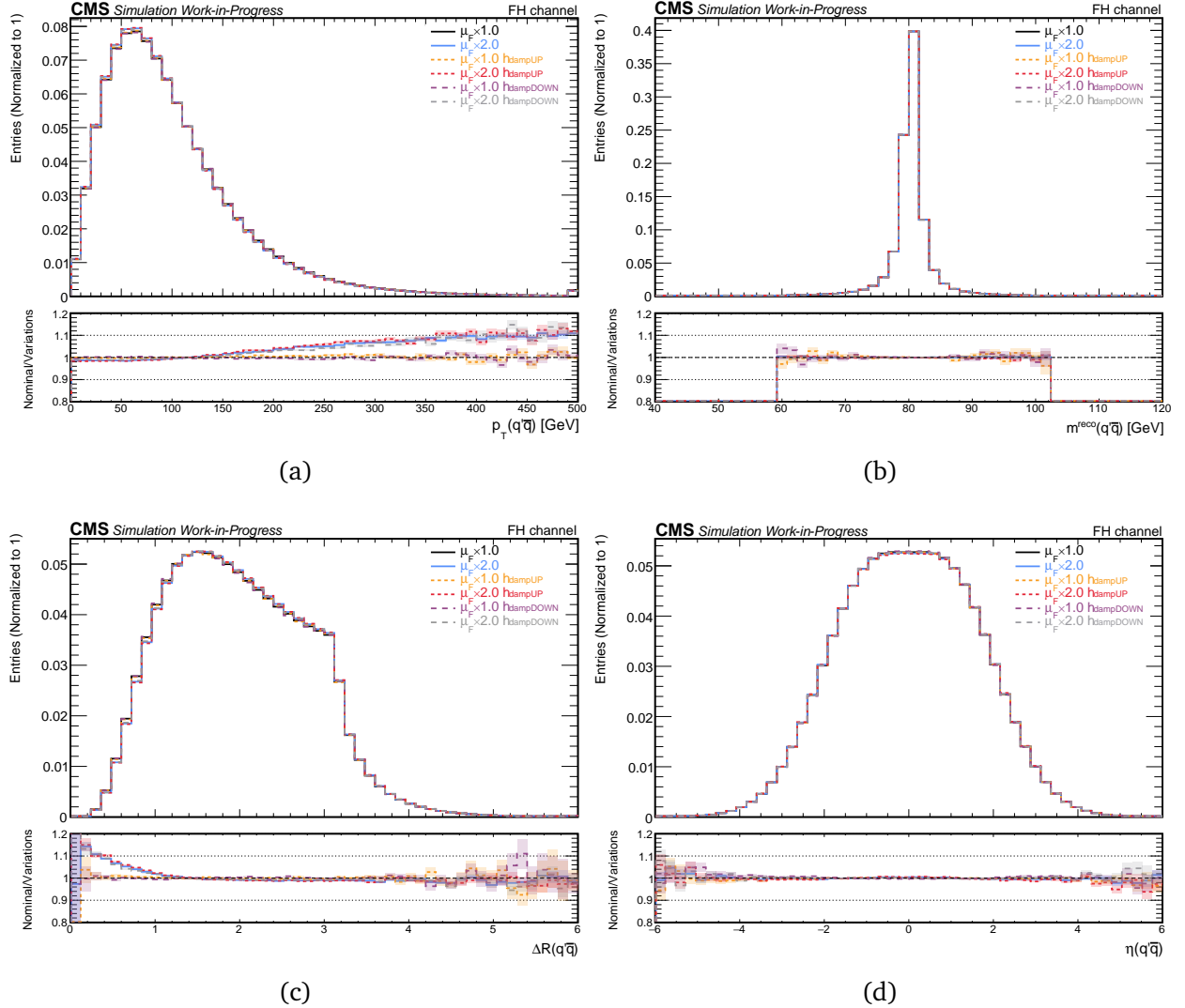


Figure B.34. Distributions of (a) transverse momentum, (b) invariant mass, (c) angular separation and (d) rapidity of the  $q\bar{q}$  system for the six different settings used in the simulation. The lower panel shows the ratio of the nominal setting to the variations. The shaded bands represent statistical uncertainties. The last bins contain the overflow events.

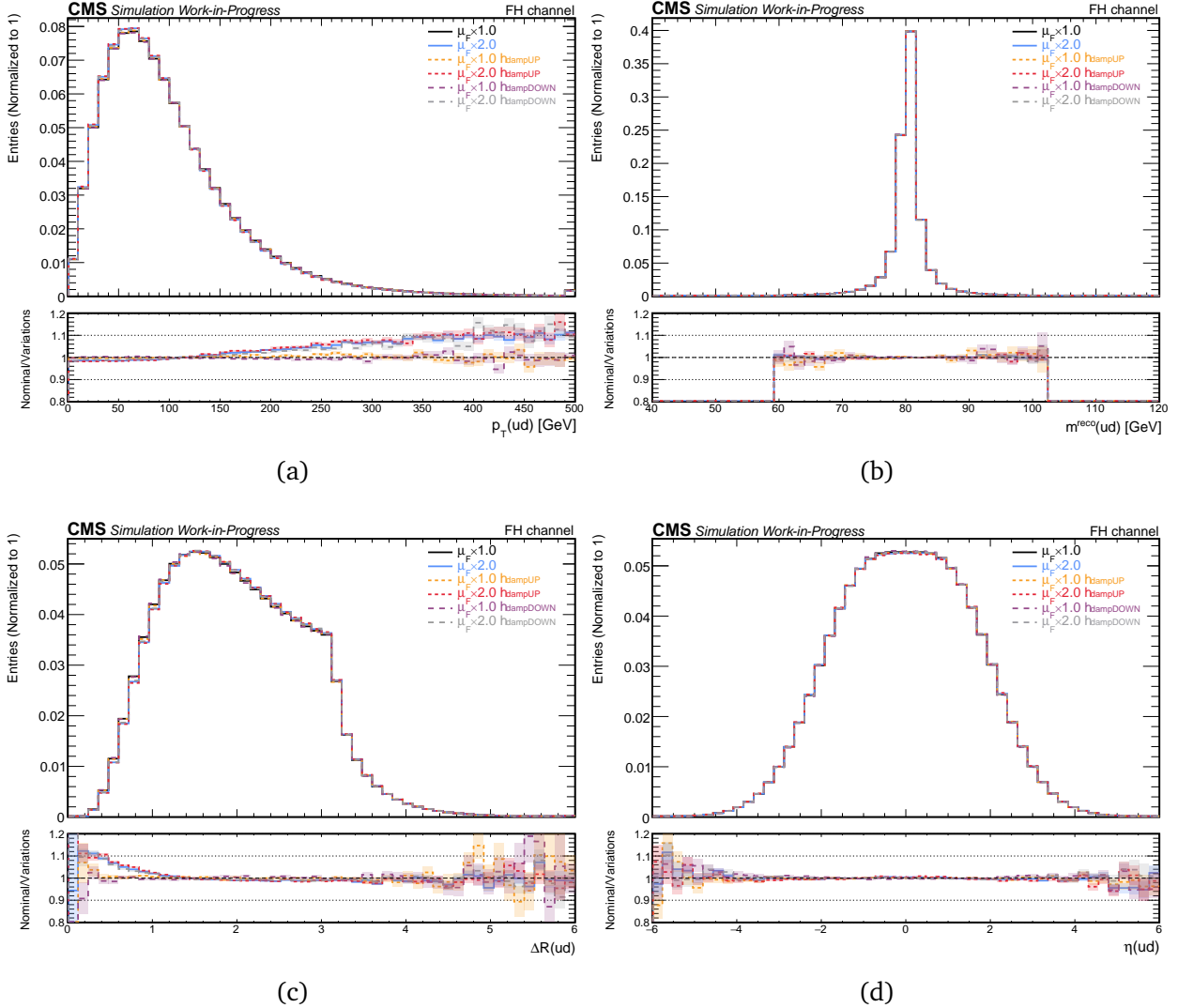


Figure B.35. Distributions of (a) transverse momentum, (b) invariant mass, (c) angular separation and (d) rapidity of the ud system for the six different settings used in the simulation. The lower panel shows the ratio of the nominal setting to the variations. The shaded bands represent statistical uncertainties. The last bins contain the overflow events.

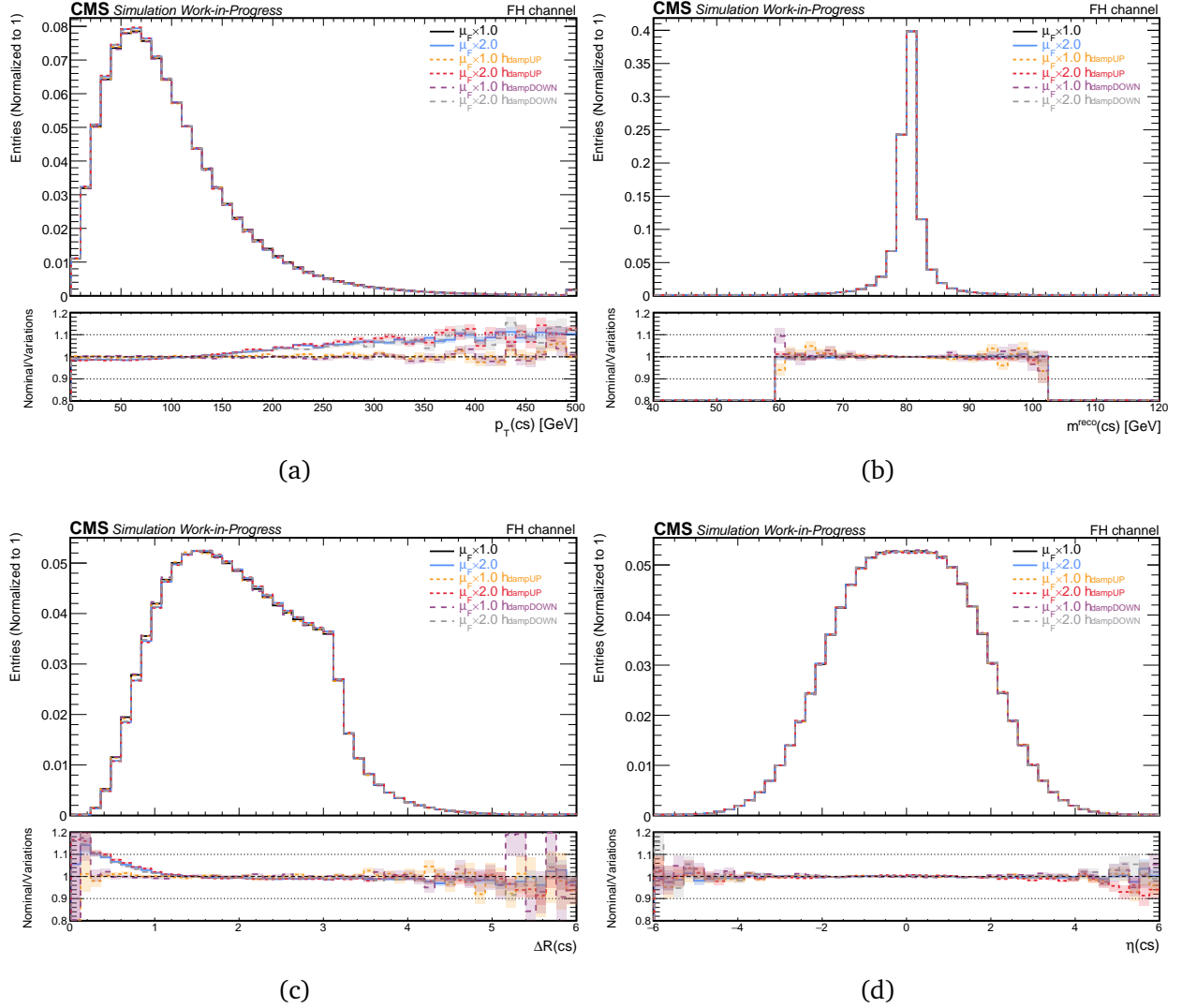


Figure B.36. Distributions of (a) transverse momentum, (b) invariant mass, (c) angular separation and (d) rapidity of the cs system for the six different settings used in the simulation. The lower panel shows the ratio of the nominal setting to the variations. The shaded bands represent statistical uncertainties. The last bins contain the overflow events.

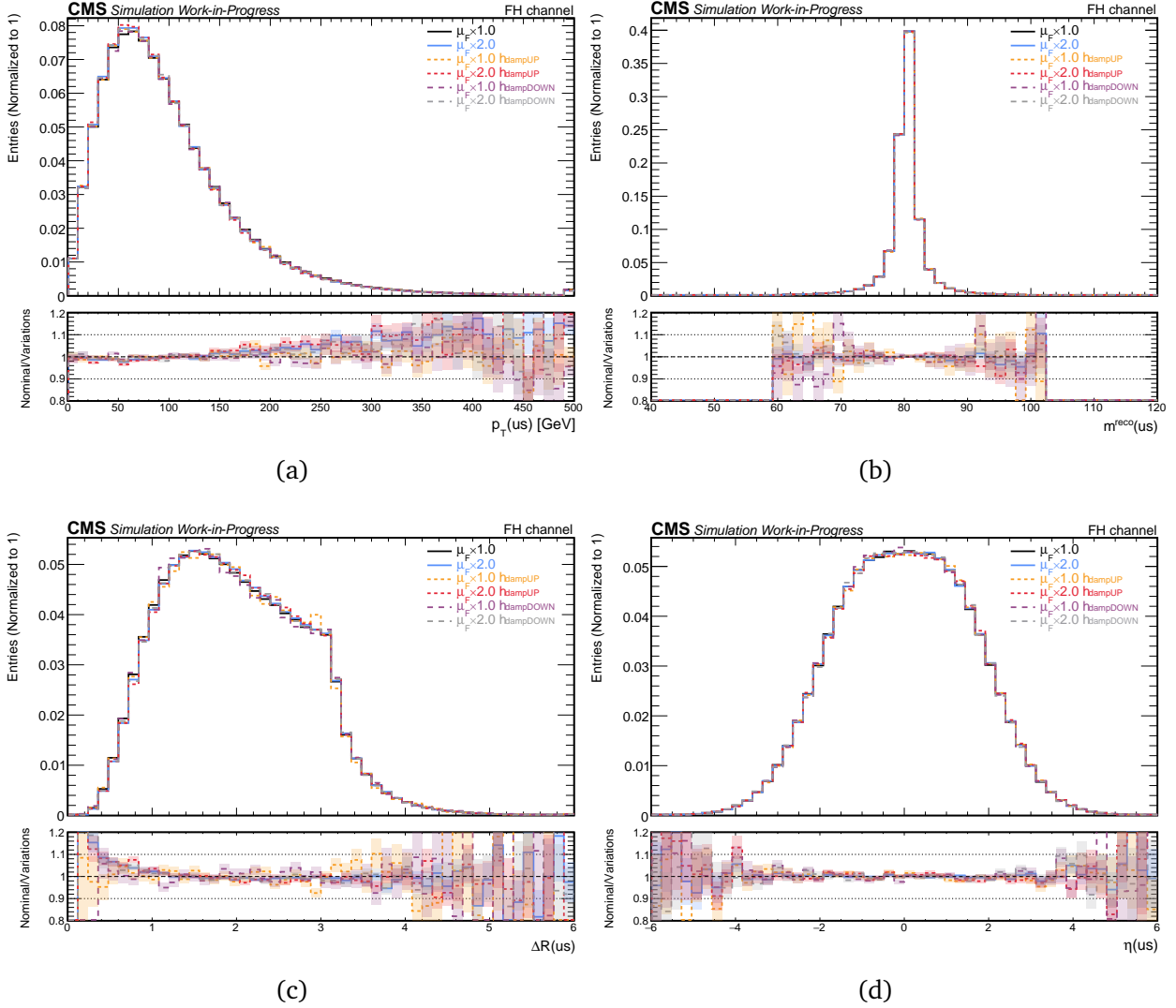


Figure B.37. Distributions of (a) transverse momentum, (b) invariant mass, (c) angular separation and (d) rapidity of the us system for the six different settings used in the simulation. The lower panel shows the ratio of the nominal setting to the variations. The shaded bands represent statistical uncertainties. The last bins contain the overflow events.

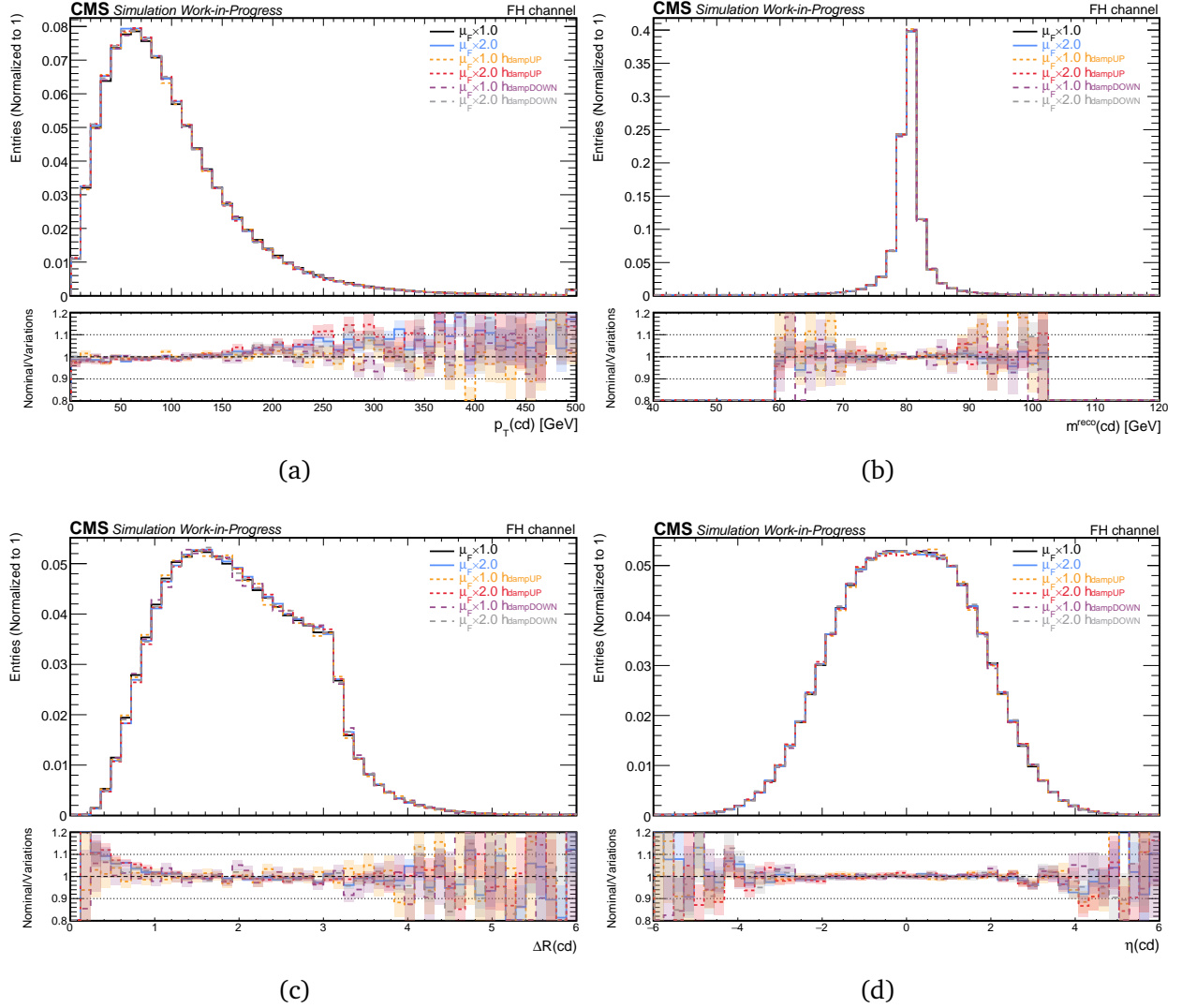


Figure B.38. Distributions of (a) transverse momentum, (b) invariant mass, (c) angular separation and (d) rapidity of the cd system for the six different settings used in the simulation. The lower panel shows the ratio of the nominal setting to the variations. The shaded bands represent statistical uncertainties. The last bins contain the overflow events.

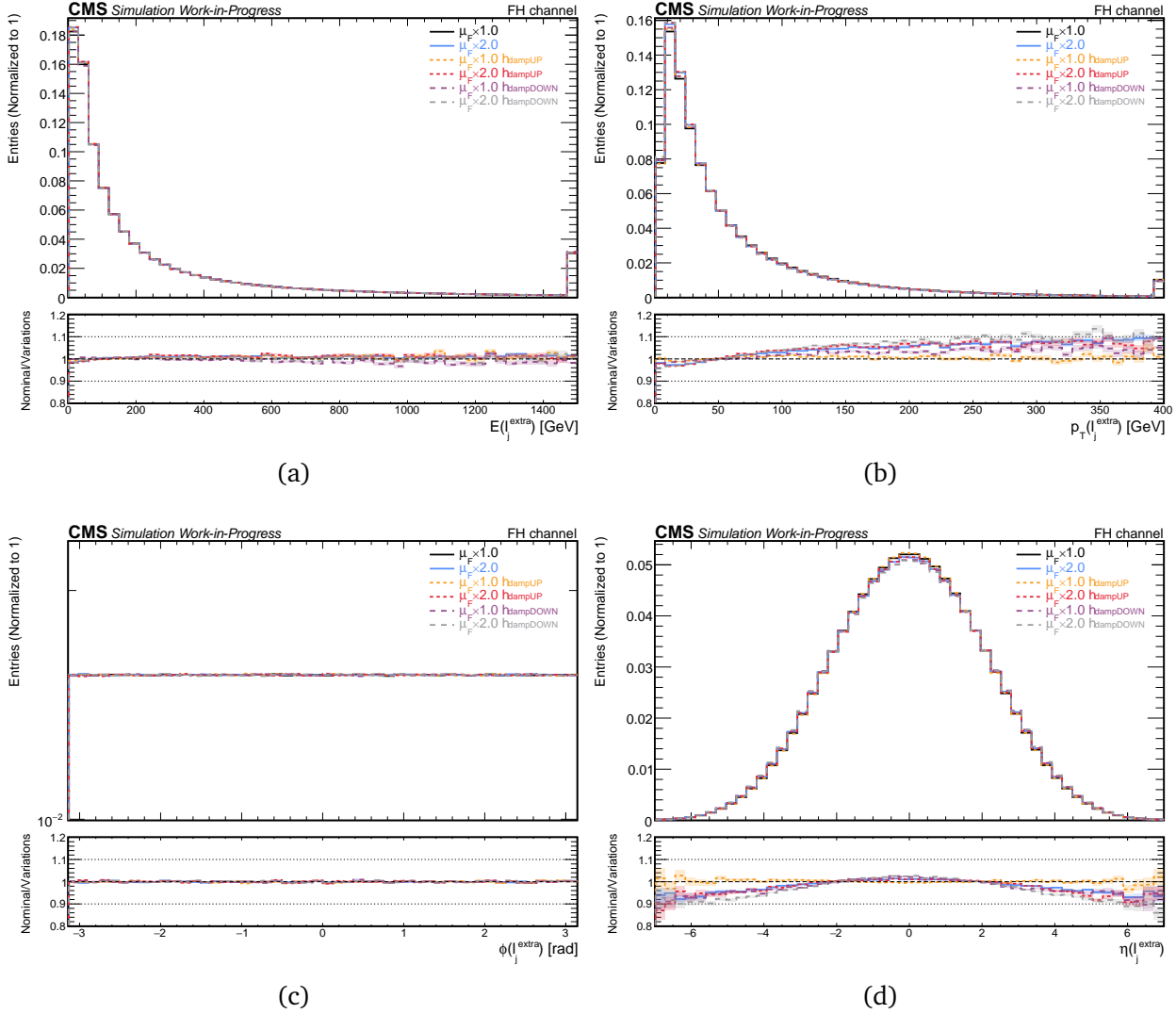


Figure B.39. Distributions of (a) energy, (b) transverse momentum, (c) azimuthal angle and (d) pseudorapidity of the extra light jet for the six different settings used in the simulation. The lower panel shows the ratio of the nominal setting to the variations. The shaded bands represent statistical uncertainties. The last bins contain the overflow events.